Carrying forward the legacy….

ISBN 978-90-365-2993-8
9 789036 529938 >

From Cells to Bone: Raman Microspectroscopy of the Mineralization of Stromal Cells

Vishnu Vardhan Pully

2010

From Cells to Bone:

Raman Microspectroscopy of the Mineralization of Stromal Cells

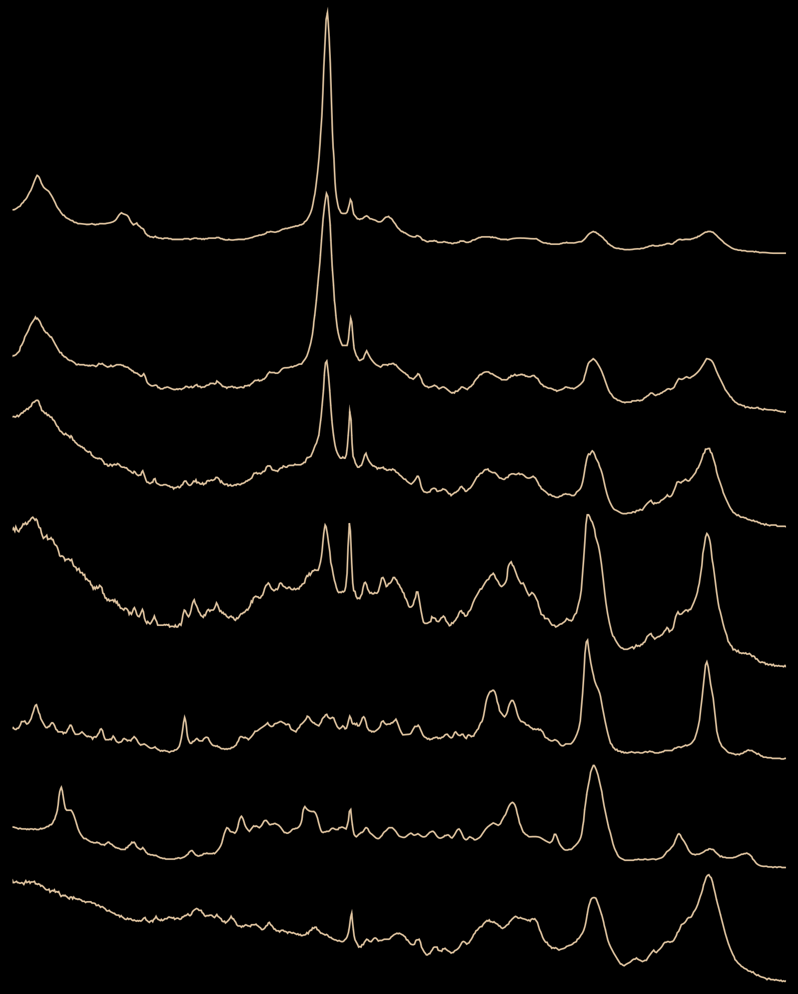

Vishnu Vardhan Pully

From Cells to Bone:

Raman Microspectroscopy of the Mineralization of Stromal Cells

Vishnu Vardhan Pully

Thesis committee members:

Prof. Dr. G. van der Steenhoven	University of Twente (chairman)
Prof. Dr. V. Subramaniam	University of Twente (thesis advisor)
Dr. C. Otto	University of Twente (assistant advisor)
Prof. Dr. M. Morris	University of Michigan-Ann Arbor
Dr. B. Vaandrager	Utrecht University
Prof. Dr. C. A. van Blitterswijk	University of Twente
Prof. Dr. J. L. Herek	University of Twente

The research described in this thesis was carried out at the Biophysical Engineering Group, MIRA Institute for Biomedical Technology and Technical Medicine, MESA+ Institute for Nanotechnology and Faculty of Science and Technology, University of Twente, P. O. Box 217, 7500 AE Enschede, The Netherlands.

This research has been financially supported by the Dutch Program for Tissue Engineering (DPTE) through the Grant number TGT.6737.

Cover Design: Vishnu Vardhan Pully & Remco Verdoold

Front cover page illustrates the Raman spectroscopic information of osteogenic differentiation and mineralization of human bone marrow stromal cells over a 60 day culture period (bottom to up, spectra acquired on Day 0, 25, 30, 35, 40, 45 and 60). Back cover page shows picture of Sir C.V. Raman along with his spectrograph (top image, source: http://www.photonics.cusat.edu/Article5.html) and picture from author of this thesis (bottom image).

Printed by: Wöhrmann Print Service, Zutphen, The Netherlands.

ISBN: 978-90-365-2993-8
DOI: 10.3990/1.9789036529938

FROM CELLS TO BONE: RAMAN MICROSPECTROSCOPY OF THE MINERALIZATION OF STROMAL CELLS

DISSERTATION

to obtain
the degree of doctor at the University of Twente,
on the authority of the rector magnificus,
prof. dr. H. Brinksma,
on account of the decision of the graduation committee,
to be publicly defended
on Friday, March 19th 2010, at 13.15

by

Vishnu Vardhan Pully
born on September 9th, 1981
in Bellary, India

This dissertation has been approved by:

Prof. Dr. V. Subramaniam (Promotor)

Dr. C. Otto (Assistant Promotor)

To my parents

Table of contents

Chapter 1

Introduction

Bone is the largest connective tissue which is regenerated throughout life. During embryogenesis, mesenchymal stem cells play a significant role in the development of skeletal structures by intra-membranous ossification and endochondral bone formation. In vitro bone formation studies with similar cells to understand the in vivo process have been established. However there is a lack of understanding at the molecular level of the bone formation. The molecular level understanding of these processes can enable better treatment methods for bone related disorders.

This chapter introduces the concepts of bone biology and Raman microscopy in the context of the research question we wish to address. In this work we show the feasibility of vibrational Raman microspectroscopy to elucidate in vitro bone formation. This method enables a non-invasive and label free approach to obtain chemical information from in vitro cultures. We focus on bone marrow derived stromal stem cells and their differentiation towards osteogenic lineage leading to bone formation to define Raman biomarkers which illustrate early stage of differentiation of stromal cells to osteoblasts and to late stage of mineralization. The mineralization studies over the in vitro differentiated stem cells showed variation in composition of minerals at the de novo stage until a more mature nodule was formed.

Parts of this chapter have been submitted as a book chapter: V. V. Pully and C. Otto, "Raman microspectroscopy to monitor tissue development in microbioreactors" in Biomedical Applications of Raman and Infrared Spectroscopy (Edited by M. Ghomi), IOP press.

1.1 Bone biology

Bone is dynamic and extremely well organised connective tissue that enables protection of internal organs, supports muscular contraction, and withstands load that gives stability in all higher vertebrates.[1, 2] It is a highly vascularised living tissue with a unique capability to heal and remodel without leaving a scar.[2] Bone plays a significant role in haematopoiesis and maintaining mineral homeostasis of the body due to which it is considered as an ultimate smart material. Bone is a complex tissue which is made up of both organic and inorganic materials. The inorganic part is mainly calcium hydroxyapatite that provides a high compressive strength. The organic part is mainly collagen type-I which imparts significant degree of elasticity to the bone.

The human body contains 213 bones which are structurally classified as long bones, short bones, flat bones, irregular bones and sesamoid bones. Morphologically, each bone is not a uniform solid material; rather they are of two distinct forms, cortical bone and trabecular bone. Cortical bone or compact bone is the hard outer layer which plays a crucial role in mechanical and protective functions. This part of the bone has a smooth, white and solid appearance which accounts for 80% of the total bone mass of the adult skeleton. On the other hand trabecular bone has loosely organised networks forming a porous structure that enables room for blood vessels and marrow. Trabecular bone, also known as cancellous bone, forms the remaining 20% of the total bone mass, but has ten times more surface area than compact bone.[3]

Typically bone is composed of four main types of cells; osteoblast, osteocyte, bone lining cells and osteoclasts. Osteoblasts are mono-nucleated bone forming cells originating from the osteoprogenitor cells located in the periosteum (outer layer) and endosteum (inner layer) of the bone or from mesenchymal stem cells in the bone marrow. Osteoblasts are the mature bone cells located on the surface of the existing matrix. Osteoblasts make a protein mixture known as osteoid which is composed mainly of collagen type-I and also non-collagenous proteins such as proteoglycans, γ-carboxylated (gla) proteins, and glycosylated proteins with and without potential cell attachment activities.[4] The osteoid gets deposited with hydroxyapatite crystals and convert to a hard matrix in a cell mediated process. The osteoblasts which are deeply embedded within mineralised matrix are called osteocytes, which are able to produce bone matrix in small amounts, but cannot divide any further. Osteocytes communicate with other osteocytes or osteoblasts by tiny channels called gap junctions made of membrane proteins known as connexins. Gap junctions enable osteocyte maturation, survival and activity such as bone formation, matrix maintenance and calcium homeostasis.[5] Bone lining cells cover the inactive non-remodelling surface of the bone. These cells are flat, elongated, having slightly ovoid nuclei. These cells can be induced to proliferate and differentiate to osteoprogenitor cells. Bone lining cells play a vital role in mineral homeostasis by maintaining the bone fluids and the fluxes of ions between bone fluids and interstitial fluid compartments.[6] Osteoclasts are multinucleated cells originating from hematopoietic stem cells in the bone marrow, which are responsible for bone resorption. They are derived from monocytes in the blood stream which collect at the sites of bone resorption. There they fuse to form active multinucleated osteoclast cells.[7] Both osteoblasts and osteoclasts help in bone remodelling, which is a dynamic and life long process during which old bone is removed from the skeleton by osteoclasts and new bone is added by osteoblasts.

During embryogenesis, skeletal development takes place by two forms of cell mediated mineralization processes, recognised as intramembranous ossification and endochondral ossification. Bones corresponding to the craniofacial skeleton are formed by intramembranous ossification, which occurs by direct transformation of embryonic stem cells to osteoblasts. The axial and limb skeletal bones are first formed by endochondral ossification, wherein the embryonic stem cells first differentiate to chondrocytes that forms a framework of cartilage, which is then replaced by bone and bone marrow with the help of osteoblasts.[8, 9]

1.2 Current trends and prospects

Every year, in the United States alone more than 1 million surgical procedures related to bone deficiencies are performed costing billions of dollars.[10] These procedures vary from joint replacements, bone grafts, and internal fixations to facial reconstruction. In the years to come due to ageing of the population as well as its increase, the socioeconomic consequence of treating patients affected with above problems is a major concern not only for the United States but also for the European Union. Current treatments include autogenous bone grafts, allogenous bone grafts and synthetic biomaterials.[11]

The preparation of autogenous bone grafts involves the harvesting of bone taken from another part of the patient's own body. This procedure is widely used and considered to be the golden standard since it provides osteogenic cells and essential osteogenic factors necessary for bone healing and regeneration. Although it shows a high success rate, it is restricted due to the limited amount of bone-graft material that can be obtained from the donor site. Allogenous bone grafts are prepared by bone harvest from different subjects but of the same species. This procedure offers lower success rates than the autogenous grafts, due to immune rejection, pathogen transmission from donor to host and an absence of viable cells. Synthetic biomaterials such as metals, ceramics and plastics are also used in addition to the other two procedures. However these approaches also have their own disadvantages like inferior mechanical properties, tissue rejection, non-biocompatibility, toxicity and wear.

These drawbacks show a clear need for an alternative and adequate method for bone replacement. A possible solution could be cell-based bone tissue engineering, which may enable effective substitutes for bone related disorders.

1.3 Cell-based bone tissue engineering

The definition of tissue engineering by Langer and Vacanti,[10, 12] is "an interdisciplinary field that applies the principles of engineering and life sciences toward the development of biological substitutes that restore, maintain, or improve tissue function or a whole organ". The drawbacks of the earlier stated treatment methodologies are overcome by the combined knowledge from physics, chemistry, biology, material sciences, engineering and medicine.[10, 13]

Bone tissue engineering deals with isolation and expansion of osteoprogenitor cells from patients or donors and seeding them onto biocompatible and biodegradable scaffolds. Osteoprogenitor cells are generally osteoblasts that can be derived from mesenchymal stem cells, embryonic stem cells and adult stem cells.[14] *In vitro* culture of these cells in suitable osteogenic media, which contains proper proteins, growth factors and osteo-inductive molecules, differentiate the cells into osteogenic lineage. This leads to hydroxyapatite mineralization in these differentiated cells, which is chemically similar to *in vivo* bone. Scaffolds are used in cell-based tissue engineering to provide a temporary 3-dimensional (3D) environment for the cells to grow, hence accommodate the 3D structure of *in vivo* bone.[14] Cells seeded over scaffolds and implanted in the body to replace the damaged tissue show growth of bone with subsequent degradation of the scaffold. The scaffolds for tissue engineering mainly include ceramics and natural and synthetic biodegradable polymers. These scaffolds for bone tissue engineering must be biocompatible, biodegradable, osteoinductive, have appropriate surface properties that enable cell adhesion and proliferation (osteoconductive), have enough porosity to enable cell in-growth, and possess sufficient mechanical properties to withstand pressure.[14]

The most common choice for cell-based bone tissue engineering includes osteoblasts from bone marrow or stem cells from autologous source. Unlike osteoblasts, stem cells are undifferentiated cells with high capability for proliferation, self renewal and pluripotency.[15] Based on the source, the stem cells can be classified as embryonic stem cells (ESC) and adult stem cells (ASC). ESCs are obtained from the inner cell mass of the blastocyst stage during the embryogenesis of the fertilized oocyte.[16, 17] ASC can be obtained from fully differentiated tissues such as bone marrow, periosteum, muscle, fat, brain and skin. Both ASCs and ESCs have very good differentiation potential, showing a very good pluripotency towards various lineages[18, 19] such as cardiomyocyte,[20] haematopoietic,[21] bone,[18, 19] neuron,[22] chondrocyte,[23-25] tendon,[26, 27] adipocyte[28] and hepatocyte.[29, 30] The ASCs are more commonly referred to as mesenchymal stem cells (MSC).[18, 31-33] The source of these cells is from any of the mesenchymal tissues, and under suitable culture conditions, these cells can be differentiated towards the mesenchymal origins or to any other lineages. This process is referred to as mesengenic process.

ESCs have enormous potential for cell-based tissue engineering; however protocols for direct differentiation of these cells are yet to develop completely. Also the ESCs have drawbacks regarding immunological incompatibility with the host cells.[34] These cells are considered to be tumorigenic because of their excessive uncontrolled proliferation capability. Due to these socio-ethical problems, ESCs are less frequently used. On the whole, MSCs have an edge over the ESCs with respect to cell-based bone tissue engineering. MSCs have their own disadvantages like availability (1 in 100 000 cells)[32] and reduced differentiation capability particularly when derived from elderly patients.

1.4 Lineage commitment and mineralization

In vitro culture of ASCs or MSCs obtained from bone marrow biopsies in foetal bovine serum show fibroblast colonies which are derived from single cells. These are referred to as colony forming unit fibroblasts[35] and addressed by researchers as bone marrow stromal cells (BMSCs), multipotent adult progenitor cells (MAPCs), mesenchymal stem cells (MSCs), bone marrow stromal stem cells (BMSSCs), and mesodermal progenitor cells (MPCs).[36] The term ‘stromal cell’ is used to refer to the adherent nature of these cells. *In vitro* cell-based bone tissue engineering requires a large number of pluripotent or multipotent BMSCs. BMSCs thereafter need to be proliferated without any compromise on their multipotency.[36] Once a certain numbers of BMSCs are obtained, they are directed towards osteogenic lineage by various developmental signalling pathways and transcriptional regulators.[37] The osteogenic lineage can be characterised by various intermediate stages such as osteoprogenitor cells, preosteoblast, mature osteoblast and osteocyte before showing *in vitro* mineralization as seen in Figure 1.[37]

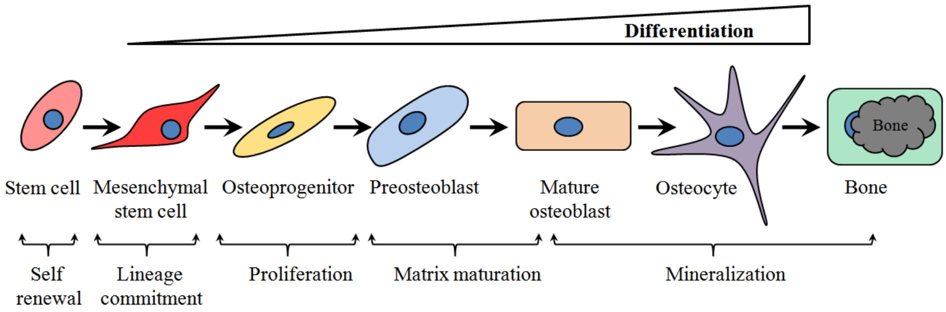

Figure 1: Schematic overview of growth and differentiation of BMSCs towards osteoblast leading to *in vitro* bone formation.

The basic building block of bone is composed of collagen type-I for 90% and remaining 10% forms non-collagenous proteins (proteoglycans, glycosylated proteins, glycosylated proteins with potential cell attachment activities and γ-carboxylated (gla) proteins), lipids and other collagen types secreted during the osteoblast stage.

Collagen type-I is a triple helical molecule composed of two identical α_1 chains and one α_2 chain cross linked by hydrogen bonding. Collagen chains (each made of 1000 amino acids) are mainly Glycine-X-Y repeating triplet (where usually X= proline and Y= Hydroxyproline) molecule. Amino acids in the cells such as lysine and proline undergo hydroxylation over individual α chains resulting in hydroxylysine and hydroxyproline. Hydroxylation is followed by glycosylation of lysine or hydroxylysine with glucose or galactose. This is followed by the formation of intra- and inter-molecular covalent cross links. The triple helix structure formed in the rough endoplasmic reticulum is referred as procollagen. Procollagen is then exocytosed by Golgi bodies. Post translational processing of procollagen results in collagen which adheres to the cell membrane by certain proteins like integrins and fibronectin. Each linear molecule of collagen is ~300 nm long, and is aligned to the next in a parallel fashion to form a collagen fibril. These fibrils are bundled together to form fibres. Within the collagen fibrils, gaps exist at the ends of the molecules which are referred to ‘hole zones’. Also ‘pores’ are created along the sides of two parallel molecules. These holes and pores are composed of non-collagenous proteins and phospholipids as mentioned before which help in early mineralization.[4, 38]

Mineralization of the skeletal tissues occurs in two distinct phases; first, formation of initial mineral deposit (nucleation) and second, accretion of additional mineral crystals on the initial mineral deposit. The formation of the initial mineral deposit, the size of which is one or two hydroxyapatite unit cells[39] is a more energy demanding step compared to the addition of ions to already existing crystals. To avoid that excessive energy is required to form initial depositions, sometimes a less stable (metastable) precursor is first formed which serves as a heterogeneous nucleation site that is later converted directly to hydroxyapatite.[38] Initiation of mineralization is influenced by a combination of events, such as the increase in the local concentration of precipitating ions, formation of mineral nucleation sites and the removal of mineral inhibitors. The initial apatite crystals that are formed are around 20 to 80 nm in size and are chemically similar to $Ca_{10}(PO_4)_6(OH)_2$. With age, carbonates, which are contained in body fluids, substitute for OH^- and PO_4^{3-} in the calcium phosphate lattice, which results in carbonated hydroxyapatite.

1.5 Bioreactors

Both static and dynamic culture methods exist to accomplish proliferation and differentiation of cells *in vitro* to form tissues.[8] Cells developing into tissues adapt their structures and compositions depending on specific and functional demand. Thus, culturing cells over a scaffold in static culture medium is not enough to obtain a functional tissue. Therefore, bioreactors play a vital role in regeneration of complex 3D tissue. However, different types of tissues require a specific type of bioreactor. Since early times, static culture systems such as T-flasks and Petri dishes have been the most widely used culture devices for expanding cells.[40] However, these systems have several limitations, such as: improper distribution of pH, dissolved oxygen, cytokines and metabolites due to lack of mixing. These static cultures show difficulties in online monitoring and control that result in repeated handling to feed cultures and obtain data on culture performance.[41] Dynamic culture systems represent an alternative approach to standard static cultures of cells *in vitro*. Due to the demand of thicker scaffolds, that require stirred or perfused conditions to achieve uniformity and high yield, the use of these bioreactors has gained acceptance in tissue engineering laboratories.

Bioreactors are devices in which the biological and/or biochemical processes occur under closely monitored and tightly controlled environmental and operating conditions (e.g. pH, temperature, pressure, nutrient supply and waste removal).[42] The greatest advantage of these dynamic culture systems over the static ones is effective transfer of nutrients, gasses, metabolites and regulatory molecules that regulate the size and structure of the developing tissue.[43] *In vitro* tissue culture conditions vary for specific cell types, based on acceptable physiological ranges of tissue culture parameters, such as pH levels, nutrient and gas exchange.[44] Most of the culture systems and bioreactors were first developed for normal expansion of mammalian cells and then adapted to the engineering of 3D tissue constructs.

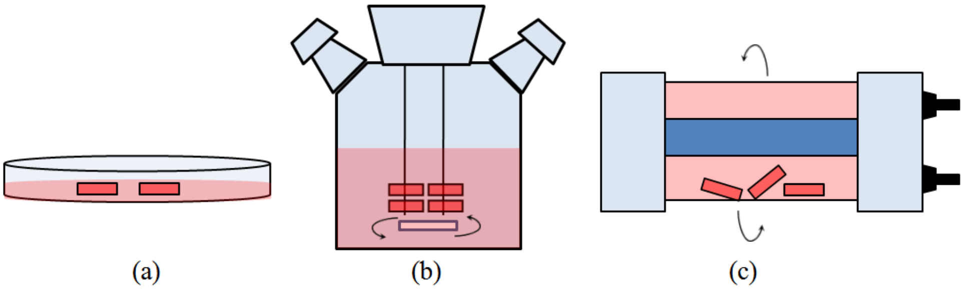

Figure 2: Cell culture systems used in bone tissue engineering. (a) Static culture system, (b) Perfusion type bioreactor and (c) Rotating wall type bioreactor.

In general, bioreactors can be classified into two main types, perfusion type (non-rotating) and rotating wall type shown in Figure 2. Perfusion type bioreactors have a fixed culture chamber and are mainly used for culturing complex tissues that require specific mechanical stresses to be applied over them while under culture. The mechanical stress is introduced by the flow of the perfused solution through the culture chamber and eventually through the tissues.[45] In contrast, rotating wall type bioreactors have a culture chamber permanently in rotation. The rotation speed of the culture chamber can be adjusted to produce a free falling state. These bioreactors are mainly used for fragile tissues as they decrease shear stress for the growing cells and avoid contact between cells and the inner walls of the bioreactors.[46] Researchers prefer the perfusion type over the rotating wall type for bone tissue engineering application as the microgravity caused due to the free falling state in the latter results in loss of total bone mass which is detrimental for bone.[47, 48]

In most of the conventional static cell culture systems and dynamic cell culture system like macroscale bioreactors, it is quite difficult to optically monitor nutrient supply, oxygen supply, waste removal, interaction with extracellular matrix and cell-cell interaction throughout the culture period. This is due to the practical problems in design and fabrication of large complex bioreactors that could be optically coupled to microscopes in which the cells are fed by a spatially homogenous distribution of the fluid flow. With the advent of microfabricated systems in tissue engineering, it has become possible to devise new and innovative ways to analyze cellular interaction and their behaviour in microfluidic environment that mimic *in vivo* conditions.[44, 49] The use of these microbioreactors offering a suitable environment for various cell cultures has been widely demonstrated.[50]

1.6 Raman Theory

Inelastic scattering of photons by matter was first predicted by Adolf Smekal[51] in 1923, however the experimental confirmation of this theory was shown in the year 1928 for the first time by Sir Chandrasekhara Venkata Raman[52] of Calcutta University, India. The significant discovery in the fundamentals of physics was well recognised and earned him the Nobel Prize in physics. This effect has been known as the 'Raman effect' henceforth.

There are many inelastic light scattering phenomena that have been developed based on Raman theory. The main purpose is to enhance sensitivity, spatial resolution and acquire specific information. The principle ones are spontaneous Raman scattering, resonance Raman scattering, stimulated Raman scattering, surface enhanced Raman scattering, hyper-Raman scattering, coherent anti-Stokes Raman scattering, Raman optical activity. Over the years, these techniques have been applied widely to investigate many biological and non-biological questions.[53, 54]

In Figure 3 molecular energy level diagrams are shown which illustrate the basic processes involved in light scattering. The electronic ground state and electronic excited state is indicated by e_0 and e_1 respectively. The various vibrational states are indicated by v_1, v_2, v_3.... When a monochromatic light source with frequency (ω_1) interacts with matter, most of the light is absorbed or transmitted and a small fraction of light is scattered (Figure 3(a), 3(b)). In a light scattering process, when an incident photon at frequency (ω_1) interacts with a molecule resulting in the scattered photon that has same frequency as incident photon, the process is called Rayleigh scattering. This process is signified by the absence of energy transfer as seen in Figure 3(c).

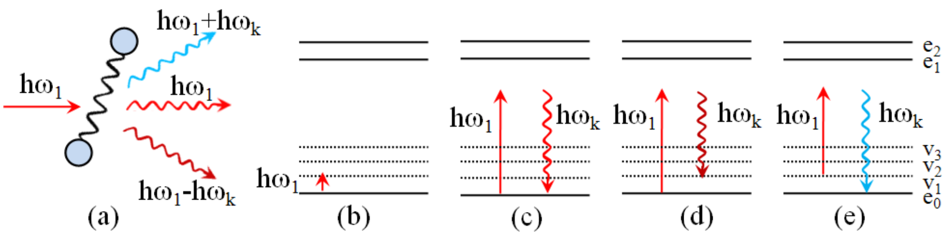

Figure 3: Interaction of molecule with photon, (a) elastic and inelastic scattering by the molecule, (b) Infrared absorption, (c) Rayleigh scattering, (d) Stokes Raman scattering and (e) Anti-Stokes Raman scattering.

In case the final state after scattering is not equal to the original state, e.g. due to the presence of rotational or vibrational states in the molecules, the light scattering process is accompanied by a shift in frequency (ω_k) with respect to the incident frequency. The light scattering accompanied by a shift in frequency is called Raman scattering. Raman scattering with frequencies less than the incident frequency (ω_l - ω_k) is called Stokes Raman scattering. (Figure 3(a), 3(d)). On the other hand, Raman scattering with a higher frequency than the incident frequency (ω_l + ω_k) is called anti-Stokes Raman scattering and occurs at the blue side of the incident photon. Here, the molecule already at a higher vibrational energy level loses energy and ends up in a lower vibrational energy level after interaction with an incident photon (Figure 3(a), 3(e)).

The classical approach to the Raman Effect was developed by Placzek.[53, 55] The frequency-dependent linear induced dipole moment $\vec{P}$ for a molecule is given by the relationship,

$$\vec{P} = \overleftrightarrow{\alpha}\vec{E} \qquad 1.1$$

Where E = $E_0 \cos(\omega_l t)$ is the electric field vector of the incident plane wave monochromatic radiation with frequency ω_l and $\overleftrightarrow{\alpha}$ is the polarizability of the molecule which is a second rank tensor. The polarizability depends on the precise vibration of the molecule. This is expressed by expanding each of the components $\alpha_{\rho\sigma}$ of the polarizability tensor α in a Taylor series with respect to the normal coordinates of the vibrations of the molecule;

$$\alpha_{\rho\sigma} = (\alpha_{\rho\sigma})_o + \sum_k \left(\frac{\partial \alpha_{\rho\sigma}}{\partial Q_k}\right)_o Q_k + \frac{1}{2}\sum_{k,l}\left(\frac{\partial^2 \alpha_{\rho\sigma}}{\partial Q_k \partial Q_l}\right)_o Q_k Q_l .... \qquad 1.2$$

where $(\alpha_{\rho\sigma})_o$ is the value of $\alpha_{\rho\sigma}$ at the equilibrium configuration, Q_k, Q_l, ... are normal coordinates of vibration associated with the molecular vibrational frequencies ω_k, ω_l, ... and the summation is done over all normal coordinates. The subscript ‘0’ on the derivatives indicate that these are to be taken at the equilibrium configuration. In the harmonic apporoximation the response is adequately described by the term up to the first order derivative. For one normal mode of vibration Q_k, Eq. 1.2 can be rewritten as

$$(\alpha_{\rho\sigma})_k = (\alpha_{\rho\sigma})_o + (\alpha'_{\rho\sigma})_k Q_k \qquad 1.3$$

Where,

$$(\alpha'_{\rho\sigma})_k = \left(\frac{\partial \alpha_{\rho\sigma}}{\partial Q_k}\right)_o \qquad 1.4$$

The $(\alpha'_{\rho\sigma})_k$ are components of a new tensor $\overleftrightarrow{\alpha'}_k$, which is called the derived polarizability tensor with respect to normal coordinate Q_k. Assuming a harmonic motion, the time dependence of Q_k is given by

$$Q_k = Q_{ko} \cos(\omega_k t + \delta_k) \qquad 1.5$$

where Q_{ko} is the normal coordinate amplitude, ω_k is the frequency and δ_k is the phase of k^{th} vibration. Combining Eq. 1.5 and 1.3 into Eq. 1.1 we attain a scalar rotation,

$$P = \alpha_o E_o \cos(\omega_1 t) + \alpha'_k E_o Q_{ko} \cos(\omega_k t + \delta_k)\cos(\omega_1 t) \qquad 1.6$$

Using the trigonometric identity,

$$\cos A.\cos B = \frac{1}{2}\{\cos(A+B) + \cos(A-B)\} \qquad 1.7$$

the second term in Eq. 1.6 can be rewritten as

$$P = P(\omega_1) + P(\omega_1 - \omega_k) + P(\omega_1 + \omega_k) \qquad 1.8$$

with

$$P(\omega_1) = \alpha_o E_o \cos(\omega_1 t) \qquad 1.9$$

And

$$P(\omega_1 \pm \omega_k) = \frac{1}{2}\alpha'_k Q_{ko} E_o \cos(\omega_1 t \pm \omega_k t \pm \delta_k) \qquad 1.10$$

The cosine functions in Eq. 1.9 and 1.10 define the frequencies of the induced dipoles. The intensity of the scattered photons depends on the initial population of the energy level of the molecule, the intensity of the incident radiation and the polarizability tensor. The first term in Eq 1.8 relates to scattered light of the original frequency and is referred to as Rayleigh scattering. The second and third terms represent scattered light of slightly different frequency and are named as Stokes Raman and anti-Stokes Raman scattering respectively. The probability of the molecule to stay in the ground state is higher than in a vibrationally excited state and also Stokes line starts from $n = 0$ state and the anti-Stokes starts from $n = 1$ state, hence population of high frequency normal modes is low. Therefore the probability of occurrence of anti-Stokes Raman effect is less than Stokes Raman effect

The classical theory gives prediction about the Stokes and anti-Stokes scattered frequencies, the intensity of the bands can be obtained from the quantum mechanical theory.[53] The power of Raman scattered light[56] is expressed using the differential cross section $d\sigma/d\Omega$ as,

$$P = 4\pi N\left(\frac{d\sigma}{d\Omega}\right)P_o \qquad 1.11$$

where N is the number of molecules in the measured volume, Ω is the solid angle of detection and P_0 is the power of excitation source. The factor 4π represents the whole solid angle. Typical values of the Raman scattering cross section $d\sigma/d\Omega$ are 10^{-34} m^2/sr for nonresonant processes and up to four orders of magnitude higher for resonant Raman scattering.

The intensity of the scattered light in a Raman spectrum is represented as a function of the wavenumber shift Δ (cm^{-1}), which is given by

$$\Delta cm^{-1} = \left(\frac{1}{\lambda_o} - \frac{1}{\lambda_s}\right)10^7 \qquad 1.12$$

where λ_0 (nm) and λ_S (nm) are the wavelengths of the excitation and scattered photons respectively. For a molecule under consideration, the respective Raman spectrum contains several narrow bands at positions that correspond with the molecule's vibrational states. The energy of the vibrations depends on the mass of the atoms involved in the vibrational motion and the strength of the bonds between these atoms. Hence, each molecule or a molecular group shows up with a unique Raman spectrum, which can be used to identify molecules present in the sample.

1.7 Why Raman microspectroscopy

Bone formation *in vitro* from BMSCs undergoes various stages as seen in Figure 1. BMSCs are fibroblast type cells and have enormous proliferation potential. Once enough population of BMSCs are attained, under the influence of osteoinductive growth factors they commit towards osteoprogenitor lineage. Further culture results in preosteoblast leading to a mature osteoblast stage. The mature osteoblast cell terminally differentiates to osteocyte. The mature osteoblast and osteocyte secrete collagen type-I which form the extracellular matrix of the cells. Extracellular matrix composed of collagenous and non-collagenous proteins mineralises under the influence of exogenous phosphate sources. Each stage of osteogenesis is characterised by the expression of various genes that represent structural, functional and phenotypical properties during the differentiation process.

Over the years, biologists have been using various procedures and technologies to investigate and understand the process of bone formation. Conventional techniques like microarray analysis and reverse transcriptase-polymerase chain reaction (RT-PCR) mostly focus on gene expression for matrix proteins during proliferation and differentiation.[19, 57, 58] However, only few of these studies have focused on the formation of the bone like mineral apatite.[59-62] Popular conventional methods to show the presence and formation of bone-like apatite are histochemical staining procedures such as von Kossa staining for phosphates and alizarin red staining for calcium ions. Von Kossa staining gives a positive reaction for phosphate containing samples and is not specific to exact phosphate minerals that are formed.[4, 59] Similarly, calcium ion specific alizarin red cannot distinguish between calcium ions bound to the organic matrix from calcium ion bound to phosphates.[4] Both von Kossa and alizarin red staining techniques are highly toxic and destructive to the cells and co-localisation of these two stains does not prove the presence of mineral apatite. Thus there is a clear need for non-invasive and label free methods for analysis of cellular mineralization processes.

In the last two decades, advanced technologies like electron multi-probe and electron diffraction, X-ray diffraction (XRD), solid state nuclear magnetic resonance (NMR) spectroscopy and vibrational spectroscopy techniques like Fourier transform infrared (FTIR) and Raman spectroscopy have been applied to elucidate *in vitro* bone formation. Micrographs obtained with electron microscopy show the morphology of collagen fibrils and apatite needles and plates at submicron level.[59, 60] The chemical composition is however not revealed. Electron microscopy in combination with diffraction techniques like electron diffraction, X-Ray diffraction (XRD), synchrotron or neutron scattering show the presence of mineral formation with definitive structure and phase information.[59-65] Solid state NMR spectroscopy could identify unique protonated phosphate groups in biologically formed apatite that was not seen in synthetically formed ones.[66] FTIR microspectroscopy enables access to relative chemical information of the organic matrix and the mineral deposits, which is not feasible with diffraction methods.[67] All the above mentioned techniques are not straightforward to apply to water containing specimens. Mostly these techniques require extensive sample pre-treatment, which limits the feasibility for living tissues.

Vibrational spectroscopies like non-resonant Raman spectroscopy,[68] resonance Raman (RR) spectroscopy[69] and coherent anti-Stokes Raman spectroscopy (CARS)[70] provide a wealth of biochemical information at the molecular level at high spatial resolution. Non-resonant Raman spectroscopy and RR spectroscopy provide similar results as FTIR spectroscopy at a higher spatial resolution (~ 0.3 to 1.0 µm), due to the use of shorter wavelengths in the process. RR spectroscopy is selective for molecules with absorption near the excitation wavelength. CARS provide a high speed of imaging compared to non-resonant Raman imaging within a narrow bandwidth. However, this procedure requires high peak powers in the laser beam for the generation of the coherent signal.

In contrast with FTIR spectroscopy, which is based on light absorption, non-resonant Raman spectroscopy, RR spectroscopy and CARS work on the principle of light scattering. The application of vibrational spectroscopy for studying mineralized tissue has recently been reviewed.[71] It was concluded that Raman spectroscopy is technically superior to FTIR spectroscopy. Raman spectroscopy gives chemical information that is complementary to FTIR, since many infrared vibrational modes are Raman active. Raman spectroscopy has vibrational bands that are narrow, hence small frequency shifts and band shape changes can be more easily observed. Additional advantages of Raman spectroscopy are that this technique hardly requires sample preparation, the sample does not need to be transparent, it is non destructive and the sample does not need to be dehydrated. It follows that the potential of Raman microspectroscopy for applications in life sciences is large.

1.8 Raman microspectroscopy - Cell biology and bone tissue engineering

Over the last two decades, the advances in NIR lasers and CCD cameras have revolutionised the approach of Raman microspectroscopy imaging over cell biology and tissue based applications. Selection of excitation wavelength in the near infra red region, better signal generation and efficient data accumulation has led to single cell Raman imaging without causing degradation to the cells. Technological advances have resulted in high resolution Raman micro-spectroscopic imaging (spatial resolution < 500 nm full width at half maximum), and low light doses where pixel dwell times of 100 ms and a light dose of 3.5 mJ/pixel enabled single living cell Raman imaging.[72]

The literature describes Raman microspectroscopy as an elegant tool for single cell molecular imaging. The first confocal Raman microspectroscopic studies done over single living cells and chromosomes[68] laid the foundation for Raman spectroscopy as a valuable tool for single cell imaging applications. Since then confocal Raman microspectroscopy has been used extensively to study living cells,[73, 74] dead cells,[75] cell death due to apoptosis,[76] mitotic stage of a dividing cells,[77] proliferating cells[78] and differentiating cells.[79] Cellular distribution of certain organelles like mitochondria[80] and intracellular redistribution of lipid vesicles upon phagocytosis[81] have been successfully shown. Raman microspectroscopy has been used to detect the presence of certain molecules like carotenoids (β-Carotene) in a single cell and its concentration in various phenotypes of peripheral blood lymphocyte cells.[69, 82]

The advantages of Raman microspectroscopy have enabled its application to the study of developing tissues over a period of time.[83] Over the last decade, Raman spectroscopy has been used to study the process of osteogenesis, however these studies were focused on the onset and growth of mineralization over adult stem cells.[71, 83-89] Raman spectroscopy could show the variation in the formation of hydroxyapatite, from normal apatite to crystalline apatite over the culture period.[62, 84, 90, 91] Studies have also revealed the occurrence of precursors of hydroxyapatite such as β-tricalcium phosphate (β-TCP), amorphous calcium phosphate (ACP) and octacalcium phosphate (OCP) in the osteoblast differentiated cells.[83, 85] Raman spectroscopic evidence of the onset of mineralization was shown to occur early in the culture period when the osteogenic cells were cultured in serum free media under the influence of transforming growth factor (TGF)-β1.[92]

Osteogenesis of BMSCs includes various stages like preosteoblast, osteoblasts and osteocytes before completely differentiating towards mineralized tissue which resembles *in vivo* bone.[18, 31-33] Identifying the markers at each stage of osteogenesis is an essential step to understand the process of bone formation. The literature shows extensive work done to understand the process of adult stem cell differentiation towards osteoblasts before forming bone. However, hardly any work shows Raman spectroscopic studies of osteogenic differentiation at very early stages, during lineage commitment and pluripotency and while early and late stage of mineralization occurs. Understanding the biomarkers signifying various stages of osteogenesis could be very useful for researchers and scientists working in bone tissue engineering. The potential of stem cells to differentiate towards osteogenic lineage in combination with Raman microspectroscopy can help elucidate the scientific theory behind bone formation.

1.9 Scope of this thesis

Over the years there have been various approaches used to understand the science behind bone formation, however the number of non-invasive research methods applied for this purpose is very limited. We use confocal Raman microspectroscopy which is a non-invasive and label free technique with enough spatial resolution and appropriate molecular specificity to enable chemical investigation at various stages of *in vitro* bone forming process. The objective of this thesis is to elucidate various stages of bone formation, i.e. from differentiation of bone marrow stromal cells to osteoblasts till early and late stage of bone formation, with emphasis on non-invasive confocal Raman microspectroscopy imaging for qualitative and quantitative analysis at molecular level.

Chapter 2 of this thesis discusses the design and implementation of the hybrid confocal microspectroscopy for cell and tissue based applications, which houses fast “amplitude-only” TPE-fluorescence imaging, high spectral resolution Raman imaging and low frequency resolution Raman imaging in combination with two photon fluorescence spectral imaging and Rayleigh scatter imaging. In chapter 3, we show the concept of time lapse Raman imaging, wherein the efficiency of the instrument to perform fast imaging enabled identification and quantification of photodegradable molecules like carotenoids. In chapter 4 we show the design and development of microbioreactors for bone tissue engineering applications, which mimics *in vivo* body conditions and enables non-invasive and label free optical measurements for monitoring cellular activities and bone formation.

With this efficiency of the instrument, we are now in a position to study the evolution of bone formation from single stromal cells. Chapter 5 shows Raman biomarkers which define very early differentiation stage of human immortalized bone marrow stromal cells (iMSCs) cultured in various osteogenesis inducing media compared with basic culture media. In chapter 6, we show the spectroscopic evidence that signifies the lineage commitment of iMSCs towards adipogenesis and osteogenesis (such as preosteoblast, osteoblast, osteocyte and various stages of mineralization). Chapter 7 shows occurrence of *de novo* apatites and its conversion towards more mature hydroxyapatite. The formation of hydroxyapatite is accompanied by addition of carbonate ions resulting in the crystalline nature of apatite as culture period progresses which resembles *in vivo* bone. Chapter 8 focuses in detail on the role of phospholipids, cholesterols and collagen in the mineralization of bone forming cells. We use the principles of Raman spectroscopy to monitor the role of phospholipids and collagen in bone formation from early till later stages and support the results with coherent anti-Stokes Raman spectroscopic and second harmonic generated imaging.

As a step ahead, in chapter 9 we discuss miscellaneous Raman spectroscopy results related to bone tissue engineering and other applications, which could define the future course of research. Further, the summary of results obtained from chapter 2 till chapter 9, in view of the application of vibrational spectroscopy for cell-based bone tissue engineering is presented.

References

1. Rodan, G. A., Introduction to bone biology. *Bone* **1992,** 13, (Suppl. 1), S3-S6.
2. Sommerfeldt, D. W.; Rubin, C. T., Biology of bone and how it orchestrates the form and function of the skeleton. *Eur Spine J* **2001,** 10 Suppl 2, S86-95.
3. Dempster, D. W., *Primer on the metabolic bone diseases and disorders of mineral metabolism*. 6th ed.; ASMBR: Washington, D. C., 2006; p 7-11.
4. Robey, P. G.; Boskey, A. L., *Primer on the metabolic bone diseases and disorders of mineral metabolism*. 6th ed.; ASMBR: Washington, D. C., 2006; p 12-19.
5. Heino, T. J.; Hentunen, T. A.; Vaananen, H. K., Osteocytes inhibit osteoclastic bone resorption through transforming growth factor-beta : enhancement by estrogen. *J. Cell. Biochem.* **2002,** 85, (1), 185-197.
6. Miller, S. C.; de Saint-Georges, L.; Bowman, B. M.; Jee, W. S., Bone lining cells: structure and function. *Scanning Microsc* **1989,** 3, (3), 953-60; discussion 960-1.
7. Ross, F. P., *Primer on the metabolic bone diseases and disorders of mineral metabolism*. 6th ed.; ASMBR: Washington, D. C., 2006; p 30-35.
8. Huitema, L. F. A.; Vaandrager, A. B., What triggers cell-mediated mineralization? *Front. Biosci.* **2007,** 12, 2631-2645.
9. van de Lest, C. H. A.; Vaandrager, A. B., Mechanism of cell-mediated mineralization. *Curr. Opin. Orthop.* **2007,** 18, (5), 434-443.
10. Langer, R.; Vacanti, J. P., Tissue engineering. *Science* **1993,** 260, (5110), 920-6.
11. Yaszemski, M. J.; Oldham, J. B.; Lu, L.; Currier, B. L., *Bone Engineering*. 1st ed.; Em Squared Inc.: Toronto, 2000; p 541-547.
12. Langer, R., Tissue engineering. *Mol Ther* **2000,** 1, (1), 12-5.
13. Laurencin, C. T.; Ambrosio, A. M. A.; Borden, M. D.; Cooper, J. A., Jr., Tissue engineering: orthopedic applications. *Annu. Rev. Biomed. Eng.* **1999,** 1, 19-46.
14. Salgado, A. J.; Coutinho, O. P.; Reis, R. L., Bone tissue engineering: State of the art and future trends. *Macromol. Biosci.* **2004,** 4, (8), 743-765.
15. Blau, H. M.; Brazelton, T. R.; Weimann, J. M., The evolving concept of a stem cell: entity or function? *Cell* **2001,** 105, (7), 829-841.
16. Alison Malcolm, R.; Poulsom, R.; Forbes, S.; Wright Nicholas, A., An introduction to stem cells. *J Pathol* **2002,** 197, (4), 419-23.
17. Preston, S. L.; Alison, M. R.; Forbes, S. J.; Direkze, N. C.; Poulsom, R.; Wright, N. A., The new stem cell biology: something for everyone. *Mol Pathol* **2003,** 56, (2), 86-96.
18. Caplan, A. I., Mesenchymal stem cells. *J Orthop Res* **1991,** 9, (5), 641-50.
19. Pittenger, M. F., Multilineage potential of adult human mesenchymal stem cells. *Science* **1999,** 285, (5428), 665.
20. Yamashita, J.; Itoh, H.; Hirashima, M.; Ogawa, M.; Nishikawa, S.; Yurugi, T.; Naito, M.; Nakao, K.; Nishikawa, S., Flk1-positive cells derived from embryonic stem cells serve as vascular progenitors. *Nature* **2000,** 408, (6808), 92-6.
21. Wiles, M. V.; Keller, G., Multiple hematopoietic lineages develop from embryonic stem (ES) cells in culture. *Development* **1991,** 111, (2), 259-67.
22. Guan, K.; Chang, H.; Rolletschek, A.; Wobus, A. M., Embryonic stem cell-derived neurogenesis: Retinoic acid induction and lineage selection of neuronal cells. *Cell Tissue Res.* **2001,** 305, (2), 171-176.
23. Kramer, J.; Hegert, C.; Guan, K.; Wobus, A. M.; Muller, P. K.; Rohwedel, J., Embryonic stem cell-derived chondrogenic differentiation *in vitro*: activation by BMP-2 and BMP-4. *Mech. Dev.* **2000,** 92, (2), 193-205.
24. Johnstone, B.; Hering, T. M.; Caplan, A. I.; Goldberg, V. M.; Yoo, J. U., *In vitro* chondrogenesis of bone marrow-derived mesenchymal progenitor cells. *Exp Cell Res* **1998,** 238, (1), 265-72.
25. Mackay, A. M.; Beck, S. C.; Murphy, J. M.; Barry, F. P.; Chichester, C. O.; Pittenger, M. F., Chondrogenic differentiation of cultured human mesenchymal stem cells from marrow. *Tissue Eng* **1998,** 4, (4), 415-28.

26. Awad, H. A.; Butler, D. L.; Boivin, G. P.; Smith, F. N.; Malaviya, P.; Huibregtse, B.; Caplan, A. I., Autologous mesenchymal stem cell-mediated repair of tendon. *Tissue Eng* **1999,** 5, (3), 267-77.
27. Young, R. G.; Butler, D. L.; Weber, W.; Caplan, A. I.; Gordon, S. L.; Fink, D. J., Use of mesenchymal stem cells in a collagen matrix for Achilles tendon repair. *J Orthop Res* **1998,** 16, (4), 406-13.
28. Dani, C.; Smith, A. G.; Dessolin, S.; Leroy, P.; Staccini, L.; Villageois, P.; Darimont, C.; Ailhaud, G., Differentiation of embryonic stem cells into adipocytes *in vitro*. *J. Cell Sci.* **1997,** 110, (11), 1279-1285.
29. Choi, D.; Oh, H.-J.; Chang, U.-J.; Koo Soo, K.; Jiang Jean, X.; Hwang, S.-Y.; Lee, J.-D.; Yeoh George, C.; Shin, H.-S.; Lee, J.-S.; Oh, B., *In vivo* differentiation of mouse embryonic stem cells into hepatocytes. *Cell Transplant* **2002,** 11, (4), 359-68.
30. Hamazaki, T.; Iiboshi, Y.; Oka, M.; Papst, P. J.; Meacham, A. M.; Zon, L. I.; Terada, N., Hepatic maturation in differentiating embryonic stem cells *in vitro*. *FEBS Lett.* **2001,** 497, (1), 15-19.
31. Caplan, A. I., Adult mesenchymal stem cells for tissue engineering versus regenerative medicine. *J. Cell. Physiol.* **2007,** 213, (2), 341-347.
32. Caplan, A. I., The mesengenic process. *Clin Plast Surg* **1994,** 21, (3), 429-35.
33. Caplan, A. I.; Bruder, S. P., Mesenchymal stem cells: building blocks for molecular medicine in the 21st century. *Trends Mol Med* **2001,** 7, (6), 259-64.
34. Wobus, A. M., Potential of embryonic stem cells. *Mol. Aspects Med.* **2001,** 22, (3), 149-164.
35. Owen, M.; Friedenstein, A. J., Stromal stem cells: marrow-derived osteogenic precursors. *Ciba Found Symp* **1988,** 136, 42-60.
36. Derubeis Anna, R.; Cancedda, R., Bone marrow stromal cells (BMSCs) in bone engineering: limitations and recent advances. *Ann Biomed Eng* **2004,** 32, (1), 160-5.
37. Aubin, J. E.; Lian, J. B.; Stein, G. S., *Primer on the metabolic bone diseases and disorders of mineral metabolism*. 6th ed.; ASMBR: Washington, D. C., 2006; p 20-29.
38. Simon, S. R., *Orthopaedic Basic Science*. 1st ed.; American Academy of Orthopaedic Surgeons: Illinois, 1994.
39. Eppell, S. J.; Tong, W.; Katz, J. L.; Kuhn, L.; Glimcher, M. J., Shape and size of isolated bone mineralites measured using atomic force microscopy. *J Orthop Res* **2001,** 19, (6), 1027-34.
40. Dexter, T. M.; Allen, T. D.; Lajtha, L. G.; Schofield, R.; Lord, B. I., Stimulation of differentiation and proliferation of haemopoietic cells *in vitro*. *J Cell Physiol* **1973,** 82, (3), 461-73.
41. Collins, P. C.; Miller, W. M.; Papoutsakis, E. T., Stirred culture of peripheral and cord blood hematopoietic cells offers advantages over traditional static systems for clinically relevant applications. *Biotechnol Bioeng* **1998,** 59, (5), 534-43.
42. Martin, I.; Wendt, D.; Heberer, M., The role of bioreactors in tissue engineering. *Trends Biotechnol.* **2004,** 22, (2), 80-86.
43. Lalan, S.; Pomerantseva, I.; Vacanti, J. P., Tissue engineering and its potential impact on surgery. *World J Surg* **2001,** 25, (11), 1458-66.
44. Griffith Linda, G.; Naughton, G., Tissue engineering--current challenges and expanding opportunities. *Science* **2002,** 295, (5557), 1009-14.
45. Sodian, R.; Lemke, T.; Loebe, M.; Hoerstrup, S. P.; Potapov, E. V.; Hausmann, H.; Meyer, R.; Hetzer, R., New pulsatile bioreactor for fabrication of tissue-engineered patches. *J. Biomed. Mater. Res.* **2001,** 58, (4), 401-405.
46. Begley, C. M.; Kleis, S. J., The fluid dynamic and shear environment in the NASA/JSC rotating-wall perfused-vessel bioreactor. *Biotechnol. Bioeng.* **2000,** 70, (1), 32-40.
47. Droppert, P. M., The effects of microgravity on the skeletal system--a review. *J Br Interplanet Soc* **1990,** 43, (1), 19-24.
48. Sinha Raj, K.; Shah Suken, A.; Hume Eric, L.; Tuan Rocky, S., The effect of a 5-day space flight on the immature rat spine. *Spine J* **2002,** 2, (4), 239-43.

49. Strain Alastair, J.; Neuberger James, M., A bioartificial liver--state of the art. *Science* **2002,** 295, (5557), 1005-9.
50. Andersson, H.; van den Berg, A., Microfluidic devices for cellomics: a review. *Sens. Actuators, B* **2003,** B92, (3), 315-325.
51. Smekal, A., The quantum theory of dispersion. *Naturwissenschaften* **1923,** 11, 873-5.
52. Raman, C. V.; Krishnan, K. S., A new type of secondary radiation. *Nature* **1928,** 121, 501-2.
53. Long, D. A., *The Raman Effect*. John Wiley and Sons Ltd.: 1982.
54. Tu, A. T., *Raman Spectroscopy in Biology: Principles and Applications*. 1982; p 448.
55. Placzek, G., *Handbuch der Radiologie*. Akademische Verlag: Leipzeg, 1934; Vol. 1, p 205-374.
56. Schroetter, H. W.; Kloeckner, H. W., Raman scattering cross sections in gases and liquids. *Top. Curr. Phys.* **1979,** 11, (Raman Spectrosc. Gases Liq.), 123-66.
57. Raouf, A.; Ganss, B.; McMahon, C.; Vary, C.; Roughley, P. J.; Seth, A., Lumican is a major proteoglycan component of the bone matrix. *Matrix Biol.* **2002,** 21, (4), 361-367.
58. Siggelkow, H.; Rebenstorff, K.; Kurre, W.; Niedhart, C.; Engel, I.; Schulz, H.; Atkinson, M. J.; Hufner, M., Development of the osteoblast phenotype in primary human osteoblasts in culture: comparison with rat calvarial cells in osteoblast differentiation. *J. Cell. Biochem.* **1999,** 75, (1), 22-35.
59. Bonewald, L. F.; Harris, S. E.; Rosser, J.; Dallas, M. R.; Dallas, S. L.; Camacho, N. P.; Boyan, B.; Boskey, A., Von Kossa staining alone is not sufficient to confirm that mineralization *in vitro* represents bone formation. *Calcif. Tissue Int.* **2003,** 72, (5), 537-547.
60. Ecarot-Charrier, B.; Glorieux, F. H.; Van der Rest, M.; Pereira, G., Osteoblasts isolated from mouse calvaria initiate matrix mineralization in culture. *J. Cell Biol.* **1983,** 96, (3), 639-43.
61. Gerstenfeld, L. C.; Chipman, S. D.; Kelly, C. M.; Hodgens, K. J.; Lee, D. D.; Landis, W. J., Collagen expression, ultrastructural assembly, and mineralization in cultures of chicken embryo osteoblasts. *J. Cell Biol.* **1988,** 106, (3), 979-89.
62. Rey, C.; Kim, H. M.; Gerstenfeld, L.; Glimcher, M. J., Characterization of the apatite crystals of bone and their maturation in osteoblast cell culture: comparison with native bone crystals. *Connect Tissue Res* **1996,** 35, (1-4), 343-9.
63. Chaudhary, L. R.; Hofmeister, A. M.; Hruska, K. A., Differential growth factor control of bone formation through osteoprogenitor differentiation. *Bone* **2004,** 34, (3), 402-411.
64. Kato, Y.; Boskey, A.; Spevak, L.; Dallas, M.; Hori, M.; Bonewald, L. F., Establishment of an osteoid preosteocyte-like cell MLO-A5 that spontaneously mineralizes in culture. *J. Bone Miner. Res.* **2001,** 16, (9), 1622-1633.
65. Stanford, C. M.; Jacobson, P. A.; Eanes, E. D.; Lembke, L. A.; Midura, R. J., Rapidly forming apatitic mineral in an osteoblastic cell line (UMR 106-01 BSP). *J Biol Chem* **1995,** 270, (16), 9420-8.
66. Wu, Y.; Glimcher, M. J.; Rey, C.; Ackerman, J. L., A unique protonated phosphate group in bone mineral not present in synthetic calcium phosphates. Identification by phosphorus-31 solid state NMR spectroscopy. *J Mol Biol* **1994,** 244, (4), 423-35.
67. Boskey, A. L.; Camacho, N. P.; Mendelsohn, R.; Doty, S. B.; Binderman, I., FT-IR microscopic mappings of early mineralization in chick limb bud mesenchymal cell cultures. *Calcif Tissue Int* **1992,** 51, (6), 443-8.
68. Puppels, G. J.; De Mul, F. F. M.; Otto, C.; Greve, J.; Robert-Nicoud, M.; Arndt-Jovin, D. J.; Jovin, T. M., Studying single living cells and chromosomes by confocal Raman microspectroscopy. *Nature* **1990,** 347, (6290), 301-3.
69. Puppels, G. J.; Garritsen, H. S.; Kummer, J. A.; Greve, J., Carotenoids located in human lymphocyte subpopulations and natural killer cells by Raman microspectroscopy. *Cytometry* **1993,** 14, (3), 251-6.
70. Cheng, J.-X.; Volkmer, A.; Book, L. D.; Xie, X. S., An Epi-detected Coherent Anti-Stokes Raman Scattering (E-CARS) microscope with high spectral resolution and high sensitivity. *J. Phys. Chem. B* **2001,** 105, (7), 1277-1280.

71. Carden, A.; Morris, M. D., Application of vibrational spectroscopy to the study of mineralized tissues (review). *J. Biomed. Opt.* **2000,** 5, (3), 259-268.
72. Pully, V. V.; Otto, C., The intensity of the 1602 cm^{-1} band in human cells is related to mitochondrial activity. *J. Raman Spectrosc.* **2009,** 40, (5), 473-475.
73. Notingher, I.; Verrier, S.; Romanska, H.; Bishop, A. E.; Polak, J. M.; Hench, L. L., In situ characterization of living cells by Raman spectroscopy. *Spectroscopy* **2002,** 16, (2), 43-51.
74. Puppels, G. J.; Olminkhof, J. H.; Segers-Nolten, G. M.; Otto, C.; de Mul, F. F.; Greve, J., Laser irradiation and Raman spectroscopy of single living cells and chromosomes: sample degradation occurs with 514.5 nm but not with 660 nm laser light. *Exp Cell Res* **1991,** 195, (2), 361-7.
75. Verrier, S.; Notingher, I.; Polak, J. M.; Hench, L. L., In situ monitoring of cell death using Raman microspectroscopy. *Biopolymers* **2004,** 74, (1-2), 157-62.
76. Uzunbajakava, N.; Lenferink, A.; Kraan, Y.; Volokhina, E.; Vrensen, G.; Greve, J.; Otto, C., Nonresonant confocal Raman imaging of DNA and protein distribution in apoptotic cells. *Biophys. J.* **2003,** 84, (6), 3968-3981.
77. Matthaus, C.; Boydston-White, S.; Miljkovic, M.; Romeo, M.; Diem, M., Raman and infrared microspectral imaging of mitotic cells. *Appl. Spectrosc.* **2006,** 60, (1), 1-8.
78. Short, K. W.; Carpenter, S.; Freyer, J. P.; Mourant, J. R., Raman spectroscopy detects biochemical changes due to proliferation in mammalian cell cultures. *Biophys. J.* **2005,** 88, (6), 4274-4288.
79. Notingher, I.; Jell, G.; Lohbauer, U.; Salih, V.; Hench, L. L., In situ non-invasive spectral discrimination between bone cell phenotypes used in tissue engineering. *J. Cell. Biochem.* **2004,** 92, (6), 1180-1192.
80. Matthaus, C.; Chernenko, T.; Newmark, J. A.; Warner, C. M.; Diem, M., Label-free detection of mitochondrial distribution in cells by nonresonant raman microspectroscopy. *Biophys. J.* **2007,** 93, (2), 668-673.
81. van Manen, H.-J.; Kraan, Y. M.; Roos, D.; Otto, C., Single-cell raman and fluorescence microscopy reveal the association of lipid bodies with phagosomes in leukocytes. *Proc. Natl. Acad. Sci. U. S. A.* **2005,** 102, (29), 10159-10164.
82. Arikan, S.; Sands, H. S.; Rodway, R. G.; Batchelder, D. N., Raman spectroscopy and imaging of beta - carotene in live corpus luteum cells. *Anim. Reprod. Sci.* **2002,** 71, (3,4), 249-266.
83. Crane, N. J.; Popescu, V.; Morris, M. D.; Steenhuis, P.; Ignelzi, M. A., Raman spectroscopic evidence for octacalcium phosphate and other transient mineral species deposited during intramembranous mineralization. *Bone* **2006,** 39, (3), 434-442.
84. Chiang, H. K.; Peng, F.-Y.; Hung, S.-C.; Feng, Y.-C., In situ Raman spectroscopic monitoring of hydroxyapatite as human mesenchymal stem cells differentiate into osteoblasts. *J. Raman Spectrosc.* **2009,** 40, (5), 546-549.
85. Stewart, S.; Shea, D. A.; Tarnowski, C. P.; Morris, M. D.; Wang, D.; Franceschi, R.; Lin, D. L.; Keller, E., Trends in early mineralization of murine calvarial osteoblastic cultures: A Raman microscopic study. *J. Raman Spectrosc.* **2002,** 33, (7), 536-543.
86. Tarnowski Catherine, P.; Ignelzi Michael, A., Jr.; Morris Michael, D., Mineralization of developing mouse calvaria as revealed by Raman microspectroscopy. *J Bone Miner Res* **2002,** 17, (6), 1118-26.
87. Timlin, J. A.; Carden, A.; Morris, M. D., Chemical microstructure of cortical bone probed by Raman transects. *Appl. Spectrosc.* **1999,** 53, (11), 1429-1435.
88. Timlin, J. A.; Carden, A.; Morris, M. D.; Rajachar, R. M.; Kohn, D. H., Raman Spectroscopic Imaging Markers for Fatigue-Related Microdamage in Bovine Bone. *Anal. Chem.* **2000,** 72, (10), 2229-2236.
89. Gentleman, E.; Swain, R. J.; Evans, N. D.; Boonrungsiman, S.; Jell, G.; Ball, M. D.; Shean, T. A. V.; Oyen, M. L.; Porter, A.; Stevens, M. M., Comparative materials differences revealed in engineered bone as a function of cell-specific differentiation. *Nat. Mater.* **2009,** 8, (9), 763-770.

90. Kuhn, L. T.; Wu, Y.; Rey, C.; Gerstenfeld, L. C.; Grynpas, M. D.; Ackerman, J. L.; Kim, H.-m.; Glimcher, M. J., Structure, composition, and maturation of newly deposited calcium-phosphate crystals in chicken osteoblast cell cultures. *J. Bone Miner. Res.* **2000,** 15, (7), 1301-1309.
91. Rey, C.; Kim, H. M.; Gerstenfeld, L.; Glimcher, M. J., Structural and chemical characteristics and maturation of the calcium-phosphate crystals formed during the calcification of the organic matrix synthesized by chicken osteoblasts in cell culture. *J. Bone Miner. Res.* **1995,** 10, (10), 1577-88.
92. Kale, S.; Biermann, S.; Edwards, C.; Tarnowski, C.; Morris, M.; Long, M. W., Three-dimensional cellular development is essential for ex vivo formation of human bone. *Nat Biotechnol* **2000,** 18, (9), 954-8.

Chapter 2

Hybrid Rayleigh, Raman and TPE fluorescence spectral confocal microscopy of living cells

We present a hybrid fluorescence-Raman confocal microscopy platform, which integrates low wavenumber resolution Raman imaging, Rayleigh scatter imaging and two photon fluorescence (TPE) spectral imaging, fast "amplitude-only" TPE-fluorescence imaging and high spectral resolution Raman imaging. This multi-dimensional fluorescence-Raman microscopy platform enables rapid imaging along the fluorescence emission and/or Rayleigh scatter dimensions. We show that optical contrast in these images can be used to select an area of interest prior to subsequent investigation with high spatially- and spectrally resolved Raman imaging. This new microscopy platform combines the strengths of Raman "chemical" imaging with light scattering and fluorescence microscopies and provides new modes of correlative light microscopy. Simultaneous acquisition of TPE hyperspectral fluorescence imaging and Raman imaging illustrates spatial relationships of fluorophores, water, lipid and protein in cells. The fluorescence-Raman microscope is used to characterize living human bone marrow stromal cells.

This chapter has been published in the Journal of Raman Spectroscopy, 2009 DOI 10.1002/jrs.2501.

2.1 Introduction:

Since the first application of Raman spectroscopy and imaging on cells,[1] there have been significant developments in technology towards cell and tissue based applications. Spontaneous Raman imaging has been used to identify various organelles of a cell[2] and to determine the physical state of a cell, such as the viability,[3] apoptosis or necrosis,[4] cell division[5] or proliferation,[6] and to distinguish between cancerous[7] and differentiating cells.[7]

The strength of spontaneous Raman imaging resides in the ability to generate a broad bandwidth response, which reflects the presence of many chemical parameters simultaneously. The signal-to-noise ratio is determined by the photon shot noise with a minor contribution from the detector properties. The spontaneous nature of non-coherent Raman scattering, as opposed to coherent Raman scattering processes, which are enhanced by stimulated emission, gives rise to a relatively low imaging speed, however with the advantage of obtaining full spectral information during an image-timeframe. A combination of spectrally resolved Raman microspectroscopy with amplitude only continuous wave (cw) two photon-excited (TPE) fluorescence microscopy has previously been shown.[8] Two-photon fluorescence was excited from an organic dye with an absorption band around 325 nm, which could be efficiently excited at the higher harmonic of the continuous wave fundamental krypton-laser emission at 647.1 nm. More recently, it has been shown that also fluorescence of quantum dots can be favorably combined with spontaneous Raman imaging[9] and that individual quantum dots may serve to recognize certain areas or events in a cell. Here, a new fluorescence-Raman hybrid microscopy platform is presented, which integrates 1) TPE-fluorescence “amplitude-only” imaging, 2) Low Wavenumber Resolution Imaging (LWRI) simultaneously with spectrally resolved cwTPE fluorescence microscopy, Rayleigh scattering imaging and Low Resolution Raman Imaging (LRRI), and 3) high wavenumber and spatially resolved confocal Raman microspectroscopy. This platform enables fast acquisition of data along fluorescence and scattering dimensions in combination with Raman chemical imaging without perturbation of the sample.

2.2 Materials and methods

Hybrid microscope

The hybrid Rayleigh-, Raman and TPE-fluorescence microscope (Figure 1) integrates a single light source, an adapted microscope and different spectrograph and detector modalities. TPE-fluorescence amplitude-only imaging was performed with avalanche photodiodes (APD) in rapid photon counting mode (Figure 1). A second detection branch comprises of a spectrograph (Spectrograph-1 in Figure 1), which was optimized for broadband (344 nm to 1173 nm) low wavenumber-resolved (0.1 to 1.8 nm/pixel corresponding to 7 to 22 cm^{-1}/pixel) Raman/ fluorescence measurements. A third detection branch (Spectrograph-2), was optimized for broadband (+20 to -3670 cm^{-1}) high wavenumber resolution (1.85 to 2.85 cm^{-1}/pixel) Raman microspectroscopy. The pinholes, which act simultaneously as spectrograph entrance ports in all spectrograph/detector combinations, are confocal with the same sample-plane of the microscope objective. Lenses and pinholes were selected for high spatial confocal resolution at a sustainable loss of photons on the apertures. The design criteria for the size of the pinholes complied with a truncation of the TEM00-Gaussian beam at the $1/e^2$-points.

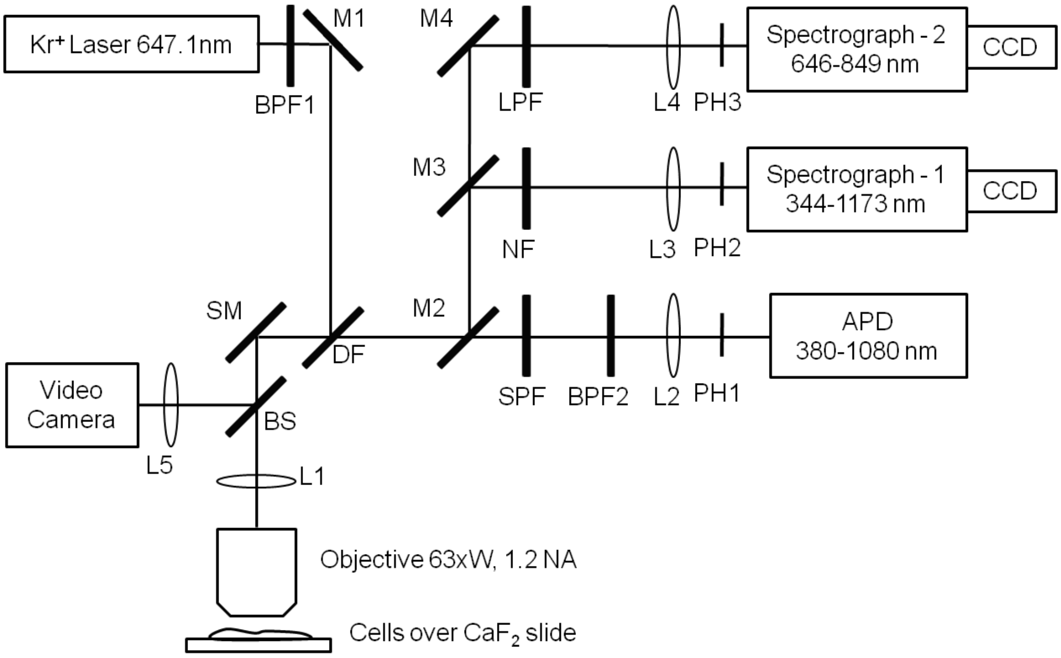

Figure 1: Illustration of hybrid Rayleigh-, Raman and TPE-fluorescence microscope showing the combination of TPE confocal fluorescence microscopy, LWRI in synchrony with spectrally resolved cwTPE fluorescence microscopy, Rayleigh scattering imaging and LRRI, and high spectral and wavenumber resolution Raman microspectroscopy. The hybrid microscope uses excitation with the 647.1nm line of a Krypton ion laser. DF, dichroic notch filter; SM, scanning mirror; M1, M2, M3, M4, high reflectance mirrors; NF, notch filter; SPF, short pass filter; LPF, long pass filter; BPF1, BPF2, band pass filter; L1, L2, L3, L4, L5, lenses with focal lengths of 100, 100, 35, 30, 75 mm respectively; PH1, PH2, PH3, confocal pinholes of diameter 50, 15, 15 µm respectively; APD, avalanche photo diode detecting in the range of 380-1080 nm; Spectrograph-1, Spectrograph-2, polychromators dispersing in the range of 344-1173 nm and 646-849 nm respectively; CCD, CCD cameras; BS, pellicle beam splitter for monitoring bright field micrographs of the sample and the position of the laser beam in the sample on the video camera.

The detection path towards a spectrograph/detector unit was selected with foldable mirror mounts (MMF, Siskiyou, OR, USA). Mirrors were acquired from Semrock (Maxmirror, MM1-311-25, 350-1100nm, NY, USA). A continuous wave krypton ion laser (Coherent, Innova 90K, Santa Clara, CA; $\lambda_{emission}$= 647.1 nm) was used as a single excitation source for the optical response (TPE-fluorescence, Rayleigh scattering and Raman scattering) in the sample. A band pass filter (BPF1 in Figure 1; Z647BP, Chroma Technology, Rockingham, VT) was used to transmit 647.1 nm and remove laser plasma emission. The excitation- and detection-path were separated by a dichroic beam-splitter (DF in Figure 1; Z647RDC, Chroma technology, Rockingham, VT). The beam-splitter has a typical transmission of 95% and 75% respectively for Stokes- and anti-Stokes emitted or scattered light. The cut-on wavelength,[10] defined as the wavelength at which the transmission is 25% of the difference between the maximum and minimum intensities (I_{max}-I_{min}) above $I_{min,}$ is 660 nm and 625 nm on the Stokes and anti-Stokes side respectively. A water immersion objective (Zeiss Plan, Neofluar, Carl Zeiss, Thornwood, NY; 63×, 1.2 NA) was used for illumination of the sample and for collection of Raman scattered photons, Rayleigh scattered photons and cwTPE fluorescence emission in epi-detection mode.

The Raman and TPE images were obtained from three-dimensional hyperspectral (spatial × spatial × spectral) datasets, which were acquired by collecting the full spectral information from spectrograph-1 and spectrograph-2 at each step during a raster scan of the sample. The samples were scanned with a scanning mirror system (SM in Figure 1; MG325D and G120D, General Scanning, Bedford, USA), with a position resolution of ~100 nm after magnification by the objective. Typical step sizes of 175 and 350 nm were used for the data acquired from APD and spectrograph-1 as shown in Figure 2 and Figure 3 respectively, and a step size of 150 nm was used for the data acquired from spectrograph-2 as shown in Figure 5. In cwTPE microscopy, TPE light first passes through a short pass filter (SPF in Figure 1; SP01-633RU, Semrock, Rochester, NY) to suppress the intense Rayleigh scattering to $\sim 10^{-5}$. A short pass filter followed by a "pass through" band pass filter (BPF2 in Figure 1; FF01-439/154, Semrock, Rochester, NY) selects the spectral region of the fluorescence emission. The TPE photons transmitted through BPF2 are detected on an avalanche photodiode (APD in Figure 1; SPCM-200/CD1705, EG&G Optoelectronics, Fremont, California) after passing through a confocal pinhole (PH1 in Figure 1) with a diameter of 50 µm and sample to pinhole magnification of 63×.

The spectrograph/detector modality (spectrograph-1 in Figure 1) in low wavenumber resolved broadband confocal micro-spectroscopy consisted of a prism (glass type: LLF1, side

68.6mm) spectrograph and a thermo-electrically cooled CCD camera (Pixis 100B, Princeton Instruments, Roper Scientific, USA). Before entering spectrograph-1 the light has passed a super notch filter (NF in Figure 1; < 10 nm, Kaiser Optical Systems, Inc., Ann Arbor, MI) to suppress the laser line and a confocal pinhole (PH2 in Figure 1) with a diameter of 15 µm. This suppression factor accommodates the Rayleigh scatter signal to the dynamic range of the CCD camera, which is used to detect Rayleigh scattering simultaneously with the fluorescence emission and Raman scattering. The sample to pinhole magnification is 22×. Spectrograph-1 covers a spectral interval from 344 to 1173 nm and simultaneously acquires spectral information in TPE fluorescence, Rayleigh scattering and Stokes Raman scattering. This spectral range corresponds to +13604 cm^{-1} to -6932 cm^{-1} in relative units with respect to the excitation wavelength of the laser at 15453.6 cm^{-1} (= 647.1 nm). The average spectral resolution per pixel varies from 12 cm^{-1} on the anti-Stokes side of the excitation wavelength to 23 cm^{-1} on the Stokes side.

The spectrograph/detector modality for high wavenumber resolution confocal Raman microscopy (spectrograph-2 in Figure 1) records the spectral information from 646 to 849 nm in 1600 pixels on a TE-cooled EMCCD (Newton DU-970N, Andor Technology, Belfast, Northern Ireland). Before entering spectrograph-2 through a confocal pinhole (PH3 in Figure 1) with a diameter of 15 µm and sample to pinhole magnification of 19×, the Raman scattered photons pass through the long pass filter (LPF in Figure 1; LP02-647RU, Semrock, Rochester, NY) to suppress Rayleigh scattering.

Cell culture and Hoechst-33342 staining

Human bone marrow stromal cells (hBMSC) from bone marrow aspirates were obtained from healthy individuals and subsequently seeded at 1000 cells/cm^2 over UV grade calcium fluoride substrate (CaF_2) (Crystran Ltd., UK) and cultured overnight in a Petri dish in cell culture medium prepared from α-MEM (GIBCO, Carlsbad, CA), 10% fetal bovine serum (FBS; Bio Whittaker, Australia), 0.2 mM L-ascorbic acid-2-phosphate (AsAP; Sigma, St. Louis, MO), 100 U/mL Pencillin G (Invitrogen, Carlsbad, CA); 100 µg/mL Streptomycin (Invitrogen) and 2 mM L-Glutamine (L-Glu; Sigma). hBMSC's were cultured at 37°C in an incubator that maintained an atmosphere of 95% humidity and 5% partial pressure of CO_2. Individual cells adhered well and spread over the CaF_2 substrate under the influence of cell culture medium. The overnight cell cultures were washed with phosphate buffer solution (PBS, GIBCO) to replace the culture media. The cells were subsequently incubated with 26 µM of Hoechst-33342 in PBS for 20 minutes. The cells were then washed twice with PBS to remove excess staining. Hoechst-33342 has a high affinity for DNA and results in a preferential binding particularly to the A-T base pairs of DNA located in the nucleus of the cell.

Data Analysis

The experimentally acquired data were converted to real Raman data by consecutive application of software that 1) removes cosmic ray events, 2) subtracts the fixed CCD camera off-set, 3) corrects for the variation in spectral transmissivity of the total set up from the microscope objective to the CCD camera of spectrograph-2, and 4) converts the wavenumber axis from pixels to wavenumbers using the well known bands of toluene as a calibration. The spectral transmissivity was corrected using a tungsten halogen light source (Avalight-HAL; Avantes BV, Eerbeek, The Netherlands) with a known emission spectrum. This correction is particularly important to remove the pronounced etalon effect inherent to back-illuminated CCD cameras. Since the output of the calibration lamp is close to zero between 344 and 410 nm, no correction was applied for the spectral transmissivity obtained with spectrograph-1 (Figure 2(A) and 2(B)). The spectra were organized in a matrix format with the position at which spectra are taken along the column dimension and spectral position along the row dimension.

Singular value decomposition (SVD) of this data matrix was performed for all hyperspectral data cubes to reduce noise.[4, 11] Univariate Raman images of the specific vibration band of interest were constructed by integrating the band intensities after local baseline subtraction. Hierarchical cluster analysis (HCA) was used as a multivariate data analysis technique to visualize the regions with high spectral similarity.[12] The results presented here are based on the inclusion of the complete spectral regions from spectrograph-1 and spectrograph-2 in this analysis.

All data manipulations were performed with routines written in MATLAB 7.4 (The Math Works Inc., Natick, MA).

2.3 Results and discussion

Amplitude-only cwTPE fluorescence imaging of cells labeled with Hoechst-33342 (Figure 2(A), inset (b), acquired with the APD-branch (Figure 1), clearly outlines the nucleus and the distribution of AT-rich chromatin in the nucleus of the cell. Relatively dark areas in the nucleus reflect the position of the nucleoli. The apparent variation in AT-rich DNA regions illustrates the state of the cell as in the interphase. The image contains 128 × 128 pixels with a total image acquisition time of 16 seconds. The area of the image was 22.5 µm × 22.5 µm with a pixel size of 175 nm. The pixel size corresponds to the Nyquist theorem, which states that sampling at twice the optical resolution is sufficient to acquire maximum spatial wavenumber information. Each pixel was measured during an accumulation time of 1ms/pixel and 100 mW laser power, resulting in a dose per pixel of 100 µJ. In spite of this low dose of cw-light/pixel a pronounced non-linear response can be obtained.

To establish a relationship between the distribution of the two-photon fluorescence and chemical properties of a sample, a hyperspectral dataset was acquired with spectrograph-1 (Figure 1) after folding a mirror (M2 in Figure 1) into the light path. The hyperspectral data set contains spectral emission from 344 to 1173 nm, which contains spectrally resolved cwTPE fluorescence emission, Rayleigh scattering and low wavenumber resolved Raman scattering. Each spectrum was acquired for 100 msec. The image contains 64 × 64 pixels from an area of 22.5 µm × 22.5 µm with a pixel size equal to the optical resolution of 350 nm. The total image time is 409.6 seconds and the effective "voxel"-volume was 0.3 femtoliter. The average accumulated spectrum of all pixels is shown in Figure 2A, together with the white light image (Figure 2A; inset (a)) and TPE fluorescence image (Figure 2A; inset (b)) as acquired by the APD detector (Figure 1). Figure 2A (inset (c)) shows the average over all pixels of the spectrally resolved TPE amplitude region.

The spectrum in Figure 2A can be divided in the following regions. Region (i) is the spectral region on the anti-Stokes side of the excitation wavelength at 647.1 nm and the amplitude arises from photons emitted in a two-photon excited fluorescence emission process. Figure 2A; inset (c) shows a magnification of this region to which the anti-Stokes Raman spectrum potentially also contributes. Since the measurements are conducted at room temperature, the amplitude of the anti-Stokes Raman spectrum is too feeble to contribute significantly and can therefore be completely neglected under these conditions. Indicated by star '*' are spectral features caused by the transmission properties of the super notch filter, which is in place to suppress the Rayleigh scattering by ~6 orders of magnitude. Furthermore, in the spectral region indicated with a plus '+', the transmission of the super notch filter is almost "zero", giving rise to a gap in the spectrum. Region (ii) contains the Rayleigh scattering of the laser line (647.1 nm), which is transmitted by the super notch filter. The amplitude of the Rayleigh scattering is now of similar magnitude as all other signals and can be accommodated within the dynamic range of the CCD camera. Region (iii) contains the Stokes Raman spectrum. The modulation, which increases towards the "red" edge of the spectrum indicated by '++', is a result of interference effects in the thin photo-sensitive layer of the back-illuminated CCD camera, commonly known as “the etaloning effect”. The Stokes Raman spectrum is limited on the blue edge by the super notch filter, which opens (50%) at -300 cm^{-1} as indicated by ‘#’ in Figure 2A. The Stokes Raman spectrum covers 300 pixels from -300 cm^{-1} to -6932 cm^{-1}, resulting in an average resolution of 22 cm^{-1}/pixel. The spectra are dominated by the intense Raman scattering of water throughout the spectrum with the main band of water at -3300 cm^{-1}. Even at this low resolution and in spite of the high water background, clear signals can be observed that originate from lipid/protein distribution (-1430 to -1450 cm^{-1}), and high wavenumber OH vibrations (around -3300 cm^{-1}).[13]

HCA from +9000 cm^{-1} to -4000 cm^{-1} of the hyperspectral dataset and subsequent subtraction of the buffer spectrum, from an area outside the hBMSC, results in the cluster-spectra in Figure 2B. The spectra are marked as (i), (ii) and (iii) and are representative for the corresponding locations in Figure 2B inset (a). These locations also correspond to the cluster areas in the cluster-image (Figure 2B inset (b)). The spectra and images together suggest the following description of these regions: (i) cytoplasm with prominent presence of lipid droplets, (ii) nucleus and (iii) cytoplasm with reduced contributions of lipids and (iv) background corresponding to PBS buffer. After buffer subtraction all cluster-spectra are dominated by intense bands of the C-H stretching motion in lipids and proteins near -3000 cm^{-1}. Residual “etaloning” is predominantly occurring above -2000 cm^{-1} in agreement with the specifications of CCD cameras. Other prominent Raman-bands can be observed in the fingerprint region around -1640 cm^{-1} (Water, amide-I of proteins), -1556 cm^{-1} (Hoechst-33342), -1432 cm^{-1} (lipids and proteins), around -900 cm^{-1} and -1100 cm^{-1} (backbone vibrations of proteins, side chain vibrations of proteins and bands of lipids). At the anti-Stokes side from + 9000 cm^{-1} (409 nm) to +1000 cm^{-1} (608 nm) the TPE fluorescence emission of Hoechst is observed. Since the spectra, coded by color, belong to the same cluster a direct relation of the spectral information in TPE fluorescence microspectroscopy (Figure 2B, inset (b) and Raman microspectroscopy (Figure 2B) can be made. The intense TPE fluorescence emission (red spectrum) correlates with the Raman scattering from Hoechst at -1556 cm^{-1}. Minor contributions from Hoechst are still clearly visible in the “black” and “blue” cluster, particularly in the anti-Stokes side indicated by Region (i). This contribution is due to unspecific Hoechst binding to other substrates in the cell, which is well known to occur for the incubation parameters that were used here.[14] The integrated band area intensity of the TPE fluorescence emission in the anti-Stokes region as seen in Figure 2B, inset (b), show that the fluorescence of Hoechst-33342 bound to the nucleus (red spectra) is respectively 7 and 9.5 times higher than that shown for cytoplasm with prominent presence of lipid droplets (black spectra) and cytoplasm with reduced contributions of lipids (blue spectra) respectively. The increase in fluorescence correlates with the number of molecules bound to AT base pairs of DNA in the nucleus of the cell.

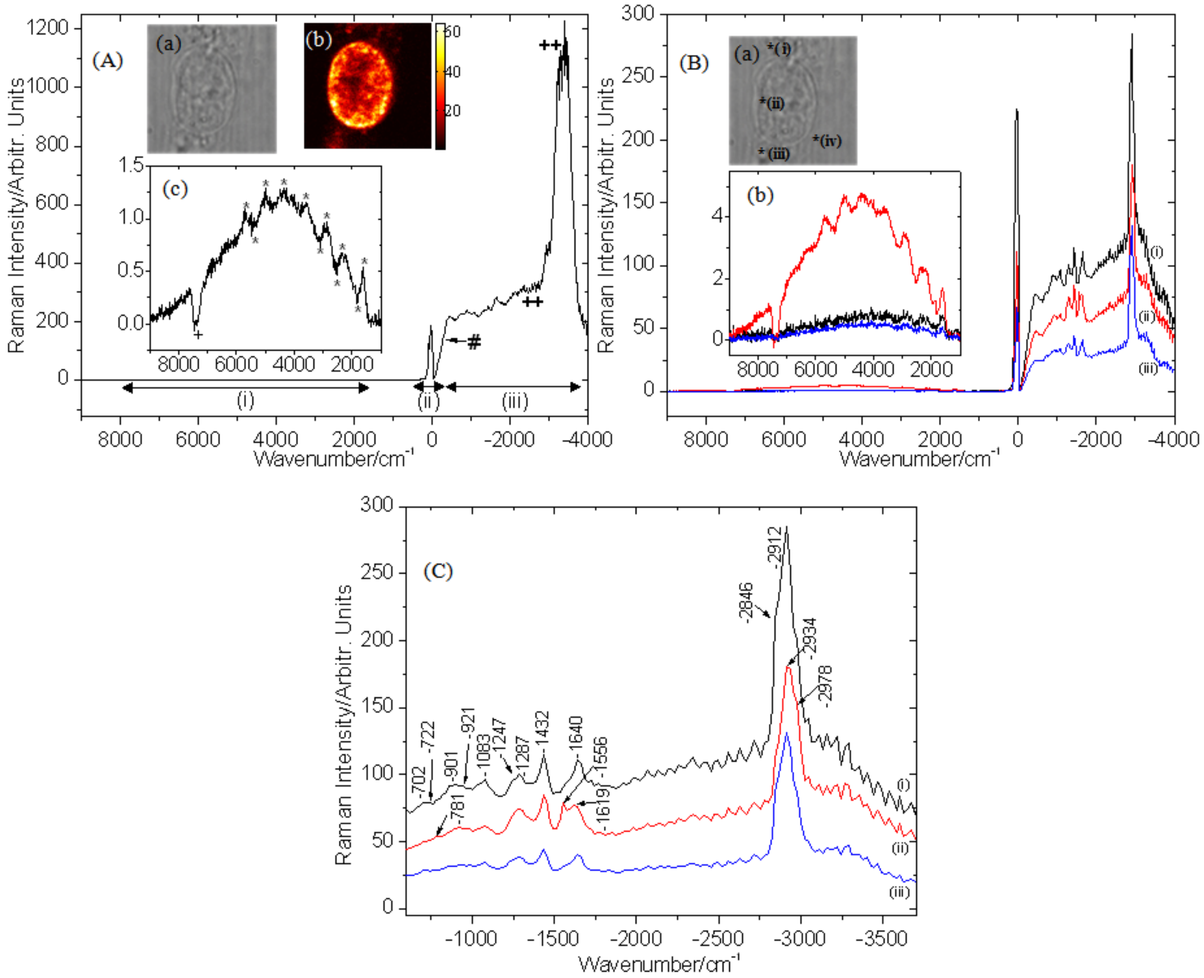

Figure 2: LWRI confocal Raman spectral information containing (A) average spectral information showing combined spectral information over Region (i) TPE at anti-Stokes side (left side) +9000 to +1000 cm^{-1} (409 to 608nm)), Region (ii) Rayleigh scattering (+125 to -25 cm^{-1}) and Region (iii) LRRI at Stokes side (right side) (-600 to -3700 cm^{-1}); Inset (a) White light micrograph of single living hBMSC, Inset (b) Nucleotide distribution in the nucleus of the living hBMSC obtained from cwTPE fluorescence microscopy of Hoechst-33342, Inset (c) Enlarged view of average spectra of the TPE of Hoechst-33342 in the region 9000 to -1000 cm^{-1} (409 to 608nm) as seen in Region (i); (B) Average spectra after background buffer subtraction obtained after HCA corresponding to (i) cytoplasm with prominent presence of lipid droplets, (ii) nucleus and (iii) cytoplasm with reduced contributions of lipids; Inset (a) White light micrograph of single living hBMSC cell showing regions of interests (i) cytoplasm with prominent presence of lipid droplets, (ii) nucleus, (iii) cytoplasm with reduced contribution of lipids and (iv) Background composed of PBS buffer. Inset (b) Enlarged view of the TPE of Hoechst-33342 in the region 9000 to -1000 cm^{-1} (409 to 608nm); (C) Average spectra after background buffer subtraction obtained after HCA in the Stokes region (-600 to -3700 cm^{-1}) corresponding to (i) cytoplasm with prominent presence of lipid droplets, (ii) nucleus and (iii) cytoplasm with reduced contributions of lipids.

In the Stokes region, shown in Figure 2C, the spectra show bands at -702, -722, -781, -901, -921, -1083, -1247, -1287, -1432, -1556, -1619, -1640, -2846, -2912, -2934 and -2978 cm^{-1}, that signify the molecular composition corresponding to proteins, lipids and nucleotides in the region of interest. These spectral markers merely indicate the wave number assignment to the pixel and not the “true” position of this band, since in the low wavenumber-resolved mode a pixel corresponds, on average, to 22 cm^{-1}. The cluster spectrum in Figure 2(B)(i) shows prominent strong bands at positions -901, -1083, -1640, -2846 (shoulder band) and -2912 cm^{-1} and confirms the presence of lipids. The presence of bands at -781 and -1556 cm^{-1} in the cluster spectrum of Figure 2(B)(ii) corresponds to nucleotides and Hoechst-33342 bound to AT base pairs of DNA in the nucleus of the cell. The presence of bands around -1619, -2934 and -2978 cm^{-1} (shoulder band) signifies the occurrence of proteins in the nucleus of the cell. The same spectrum in the anti-Stokes region shows intense TPE fluorescence emission due to Hoechst-33342, which is in agreement with the Raman spectrum. The Stokes region of the spectrum in Figure 2(B)(iii) shows bands at similar positions as that seen in Figure 2(B)(i), however the bands are much weaker in intensity, which reflects a lower lipid and protein concentration in the region under consideration.

Naturally the relatively low wavenumber resolved Raman microspectroscopy data sets convey less molecular specific information than do high resolution Raman microspectroscopy data (vide infra). The Raman spectra are, however, distinctive enough to extract useful amplitudes for correlation imaging. In Figure 3 Raman images are prepared from the hyperspectral data set. The distribution of water in Figure 3(b), Rayleigh scattering in Figure 3(c), lipids/proteins in Figure 3(d), spectrally resolved TPE fluorescence in Figure 3(e) and Raman scattering from Hoechst-33342 in Figure 3(f) are shown together with the white light image in Figure 3(a). The spectrally resolved cwTPE fluorescence image (Figure 3(e)) correlates well with the amplitude-only cwTPE fluorescence image shown in inset Figure 2A, inset (b) and the Raman scattering from Hoechst in Figure 3(f), as expected. The Raman image for the band at ~-1432 cm^{-1} in Figure 3(d) shows the distribution of lipids/proteins in a cell. The Rayleigh scattering image (Figure 3(c)) is constructed from the amplitude in 8 pixels around 0 cm^{-1} and shows the location of highly scattering areas in the cell, such as the endoplasmic reticulum. Cell organelles composed of lipids contribute strongly to Rayleigh scattering as a result of relatively large variations of the refractive index of those organelles with the surrounding cytoplasm. The Rayleigh scattering image from highly scattering, lipid-rich heterogeneous areas anti-correlates with the image of the high wavenumber OH-stretch-vibration around -3300 cm^{-1} (Figure 3(b)). The understanding behind this observation is that lipid-rich areas are relatively low in water content. The relatively high Rayleigh scattering for lipid rich regions in the cytoplasm correlates positively with the Raman band integration image constructed from the amplitude around -1432 cm^{-1}, which corresponds to the CH_2 deformation mode of lipids/ proteins in Figure 3(c) and 3(d) respectively.

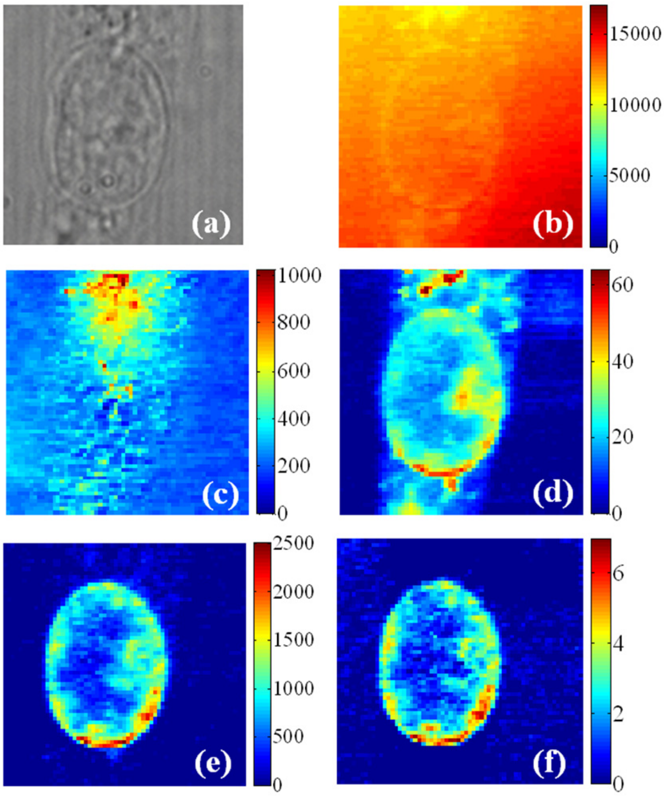

Figure 3: Hybrid microscopy images of a single living hBMSC in physiological buffer solution. (a) White light micrograph of single living hBMSC showing region of interest for LWRI. (b) Raman band integration image of high wavenumber OH vibrations around -3300 cm^{-1} band (Δ = 670 cm^{-1}), (c) Band integration image over 8 pixels around 0 cm^{-1} showing Rayleigh scattering, (d) Raman band integration imaging of CH_2 deformation on the basis of -1430 cm^{-1} band (Δ = 83 cm^{-1}), (e) Band integration image over 435 nm to 600 nm showing nucleotide distributions in the nucleus of the living hBMSC cell obtained from the cwTPE fluorescence microspectroscopy of Hoechst-33342, (f) Raman band integration imaging of Hoechst-33342 bound to AT base pairs of DNA around -1560 cm^{-1} band (Δ = 41 cm^{-1}). The confocal broadband microspectroscopy were acquired by scanning in 64 × 64 steps respectively in an area of 22.5 µm × 22.5 µm with 100 mW laser power. The imaging time for confocal broadband microspectroscopy was around 7 minutes.

Figure 4(a), 4(b) and 4(c) show the two level hierarchical cluster analysis (HCA) over the hyperspectral data acquired from spectrograph-1 in spectral region corresponding to TPE at anti-Stokes region (+9000 to +1000 cm^{-1}), Rayleigh scattering (8 pixels around 0 cm^{-1}) and LRRI at Stokes region (-600 to -3700 cm^{-1}) respectively. Two level cluster analysis indicates that the hyperspectral dataset was clustered up to two clusters. Two level cluster analysis is a useful method to identify the object in the buffer environment. The average spectra for each cluster image presented in Figure 4(a), and 4(c) are shown in Figure 4(d) and 4(e). The two level HCA image of spectral information in the range -9000 to -1000 cm^{-1} clearly outlines the nucleus. Black pixels in the nucleus locate the nucleolus, which is characterized by a relatively low DNA content and therefore a low contribution of Hoechst-33342. The spectrum corresponding to the grey cluster in Figure 4(a) is shown in Figure 4(d). The cluster assigned by grey pixels in Figure 4(a) corresponds to images shown in Figure 2A, inset (b) and Figure 3(e) respectively to cwTPE fluorescence microscopy image from APD and band integration image of cwTPE fluorescence spectroscopic data from spectrograph-1 in the anti-Stokes region. The two level HCA image over the range corresponding to Rayleigh scattering is shown in Figure 4(b). The cluster image (grey pixels) shows a similar pattern as observed in Figure 3(c) and Figure 3(d), which corresponds to band integration image for the Rayleigh band and 1430 cm^{-1} band for CH_2 deformation of lipids/proteins. The high intensity regions in Figure 3(c) and Figure 3(d) are in good agreement with the grey cluster. The spectra corresponding to grey pixels show higher intensity due to the higher scattering capabilities of lipid-based organelles compared to the spectra of pixels corresponding to the black cluster, which reflect the more aqueous cytoplasmic area in the cell and PBS buffer media as seen in Figure 4(b). Two-level HCA image over Stokes region from -600 to -3700 cm^{-1} shows low wavenumber resolution Raman imaging as seen in Figure 4(c) and the respective average cluster spectrum is shown in Figure 4(e). The grey and black clusters relates to the complete cell in the region of interest and PBS buffer signifying background respectively. The distribution of grey pixels corresponds to the hBMSC, whose white light micrograph is shown in Figure 2A, inset (a) and is similar to band integration image of -1432 cm^{-1} band for CH_2 deformation of lipids/proteins as seen in Figure 3(d). The average spectra of all the pixels corresponding to grey pixels show prominent bands at -722, -781, -921, -1083, -1287, -1432, -1640, and -2934 cm^{-1} corresponding to proteins, lipids and nucleotides as seen in Figure 4(e) unlike the average spectra of pixels corresponding to black cluster. The grey cluster obtained from two-level HCA over different spectral regions shown in Figure 4(a), 4(b) and 4(c) are influenced by the chemical variations in the hBMSC under consideration.

The results from confocal fluorescence microscopy and confocal broadband microspectroscopy enable selection of regions of interest for high wavenumber- and spatially resolved Raman microspectroscopy as shown in Figure 5(a) (white dotted square) obtained from spectrograph-2. An area of 4.9 μm × 4.9 μm was selected to contain a recognizable area in the nucleus, the curved shape of the nuclear membrane and an area in the cytoplasm. Figure 5(b) shows the enlarged view of the region of interest, which was shown in Figure 5(a). High wavenumber and spatially resolved Raman spectroscopy was achieved by folding mirrors M2 and M4 (Figure 1). The area was imaged with a pixel size of 150 nm, an accumulation time of 500 ms/pixel and a laser power of 100 mW, which results in a total image time of ~8 minutes. The high wavenumber resolution in the hyperspectral Raman dataset has now been used to generate univariate images of bands at -717, -785, -1003, -1560, -2845 and -2935 cm^{-1}, respectively in Figure 5(c), 5(d), 5(e), 5(f), 5(g) and 5(h). These bands correspond, respectively, to membrane lipids, DNA, phenylalanine, Hoechst-33342 molecules, lipids and proteins.[13, 15-17] The band integration image of Hoechst-33342 at -1560 cm^{-1} (Figure 5(f)) corresponds with Raman image (Figure 5(d)) for DNA, which is in accordance with expectation, based on the fluorophore interaction with DNA. The Raman image (Figure 5(e)) for the band at -1003 cm^{-1} shows the distribution of phenylalanine over the cell, which is in accordance with the Raman image for the protein distribution derived from the band around -2935 cm^{-1} (Figure 5(h)), as must be expected. The Raman image for the band at -2845 cm^{-1} (Figure 5(g)) shows the distribution of lipids. The Raman image (Figure 5(c)) for membrane phospholipids characterized by a band at -717 cm^{-1}, represents the distribution of phosphatidylcholine.

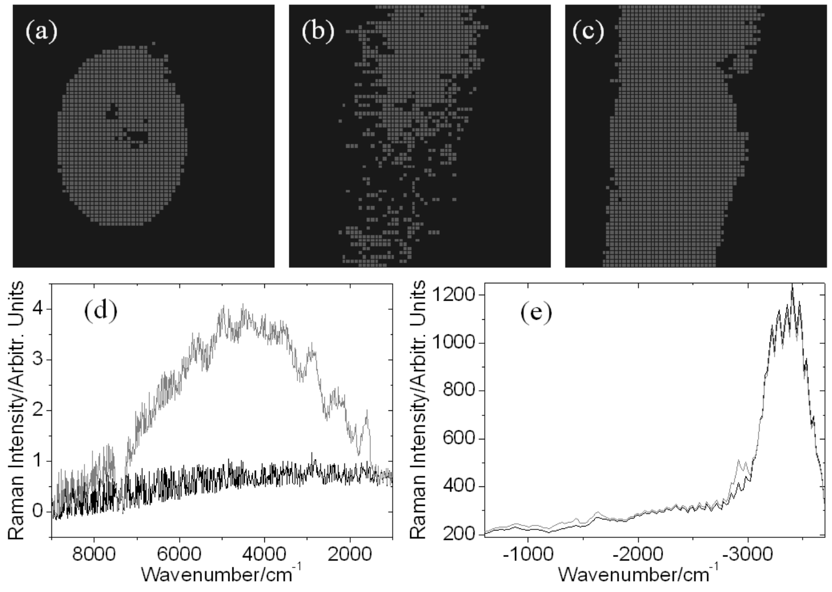

Figure 4: Two level HCA of the acquired hyperspectral data from the living hBMSC shown in Figure 2(a) over the spectral region corresponding to (a) TPE at anti-Stokes side (+9000 to +1000 cm^{-1}), (b) Rayleigh scattering (8 pixels around 0 cm^{-1}), (c) LRRI at Stokes region (-600 to -3700 cm^{-1}), (d) Average spectra of all pixels corresponding to respective cluster seen in (a) for anti-Stokes region, and (e) Average spectra of all pixels corresponding to respective cluster seen in (c) for Stokes region.

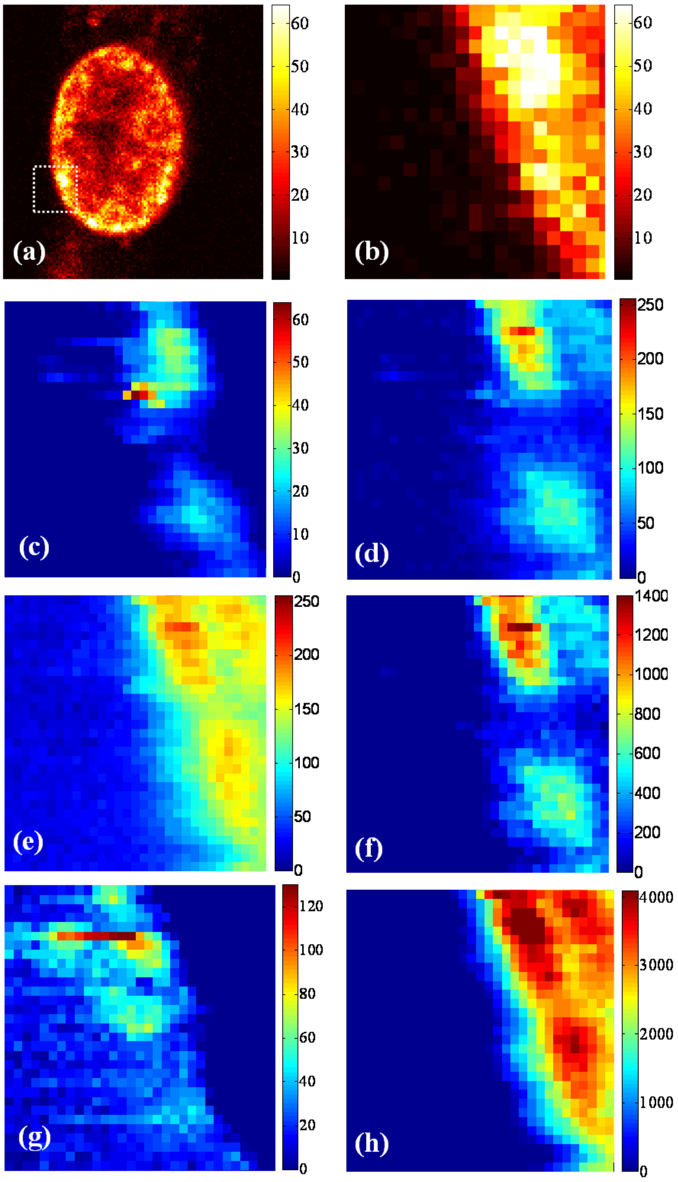

Figure 5: Hybrid microscopy images of a single living hBMSC in physiological buffer solution obtained from high wavenumber resolution Raman microspectroscopy. (a) Nucleotide distribution in the nucleus of the living hBMSC cell obtained from cwTPE fluorescence microscopy of Hoechst-33342. (b) Enlarged view of region of interest from Figure 5(a) (4.9 µm × 4.9 µm, white dotted square) for high wavenumber resolution confocal Raman microspectroscopy. (c) Raman imaging for C-N of membrane lipids around -717 cm^{-1} band (Δ = 29 cm^{-1}). (d) Raman imaging for backbone O-P-O of DNA around -785 cm^{-1} band (Δ = 35 cm^{-1}). (e) Raman imaging for Phenylalanine around -1003 cm^{-1} band (Δ = 25 cm^{-1}). (f) Raman imaging for Hoechst-33342 bound to AT regions of the nucleus around -1560 cm^{-1} band (Δ = 68 cm^{-1}). (g) Raman imaging for CH_2 antisymmetric stretch of lipids around -2845 cm^{-1} band (Δ = 76 cm^{-1}). (h) Raman imaging for CH_2 antisymmetric stretch of protein around -2935 cm^{-1} band (Δ = 120 cm^{-1}). The high wavenumber resolution Raman images were acquired by scanning in 32 × 32 steps respectively in an area of 4.9 µm × 4.9 µm with an imaging time around 8 minutes and 100 mW laser power.

The univariate images can be compared with a hierarchical cluster analysis image in Figure 6A. This Figure shows 12 levels of cluster analysis of the hyper spectral data acquired from the region of interest (dotted white line in Figure 5(a)) of 4.9 µm × 4.9 µm with a pixel resolution of 150 nm. The clusters marked with numbers 1 to 5 and 8 to 12 correspond to major cellular features and clusters 6 and 7 correspond to the background PBS buffer, with a minor difference in the intensity of water band around -3300 cm^{-1} in cluster 6. The influence of PBS is removed from each of the cluster by subtracting the average spectra of all pixels corresponding to cluster 6 and 7 with the average spectra obtained from pixels corresponding to other respective clusters. Figure 6(B)(i) and 6(B)(ii) show background free spectra for the clusters 1, 2, 3, 4, 10 and 12 in the fingerprint region and high wavenumber region respectively. The intense bands at -980, -1450, -1560, -1610 and -1658 cm^{-1} in the fingerprint region (Figure 6(B)(i)) correspond to Hoechst-33342 molecule bound to AT base pairs in DNA.[8] The band at -1560 cm^{-1} observed in the data acquired from spectrograph-2 is also observed in the data acquired from spectrograph-1 at a pixel with wavenumber assignment -1556 cm^{-1} (Figure 2(C)(ii)). The bands at the positions -723 and -1092 cm^{-1} correspond to the presence of adenine molecule and nucleic acid phosphate backbone respectively. The highest intensity in these bands is shown by cluster 3 (magenta color pixels), which corresponds to an area with a high density of DNA in the nucleus. This area corresponds well with the amplitude only cwTPE fluorescence microscopy image and to the pixels corresponding to the univariate Raman images for backbone O-P-O of DNA around -785 cm^{-1} band (Figure 5(b) and 5(d)). The bands around -1658 and -2935 cm^{-1} in Figure 6(B)(i) and 6(B)(ii) signify the occurrence of proteins in the region of interest.

The background free spectra associated with clusters 5, 8 and 9 for the fingerprint region and the high wavenumber region, respectively, are shown in Figure 6(C)(i) and 6(C)(ii). There are prominent bands at -1450, -1560, and -1610 cm^{-1} (Figure 6(C)(i)), however these bands are weaker by comparison than the same bands represented in Figure 6(B)(i). The presence of a band at -717 cm^{-1} signifies the presence of membrane lipid phosphatidylcholine.[13] The region over the clusters 5, 8 and 9 correspond to the membrane as can be observed from the presence of the -717 cm^{-1} and the absence of the -723 cm^{-1} band for nucleotide. The assignment of these clusters to lipid-rich nuclear membrane is further supported by -1064 cm^{-1} for skeletal C-C stretch of lipids in Figure 6(C)(i) and by bands in the high wavenumber region at -2850 cm^{-1} in Figure 6(C)(ii), which is not present in the spectra corresponding to nucleus (Figure 6(B)(ii)). The area of the clusters 5, 8 and 9 corresponds to the pixels in the univariate Raman image for the band around -717 cm^{-1}

(Figure 5(c)) and the Raman image for the CH_2 antisymmetric stretch mode of lipids around -2890 cm^{-1} band (Figure 5(g)), respectively.

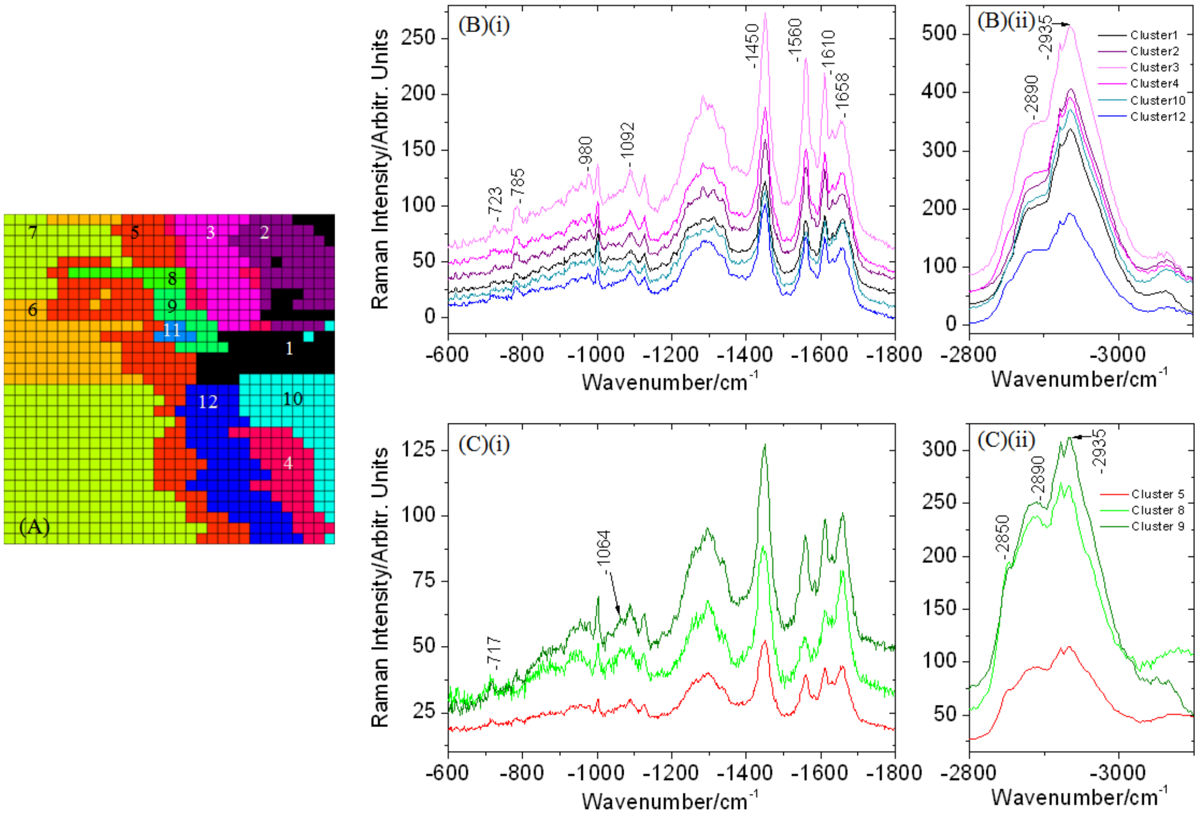

Figure 6: High wavenumber resolution confocal Raman spectral information showing (A) HCA up to 12 clusters over the region of interest shown in Figure 5(a). (B) Average spectra after background buffer subtraction for clusters 1, 2, 3, 4, 10 and 12 shown over the (i) finger print region (-600 to -1800 cm^{-1}), and (ii) high wavenumber region (-2800 to -3100cm^{-1}) indicating prominent bands for nucleotides and Hoechst-33342 bound to AT base pair of DNA of nucleus of the cell; and (C) Average spectra after background buffer subtraction for clusters 5, 8, and 9 shown over the (i) finger print region (-600 to -1800 cm^{-1}), and (ii) high wavenumber region (-2800 to -3100 cm^{-1}) indicating significant bands for membrane lipid phosphatidylcholine and lipids respectively.

The univariate images in Figure 5 are in good correspondence with the image after cluster analysis (Figure 6(A)). Since the spectral information of the nuclear region in Figure 6(B) and 6(C) is dominated by variations in the concentration of Hoechst-33342 it is interesting to quantify the difference. We have defined ratio spectra, R, from cluster spectra "i" and "j", respectively $C_i(\nu)$ and $\mathrm{C_j}(\nu)$, as follows

$$\mathrm{R}(\nu)=\frac{\mathrm{C_i}(\nu)-\mathrm{C_j}(\nu)}{\left(\mathrm{C_i}(\nu)+\mathrm{C_j}(\nu)\right)}$$

Defined in this way, the ratio-spectrum reflects the percentage variation with respect to the average of spectrum “i” and “j”. Figure 7(A) shows the ratio spectrum of cluster area “i=3” and “j=12”, where “i=3” is a region with high DNA concentration and “j=12” is an area with relatively low DNA concentration. The Raman bands for Hoechst-33342 are visible at an excellent signal-to-noise ratio. The negative value of the OH-band in the ratio-spectrum around -3300 cm^{-1} indicates the decrease of water in areas of higher concentration of DNA, here in cluster 3 as compared to cluster 12. The ratio spectroscopy for the presence of membrane lipids over the clusters 5 and 8 corresponding to minimum and maximum distribution is shown in Figure 7(B). The ratio spectrum shows a significant band at -717 cm^{-1} for phosphatidylcholine and other band positions that can be assigned to lipids at -1064, -1299, -1434, -1654, and -2850 cm^{-1} similar to that seen in Figure 6(C)(i) and 6(C)(ii). The presence of OH band around -3300 cm^{-1} which is almost of same intensity as the baseline indicates similar amounts of water over the clusters corresponding to lipid membranes.

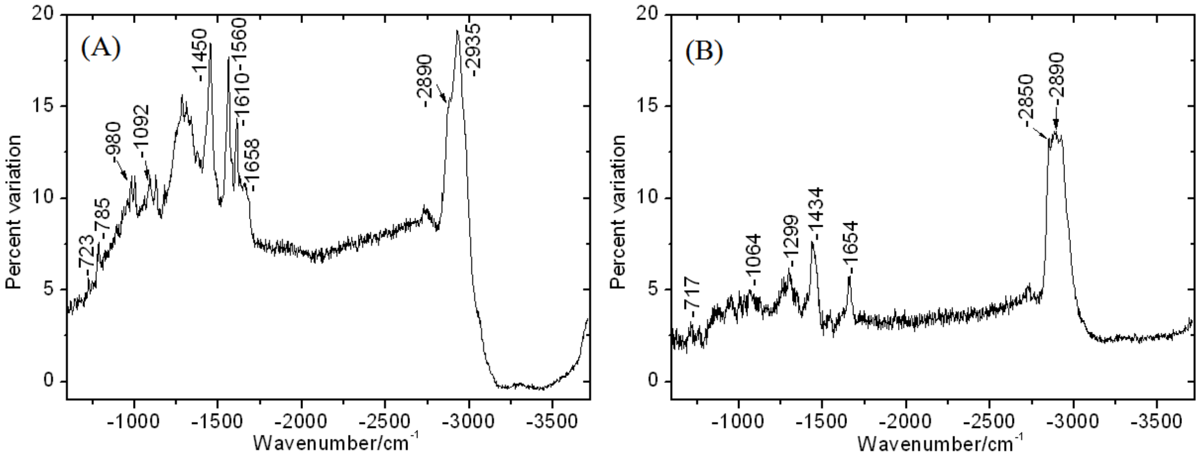

Figure 7: Ratio spectroscopy showing percentage variation over the 12 level cluster image showing the maximum and minimum distribution of molecules, (A) Percentage variation of Hoechst-33342 bound to the AT base pairs of DNA over the pixels corresponding to cluster 3 and cluster 12 for maximum and minimum distribution respectively, (B) Percentage variation of membrane lipids present over the pixels corresponding to cluster 8 and cluster 5 for maximum and minimum distribution respectively.

2.4 Conclusion

We have presented a flexible and versatile Rayleigh/Raman/fluorescence microscope system, which is based on a single laser emission wavelength of 647.1 nm. This system comprises of three detection modalities, which are all confocal with the same sample-plane. The three detection modalities include: 1) a detector for an amplitude-only TPE fluorescence microscopy, 2) a low wavenumber resolution prism spectrograph covering a bandwidth from

344 nm to 1173 nm, which offers a spectrally resolved TPE signal, a Rayleigh scatter signal and a spectrally resolved, low resolution Raman signal. All signals fall within the dynamic range of the CCD camera and it has been shown (vide supra) that all signals can be simultaneously acquired within a single camera read-out, and 3) a high-resolution hyperspectral Raman detection system covering a bandwidth of 646 nm to 849 nm, which corresponds with a Raman spectrum from +20 cm^{-1} to -3670 cm^{-1}. The strength of the fluorescence-Raman microscope is that fluorescence microscopy, as a “golden standard” microscope method in biology, can be combined with Raman- and Rayleigh-scattering microscopy. The latter microscopy techniques give complementary information, respectively on the chemical composition and the light scattering, from spatially correlated events. The development of hybrid microscopy techniques acquires intense interest currently, precisely because of the ability to correlate diverse molecular properties through distinct optical signals.[8, 18, 19]

We have furthermore shown that amplitude-only cwTPE (modality 1) provides a fast and easy way to scan a large field of view that enables subsequent selection of areas of interest for detailed investigation with Rayleigh and Raman scattering. A subsequent measurement with modality 2 acquires in a single camera read-out of the spectrally resolved TPE emission, the Rayleigh scattering at 0 cm^{-1} and the LRRI. This mode offers strict image correlation between diverse optical signals. All information from modality 1 and 2 is available to zoom into an area of interest for high spatial resolution Raman imaging. Raman images were acquired that fulfill the Nyquist theorem at an optical far field resolution of approximately 370 nm. Finally, the Rayleigh/Raman/fluorescence microscope was used to characterize living bone marrow derived human mesenchymal stromal cells.

References

1. Puppels, G. J.; De Mul, F. F. M.; Otto, C.; Greve, J.; Robert-Nicoud, M.; Arndt-Jovin, D. J.; Jovin, T. M., Studying single living cells and chromosomes by confocal Raman microspectroscopy. *Nature* **1990,** 347, (6290), 301-3.
2. Uzunbajakava, N.; Lenferink, A.; Kraan, Y.; Willekens, B.; Vrensen, G.; Greve, J.; Otto, C., Nonresonant Raman imaging of protein distribution in single human cells. *Biopolymers* **2002,** 72, (1), 1-9.
3. Notingher, I.; Verrier, S.; Romanska, H.; Bishop, A. E.; Polak, J. M.; Hench, L. L., In situ characterization of living cells by Raman spectroscopy. *Spectroscopy* **2002,** 16, (2), 43-51.
4. Uzunbajakava, N.; Lenferink, A.; Kraan, Y.; Volokhina, E.; Vrensen, G.; Greve, J.; Otto, C., Nonresonant confocal Raman imaging of DNA and protein distribution in apoptotic cells. *Biophys. J.* **2003,** 84, (6), 3968-3981.
5. Matthaus, C.; Boydston-White, S.; Miljkovic, M.; Romeo, M.; Diem, M., Raman and infrared microspectral imaging of mitotic cells. *Appl. Spectrosc.* **2006,** 60, (1), 1-8.
6. Short, K. W.; Carpenter, S.; Freyer, J. P.; Mourant, J. R., Raman spectroscopy detects biochemical changes due to proliferation in mammalian cell cultures. *Biophys. J.* **2005,** 88, (6), 4274-4288.
7. Notingher, I.; Jell, G.; Lohbauer, U.; Salih, V.; Hench, L. L., In situ non-invasive spectral discrimination between bone cell phenotypes used in tissue engineering. *J. Cell. Biochem.* **2004,** 92, (6), 1180-1192.
8. Uzunbajakava, N.; Otto, C., Combined Raman and continuous-wave-excited two-photon fluorescence cell imaging. *Opt. Lett.* **2003,** 28, (21), 2073-2075.
9. Van Manen, H.-J.; Otto, C., Hybrid Confocal Raman Fluorescence Microscopy on Single Cells Using Semiconductor Quantum Dots. *Nano Lett.* **2007,** 7, (6), 1631-1636.
10. Froehlich, P. M.; Guilbault, G. G., *Practical Fluorescence*. 2nd ed.; CRC Press: New York, 1990; p 41-74.
11. Uzunbajakava, N.; Greve, J.; Otto, C., Raman microscopy of cells: chemical imaging of apoptosis. *Proc. SPIE-Int. Soc. Opt. Eng.* **2003,** 4963, (Multiphoton Microscopy in the Biomedical Sciences III), 223-230.
12. van Manen, H.-J.; Kraan, Y. M.; Roos, D.; Otto, C., Single-cell raman and fluorescence microscopy reveal the association of lipid bodies with phagosomes in leukocytes. *Proc. Natl. Acad. Sci. U. S. A.* **2005,** 102, (29), 10159-10164.
13. Krafft, C.; Neudert, L.; Simat, T.; Salzer, R., Near infrared Raman spectra of human brain lipids. *Spectrochim. Acta, Part A* **2005,** 61A, (7), 1529-1535.
14. Shapiro, H. M., *Practical Flow Cytometry*. 4th ed.; John Wiley & Sons: New Jersey, 2003.
15. Peticolas, W.; Kubasek, G.; Thomas, G.; Tsuboi, M., *Biological Applications of Raman Spectroscopy*. Wiley: New York, 1987; Vol. 1, p 81-133.
16. Tu, A. T., *Raman Spectroscopy in Biology: Principles and Applications*. 1982.
17. Zimmermann, F.; Zimmermann, B.; Panitz, J. C.; Wokaun, A., Surface-enhanced resonance Raman scattering study of the groove binding dye Hoechst-33258. *J. Raman Spectrosc.* **1995,** 26, (6), 435-41.
18. Chen, H.; Wang, H.; Slipchenko, M. N.; Jung, Y.; Shi, Y.; Zhu, J.; Buhman, K. K.; Cheng, J.-X., A multimodal platform for nonlinear optical microscopy and microspectroscopy. *Opt. Express* **2009,** 17, (3), 1282-1290.
19. Krause, M.; Rosch, P.; Radt, B.; Popp, J., Localizing and Identifying Living Bacteria in an Abiotic Environment by a Combination of Raman and Fluorescence Microscopy. *Anal. Chem.* **2008,** 80, (22), 8568-8575.

Chapter 3

Time Lapse Raman Imaging of single live lymphocytes

We present Time Lapse Raman Imaging (TLRI) of living cells as a new approach in label-free chemical imaging through non-electronic resonant, spontaneous Raman microspectroscopy. Raman hyperspectral data cubes of individual live peripheral blood lymphocytes (PBL) were successively acquired. The Raman imaging time per voxel, with a volume of 0.3 femtoliter, was 100 ms and the total image time of a 32 × 32 pixels image was less than 2 minutes. Multiple images of an individual cell have been obtained. A full series of TLRI images typically resulted in more than 1.6 million data points per image. We analyzed the data sets using hierarchical cluster analysis. A fingerprint of molecular changes was observed before the cell was blebbing. The molecular fingerprint was related to a gradual disappearance of the Raman signal from carotenoids. Concomitant changes occurred in the C-H-stretch high wavenumber region, presumably due to a change in the protein and lipid environment of carotenoids. These changes were smaller than 5% of the total signal at 2937 cm^{-1}. We hypothesize that the lipid environment of the carotenoids changes as a result of the photophysics in the carotenoid molecules. The detectability of carotenoids was shown to be 2.3 µM per voxel, which corresponds to 415 molecules. TLRI enables high-speed chemical imaging not only in the intense high wavenumber region of the Raman spectrum, but particularly in the more informative fingerprint region from 500 - 1800 cm^{-1}.

This chapter has been published in Journal of Raman Spectroscopy

3.1 Introduction

In recent years many new technologies for single cell imaging have been developed. The development of vibrational spectroscopy based imaging methods play a pivotal role because of their ability to perform label-free chemical analysis by optical fields. Vibrational spectroscopic techniques like non-resonant Raman spectroscopy,[1] resonance Raman (RR) spectroscopy and imaging,[2] coherent anti-Stokes Raman spectroscopy (CARS)[3, 4] and Fourier transform infrared (FTIR) spectroscopy[5] provide a wealth of biochemical information at the molecular level from single cells by spatially resolved chemical analysis. The strength of these optical spectroscopic techniques is that they are based on a measurement of chemically specific vibrations of (biological) molecules. The dipole moments and the polarizability associated with the vibrational motions provide rapid, label-free, and non-invasive chemical analysis of single cells with sub-cellular resolution.

In contrast to FTIR spectroscopy, which is based on light absorption, non-resonant Raman spectroscopy, RR spectroscopy and CARS work on the principle of light scattering. Non-resonant Raman spectroscopy and RR spectroscopy provide results similar to that of FTIR spectroscopy. RR spectroscopy is selective for molecules with absorption near the excitation wavelength; however the high photon flux in Raman microspectroscopy may result in competitive processes such as optical absorption and dissipation, fluorescence emission and photochemical changes in molecules. Four-wave mixing techniques, such as CARS, CSRS (coherent Stokes Raman scattering)[6] and stRS (stimulated Raman scattering)[7-9] on the other hand, enable the acquisition of images with a high speed compared to non-resonant Raman imaging. Four-wave mixing microscopy and spectroscopy, however, require high peak powers in the laser beams, which are used to generate a coherent signal. Recently, the development of broadband CARS[6, 10-12] has been shown to provide broadband spectral information similar to spontaneous Raman microscopy.

Here, we demonstrate the concept of time-lapse Raman imaging (TLRI) of single cells, which is an important step towards Raman imaging of dynamic processes in individual living cells. We have selected peripheral blood lymphocytes (PBL) because of their importance to the immune system. The influence of physiology and phenotype of the PBL cell on the Raman microspectroscopic signatures has been explained elsewhere.[2, 13-15] TLRI of living cells is possible through the interplay between a sensitive home-built confocal Raman microspectrometer[16] and data analysis techniques like Raman band integration imaging, singular value decomposition (SVD)[17, 18] and hierarchical cluster analysis (HCA)[19] to analyze large data sets. The Raman images were recorded over the entire spectral range (~

3600 cm^{-1}) including both the fingerprint and the high wavenumber spectral region, where C-H-stretch, N-H-stretch and O-H-stretch vibrations predominantly contribute.

Over the last two decades, there has been a rapid development with respect to single cell Raman imaging. The use of near-infrared (NIR) lasers and sensitive charge-coupled device (CCD) cameras enabled a better signal generation and efficient data accumulation without visibly causing degradation to cells.[2, 18, 20, 21] However, when working with laser wavelengths at 488 nm and 514.5 nm, even low laser powers (~ 5mW) for time periods of 60 seconds resulted in significant morphological changes in the cells[20, 22]. Energies of ~750 mJ were used in the first confocal Raman spectroscopic studies of single living cells and chromosomes.[1] Initially, Raman microspectroscopic imaging was used to visualize organelles in chemical images of single cells fixed with alcohols or aldehydes, but required high laser powers around 100 mW and long accumulation times from 1 second[21] to 30 seconds.[23] Confocal Raman microspectroscopy has proven to be an efficient tool to identify living cells,[20, 22] dead cells,[24] cell death due to apoptosis,[18] mitosis in dividing cells,[25] proliferating cells[26] and differentiating cells.[27] Cellular distributions of certain organelles like mitochondria[28, 29] and intracellular redistribution of lipid vesicles upon phagocytosis[19] have been successfully shown. Raman microspectroscopic imaging enables detection of the localization of molecules like carotenoids (β-Carotene) in organelles and the cytoplasm of a single cell.[2, 13]

Raman microspectroscopy is an elegant tool for single cell molecular imaging. In hyperspectral Raman imaging, long pixel dwell times of 1.0 second,[18, 21] 30 seconds[23, 25, 30] or 60 seconds[25] with laser excitation powers of approximately 100 mW[18, 21, 30] results in intense Raman scattering but also in significant energy dissipation per pixel. We have optimized a confocal Raman microspectrometer[16] for fast high-resolution imaging (spatial resolution < 400nm full width half maximum). We demonstrate multiple hyperspectral Raman images of single cells with image acquisition times of less than two minutes. Each image was acquired with a pixel dwell time of 100 ms and a light dose of 3.5 mJ/pixel. We show the feasibility of repeated imaging of a single live, unfixed PBL cell. We also discuss variations in chemical information and the fidelity of Raman imaging of cells with respect to the different chemical signals. TLRI will make it possible to monitor biological processes like cell division and phagocytosis with high chemical specificity.

3.2 Materials and Methods

Peripheral Blood Lymphocyte cell isolation

Whole blood from healthy human donors was obtained by venipuncture and collected in sterile heparinized tubes. Around 10 ml of whole blood was diluted with 12 ml of PBS buffer (Gibco, USA) supplemented with 10% milli-Q water, 0.50% bovine serum albumin (Sigma, USA) and 0.38% Tri-sodium citrate (Merck, Germany). Approximately 6.0 ml of the diluted blood is very slowly brought into Ficoll-Paque™ PLUS solution with a density gradient of 1.077 g/cm^3 and centrifuged at 20°C for 20 minutes at 1000 g (2044 rpm). The mononuclear cells, which accumulate at the interface of Ficoll-Paque™ PLUS solution and the blood plasma, were carefully harvested and washed three times with PBS buffer. The mononuclear cells were then re-suspended in 12 ml of RPMI-1640 without phenol red (Gibco, USA) supplemented with 10% fetal bovine serum (Sigma-Aldrich Chemie BV, Netherlands) and 1% Antibiotic/Antimycotic solution (100 U Penicillin/100 µg Streptomycin /0.25 µg/mL) (Gibco, USA) and incubated for 60 minutes in a T75 culture flask at 37°C to separate out the adherent monocytes. The PBL cells, obtained in this way, consisted of T-lymphocytes, B-lymphocytes and Killer-cells, respectively T-, B-, and K-cells. CaF_2 slides were used as substrates for the cells in all Raman experiments.[18, 21, 31] The calcium fluoride (CaF_2) substrates were coated with 0.01% poly-L-lysine (PLL, P-1274, Sigma) to enable cell adhesion. After incubation for 30 minutes at 37°C, the CaF_2 substrates with adhered cells were transferred to a Petri dish (diameter 5.5 cm), which was filled with 10 ml of PBS buffer.

Confocal Raman microspectroscopy

Raman imaging of living cells was performed using a custom-built confocal Raman microspectrometer.[16] The excitation wavelength of 647.1 nm emitting from a Kr-ion laser (Coherent, Innova 90-K, Santa Clara, CA) was transmitted through a band pass filter (Z647BP, Chroma Technology, Rockingham, VT 05101, USA) to suppress unwanted laser emission. The laser light is reflected by a dichroic beam splitter (Z647RDC, Chroma technology, Rockingham, 05101 VT, USA), which separates the excitation and detection wavelengths. A water immersion objective (63× /1.2 NA; Plan Neofluar; Carl Zeiss, Jena, Germany) was used to focus the light on the sample. The scattered light from the sample was collected by the same objective in an epi-detection configuration and transmitted through the dichroic beamsplitter. The reflections of the laser line and the elastically scattered light were filtered with a razor edge long pass filter (LP02-647RU, Semrock, Buffalo, NY). The Raman scattered light was focused by a lens (f = 30 mm, AC127-030-B, Thor Labs, Newton, New

Jersey) on to a confocal pinhole (diameter = 15 μm) at the entrance of the spectrograph. The combination of the objective and the lens results in a 23× magnification on the pinhole. The pinhole truncates the Gaussian beam close to the $1/e^2$ points, which results in a spatial resolution of ~390 nm full width at half maximum (FWHM). The spectrograph disperses the light on to an electron multiplying charge coupled device (EMCCD) chip with 1600 × 200 pixels (Newton DU-970N, Andor Technology, Belfast, Northern Ireland). The back illuminated and thermo electrically cooled EMCCD chip has an image area of 25.6 mm × 3.2 mm. The spectra are measured with an average spectral resolution of 2.25 cm^{-1}/pixel.

Confocal Raman imaging and data analysis

The Raman images were constructed from the full spectral information (~ 3600 cm^{-1}) collected at each step of the raster scan, which resulted from the displacement of a scanning mirror (Leica Laser technique, GmbH, Heidelberg, Germany). The image area of the cells of interest had a size of 8.97 μm × 8.97 μm with a step size of 280 nm. The lateral optical resolution of the setup was ~390 nm. The axial resolution was 1400 nm. The spectral accumulation time was 100 ms/pixel. The excitation power was 35 mW throughout the experiment. Successive images of single living cells were obtained until the cell moved from the measurement area or was damaged due to prolonged exposure by the laser light. Each image results in a 3D hyper-spectral datacube (spatial × spatial × spectral), which is converted to a 2D data matrix (spatial × spectral) for subsequent corrections. The hyper-spectral datacubes were pre-processed by 1) removal of cosmic ray events, 2) subtraction of the camera offset, 3) calibration of the wave number axis, and 4) correction of wavenumber dependent transmission. The well-known band-positions of toluene were used to relate wavenumbers to pixels. The wavenumber-dependent optical detection efficiency of the setup is corrected using a tungsten halogen light source (Avalight-HAL; Avantes BV, Eerbeek, The Netherlands) with a known emission spectrum. The detector-induced etaloning effect was also compensated by this procedure.[16] Singular value decomposition (SVD) was applied to the hyper spectral data cubes to reduce the uncorrelated noise.[17] The SVD treated data was analyzed by both univariate and multivariate data analyses procedures. Univariate Raman images for the specific vibrational band of interest as a function of position were constructed by integrating the band intensities after baseline subtraction.[18] In multivariate analysis, both hierarchical cluster analysis (HCA) and principal component analysis (PCA) were performed. HCA makes use of the scores obtained from the PCA to visualize the regions of high spectral similarities.[19] The data treatment and analysis was performed using routines written in MATLAB 7.4 (The Math Works, Inc., Natick, MA.).

3.3 Results and Discussions

Repeated Raman imaging on single PBL cells resulted in a large hyperspectral data cube (spatial × spatial × spectral) for each individual cell of the order of 1.6 million data points (32 × 32 × 1600 pixels) per image. Each image was acquired in 102.4 seconds. Several cells were measured until cell death became apparent from "blebs". Figure 1A shows the average of 1024 Raman spectra of the entire area for 12 subsequent images. Two level hierarchical cluster analysis of each image data set was performed over the spectral range of 500 to 3600 cm^{-1}. One cluster contained information on the medium outside the cell, which was used as a background spectrum, while the other cluster contained all the cellular information. The background-free cell spectrum for each individual image is obtained after subtraction of the background spectrum from the cell spectrum. The coefficient of subtraction was 0.97 for all spectra. The resultant background-free cell spectra for each individual image-dataset have a baseline close to zero and many bands, typical for polynucleotides, proteins and lipids, can be observed in Figure 1B. The assignment of the vibrational bands has been made on the basis of literature data.[32-35] Univariate Raman images for the nucleotide-band at 788 cm^{-1} are shown in Figure 2A for the first image dataset and in Figure 2D for the 7th image dataset. The general distribution is similar with small variations because of internal motion of the cell nucleus during the time in between the acquisition of the two images. The corresponding images after 4-level hierarchical cluster analysis in Figure 2B for the first image and Figure 2E for the 7th image show a high correspondence of information for each cluster. The first cluster spectrum, associated with "black", is used as a background spectrum for subtraction of all other cluster spectra in both Figure 2B and Figure 2E. The red cluster is the extreme periphery of the cell, while the green and the blue cluster represent the cytoplasm and the cell nucleus, respectively. The Raman difference spectrum of the nucleus minus the cytoplasm is shown for the first image dataset in Figure 2C and for the 7th image dataset in Figure 2F.

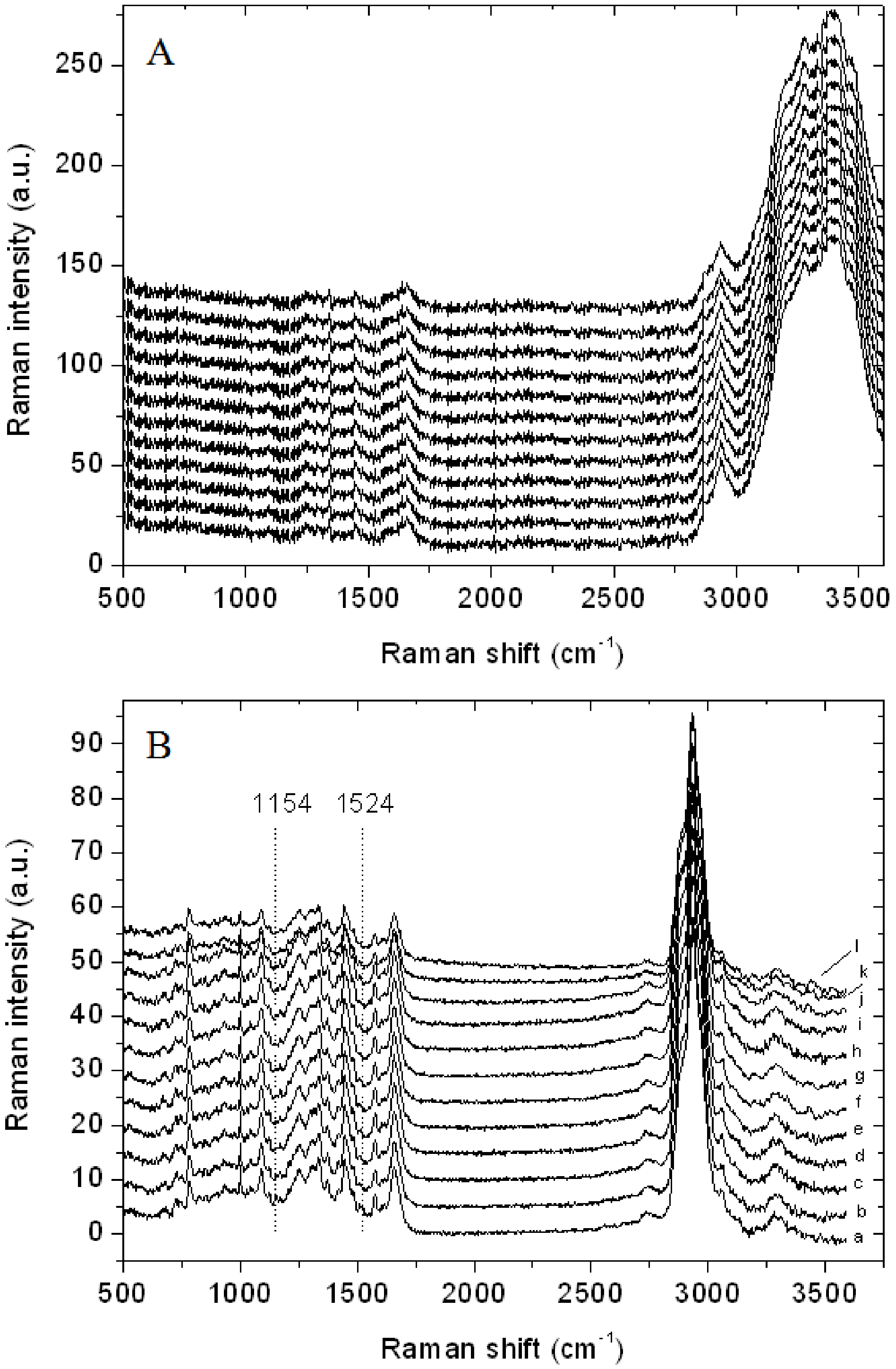

Figure 1: (A) Average of 1024 Raman spectra of the entire area for 12 subsequent images (image 1 to image 12, bottom to up); (B) Background free cell spectrum derived from the subtraction of average spectra of the cell minus correlation coefficient times the average spectra of the background obtained from two level HCA for (a) image 1, (b) image 2, (c) image 3, (d) image 4, (e) image 5, (f) image 6, (g) image 7, (h) image 8, (i) image 9, (j) image 10, (k) image 11 and (l) image 12.

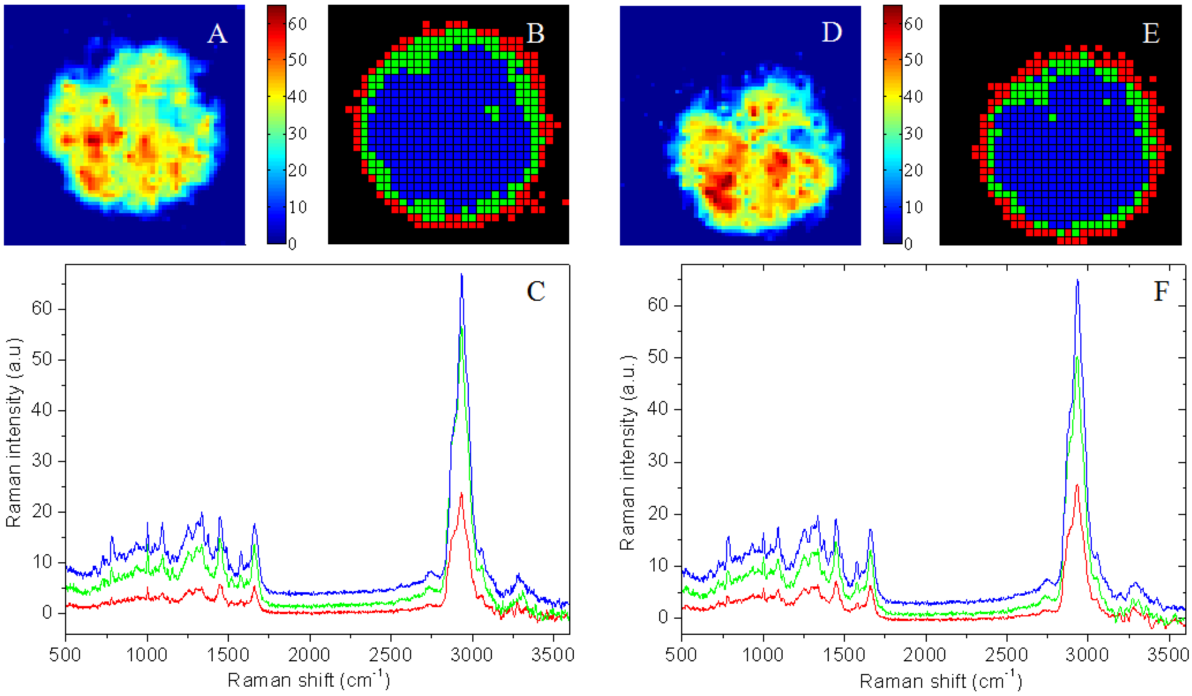

Figure 2: (A) Univariate Raman image for the band 788 cm^{-1} showing the distribution of DNA in the nucleus corresponding to blue cluster in B, (B) Four cluster Raman image of PBL cell from 1st image, (C) Respective background free cluster spectra for 1st image, (D) Univariate Raman image for the band 788 cm^{-1} showing the distribution of DNA in the nucleus corresponding to blue cluster in E, (E) Four cluster Raman image of PBL cell from 7th image and (F) Respective background free cluster spectra for 7th image.

The cluster spectrum of the nucleus (blue) shows Raman bands at 783/788, 1335, 1421, 1447, 1487, 1661, 2750 and 2937 cm^{-1}, which are characteristic of DNA, RNA and proteins. The green spectrum shows vibrations at 779, 802, 1445, 1658, 2731 and 2933 cm^{-1} for RNA and lipids that are typical for the cytoplasm. The green spectrum also has bands at 1002, 1154 and 1524 cm^{-1} that correspond to the CH$_3$ in plane rocking vibrations,[36] =C−C= (v_2) and −C=C− (v_1) vibrations of carotenoid molecules.[37] The Raman difference spectrum of the nucleus minus cytoplasm of 1st image (i.e. blue - green) (Figure 3A) shows positive Raman bands at 679, 726, 787, 830, 1090, 1250, 1334, 1375, 1490, 1576, 1674, 2750, 2945 and 2974 cm^{-1} and negative Raman bands at 703, 860, 1154, 1434, 1524, 2848 and 2879 cm^{-1}. The positive bands indicate the presence of proteins and nucleotides in the nucleus and the negative bands indicate presence of lipids and carotenoids in the cytoplasm. The Raman difference spectrum (Figure 3A), which was derived from the first image, shows negative features for bands at 1154 cm^{-1} and 1524 cm^{-1}, which suggests that carotenoid molecules are far more abundant in the cytoplasm than in the nucleus. The carotenoids function as efficient oxygen scavengers after photo-excitation. Photo-excitation also leads to photobleaching of carotene. The bands of carotenoids gradually disappear in subsequent spectra as a result of gradual photobleaching (vide infra).

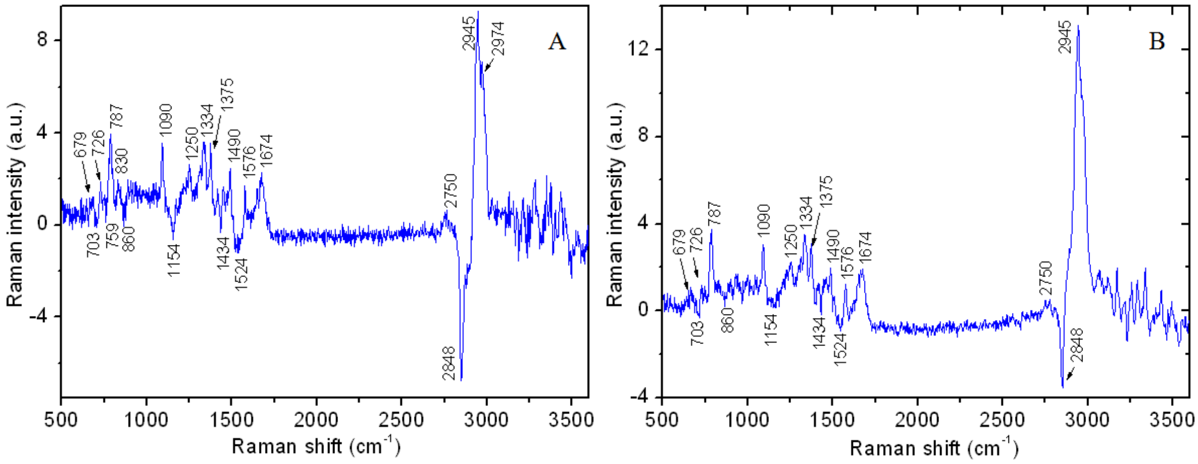

Figure 3: Raman difference spectra for the spectra corresponding to nucleus minus cytoplasm showing positive bands for nucleotides and proteins and negative bands for RNA, lipids and carotenoids. (A) for image 1, and (B) for image 7.

The Raman difference spectrum (Figure 3A) reveals contributions of carotenoids. The difference spectrum shows three distinct Raman bands for carotenoids at 1524 (v_1), 1154 (v_2) and 1002 (v_3) cm^{-1} in the fingerprint region. The Raman difference spectrum of the 7th image (Figure 3B) reveals a decreased amount of carotene, which is likely to be the result of photobleaching of carotenoids. The Raman band intensities of the carotenoid bands v_1, v_2 and v_3 reflect that the amplitude of the carotenoid signals is only 10% of the most intense Raman band in the finger print region. The decrease in carotenoids is further highlighted in Figure 4A where Raman difference spectra are shown for the spectrum of the first image frame minus the spectrum of all subsequent image frames (seen in Figure 1B). The difference spectra reveal a gradual increase in the intensity of the carotenoid-bands v_1, v_2 and v_3. This increase in the band intensities in the difference spectrum corresponds to a decrease in the carotenoid content in the cell from 1st image to 10th image. We notice that the change observed for 1st image minus 2nd image is approximately 20% to 30% of the amplitude in Figure 4A(i) after 10th image. Figure 4B shows the decrease in carotenoids (1154 and 1524 cm^{-1}) and compares it with the behavior of nucleotide (788 cm^{-1}) and protein (2930 cm^{-1}) bands in Figure 4C. The nucleotide (788 cm^{-1}) and protein (2930 cm^{-1}) content does not change until the 10th image. Inspection of the cell with the bright field microscope revealed that the cell was blebbing after 10th image, with a concomitant loss of cytoplasmic and nuclear material.

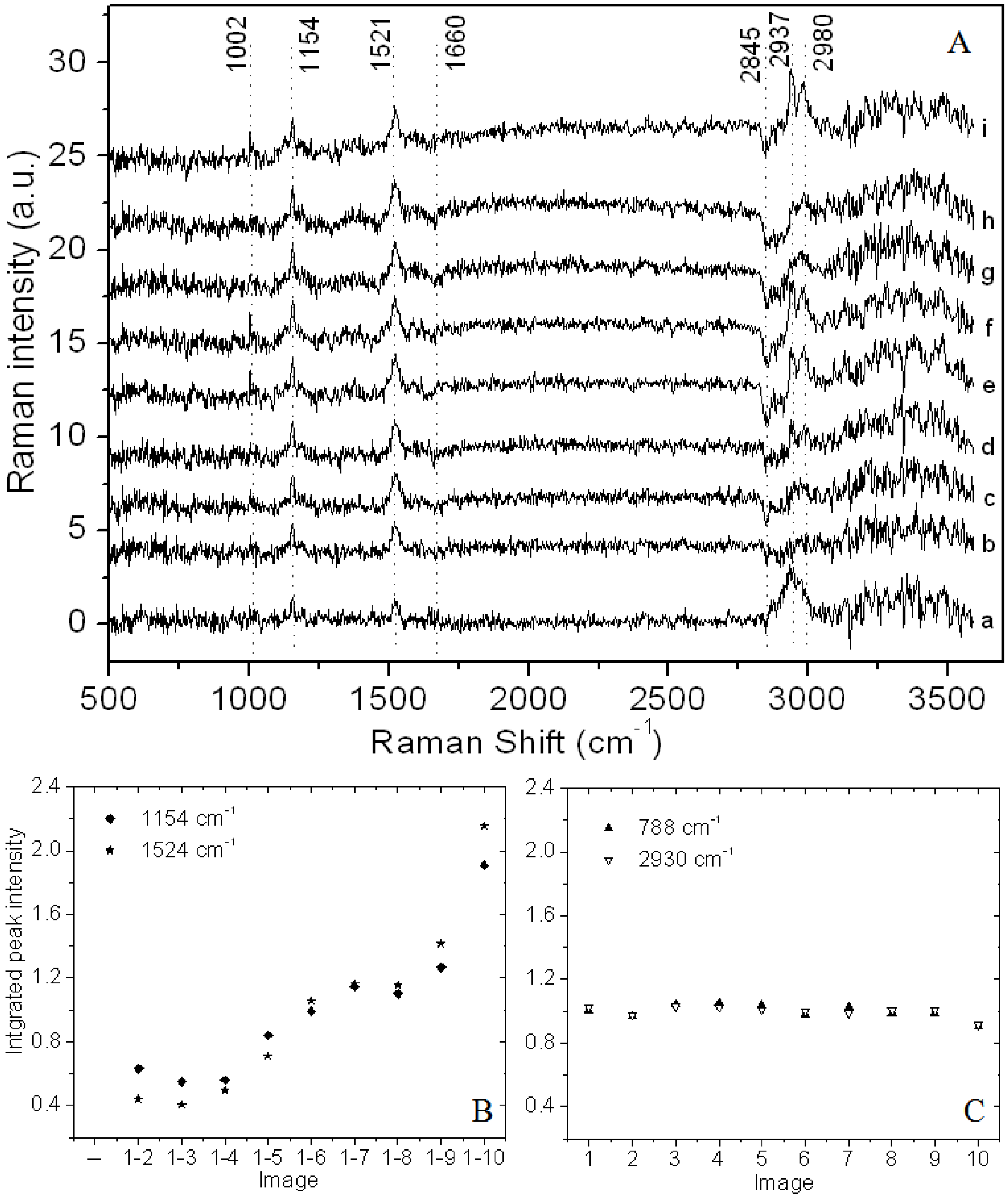

Figure 4: (A) Plot for the Raman difference spectroscopy results for background free cell spectra of first image minus background free cell spectra of other images seen Figure 1B showing variations in the carotenoid molecules and subsequent appearance of the photo products. (a) image 1 - image 2, (b) image 1 - image 3, (c) image 1 - image 4, (d) image 1 - image 5, (e) image 1 - image 6, (f) image 1 - image 7, (g) image 1 - image 8, (h) image 1 - image 9, and (i) image 1 - image 10; Plot showing the variation in the integrated band intensities for Raman bands for (B) carotenoids at 1154 cm^{-1} and 1524 cm^{-1} from Figure 4A and (C) DNA 788 cm^{-1} and protein 2930 cm^{-1} from Figure 1B.

The distribution of carotenoids in the cytoplasm of the cell is shown in the univariate Raman image (Figure 5), which was obtained from the sum of the spectral amplitudes at 1154 and 1524 cm^{-1}. The carotenoids are not homogeneously distributed over the cell, as they are predominantly present in the cytoplasm, which is in agreement with earlier reports.[2] This is also in agreement with the complementary contrast in the image of the carotenoid distribution (Figure 5) and that of the nucleotide distribution (Figure 2A). Carotenoids have been found in lipid regions of the Golgi complex in the cytoplasm of the cell,[13, 38] which is all in good agreement with the present observation. Co-localization of Raman bands for carotenoids (1154 and 1524 cm^{-1}) and lipids (2848 cm^{-1}) in Figure 2B, 2C and 3A further support the presence of carotenoids in a lipid like environment.

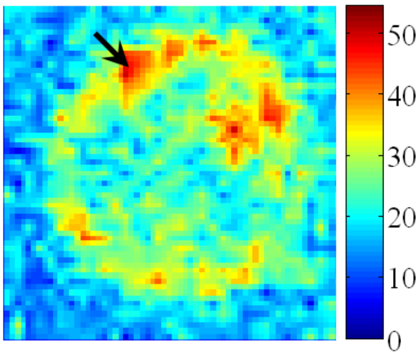

Figure 5: Integrated Raman band images for the combination of bands 1154 and 1524 cm^{-1} showing the distribution of carotenoids adhered to Golgi complex in the cytoplasm of the cell. Black arrow indicates regions of higher carotenoid concentrations.

In order to estimate the number of carotenoid molecules in a voxel of the image a calibration graph was made of the amplitude of the Raman scattering versus the concentration of β-carotene in chloroform. The β-carotene concentration ranged from 10 mM to 500 nM. The result (Figure 6) shows the expected linear behavior of the integrated band intensity of the ν_2-mode at 1154 cm^{-1} against the concentration of β-carotene over more than 4 orders of magnitude in the concentration. The number of molecules in the voxel is directly proportional to the product of the molar concentration times the focal volume times Avogadro's constant. The number of molecules detected in 100 seconds in a 500 nM solution of β-carotene is ~90 molecules. A comparison between the integrated band intensity of carotenoids of a PBL cell (Figure 5) allows the estimation of the molar concentration as 2.3 µM, which equates to approximately 415 molecules detected on average in a single voxel. The maximum concentration of the carotenoids in a voxel in the cytoplasm of the PBL cell is approximately 4.0 µM (indicated by black arrow in Figure 5), which leads to a detected number of molecules of 723.

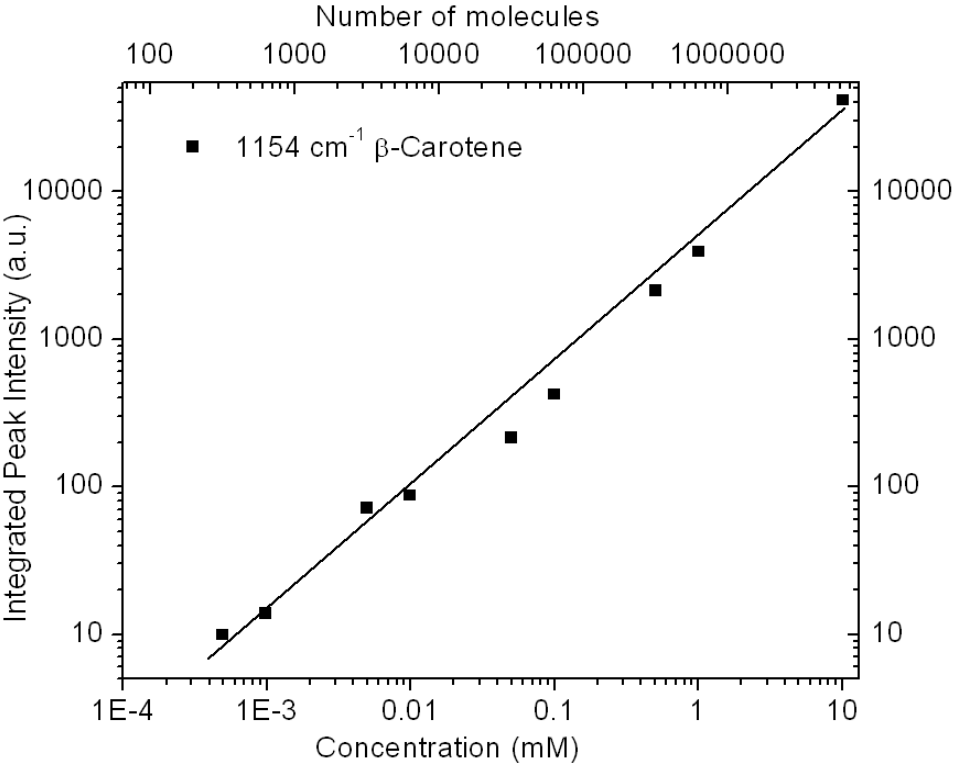

Figure 6: Plot showing integrated band intensities of Raman band at 1154 cm^{-1} for β-Carotene dissolved in chloroform varying linearly with respected to the various molar concentrations ranging from 500 nM to 10 mM plotted in logarithmic scale (bottom x-axis) and number of molecules detected in the focal volume in logarithmic scale (top x-axis).

Concurrent with the changes in carotenoid bands in the fingerprint region small changes also occur in the high wavenumber C-H-stretch region (Figure 4A). The magnitude of the changes is of the order of 5% of the C-H-stretch band (2937 cm^{-1}) seen in Figure 1B. Since carotenoids do not have strong pre-resonantly enhanced bands in the high wavenumber region,[39] the changes are probably due to changes in molecules rich in C-H-groups, such as lipids and proteins. Interestingly, in subsequent difference spectra additional changes are observed that lead to a more pronounced resolved band structure. Initially, a broad-band increase in the amplitude around 2937 cm^{-1} was observed (Figure 4A(a)), which corresponds with a decrease of the Raman scattering in this spectral area. This early difference spectrum resembles a high-wavenumber Raman spectrum of proteins. However, gradually a resolved band spectrum appears with negative amplitude near 2845 cm^{-1} and positive amplitudes near 2937 cm^{-1} and 2980 cm^{-1}. Carotenoids have been proposed to play a role in the immune response, which would explain why lymphocytes contain considerable amounts of carotenoids. Carotenoids are also known as efficient quenchers of singlet oxygen. Furthermore, after excitation, intersystem crossing to the triplet state results in an efficient reaction with the triplet ground state of oxygen, which in turn results in oxidation of carotenoids. Photo-oxidation results in photoproducts like retinal, retinoic acid, retinol and other compounds with a reduced conjugation.[40] Especially retinal is a well known photoproduct of β-carotene.[41] The most pronounced band of retinal and related compounds is at 1590 cm^{-1}, while an increased reduction of conjugation will result in a higher wavenumber of the $(–C=C–)_n$ to approximately 1656 cm^{-1} for a single –C=C– unsaturated bond. Indeed a broad band structure between 1590 and 1660 cm^{-1} can be observed in the difference spectra (Figure 4A) with amplitude opposite of the pronounced carotenoid bands. This suggests that compounds with a reduced conjugation are produced from carotenoids. Spectra in Figure 4A(b) to 4A(i) also show negative bands at high wavenumber region near 2845 cm^{-1} that simultaneously increase in correspondence with Raman band at 1660 cm^{-1}. The band at 2845 cm^{-1} is usually assigned to a -CH_3-stretch motion of saturated sections of fatty acid chains in lipids. This suggests that the lipid concentration or composition would be locally changed, presumably in correlation with the formation of photoproducts of carotenoid molecules such as retinal or retinol. However, although an assignment of the wavenumber positions 2845, 2937 and 2980 cm^{-1} to group vibrations has been presented[42] the precise interpretation in the present context is yet to be understood.

The small changes we have observed in TLRI of lymphocyte cells are clearly related to carotenoids as a result of (pre-) resonant Raman excitation. The fingerprint spectrum reveals no changes in other compounds until the 10th spectrum. This is presented for typical DNA and protein bands in Figure 4C. The integrated intensity of the band around 788 cm^{-1} for DNA and around 2930 cm^{-1} for proteins show hardly any variation until the 10th spectrum. In spectrum 11 and 12 a decrease in the intensity of the bands occurred. This was a result of cell blebbing, which led to a loss of intra-cellular material.

3.4 Conclusion

We have reported Time Lapse Raman Imaging of single cells. Raman images were acquired in ~102.4 seconds and typically 10-15 images of a cell could be acquired before cell blebbing occurred. Energy of 3.5 mJ/pixel of laser light with a wavelength of 647.1 nm was sufficient to acquire a high quality Raman spectrum from 500 cm^{-1} to 3600 cm^{-1}. The study revealed the ability to detect photo-induced biochemical changes in carotenoid molecules in the lymphocytes. The changes in carotenoids were due to (pre-)resonant Raman excitation. Non-resonant Raman scattering of DNA and proteins revelaed no changes in the first images until cell blebbing occurred. The cell was physically damaged due to the ambient temperature, the absence of nutrients, the lack of control over the pH. We conclude that utilization of a microbioreactor or a flow chamber to maintain the necessary physiological and biochemical conditions for the cells will improve the sustenance and long-term viability of the cells.

The Raman difference spectroscopy of nucleus minus cytoplasm showed prominent nucleotide and protein bands for the nucleus and RNA, lipids and carotenoids for the cytoplasm. The coexistence of carotenoids and lipids shows the lipophilic nature of the carotenoids, which are found adhered to Golgi complexes in the cytoplasm of the cell. We have shown that the detectability of carotenoids in a live cell is 2.3 μM, which corresponds to approximately 415 molecules of carotenoid in the voxel. This is the first report that presents quantitative evidence of the detectability of an important biological compound in the micromolar regime. This result is of particular interest as fluorescent labeling of these compounds is not possible without affecting their biological role. The recognition of the influence of laser light relies on the spectral information. No use was made of stimulated emission as in four-wave mixing techniques like CARS or stRS or local field enhancement as in Surface Enhanced Raman Scattering (SERS). This leads us to conclude that label-free spontaneous Raman microspectroscopy and imaging is developing into a quantitative microscopy method for molecular detection in cells.

It was further shown that no variation occurred in bands of DNA and proteins, compounds which are non-resonantly excited at the reported laser wavelength. TLRI will be useful to continuously monitor cellular activities like cell division, phagocytosis and apoptosis by a noninvasive and label-free chemical imaging approach, enabling future application of this method in tissue engineering.

References

1. Puppels, G. J.; De Mul, F. F. M.; Otto, C.; Greve, J.; Robert-Nicoud, M.; Arndt-Jovin, D. J.; Jovin, T. M., Studying single living cells and chromosomes by confocal Raman microspectroscopy. *Nature* **1990,** 347, (6290), 301-3.
2. Puppels, G. J.; Garritsen, H. S.; Kummer, J. A.; Greve, J., Carotenoids located in human lymphocyte subpopulations and natural killer cells by Raman microspectroscopy. *Cytometry* **1993,** 14, (3), 251-6.
3. Cheng, J.-X.; Jia, Y. K.; Zheng, G.; Xie, X. S., Laser-scanning coherent anti-Stokes Raman scattering microscopy and applications to cell biology. *Biophys. J.* **2002,** 83, (1), 502-509.
4. Zumbusch, A.; Holtom, G. R.; Xie, X. S., Three-Dimensional Vibrational Imaging by Coherent Anti-Stokes Raman Scattering. *Phys. Rev. Lett.* **1999,** 82, (20), 4142-4145.
5. Diem, M.; Chiriboga, L.; Lasch, P.; Pacifico, A., IR spectra and IR spectral maps of individual normal and cancerous cells. *Biopolymers* **2002,** 61, (3), 349-353.
6. Voroshilov, A.; Otto, C.; Greve, J., Secondary structure of bovine albumin as studied by polarization-sensitive multiplex CARS spectroscopy. *Appl. Spectrosc.* **1996,** 50, (1), 78-85.
7. Freudiger, C. W.; Min, W.; Saar, B. G.; Lu, S.; Holtom, G. R.; He, C.; Tsai, J. C.; Kang, J. X.; Xie, X. S., Label-Free Biomedical Imaging with High Sensitivity by Stimulated Raman Scattering Microscopy. *Science* **2008,** 322, (5909), 1857-1861.
8. Kanger, J. S.; Otto, C.; Greve, J., Stimulated Raman gain scattering in thin planar dielectric waveguides. *Opt. Lett.* **1995,** 20, (21), 2231-3.
9. Nandakumar, P.; Kovalev, A.; Volkmer, A., Vibrational imaging based on stimulated Raman scattering microscopy. *New J. Phys.* **2009,** 11, 033026 (9pp).
10. Cheng, J.-x.; Volkmer, A.; Book, L. D.; Xie, X. S., Multiplex coherent anti-stokes raman scattering microspectroscopy and study of lipid vesicles. *J. Phys. Chem. B* **2002,** 106, (34), 8493-8498.
11. Kee, T. W.; Cicerone, M. T., Simple approach to one-laser, broadband coherent anti-Stokes Raman scattering microscopy. *Opt. Lett.* **2004,** 29, (23), 2701-2703.
12. Otto, C.; Voroshilov, A.; Kruglik, S. G.; Greve, J., Vibrational bands of luminescent zinc(II)-octaethyl-porphyrin using a polarization-sensitive "microscopic" multiplex CARS technique. *J. Raman Spectrosc.* **2001,** 32, (6/7), 495-501.
13. Arikan, S.; Sands, H. S.; Rodway, R. G.; Batchelder, D. N., Raman spectroscopy and imaging of beta - carotene in live corpus luteum cells. *Anim. Reprod. Sci.* **2002,** 71, (3,4), 249-266.
14. Bakker Schut, T. C.; Puppels, G. J.; Kraan, Y. M.; Greve, J.; Van Der Maas, L. L. J.; Figdor, C. G., Intracellular carotenoid levels measured by Raman microspectroscopy: comparison of lymphocytes from lung cancer patients and healthy individuals. *Int. J. Cancer* **1997,** 74, (1), 20-25.
15. Ramanauskaite, R. B.; Segers-Nolten, I. G. M. J.; de Grauw, K. J.; Sijtsema, N. M.; van der Maas, L.; Greve, J.; Otto, C.; Figdor, C. G., Carotenoid levels in human lymphocytes, measured by Raman microspectroscopy. *Pure Appl. Chem.* **1997,** 69, (10), 2131-2134.
16. Pully, V. V.; Lenferink, A.; Otto, C., Hybrid Rayleigh, Raman and two-photon excited fluorescence spectral confocal microscopy of living cells. *J. Raman Spectrosc.* **2009,** 10.1002/jrs.2501.
17. Uzunbajakava, N.; Greve, J.; Otto, C., Raman microscopy of cells: chemical imaging of apoptosis. *Proc. SPIE-Int. Soc. Opt. Eng.* **2003,** 4963, (Multiphoton Microscopy in the Biomedical Sciences III), 223-230.
18. Uzunbajakava, N.; Lenferink, A.; Kraan, Y.; Volokhina, E.; Vrensen, G.; Greve, J.; Otto, C., Nonresonant confocal Raman imaging of DNA and protein distribution in apoptotic cells. *Biophys. J.* **2003,** 84, (6), 3968-3981.
19. van Manen, H.-J.; Kraan, Y. M.; Roos, D.; Otto, C., Single-cell raman and fluorescence microscopy reveal the association of lipid bodies with phagosomes in leukocytes. *Proc. Natl. Acad. Sci. U. S. A.* **2005,** 102, (29), 10159-10164.
20. Notingher, I.; Verrier, S.; Romanska, H.; Bishop, A. E.; Polak, J. M.; Hench, L. L., In situ characterization of living cells by Raman spectroscopy. *Spectroscopy* **2002,** 16, (2), 43-51.

21. Uzunbajakava, N.; Lenferink, A.; Kraan, Y.; Willekens, B.; Vrensen, G.; Greve, J.; Otto, C., Nonresonant Raman imaging of protein distribution in single human cells. *Biopolymers* **2002,** 72, (1), 1-9.
22. Puppels, G. J.; Olminkhof, J. H.; Segers-Nolten, G. M.; Otto, C.; de Mul, F. F.; Greve, J., Laser irradiation and Raman spectroscopy of single living cells and chromosomes: sample degradation occurs with 514.5 nm but not with 660 nm laser light. *Exp Cell Res* **1991,** 195, (2), 361-7.
23. Krafft, C.; Knetschke, T.; Funk, R. H. W.; Salzer, R., Identification of organelles and vesicles in single cells by Raman microspectroscopic mapping. *Vib. Spectrosc.* **2005,** 38, (1-2), 85-93.
24. Verrier, S.; Notingher, I.; Polak, J. M.; Hench, L. L., In situ monitoring of cell death using Raman microspectroscopy. *Biopolymers* **2004,** 74, (1-2), 157-62.
25. Matthaus, C.; Boydston-White, S.; Miljkovic, M.; Romeo, M.; Diem, M., Raman and infrared microspectral imaging of mitotic cells. *Appl. Spectrosc.* **2006,** 60, (1), 1-8.
26. Short, K. W.; Carpenter, S.; Freyer, J. P.; Mourant, J. R., Raman spectroscopy detects biochemical changes due to proliferation in mammalian cell cultures. *Biophys. J.* **2005,** 88, (6), 4274-4288.
27. Notingher, I.; Jell, G.; Lohbauer, U.; Salih, V.; Hench, L. L., In situ non-invasive spectral discrimination between bone cell phenotypes used in tissue engineering. *J. Cell. Biochem.* **2004,** 92, (6), 1180-1192.
28. Matthaus, C.; Chernenko, T.; Newmark, J. A.; Warner, C. M.; Diem, M., Label-free detection of mitochondrial distribution in cells by nonresonant raman microspectroscopy. *Biophys. J.* **2007,** 93, (2), 668-673.
29. Pully, V. V.; Otto, C., The intensity of the 1602 cm^{-1} band in human cells is related to mitochondrial activity. *J. Raman Spectrosc.* **2009,** 40, (5), 473-475.
30. Krafft, C.; Knetschke, T.; Funk, R. H. W.; Salzer, R., Studies on Stress-Induced Changes at the Subcellular Level by Raman Microspectroscopic Mapping. *Anal. Chem.* **2006,** 78, (13), 4424-4429.
31. Schuster, K. C.; Reese, I.; Urlaub, E.; Gapes, J. R.; Lendl, B., Multidimensional Information on the Chemical Composition of Single Bacterial Cells by Confocal Raman Microspectroscopy. *Anal. Chem.* **2000,** 72, (22), 5529-5534.
32. Hayashi, H.; Nishimura, Y.; Katahira, M.; Tsuboi, M., The structure of nucleosome core particles as revealed by difference Raman spectroscopy. *Nucleic Acids Res* **1986,** 14, (6), 2583-96.
33. Hightower, K. R., The role of the lens epithelium in development of UV cataract. *Curr Eye Res* **1995,** 14, (1), 71-8.
34. Thomas, G. J., Jr.; Prescott, B.; Olins, D. E., Secondary structure of histones and DNA in chromatin. *Science* **1977,** 197, (4301), 385-8.
35. Tu, A. T., *Raman Spectroscopy in Biology: Principles and Applications*. 1982; p 448.
36. Van Wijk, A. A. C.; Spaans, A.; Uzunbajakava, N.; Otto, C.; De Groot, H. J. M.; Lugtenburg, J.; Buda, F., Spectroscopy and Quantum Chemical Modeling Reveal a Predominant Contribution of Excitonic Interactions to the Bathochromic Shift in alpha -Crustacyanin, the Blue Carotenoprotein in the Carapace of the Lobster Homarus gammarus. *J. Am. Chem. Soc.* **2005,** 127, (5), 1438-1445.
37. Saito, S.; Tasumi, M.; Eugster, C. H., Resonance Raman spectra (5800-40 cm^{-1}) of all-trans and 15-cis isomers of beta -carotene in the solid state and in solution. Measurements with various laser lines from ultraviolet to red. *J. Raman Spectrosc.* **1983,** 14, (5), 299-309.
38. Briviba, K.; Bornemann, R.; Lemmer, U., Visualization of astaxanthin localization in HT29 human colon adenocarcinoma cells by combined confocal resonance Raman and fluorescence microspectroscopy. *Mol. Nutr. Food Res.* **2006,** 50, (11), 991-995.
39. Parker, S. F.; Tavender, S. M.; Dixon, N. M.; Herman, H.; Williams, K. P. J.; Maddams, W. F., Raman spectrum of beta -carotene using laser lines from green (514.5 nm) to near-infrared (1064 nm): implications for the characterization of conjugated polyenes. *Appl. Spectrosc.* **1999,** 53, (1), 86-91.
40. Handelman, G. J.; Van Kuijk, F. J. G. M.; Chatterjee, A.; Krinsky, N. I., Characterization of products formed during the autoxidation of beta -carotene. *Free Radical Biol. Med.* **1991,** 10, (6), 427-37.

41. Failloux, N.; Bonnet, I.; Baron, M.-H.; Perrier, E., Quantitative analysis of vitamin A degradation by Raman spectroscopy. *Appl. Spectrosc.* **2003,** 57, (9), 1117-1122.
42. Movasaghi, Z.; Rehman, S.; Rehman, I. U., Raman spectroscopy of biological tissues. *Appl. Spectrosc. Rev.* **2007,** 42, (5), 493-541.

Chapter 4

Microbioreactors for Raman microscopy of stromal cell differentiation

We present the development of microbioreactors with a sensitive and accurate optical coupling to a confocal Raman microspectrometer. We show that such devices enable in situ and in vitro investigation of cell cultures for tissue engineering by chemically sensitive Raman spectroscopic imaging techniques. The optical resolution of the Raman microspectrometer allows recognition and chemical analysis of sub-cellular features. Human bone marrow stromal cells (hBMSCs) have been followed after seeding through a phase of early proliferation until typically two weeks later, well after the cells have differentiated to osteoblasts. Long-term perfusion of cells in the dynamic culture conditions was shown to be compatible with experimental optical demands and off-line optical analysis. Raman optical analysis of cells and cellular differentiation in microbioreactors is feasible down to the level of sub-cellular organelles during development. We conclude that microbioreactors combined with Raman microspectroscopy are a valuable tool to study hBMSC proliferation, differentiation, and development into tissues under in situ and in vitro conditions.

This chapter has been published in Analytical Chemistry.

4.1 Introduction

Cell-to-tissue development is accompanied by a combination of events such as cell proliferation, differentiation and apoptosis. These processes are well-balanced and controlled by a number of inter- and intra-cellular biochemical and biophysical events. If these events are not or inappropriately performed, then cells dedifferentiate and become disorganized, a situation which may lead to cell death. *In vitro* cell-to-tissue development is usually performed either in static culture conditions using Petri dishes or tissue culture flasks where the culture medium is refreshed periodically or in dynamic culture conditions like bioreactors which enable continuous refreshment of the medium.[1, 2] Bioreactors offer an advantage with respect to static conditions[3, 4] in that biochemical processes which take place under controlled environmental and operating conditions (such as pH, temperature, pressure, nutrient supply and waste removal)[5] can be monitored in detail.

In most conventional static cell cultures and macro-scale bioreactors, optical monitoring of nutrient supply, oxygen supply, waste removal, interaction with the extracellular matrix and cell-cell interactions throughout the culture period is difficult. This challenge is due to the practical problem of coupling large bioreactors to non-invasive optical microscopic techniques. The advent of microfabrication technology in the field of tissue engineering has enabled new and innovative ways to analyze cellular interactions in bioreactors and cell behavior in a microfluidic environment that mimic *in vivo* body conditions.[6, 7] The microfluidic bioreactors or microbioreactors are micro-scale versions of conventional bioreactors with significant advantages in terms of cost-effectiveness, portability, performance, and materials used. The implementation of microbioreactors offers a suitable environment for various cell- and tissue-based applications as has been widely demonstrated.[8, 9] An overview is shown in Table-1.

Monitoring of cellular organelles and development of cells to tissues over a longer period of time is most frequently performed by fluorescence microscopy.[10] However; it is quite common that the fluorescent dyes used for specific sub-cellular staining interfere with the development of cells and tissues. The hydrophobicity of fluorescent stains may also cause them to adhere to glass or polymers, which are used for the fabrication of the microbioreactors. These aspects make fluorescence staining strategies less desirable.[11] Since the first application of Raman microspectroscopy to cells,[12] this technique has been widely used for biological applications. Raman microspectroscopy provides chemical information from cells or tissues in a non-invasive and label free way. Applications of Raman spectroscopy of cells has demonstrated that it is able to determine cellular status, such as living cells,[12, 13] dead cells,[14] apoptotic cells,[15] cells in mitotic stage,[16] proliferating cells,[17] and differentiating cells.[18] Recently, Raman spectroscopy has been extended to obtain chemical information over extended periods of time from cells cultured in a microfluidic environment.[19-23] The combination of optical tweezers and a microfluidic system to trap single red blood cells for Raman measurements was successfully shown.[21, 22] Surface enhanced Raman spectroscopy (SERS) using gold nanoparticles for Raman enhancement was used to study the real-time spectral response from a single living Chinese hamster ovary cell in a microfluidic system.[23] Identification of different bacteria by SERS was shown on a microfluidic platform on a single chip.[19] The combination of SERS with microfluidics and its application to molecular and cellular analysis has recently been reviewed.[20]

Table 1: Microbioreactors for cell and tissue based applications

Microbioreactor type	Application
PDMS microfabricated array bioreactor	3-dimensional liver cultures[24]
PDMS layers sealed to positive and negative silicon micromachined mold wafers	Vascularized tissue using endothelial cells[25]
Multilayered PDMS microfluidic device	Analysis of single cells[26]
PDMS and silicon hybrid biochip	Culture of *Listeria innocua* and *Escherichia coli* bacteria[27]
3D PDMS microbioreactor	Bone tissue engineering using mouse calvarial osteoblastic cells[28]
PDMS membranes resembling basal lamina laminated to collagen type I sponges	Culturing human epidermal keratinocytes to form a skin equivalent[29]
Micropatterned flexible biocompatible polysaccharide gel	Culturing chondrocytes for reparative cartilage *in vitro*[30]
PDMS and glass biochip	Nerve cell culture[31]

In this chapter we show two types of microbioreactors for cell- and tissue-based applications. The first microbioreactor (µBR-I) based on polydimethylsiloxane (PDMS) technology in combination with a calcium fluoride (CaF_2) substrate was used to study the proliferation and differentiation of hBMSCs towards mineralized tissue over a 21 day culture period. The second microbioreactor (µBR-II), made from a combination of a commercially available ibidi µ-slide I Luer (ibidi GmbH, München, Germany) and a glass cover slip, enabled chemical imaging of cells cultured over a 10 day time period. Throughout the entire culture period, normal cell development and growth rates were observed in the microbioreactors, which were continuously perfused with cell culture medium. Biochemical processes in hBMSCs in both types of microbioreactors were successfully monitored by confocal Raman microspectroscopy without causing any damage to the cells. Raman results from the µBR-I showed hBMSC proliferation, differentiation, and mineralization over the culture period. Chemical mapping of single hBMSCs cultured in µBR-II showed distributions of organelles in individual cells.

4.2 Materials and Methods

Microbioreactor design

Although many types of microbioreactors have been reported in the literature (Table - 1), the motivation behind the design of our microbioreactors µBR-I and µBR-II are to enable confocal Raman microspectroscopy to monitor cell proliferation, differentiation, and other intracellular processes inside the microbioreactor. Most bioreactors presented in the literature are fabricated using polymers. The strong Raman scattering of organic polymers, particularly in comparison with the weak Raman scattering from subcellular volumes, requires a careful design of the microbioreactor. We have chosen a combination of a polymer and optically silent materials such as CaF_2 and glass cover slips (borosilicate glass) for the design of microbioreactors. The µBR-I was fabricated from PDMS and a CaF_2 substrate (Crystran Ltd., Poole, U.K.), as shown in Figure 1A and 1B. The PDMS chip utilizes microfabrication technology which includes photolithography and replica molding. These steps have been extensively described in the literature.[28, 32, 33] The fabricated PDMS chip has a diameter of 25 mm and a thickness of 4 mm. The PDMS chip has a microchamber (12 mm (length) × 8 mm (breadth) × 400µm (height)) for cell culture and input and output microchannels for nutrient supply and waste removal. The microbioreactor is closed and sealed by laying the PDMS chip over the CaF_2 substrate (circular discs with 35 mm diameter and 2 mm thickness). The CaF_2 substrate forms the substrate for the cells in the microbioreactor. We have never observed any negative effects of CaF_2 on the development of cells. The semicircular sides of the microchamber in µBR-I (Figure 1A) forms a hydrodynamic structure that enables a good flow profile for medium perfusion through the microbioreactor, which results in the removal of air bubbles from the microchamber or microchannels, and enable effective nourishment of the cultured cells. µBR-II was fabricated from a bottomless µ-Slide 1 Luer (ibidi GmbH, München, Germany) with provisions for a inlet and outlet channel and a glass cover slip (thickness ~140 µm) (Menzel Gläser, Braunschweig, Germany) sealed to the bottom with Parafilm M® (Pechiney Plastic Packaging, Illinois, U.S.A.). A secure bonding between the ibidi µ-Slide 1 Luer and the glass cover slip was achieved by heating the Parafilm M® to around 65°C. Sealing created a well defined microchamber (50 mm (length) × 5 mm (breadth) × 400 µm (height)) where hBMSCs were cultured and where perfusion of the cells with a culture medium was feasible throughout the culture period. Silicon tubes (Pharmed BPT, Cole-Palmer, Illinois, U.S.A.) connected the inlet and outlet of the microbioreactors to the peristaltic pump via luer adaptors. The procedure for building these microbioreactors yielded tight bonds between the PDMS chip and CaF_2 substrate in µBR-I and ibidi µ-slide I Luer and glass cover slide in µBR-II. These bonds are sufficiently strong to withstand the flow rates used during long term cell culture.

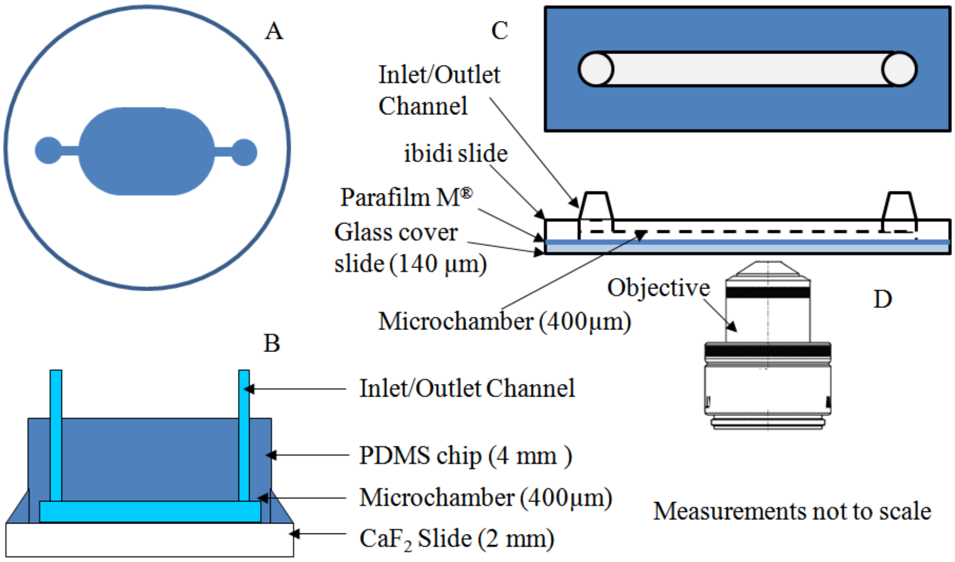

Figure 1: Microbioreactors for cell- and tissue-based applications enabling non-invasive and label-free Raman measurements. (A) top view of µBR-I, (B) cross-sectional view of µBR-I, (C) top view of µBR-II, and (D) cross-sectional view of µBR-II showing the feasibility of optical measurements through the glass cover slide.

Sterilization of the perfusion system

The perfusion circuit was realized by fixing the microbioreactors, silicon tubing, a peristaltic pump (Peri-Star PR, World Precision instruments, Florida, U.S.A.) and the culture medium flasks in a closed loop. The perfusion circuit was sterilized by perfusing 70% ethanol through the circuit and subsequently autoclaving the entire system for 35 minutes. Poly-L-lysine solution is perfused into µBR-I and µBR-II in order to coat the inner surfaces of the microchamber, while residing in an incubator for about 40 minutes at 37°C in an atmosphere with 95% humidity and 5% partial pressure of CO_2. A poly-L-lysine coating enhances stable cell adhesion on the walls of the microchamber in the microbioreactor. The perfusion circuit was then perfused with Dulbecco's phosphate buffered saline (PBS) to remove any excess poly-L-lysine solution.

Cell culture

hBMSCs were seeded at cell densities of 5000 cells/cm^2 and cultured overnight in basic medium to allow cell adhesion on the CaF_2 substrate or glass cover slide of the respective microbioreactors. Basic medium (BM), which was taken as a control condition, was prepared from α-MEM (GIBCO, Carlsbad, CA, U.S.A.), 10% fetal bovine serum (FBS; Bio Whittaker, Australia), 0.2 mM L-ascorbic acid-2-phosphate (AsAP; Sigma, St. Louis, MO, U.S.A.), 100 U/mL penicillin G (Invitrogen, Carlsbad, CA, U.S.A), 100 μg/mL streptomycin (Invitrogen) and 2 mM L-glutamine (L-glu; Sigma). After overnight culture in BM, osteogenic culture medium was continuously perfused with a flow rate of 10 μl/min to establish a dynamic culture system. Osteogenic medium (OM) was prepared by adding 0.01 M β-glycerophosphate (βGP; Sigma) and 10^{-8} M dexamethasone (Dex, Sigma) to BM. Throughout the culture period, the entire system was placed in an incubator maintained at 37°C in an atmosphere with 95% humidity and 5% partial pressure of CO_2. The stock solution of the culture medium was changed every two days during the culture period to supply sufficient nutrients to the cells. Confocal Raman measurements were performed on cells cultured in μBR-I after day 1, day 14, and day 21 of the culture period and on day 4 of the culture period for μBR-II. On each measurement day, the microbioreactors with cells cultured in them were washed three times with phosphate-buffered saline solution (PBS; Gibco) before being transferred to the confocal Raman microscopy for measurements on living cells. After the measurements μBR-II was placed into the incubator after exchanging the PBS buffer for the nutrient medium and connecting it to the continuous perfusion system for further culture.

Confocal Raman Microscopy

Raman measurements on hBMSCs were performed using a custom-built confocal Raman spectrometer[34]. A Kr-ion laser (Coherent, Innova 90-K, Santa Clara, CA) with an emission wavelength of 647.1 nm was used as an excitation source. Raman spectra from the cells cultured in μBR-I were acquired using a 63×/1.2 NA water-immersion objective (Plan Neofluar; Carl Zeiss, Jena, Germany). The scattered light is collected in epi-detection mode, filtered by a razor-edge filter (Semrock, Rochester, NY, USA) to suppress reflected laser light and Rayleigh scattered light, and focused onto a pinhole (25 μm diameter) at the entrance of an imaging spectrograph/monochromator (HR460; Jobin-Yvon, Paris, France), which contains a blazed holographic grating with 600 grooves/mm. A thermoelectrically cooled CCD detector containing a back-illuminated chip with 1340 × 100 pixels of 20 μm × 20 μm (PIXIS 100, Princeton Instruments, NJ, U.S.A.) is placed in the focal plane of the spectrograph exit port. The spectrograph/camera combination provides a spectral resolution of 2.10 cm^{-1}/pixel on average over the Raman spectral range from 300 to 2000 cm^{-1}. To obtain the Raman spectra of cells in the μBR-II, a cover slip corrected water-immersion objective 63×, 1.2 N.A (Plan Neofluar; Carl Zeiss, Jena, Germany) was used. The preprocessing of the data is performed as described in the literature.[34-36]

Raman measurements of hBMSC cells in μBR-I were acquired in so called "spectral scanning mode" on each measurement day after peeling off the PDMS layer from CaF_2 substrate. The CaF_2 substrate with live cells was placed in a Petri dish containing PBS buffer and measured with a 63× water-immersion objective. In "spectral scanning mode" a single full spectrum is obtained by raster-scanning the laser beam over an area of 15 μm × 15 μm in 60 s with a laser power of 75 mW. This procedure results in a relatively low light dose of 2 $mJ/\mu m^2$. Raman spectra were acquired from 10 randomly chosen cells in each culture medium for day 1, day 14 and day 21 of the culture period. Live-cell Raman imaging of hBMSCs cultured in μBR-II until day 4 of the culture period was performed *in situ* inside the microbioreactor (Figure 1D). Raman images were acquired over an area of 15 μm × 15 μm with a pixel size of 468 nm, an accumulation time of 0.5 s per pixel and an excitation power of 50 mW. The hyperspectral data cube obtained in Raman imaging is subjected to singular value decomposition (SVD) to improve the signal-to-noise ratio.[15, 35] Hierarchical cluster analysis (HCA), a multivariate data analysis technique, that is used to visualize regions of high spectral similarities and variations,[37] was performed over the entire spectral range of 500-1800 cm^{-1}. All data manipulations were performed with routines written in MATLAB 7.4 (The Math Works Inc., Natick, MA).

4.3 Results and Discussion

Most bioreactors described in the literature (Table 1) are fabricated with PDMS technology and sometimes in combination with glass. This robust and flexible technology was also used for μBR-I. Elastomeric materials such as PDMS are widely used for soft lithography of microbioreactor fabrication. PDMS is optically transparent down to UV ranges of about 280 nm.[38] The material is cost-effective and offers good mechanical flexibility. Furthermore, it is biocompatible with biological assays and cells and permeable to oxygen that is sufficient for cells.[39-41] Figure 1 shows the microbioreactors that we designed for long-term perfusion culture of cells. Figures 1A and 1B show the top and the cross-sectional view of the µBR-I. The upper part is made of PDMS and has a well-defined microchamber for cell culture and input and output microchannels for nutrient supply. A CaF_2 substrate forms the lower part of the microbioreactor. The hBMSCs are cultured on CaF_2 substrate. CaF_2 is optically transparent and is well known for a low contribution to background in Raman spectra. The µBR-I provided a working volume of 34.5 µl and a surface area of 86.26 mm^2 where the cells were cultured. The top and cross-sectional views of µBR-II are shown in Figure 1C and 1D, respectively. The choice of materials was guided by optical transparency and biocompatibility with long-term perfusion culture of cells. As a proof of concept, HeLa cells were successfully cultured under dynamic culture conditions in µBR-II for a period of 10 days with Raman spectroscopic imaging being performed every three days. Normal cell growth and proliferation occurred over the culture period, reflecting the feasibility of the µBR-II for long-term cell cultures. µBR-II has a working volume of 100 µl and a cell culture surface area of 250 mm^2 over the glass cover slip. The microchannels for the supply of the nutrients are prepared from silicon tubes. Both µBR-I and µBR-II microbioreactors enabled successful cell culture under long term perfusion with a uniform laminar flow of the nutrient medium through the microchamber.

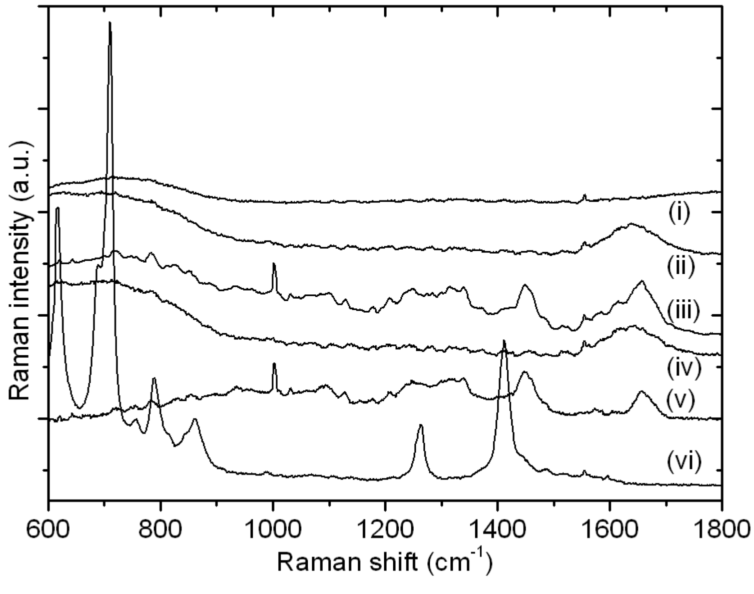

Figure 2: Raman spectra of materials used for microbioreactors. (i) CaF_2 substrate, (ii) PBS solution, (iii) average spectra from randomly chosen 10 individual hBMSCs, (iv) average of 10 spectra obtained from same height next to the hBMSCs, (v) Raman difference spectrum of (iii) minus (iv) showing background-free cell spectrum, and (vi) PDMS polymer. Each spectrum is obtained by spectral scanning over an area 15 µm × 15 µm with an accumulation time of 60 s and 75 mW laser power.

For Raman studies of cells, the choice of substrate used for cell culture is of paramount importance. Figure 2 shows the Raman spectroscopic information over the region 600-1800 cm^{-1} for different materials of choice for the fabrication of the microbioreactor. The Raman spectrum from CaF_2 has a single strong vibration at 320 cm^{-1} and none in the chosen region as seen in Figure 2(i). The spectrum of PDMS in Figure 2(vi) shows intense bands over the fingerprint region. The Raman spectrum from the PBS solution has a broad band around 1540 to 1760 cm^{-1} corresponding to the OH bending vibration of water (Figure 2(ii)). The average of 10 individual hBMSC spectra, shown in Figure 2(iii), features prominent bands for nucleotides, amides and proteins.[42-44] The spectrum in Figure 2(iv) is obtained from the average of 10 individual spectra obtained from the same focusing height adjacent to the cells on the CaF_2 substrate and is similar to the PBS spectrum shown in Figure 2(ii). The Raman difference spectrum of the average of hBMSCs minus the average spectra obtained adjacent to the corresponding cell is shown in Figure 2(v). The difference spectrum shows prominent bands for nucleotides, amides and proteins[42-44] which are free from the spectral influences of CaF_2 and PBS. The PDMS spectrum shows bands (Figure 2(vi)) which overlaps with bands from hBMSCs as seen in Figure 2(iii). Due to high Raman scattering of PDMS in the fingerprint region, CaF_2 is a better substrate for Raman studies of cell cultures in microbioreactors. All other spectra show a broad spectral response around 600-900 cm^{-1} from water and a band at 1555 cm^{-1} which is due to oxygen in the optical beam line. These features are not observed from the Raman difference spectrum in Figure 2(v).

The µBR-I and µBR-II operate under laminar flow conditions. A flow rate of around 10 µl/min was maintained throughout the culture period, providing enough nutrients to the cells without detaching them from the surface of the respective substrates by flow-force. Due to the continuous supply of the nutrient medium, no CO_2 buffering was required to maintain the pH. As the PDMS and silicon tubes are permeable to O_2, the cells acquired sufficient O_2 throughout the culture period.[45] Flow rates larger than 20 µl/min resulted in detachment of cells from the surface of the microchamber. The hBMSCs successfully proliferated in the microbioreactors after sterilization and surface treatment as described in the materials and methods. The hBMSCs were well preserved in perfusion culture until day 21 of the culture period, indicating that a sufficient supply of nutrients, oxygen and an efficient removal of waste was achieved by the action of the peristaltic pump. The experiments show that long-term culture of cells in microbioreactors under well maintained conditions is feasible.

Confocal Raman microscopy of cells results in chemical information by a label free and non-invasive method. Raman microspectroscopy as a function of time of hBMSCs cultured in the μBR-I were obtained from measurements in separate microbioreactors with different culture media conditions. hBMSCs were cultured in both basic medium and osteogenic medium until day 1, day 14, and day 21 of the culture period, respectively. Monitoring cell development in a single microbioreactor over the entire culture period was not feasible with μBR-I. This is due to the relatively thick top layer of PDMS and the intense Raman scattering of this material throughout the fingerprint region (Figure 2). Observation of the cells through the bottom layer of the CaF_2 is possible; however the optical quality of the focus is low due to aberration caused by the thickness of the CaF_2 substrate and the accompanying large refractive index mismatch. Hence, the PDMS chip was peeled off from the CaF_2 substrate to accommodate the Raman measurements on the cultured hBMSCs. The average Raman spectra from cells in the respective culture media conditions are shown in Figure 3 for each measurement day.

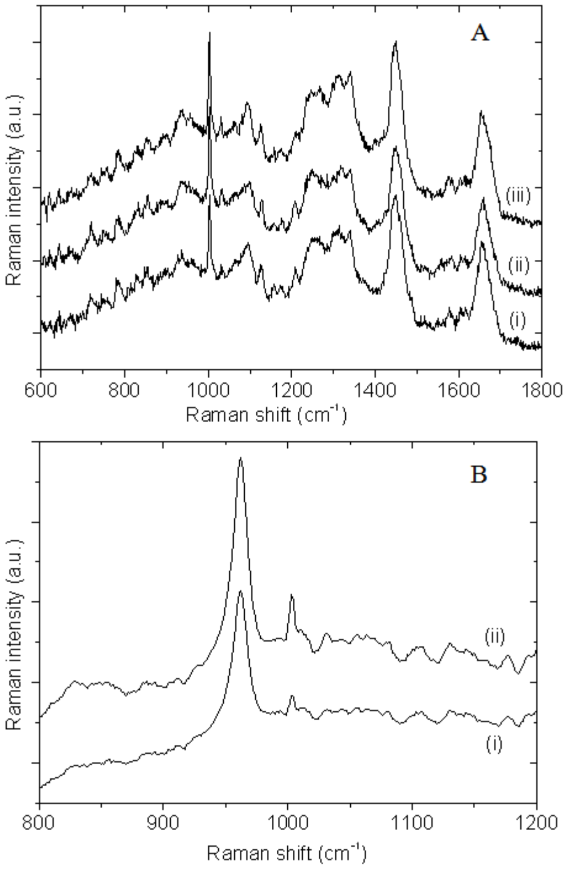

Figure 3: Raman microspectroscopy of hBMSCs cultured in μBR-I over a 21 day culture period under the influence of continuous perfusion of culture medium, (A) Average of 10 spectra from hBMSCs cultured in basic medium up to (i) day 1, (ii) day 14, and (iii) day 21 of culture, (B) Average of 10 spectra from hBMSCs cultured in osteogenic medium up to (i) day 14, and (ii) day 21 of culture showing mineralization in cells. Each spectrum is obtained by spectral scanning over an area 15 μm × 15 μm with an accumulation time of 60 s and 75 mW laser power.

hBMSCs were cultured in parallel in separate μBR-I microbioreactors. On each measurement day, ten hBMSCs from a single microbioreactor were randomly selected. The Raman spectra from all ten hBMSCs were averaged. The average Raman spectrum of hBMSCs cultured overnight in BM (day 1) is shown in Figure 3A(i). It shows Raman bands originating from the presence of biomolecules such as DNA at 788 cm^{-1}, phenylalanine at 1004 cm^{-1} and 1032 cm^{-1}, nucleotide backbone at 1094 cm^{-1}, protein at 1126 cm^{-1}, adenine at 1304 cm^{-1} and 1339 cm^{-1}, and a broad amide-I band at 1660 cm^{-1}.[42-44] Average Raman spectra from hBMSCs cultured in basic medium until day 14 and day 21 are shown in Figure 3A(ii) and 3A(iii). These spectra show bands at similar positions as those seen after overnight culture in Figure 3A(i). The spectra in Figure 3A are not significantly different, which can be expected since the basic medium maintains a normal growth of cells throughout the culture period. In order to differentiate the hBMSCs towards the osteogenic lineage, another set of μBR-I was used, which were perfused with osteogenic media after the overnight culture period. The spectral response, due to the influence of osteogenic media on the hBMSCs cultured until day 14 and day 21 of culture period, are shown in Figure 3B(i) and 3B(ii), respectively, over the spectral region 800–1200 cm^{-1}. The presence of Dex in the osteogenic media induced osteogenic differentiation of hBMSCs, whereas the presence of βGP results in mineralization of the hBMSCs within the culture period. Both spectra in Figure 3B(i) and 3B(ii) show a prominent band around 961 cm^{-1} reflecting the presence of the v_1 vibration of phosphates.[46] The position of the band corresponds to phosphates in hydroxyapatite minerals, which are part of the extra-cellular matrix of the hBMSCs. The increase in intensity of the phosphate band on day 21 compared to day 14 signifies the growth of the formed hydroxyapatite. Each of the average spectra in Figure 3A and 3B are corrected for the influence of PBS buffer. Our results show the feasibility of the μBR-I for long-term perfusion culture to study the proliferation, differentiation, and mineralization of hBMSCs. Raman difference spectra of average spectra obtained on day 14 and day 21 with respect to day 1 did not show prominent bands around 1578 cm^{-1} and 1607 cm^{-1}, which have been proposed as biomarkers for necrotic cells.[13] This observation suggests that the hBMSCs were maintained in healthy metabolic conditions up to day 21 of the culture period,[13] without any significant occurrence of cell death due to apoptosis and necrosis.

A limitation of μBR-I is that the PDMS layer had to be peeled off the CaF_2 substrate. In order to overcome this limitation we developed μBR-II, which enabled Raman imaging of the hBMSCs over the culture period through the glass cover slip with a standard microscope and a cover glass-corrected microscope objective as shown in Figure 1D. The hBMSCs were successfully cultured in these microbioreactors under the influence of basic media up to day 4 of the culture period. Live-cell Raman imaging of the hBMSC was performed by scanning in 32 × 32 steps in an area of 15 μm × 15 μm with an accumulation time of 0.5 s per pixel and 50 mW laser power. Figure 4A shows the white-light micrograph of a hBMSC with a 15 μm × 15 μm white frame showing the region of interest for Raman imaging. The corresponding two-cluster HCA image after cluster analysis over the 500-1850 cm^{-1} is shown in Figure 4B, and the respective average spectra of each cluster are shown in Figure 4D over the spectral region 600-1800 cm^{-1}. In Figure 4B, one cluster (black pixels) corresponds to the cell and the other cluster corresponds to the background (PBS buffer) (magenta pixels). The spectra corresponding to the respective clusters are shown in Figure 4D(i) and 4D(ii). The average background spectrum is influenced by contributions from the glass substrate (855 to 955 cm^{-1}) and PBS buffer. The cell spectrum shows prominent bands reflecting the presence of nucleotides, proteins and lipids. The background-free cell spectrum is obtained by subtracting the background spectrum from the cell spectrum, as shown in Figure 4D(iii). The resultant spectrum is free from the contributions of glass and PBS buffer, has a baseline close to zero and reveals many pronounced vibrational bands, which can be assigned to nucleotides, proteins and lipids in agreement with the literature.[42-44]

The cell spectra in Figure 4D(i) and 4D(ii) of hBMSC do not give specific information about various organelles in the cell. We therefore performed six-level cluster analysis which resulted in five clusters for the cell and one for the background (magenta pixels), as shown in Figure 4C. Figure 4E shows the results of subtraction of the average background spectrum from each of the cluster spectra. The color coding in Figure 4E corresponds to the colors in the cluster image in Figure 4C. The black spectrum in Figure 4E shows a prominent band at 718 cm^{-1} assigned to the C-N-vibration in the phospholipid head group of the membrane lipid phosphatidylcholine (PC). Since PC is abundantly present in the plasma membrane of the cell as well as in the membranes of cell organelles.[47] The black cluster in Figure 4C can be assigned to the cell membrane and lipoproteins in the vicinity of it. The dark blue and light blue Raman spectra in Figure 4E show intense bands of nucleotides at 729, 750, 782, 895, 1091 and 1575 cm^{-1} showing the presence of DNA distributed in the nucleus of the hBMSC. The spectral intensity of the light blue regions is higher than the dark blue region, which suggests that the DNA concentration is higher in the light blue regions than in the dark blue regions. The areas with high DNA content in the nucleus of the hBMSC are attributed to heterochromatin and the regions of low DNA content are attributed to euchromatin. The green spectrum in Figure 4E shows bands at positions 718, 1076, 1260, 1298, 1437, and 1740 cm^{-1} reflecting the presence of intracellular lipids. The clusters in Figure 4C corresponding to these spectra show the distribution of lipids in the region of interest over the hBMSC. The orange color spectrum in Figure 4E has bands corresponding to both proteins and lipids. The regions occupied by the corresponding pixels seen in Figure 4C can be attributed to the cytosol present in the cytoplasm of the cell. The spectrum of this cluster shows a small band at 1602 cm^{-1}, which can be attributed to mitochondria.[48] The spectrum also shows a band at 718 cm^{-1} for CN stretching vibration in phosphatidylcholine lipid head group which is abundantly present in the mitochondrial membrane.[48] The average spectra in Figure 4E also show bands for amino acids, amides, and proteins present in the respective clusters.[42-44]

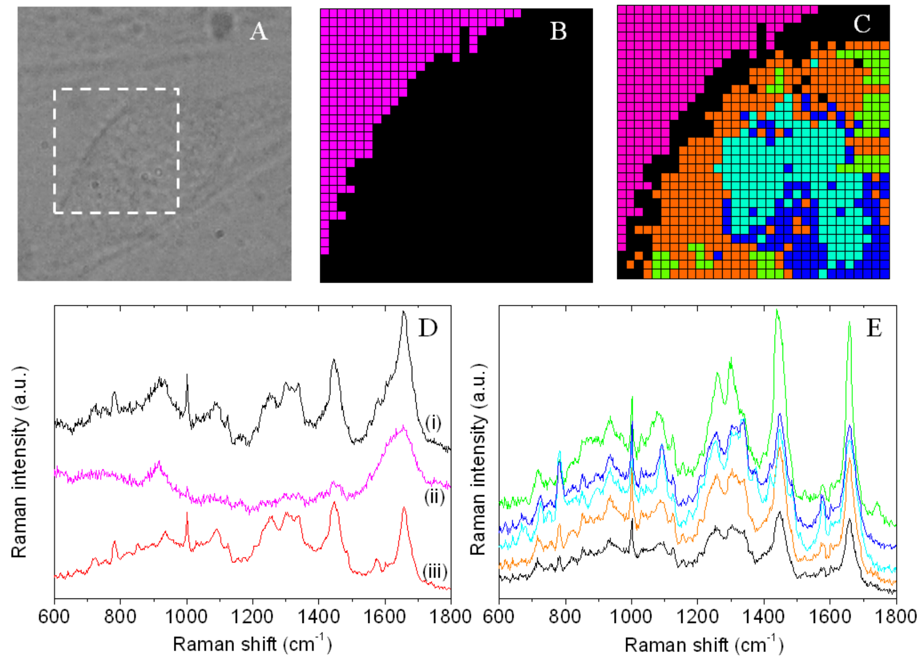

Figure 4: High spatial resolution Raman imaging performed on hBMSC cultured in µBR-II. hBMSCs were cultured under the influence of continuous perfusion of basic media up to day 4 of culture period. (A) white-light micrograph showing hBMSC adhered to glass cover slip. The white square box indicates the region of interest of 15 µm × 15 µm where Raman imaging is performed, (B) Two-cluster image of the obtained hyperspectral data (one cluster each for cell and background), (C) Six-cluster image of the hyperspectral data (five clusters for the cell and one cluster for background), (D) corresponding average cell spectra of two-cluster image over the spectral region 600 - 1800 cm^{-1}: (i) average spectrum for the cell, (ii) average spectrum for the background, (iii) Raman difference spectra of (i) minus (ii) showing background-free cell spectrum, and (E) background-free spectra for the clusters corresponding to the cell in (C) over the spectral region 600 - 1800 cm^{-1}. The color coding in (E) corresponds to cluster image (C). Raman imaging performed over living hBMSC by scanning in 32 × 32 steps over an area of 15 µm × 15 µm with an accumulation time of 0.5 s per pixel and 50 mW laser power.

4.4 Conclusions

In conclusion, we have demonstrated the fabrication and use of microbioreactors for long-term perfusion culture of cells for as long as 21 days. The hBMSCs were successfully cultured inside the microchamber of the microbioreactors under continuous perfusion of the culture medium. The cells were kept in healthy condition throughout the culture period. The microbioreactors enabled optical Raman analysis of the cells cultured inside the microbioreactor without disturbing the cells. Raman spectroscopy enabled non-invasive and label free methodology to follow the differentiation and mineralization of the hBMSCs over a 21-day culture period in μBR-I. The results showed mineralization as early as day 14 of the culture period, and increased in concentration by day 21. High spatial resolution Raman imaging of hBMSCs cultured in μBR-II showed the distribution of cell organelles in an individual hBMSC. These results show the feasibility of using confocal microspectroscopy for chemical imaging of differentiation of hBMSCs for tissue engineering in microbioreactors.

References

1. Dexter, T. M.; Allen, T. D.; Lajtha, L. G.; Schofield, R.; Lord, B. I., Stimulation of differentiation and proliferation of haemopoietic cells in vitro. *J Cell Physiol* **1973,** 82, (3), 461-73.
2. Langer, R.; Vacanti, J. P., Tissue engineering. *Science* **1993,** 260, (5110), 920-6.
3. Cabral, J. M. S., Ex vivo expansion of hematopoietic stem cells in bioreactors. *Biotechnol. Lett.* **2001,** 23, (10), 741-751.
4. Collins, P. C.; Miller, W. M.; Papoutsakis, E. T., Stirred culture of peripheral and cord blood hematopoietic cells offers advantages over traditional static systems for clinically relevant applications. *Biotechnol Bioeng* **1998,** 59, (5), 534-43.
5. Martin, I.; Wendt, D.; Heberer, M., The role of bioreactors in tissue engineering. *Trends Biotechnol.* **2004,** 22, (2), 80-86.
6. Griffith Linda, G.; Naughton, G., Tissue engineering--current challenges and expanding opportunities. *Science* **2002,** 295, (5557), 1009-14.
7. Strain Alastair, J.; Neuberger James, M., A bioartificial liver--state of the art. *Science* **2002,** 295, (5557), 1005-9.
8. Andersson, H.; van den Berg, A., Microfluidic devices for cellomics: a review. *Sens. Actuators, B* **2003,** B92, (3), 315-325.
9. Palkova, Z.; Vachova, L.; Valer, M.; Preckel, T., Single-cell analysis of yeast, mammalian cells, and fungal spores with a microfluidic pressure-driven chip-based system. *Cytometry A* **2004,** 59, (2), 246-53.
10. Olson, K. J.; Ahmadzadeh, H.; Arriaga, E. A., Within the cell: analytical techniques for subcellular analysis. *Anal. Bioanal. Chem.* **2005,** 382, (4), 906-917.
11. Piruska, A.; Nikcevic, I.; Lee, S. H.; Ahn, C.; Heineman, W. R.; Limbach, P. A.; Seliskar, C. J., The autofluorescence of plastic materials and chips measured under laser irradiation. *Lab Chip* **2005,** 5, (12), 1348-1354.
12. Puppels, G. J.; De Mul, F. F. M.; Otto, C.; Greve, J.; Robert-Nicoud, M.; Arndt-Jovin, D. J.; Jovin, T. M., Studying single living cells and chromosomes by confocal Raman microspectroscopy. *Nature* **1990,** 347, (6290), 301-3.
13. Notingher, I.; Verrier, S.; Romanska, H.; Bishop, A. E.; Polak, J. M.; Hench, L. L., In situ characterization of living cells by Raman spectroscopy. *Spectroscopy* **2002,** 16, (2), 43-51.
14. Verrier, S.; Notingher, I.; Polak, J. M.; Hench, L. L., In situ monitoring of cell death using Raman microspectroscopy. *Biopolymers* **2004,** 74, (1-2), 157-62.
15. Uzunbajakava, N.; Lenferink, A.; Kraan, Y.; Volokhina, E.; Vrensen, G.; Greve, J.; Otto, C., Nonresonant confocal Raman imaging of DNA and protein distribution in apoptotic cells. *Biophys. J.* **2003,** 84, (6), 3968-3981.
16. Matthaus, C.; Boydston-White, S.; Miljkovic, M.; Romeo, M.; Diem, M., Raman and infrared microspectral imaging of mitotic cells. *Appl. Spectrosc.* **2006,** 60, (1), 1-8.
17. Short, K. W.; Carpenter, S.; Freyer, J. P.; Mourant, J. R., Raman spectroscopy detects biochemical changes due to proliferation in mammalian cell cultures. *Biophys. J.* **2005,** 88, (6), 4274-4288.
18. Notingher, I.; Jell, G.; Lohbauer, U.; Salih, V.; Hench, L. L., In situ non-invasive spectral discrimination between bone cell phenotypes used in tissue engineering. *J. Cell. Biochem.* **2004,** 92, (6), 1180-1192.
19. Cheng, I. F.; Chang, H.-C.; Hou, D.; Chang, H.-C., An integrated dielectrophoretic chip for continuous bioparticle filtering, focusing, sorting, trapping, and detecting. *Biomicrofluidics* **2007,** 1, (2), 21503.
20. Huh, Y. S.; Chung, A. J.; Erickson, D., Surface enhanced Raman spectroscopy and its application to molecular and cellular analysis. *Microfluid. Nanofluid.* **2009,** 6, (3), 285-297.
21. Ramser, K.; Enger, J.; Goksoer, M.; Hanstorp, D.; Logg, K.; Kaell, M., A microfluidic system enabling Raman measurements of the oxygenation cycle in single optically trapped red blood cells. *Lab Chip* **2005,** 5, (4), 431-436.

22. Ramser, K.; Wenseleers, W.; Dewilde, S.; Van Doorslaer, S.; Moens, L., The combination of resonance Raman spectroscopy, optical tweezers and microfluidic systems applied to the study of various heme-containing single cells. *Spectroscopy* **2008,** 22, (4), 287-295.
23. Zhang, X.; Yin, H.; Cooper, J. M.; Haswell, S. J., Characterization of cellular chemical dynamics using combined microfluidic and Raman techniques. *Anal. Bioanal. Chem.* **2008,** 390, (3), 833-840.
24. Powers, M. J.; Domansky, K.; Kaazempur-Mofrad, M. R.; Kalezi, A.; Capitano, A.; Upadhyaya, A.; Kurzawski, P.; Wack, K. E.; Stolz, D. B.; Kamm, R.; Griffith, L. G., A microfabricated array bioreactor for perfused 3D liver culture. *Biotechnol. Bioeng.* **2002,** 78, (3), 257-269.
25. Borenstein, J. T.; Terai, H.; King, K. R.; Weinberg, E. J.; Kaazempur-Mofrad, M. R.; Vacanti, J. P., Microfabrication technol. for vascularized tissue engineering. *Biomed. Microdevices* **2002,** 4, (3), 167-175.
26. Wheeler, A. R.; Throndset, W. R.; Whelan, R. J.; Leach, A. M.; Zare, R. N.; Liao, Y. H.; Farrell, K.; Manger, I. D.; Daridon, A., Microfluidic device for single-cell analysis. *Anal. Chem.* **2003,** 75, (14), 3581-3586.
27. Chang, W.-J.; Akin, D.; Sedlak, M.; Ladisch, M. R.; Bashir, R., Poly(dimethylsiloxane) (PDMS) and Silicon Hybrid Biochip for Bacterial Culture. *Biomed. Microdevices* **2003,** 5, (4), 281-290.
28. Leclerc, E.; David, B.; Griscom, L.; Lepioufle, B.; Fujii, T.; Layrolle, P.; Legallaisa, C., Study of osteoblastic cells in a microfluidic environment. *Biomaterials* **2006,** 27, (4), 586-95.
29. Pins, G. D.; Toner, M.; Morgan, J. R., Microfabrication of an analog of the basal lamina: biocompatible membranes with complex topographies. *FASEB J.* **2000,** 14, (3), 593-602.
30. Petersen, E. F.; Spencer, R. G. S.; McFarland, E. W., Microengineering neocartilage scaffolds. *Biotechnol. Bioeng.* **2002,** 78, (7), 801-804.
31. Taylor, A. M.; Rhee, S. W.; Tu, C. H.; Cribbs, D. H.; Cotman, C. W.; Jeon, N. L., Microfluidic multicompartment device for neuroscience research. *Langmuir* **2003,** 19, (5), 1551-1556.
32. Enger, J.; Goksoer, M.; Ramser, K.; Hagberg, P.; Hanstorp, D., Optical tweezers applied to a microfluidic system. *Lab Chip* **2004,** 4, (3), 196-200.
33. Leclerc, E.; Sakai, Y.; Fujii, T., Microfluidic PDMS (Polydimethylsiloxane) Bioreactor for Large-Scale Culture of Hepatocytes. *Biotechnol. Prog.* **2004,** 20, (3), 750-755.
34. Pully, V. V.; Lenferink, A.; Otto, C., Hybrid Rayleigh, Raman and two-photon excited fluorescence spectral confocal microscopy of living cells. *J. Raman Spectrosc.* **2009,** 10.1002/jrs.2501.
35. Uzunbajakava, N.; Greve, J.; Otto, C., Raman microscopy of cells: chemical imaging of apoptosis. *Proc. SPIE-Int. Soc. Opt. Eng.* **2003,** 4963, (Multiphoton Microscopy in the Biomedical Sciences III), 223-230.
36. Van Manen, H.-J.; Kraan, Y. M.; Roos, D.; Otto, C., Intracellular Chemical Imaging of Heme-Containing Enzymes Involved in Innate Immunity Using Resonance Raman Microscopy. *J. Phys. Chem. B* **2004,** 108, (48), 18762-18771.
37. van Manen, H.-J.; Kraan, Y. M.; Roos, D.; Otto, C., Single-cell raman and fluorescence microscopy reveal the association of lipid bodies with phagosomes in leukocytes. *Proc. Natl. Acad. Sci. U. S. A.* **2005,** 102, (29), 10159-10164.
38. McDonald, J. C.; Duffy, D. C.; Anderson, J. R.; Chiu, D. T.; Wu, H.; Schueller, O. J.; Whitesides, G. M., Fabrication of microfluidic systems in poly(dimethylsiloxane). *Electrophoresis* **2000,** 21, (1), 27-40.
39. Charati, S. G.; Stern, S. A., Diffusion of Gases in Silicone Polymers: Molecular Dynamics Simulations. *Macromolecules* **1998,** 31, (16), 5529-5535.
40. El-Ali, J.; Sorger, P. K.; Jensen, K. F., Cells on chips. *Nature* **2006,** 442, (7101), 403-411.
41. Leclerc, E.; Sakai, Y.; Fujii, T., Cell culture in 3-dimensional microfluidic structure of PDMS (polydimethylsiloxane). *Biomed. Microdevices* **2003,** 5, (2), 109-114.
42. Hayashi, H.; Nishimura, Y.; Katahira, M.; Tsuboi, M., The structure of nucleosome core particles as revealed by difference Raman spectroscopy. *Nucleic Acids Res* **1986,** 14, (6), 2583-96.
43. Thomas, G. J., Jr.; Prescott, B.; Olins, D. E., Secondary structure of histones and DNA in chromatin. *Science* **1977,** 197, (4301), 385-8.

44. Tu, A. T., *Raman Spectroscopy in Biology: Principles and Applications*. 1982; p 448.
45. Hung Paul, J.; Lee Philip, J.; Sabounchi, P.; Lin, R.; Lee Luke, P., Continuous perfusion microfluidic cell culture array for high-throughput cell-based assays. *Biotechnol Bioeng* **2005,** 89, (1), 1-8.
46. Timlin, J. A.; Carden, A.; Morris, M. D., Chemical microstructure of cortical bone probed by Raman transects. *Appl. Spectrosc.* **1999,** 53, (11), 1429-1435.
47. van Manen, H.-J.; Lenferink, A.; Otto, C., Noninvasive Imaging of Protein Metabolic Labeling in Single Human Cells Using Stable Isotopes and Raman Microscopy. *Anal. Chem.* **2008,** 80, (24), 9576-9582.
48. Pully, V. V.; Otto, C., The intensity of the 1602 cm^{-1} band in human cells is related to mitochondrial activity. *J. Raman Spectrosc.* **2009,** 40, (5), 473-475.

Chapter 5

Proline as an early Raman biomarker for differentiation of human bone marrow stromal cells

In this chapter, we report proline as a Raman biomarker for early differentiation of human immortalized bone marrow stromal cell (iMSCs). The biomarker can be observed on the third day of cell culture, well before the phase of major extracellular matrix formation. The biomarker is established by a rigorous comparison of Raman spectra of iMSCs grown in osteogenic versus non-osteogenic medium. Analysis of the datasets by both hierarchical cluster analysis and principal component analysis clearly distinguish between cell sub-populations. The biomarker is attributed to the intra-cellular production of proline, an essential component of collagen and in particular collagen type-I, which in turn is an essential component of the extra-cellular matrix of osteoblasts. Early detection and characterization of stromal cell differentiation along a desired lineage is important for tissue engineering and medical applications of stromal cell grafting. Raman microspectroscopy enables characterization of osteoblast induction within three days after seeding iMSCs.

Parts of the results from this chapter have been submitted to Analytical Chemistry

5.1 Introduction

Adult mesenchymal stem-like cells (MSCs) obtained from bone marrow aspirates of healthy patients are highly multipotent[1] and can be differentiated *in vitro* towards various mesenchymal lineages like bone, cartilage, muscle and adipose tissue.[2] The multilineage potential is achieved by stimulating the differentiation of stem cells *in vitro* by various agents and growth factors added to the cell culture media. The multilineage capability of MSCs enables their application in tissue engineering, regenerative medicine and stem cell therapy.[3] Because the primary cultures have limited potential due to senescence upon *in vitro* culture, cells immortalized by transduction with telomerase were used in the present study. These cells otherwise behave like early primary cells, are non-tumorigenic and differentiate well.

Tissue engineering of adult stem cells towards osteogenic lineage leading to bone formation is a most promising approach, and involves culturing autologous cells on biocompatible and biofunctional scaffolds. Engineered tissues may help in substituting tissue damaged by trauma, cancer or infection. Differentiation of adult mesenchymal stem cells towards mineralized tissue leading to bone formation is termed osteogenesis. In the process of osteogenesis, adult stem cells undergo various precursor stages like preosteoblast, osteoblasts and osteocytes which produce mineralized tissue resembling bone.[2, 3] Identifying the markers at each stage of osteogenesis is important to understand the process. While there is extensive literature describing the process of adult stem cell differentiation towards osteoblasts before forming bone,[1-4] there are hardly any reports using non-invasive methods to study early-stage osteogenic differentiation. The detection of biomarkers that signify osteogenesis at an early stage will be useful in tissue engineering and medical applications of stem cell grafting.

One of the methods to describe early differentiation is by determining the expression of the osteogenic marker gene alkaline phosphatase (ALP) using antibodies and flow-cytometry. The ALP expression of the cells was shown to reach significant levels around day 5 of the culture and depended on the osteogenic potential of the media used.[5, 6] Accumulation of intra-cellular calcium was determined by a commercially available calcium assay kit after one week of culture and signifies the mineralization capability of the cells.[1] Variants of the polymerase chain reaction (PCR) technique showed a significant expression of osteogenic gene markers such as collagen type-I (COL-I) and non-collagenous proteins like osteocalcin (OC), and osteonectin (ON) around day 5 of culture, which declined further on.[5, 6] All these techniques have lengthy handling procedures or are invasive to varying degrees because they either require lysis, cell fixation, large numbers of cells, or fluorescent labels. Hence, these approaches do not reveal biomarkers at an early stage of differentiation without destroying the cells. Consequently there is a clear need for faster, non-invasive and label-free techniques that enable monitoring of early stages of osteogenic differentiation. Confocal Raman microspectroscopy is a powerful analytical method that enables non-invasive and label-free analysis of chemical and molecular information in sub-femtoliter volumes from a sample under consideration. The method has been successfully applied to cellular- and molecular biology and has been used to identify living cells,[7, 8] dead cells,[9] cellular apoptosis,[10] the mitotic stage in cell-division,[11] proliferating cells,[12] and differentiating cells.[13] Cellular distribution of certain organelles like mitochondria[14] and intracellular redistribution of lipid vesicles upon phagocytosis[15] have also been successfully shown. Over the last decade, Raman spectroscopy has been extensively used to study the process of osteogenesis,[16-18] however these studies have focused preponderantly on the process of late and early mineralization of adult stem cells.[17] Notingher et al. showed the differentiation of embryonic stem cells over day 4 and day 16 of a culture and reported the variation of mRNA and DNA over time.[19] Raman spectroscopy in combination with PCA has successfully shown heterogeneity in a stem cell population.[20] The feasibility of FTIR for monitoring osteogenic differentiation of human mesenchymal stem cells was shown by Krafft et al. as early as day 7 of a culture.[21] Kale et al. showed that osteogenic cells cultured in serum free media containing transforming growth factor (TGF)-β1 resulted in bone formation at day 3 of a culture.[22]

Proline is a non-essential amino acid which is necessary for the formation of collagen type-I. Collagen type-I is essential for the mineralization process in the extracellular matrix. The amino acid glutamate is used as a precursor in the biosynthesis of proline.[23] The intracellular proline concentration increases with the confluence of cells.[23] The proline concentration in cells decreases under the influence of osteogenic growth factors such as dexamethasone.[24, 25]

In the present study, we report proline as Raman biomarker of differentiation of living iMSCs to the osteogenic lineage as early as on day 3 of a culture, when grown in the presence of media, which contain osteogenic growth factors. It is also shown that once adequate populations of *in vitro* expanded cells are obtained, cells differentiate to osteoblasts as a result of the influence of osteogenic growth factors. The influence of osteogenic and non-osteogenic culture media on the biomarker proline will be shown by univariate data analysis and will be further supported by multivariate data analysis techniques such as unsupervised hierarchical cluster analysis (HCA) and principal components analysis (PCA). The identification, by Raman microspectroscopy, of proline as a biomarker is further validated by the Raman data acquired on day 7 of culture.

5.2 Materials and methods

Cell culture

The human immortalized bone marrow stromal cell line (iMSC#3) was established by retroviral transfection of human telomerase (hTert) into bone marrow stromal cells of a healthy volunteer.[26, 27] The cells grow at similar rates as early primary cultures, have normal karyotypes and do not give tumors in immuno-deficient mice. A detailed description and characterization of the cells will be published elsewhere.[28]

iMSCs were seeded at 1000 cells/cm^2 over UV grade calcium fluoride substrates (CaF_2) (Crystran Ltd., UK). The cells were cultured under the influence of various osteogenic and non-osteogenic cell culture media conditions in separate Petri dishes. Non-osteogenic cell culture basic medium (BM) was prepared from α-MEM (GIBCO, Carlsbad, CA), 10% fetal bovine serum (FBS; Bio Whittaker, Australia), 0.2 mM L-ascorbic acid-2-phosphate (AsAP; Sigma, St. Louis, MO), 100U/mL Pencillin G (Invitrogen, Carlsbad, CA); 100 μg/mL Streptomycin (Invitrogen) and 2mM L-Glutamine (L-Glu; Sigma). Proliferation medium (PM), which is another non-osteogenic cell culture medium, was prepared by adding 1ng/ml basic fibroblast growth factor (bFGF; Instruchemie, The Netherlands) to the BM. Different combinations of osteogenic media (OM) were prepared by adding 0.01 M β-Glycerophosphate (βGP; Sigma) and different osteogenic growth factors either individually or in combination with BM. Normal osteogenic media were prepared after separately adding osteogenic growth factors like 10^{-8} M dexamethasone (Dex, Sigma) (OM-Dex), 100 ng/ml recombinant human bone morphogenetic protein-2 (rhBMP2, Hangzhou Biodoor Biotechnology co., LTD, China) (OM-BMP2), 1 mM cyclic 3,5 adenosine-monophosphate (cAMP, Sigma) (OM-cAMP) and 10^{-8} M 1α, 25-Dihydroxyvitamin D3 (Vit-D3, Sigma) (OM-VitD3). Combinations of osteogenic media OM-DB, OM-DC and OM-DV were prepared after adding the osteogenic growth factor Dexamethasone to OM-BMP2, OM-cAMP and OM-VitD3 respectively. Overnight culture of cells on CaF_2 substrates was performed to enhance cell adherence to the substrates. The adhered cells were separately cultured in the different non-osteogenic media combinations BM and PM and the osteogenic media OM-Dex, OM-BMP2, OM-cAMP, OM-VitD3, OM-DB, OM-DC and OM-DV until day 3 and day 7 of culture. The cells were washed three times with phosphate buffered saline solution (PBS; Gibco) before measurement with the Raman microscope. All measurements were carried out on living cells.

Confocal Raman microscopy

We used a custom-built confocal Raman microspectrometer as described earlier[29] to perform measurements on living cells. A Krypton ion laser (Coherent, Innova 90K, Santa Clara, CA) emitting at 647.1 nm was used as an excitation source. A water immersion objective with 63× magnification and 1.2 NA (Zeiss Plan Neofluar, Carl Zeiss, Thornwood, NY) was used to focus the laser light over a sample. The microscope is operated in epi-detection mode. A spectrograph disperses the Raman scattered photons on an air-cooled charge-coupled device (EMCCD: Newton DU-970N, Andor Technology, Belfast, Northern Ireland). The conventional amplifier was used. The system provided a spectral resolution of 1.85 to 2.85 cm^{-1}/pixel over the wavenumber range from -20 to 3670 cm^{-1}. Raman spectra were acquired in so-called "spectral scanning mode". In this measurement mode a single full spectrum is obtained by raster scanning the laser beam over the sample area of 22.5 µm × 22.5 µm in 10s. A laser power of 75 mW was used. The effective dose of light was ~1.5 $mJ/\mu m^2$. Raman spectra were acquired from 16 randomly chosen cells in each culture medium for day 3 and day 7 after starting the culture.

Raman data Analysis

The Raman spectra were preprocessed by: 1) removal of cosmic ray events, 2) subtraction of the camera offset, 3) calibration of the wave number axis, and 4) correction of frequency dependent transmission. The well-known band-positions of toluene were used to relate wavenumbers to pixels. The frequency-dependent optical detection efficiency of the setup is corrected using a tungsten halogen light source (Avalight-HAL; Avantes BV, Eerbeek, The Netherlands) with a known emission spectrum. The detector-induced etaloning effect was also compensated by this procedure. The acquired spectra were analyzed with univariate and multivariate data analysis. The latter involved both principal component analysis (PCA) and hierarchical cluster analysis (HCA). HCA makes use of the scores obtained from the PCA data.

After data preprocessing, the 16 spectra from individual cells in each medium on respective measurement days were averaged. The averaged spectra were subsequently autoscaled to the mean of the spectra along the frequency axis. Univariate data analysis was performed by a selection of specific vibrational bands of interest and an integration of the band intensity after local baseline subtraction. Subsequently, band intensity ratios of selected bands of interest with respect to the integrated band intensity of the nitrogen stretch-mode at 2230 cm^{-1} were calculated. The nitrogen band originates from N_2 in air in the beam path and was constant for all measurements. The resultant band intensity ratios were normalized to the mean of the respective band integration ratio values for each of the osteogenic and non-osteogenic culture media conditions. The normalization of the band integration ratios was performed to show the results on the same scale

In order to support the findings of univariate analysis, multivariate data analysis techniques such as PCA and HCA were performed over the entire range of the Raman spectra from 380 to 3670 cm^{-1}. The 16 individual cell spectra from each of the 9 different osteogenic and non-osteogenic culture media (all together 144 spectra) were compared against each other after subtraction of the Raman spectrum of the PBS buffer solution that was acquired at the same height adjacent to the cell. The influence of a spectral background, corresponding to CaF_2 and aqueous PBS solution, was efficiently subtracted and did not contribute to variance in the dataset.

All data manipulations were performed with routines written in MATLAB 7.4 (The Math Works Inc., Natick, MA). HCA and PCA were performed using PLS toolbox (Eigenvectors Research Inc., Wenatchee, WA) in MATLAB 7.4.

5.3 Results and discussion

iMSCs were successfully cultured until day 7 of the culture in various non-osteogenic and osteogenic culture media conditions. The iMSCs showed variations in the morphology as a result of the different media.

All culture media contained ascorbic acid which is essential to the cells for production of pro-collagen and collagen. The amino acids proline, hydroxyproline and glycine are a major building block of collagen type-I, which is an important structural protein. Collagen type-I is a major constituent of bone. Proline is a non-essential amino acid that can be synthesized *in vivo* by humans. Hydroxyproline is formed from the hydroxylation of proline under the influence of ascorbic acid (AsAP), which was added to osteogenic and non-osteogenic cell culture media in this study. Proline, hydroxyproline, glycine and other amino acids constitute pro-collagen, which forms a triple helix structure inside the rough endoplasmic reticulum of the cell. Pro-collagen is exocytosed by Golgi bodies and is processed by pro-collagen peptidase to yield collagen. Collagen molecules are attached to the external side of the cell membrane in an organized way by fibronectins and integrins resulting in collagen type-I.

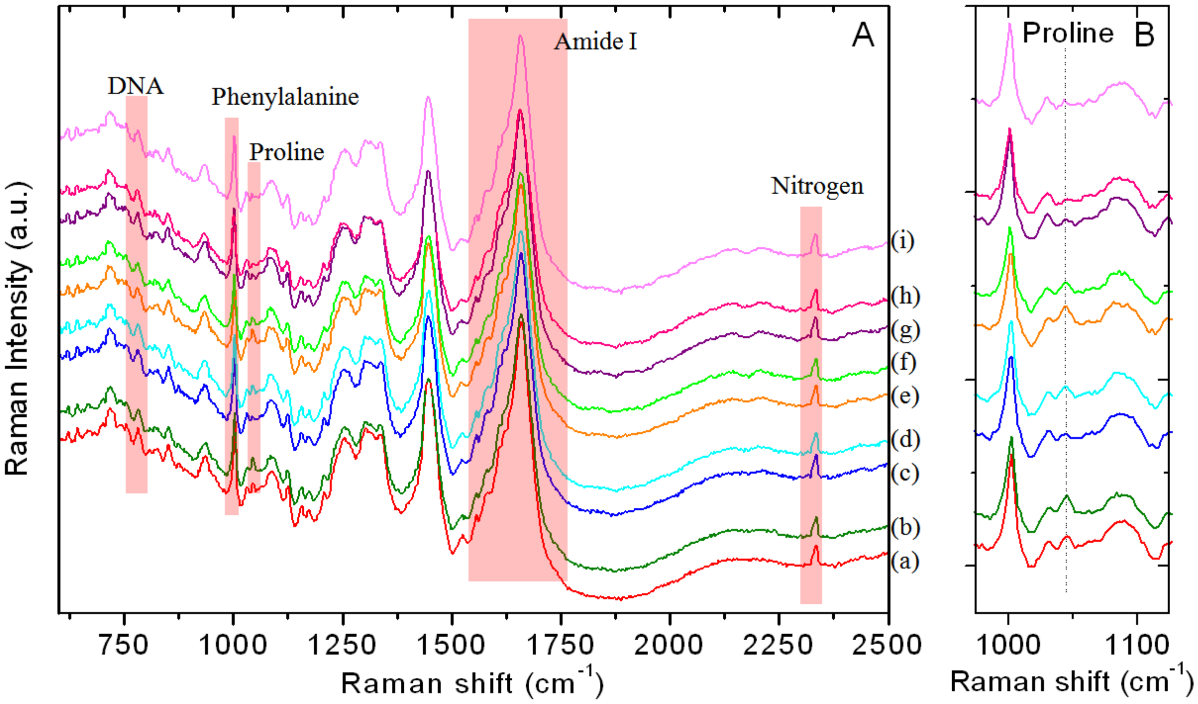

Figure 1: (A) Raman spectra in the range 600 – 2400 cm^{-1}. Each spectrum corresponds to an average of 16 randomly chosen iMSCs that were cultured under the influence of non-osteogenic and osteogenic culture media condition for 3 days. The spectra were vertically displaced for clarity. (a) BM, (b) PM, (c) OM-Dex, (d) OM-BMP, (e) OM-cAMP, (f) OM-VitD, (g) OM-DB, (h) OM-DC and (i) OM-DV. (B) Enlargement of the Raman spectra in the range from 975 – 1125 cm^{-1} around the proline-marker band at 1045 cm^{-1}. The vertical magnification is a factor 2.

iMSCs cultured in the described media until day 3 and day 7 were measured with confocal Raman microspectroscopy. Figure 1A shows the average spectra of 16 cells measured in each medium in the spectral region from 600 cm^{-1} to 2400 cm^{-1}, on day 3 of the culture. The spectra are arranged from bottom to top as: (a) BM (red), (b) PM (dark green), (c) OM-Dex (dark blue), (d) OM-BMP2 (light blue), (e) OM-cAMP (orange), (f) OM-VitD3 (light green), (g) OM-DB (violet), (h) OM-DC (magenta), and (i) OM-DV (pink). The spectra show many bands which have been assigned in the literature.[30-33] Bands at 788, 1004 and 1656 cm^{-1} correspond to nucleotide, phenylalanine and amide-I respectively. These bands appear very similar for each of the different culture media condition. A notable difference occurs between the spectra from non-osteogenic media like BM, PM and osteogenic media at 1045 cm^{-1} as can be observed from Figure 1B over the spectral region (975 cm^{-1} to 1125 cm^{-1}). This band signifies the presence of proline.[34] The Raman spectra of the free amino acids proline and glycine dissolved in aqueous buffer are shown in literature.[34, 35] Many intense bands occur that can be attributed to the amino group and the carboxylate group. However after formation of the amide bond, which links amino acids, these bands result in amide I and amide III bands in the Raman spectra of proteins. A very intense band of proline, which is little or not affected after incorporation of proline in proteins, is the band at 1045 cm^{-1}. Glycine has a slightly weaker band in this area at 1032 cm^{-1}. The Raman spectra of poly-L-hydroxyproline and proline as powders and in solution are illustrated in literature.[36] A strong band at 1047 cm^{-1} for proline powder and a strong band at 1067 cm^{-1} was observed for poly-L-hydroxyproline powder. Both proline and hydroxyproline do not show a significant shift in bands at 1047 cm^{-1} and 1067 cm^{-1} when measured in solution. The Raman spectral data of amino acids confirms the assignment of the band at 1045 cm^{-1} in Figure 1 to proline.

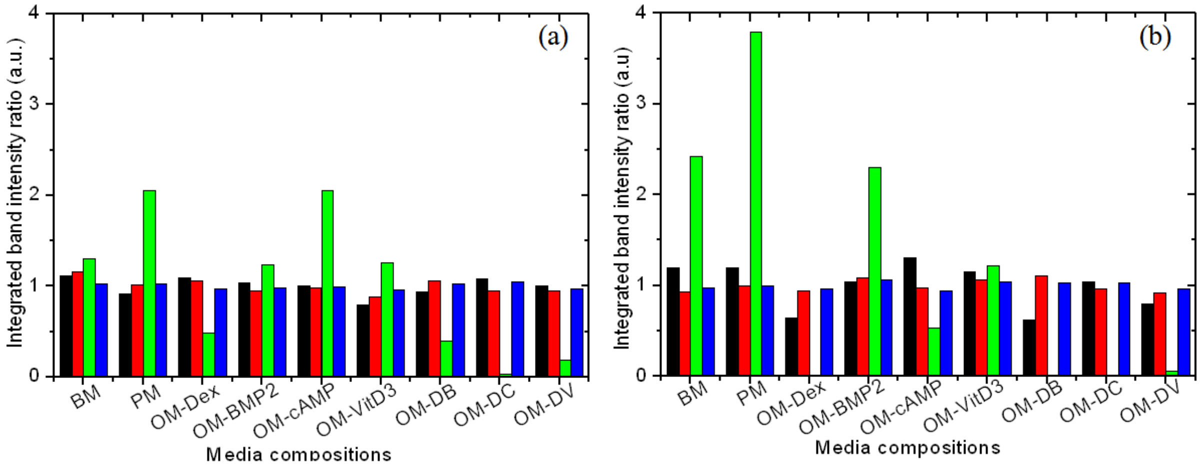

Figure 2: Univariate data analysis showing integrated band intensity ratios for the spectra shown in Figure 2 of the iMSCs cultured in various non-osteogenic and osteogenic culture media conditions up to (a) Day 3 and (b) Day 7 of culture. The band intensity ratios acquired from the ratios of selected bands of interest like DNA (black bar), phenylalanine (red bar), proline (green bar) and amide-I (blue bar) to the band of nitrogen. All bands are integrated after baseline subtraction.

The univariate data analysis in Figure 2(a) and 2(b) show band intensity ratios for DNA (black), phenylalanine (red), proline (green) and amide I (blue) plotted for different osteogenic and non-osteogenic culture media as extracted from the spectra of iMSCs on day 3 (Figure1), and on day 7 of culture, respectively. The integrated band intensity ratios for DNA, phenylalanine and amide-I show very little variation for all media. However, the proline band at 1045 cm^{-1} showed a large variation for different osteogenic and non-osteogenic culture media. Figure 2(a) shows high amounts of proline for cells grown in culture media containing PM and OM-cAMP. The proline content is quite similar for cells grown in BM, OM-BMP2 or OM-VitD3 but the proline content is less than in cells grown in PM and OM-cAMP. The proline content is minimal for cells grown in osteogenic media containing OM-Dex, OM-DB, OM-DC and OM-DV. At day 7 of the culture (Figure 2(b)), the pattern of variation in the proline content in iMSCs was similar but more pronounced as on day 3. The proline content increased twice for BM, PM and OM-BMP2, reduced to half for OM-cAMP and remained almost at the same level for OM-VitD3 compared to the proline content in cells on day 3 (Figure 2a). The band intensity ratio for proline further reduced and could hardly be discerned for iMSCs cultured in osteogenic media like OM-Dex, OM-DB, OM-DC and OM-DV on day 7 of culture.

Our data (Figure 2(a) and 2(b)) show that the proline content is markedly increased on day 3 and has further increased on day 7 of culture for iMSCs in BM medium. The BM medium supports a normal growth of cells as it does not contain any inductive or inhibitory factors that would influence the cells and we conclude that the proline that is observed in the cell is due to the normal cell growth process. The proline content for the iMSCs cultured in PM was twice that for BM for both day 3 and day 7 of the culture. This is due to the presence of bFGF in the PM medium, which stimulates cell replication.[37] Cells cultured in OM-Dex showed almost no proline present on day 7. This is due to the presence of dexamethasone in the culture media, which is known to have an inhibitory effect on collagen synthesis by cells during early stages of cell differentiation.[24, 38, 39] iMSCs cultured in osteogenic medium OM-BMP2 showed similar amounts of proline as cells cultured in BM both on day 3 and day 7 of the culture. This is attributed to the fact that BMP2 in OM-BMP2 does not lead to a response in cultured human mesenchymal cells.[40] Hence, the presence of proline in cells cultured in OM-BMP2 is a result of the natural level of proline synthesis. The osteogenic medium OM-cAMP initially showed an increase in proline content on day 3 of culture due to the presence of low levels of cAMP in the medium, which stimulated collagen synthesis. It has been reported[41] that an increase in intracellular cAMP concentration reduced the proline synthesis. We observe a similar feature on day 7 of culture when the accumulation of cAMP in the cells has increased over a period of time. The presence of cAMP reduced the collagen synthesis. The presence of proline in cells cultured in osteogenic medium OM-VitD3 on day 7 showed no significant variation compared to that on day 3. Vit-D3 is known to selectively stimulate synthesis of collagen type I, which in turn leads to a partial differentiation of the iMSCs towards the osteoblasts lineage.[42] Combinations of osteogenic media such as OM-DB, OM-DC and OM-DV which share, respectively, Dex and BMP2, Dex and cAMP, and Dex and Vit-D3, show a decrease in proline content on day 7 of culture compared to that observed on day 3. This decrease in proline content is mainly influenced by Dex in all of the three combinations of inductants, although in OM-DC, cAMP also plays a role in suppressing proline synthesis. All media containing dexamethasone show the effect of this compound on the level of proline, which is due to its role in the incorporation of proline into collagenous and non-collagenous proteins.[25] Another function of dexamethasone is to stimulate cells towards osteogenesis.[43] The observations are all based on univariate data analysis. In the next section, multivariate data analysis on the same spectra from 16 cells from each of the 9 media will be shown to give an even clearer distinction involving more complete spectral information.

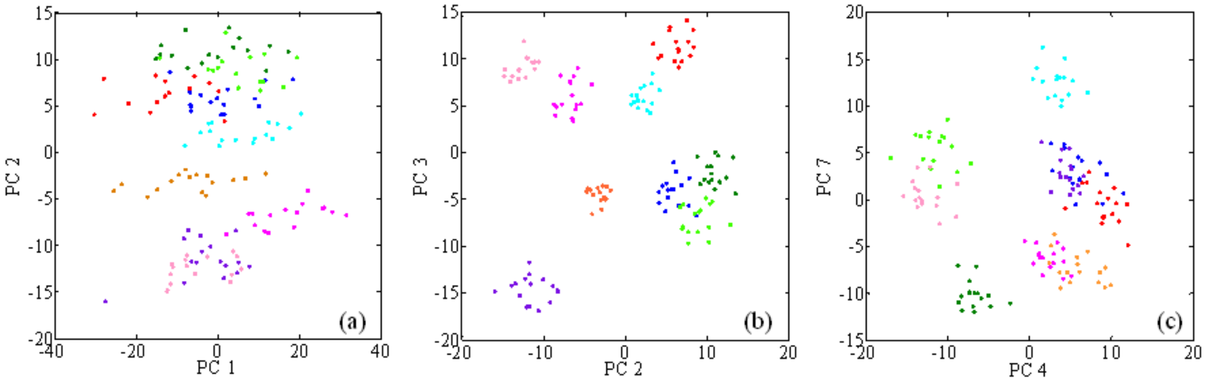

Figure 3: Multivariate data analysis showing principal component analysis score plots of the spectral information acquired on day 3 of culture from iMSCs cultured in various non-osteogenic and osteogenic culture media conditions. (a) PC1 'vs' PC2, (b) PC2 'vs' PC3 and (C) PC4 'vs' PC7. Each score plot shows grouping of spectral information based on the culture media BM (red), PM (dark green), OM-Dex (dark blue), OM-BMP (light blue), OM-cMAP (orange), OM-VitD (light green), OM-DB (violet), OM-DC (Magneta) and OM-DV (pink).

Principal component analysis (PCA) and hierarchical cluster analysis (HCA) were applied to the dataset. Figure 3 shows the principal component analysis of the 9 times 16 spectra of individual iMSCs acquired on day 3 of culture. The PCA procedure assigns scores to reveal subsequent levels of variation, where it must be understood that the first PCA component level reflects the highest amount of variation and next levels contain increasingly lower amounts of variation. Each spectrum in the original dataset acquires a 'score' with respect to each level of variation. The scores obtained from the PCA are plotted against each other, such as PC1 'vs' PC2, PC2 'vs' PC3 and PC4 'vs' PC7, as shown in Figure 3(a), 3(b) and 3(c) respectively. Each 'dot' in the graphs reflects the position of a measured spectrum in the 2-dimensional bases of the selected PC-components. It can be directly observed from Figure 3(a), 3(b) and 3(c) that the score plots gives rise to a clustering of the spectral information along the various osteogenic and non-osteogenic culture media conditions BM (red), PM (dark green), OM-Dex (dark blue), OM-BMP2 (light blue), OM-cMAP (orange), OM-VitD3 (light green), OM-DB (violet), OM-DC (Magneta) and OM-DV (pink). Score plot PC1 'vs' PC2 in Figure 3(a) shows mainly variation along the PC2 axis. Along this axis iMSCs, which are cultured in combinations of osteogenic differentiation media OM-DB (violet), OM-DC (Magneta) and OM-DV (pink), are grouped together. This similarity in Raman spectra of cells cultured in combinations of osteogenic media supports the univariate data analysis (Figure 2(a)), where it was shown that iMSCs cultured in OM-DB, OM-DC and OM-DV have lower amounts of proline. The data along PC1 (Figure 3(a)) shows significant variation in the scores in contrast to the narrow distribution along the PC2 axis for each culture condition. This is further exemplified by Figure 3(b) and Figure 3(c). Figure 3(b) shows the score plot for PC2 'vs' PC3. In the 2-dimensional space set up by these principal components, the separation along PC2 is strengthened by a further separation along PC3, rendering a clear clustering of cells according to culture medium. Each cluster shows successful grouping of all 16 iMSCs acquired from specific culture media. Clusters with a broader distribution, e.g. like the cluster for OM-DB (Violet), signifies a higher amount of variation among individual spectra in the cluster with respect to PC2 and PC3. This is unlike what can be observed for the cluster of 16 iMSCs cultured in OM-cAMP (orange), which has a narrow distribution along both PC2 and PC3 components. In Figure 3(b) it can be observed that the cells cultured in OM-Dex, OM-VitD and PM have close-lying clusters with partial overlap. The score plot of PC4 versus PC7 (Figure 3(c)) shows that the cells from these three media can be clearly separated in this two-dimensional space. The cluster for PM (dark green) is well separated from any other cluster, which must be related to the influence of bFGF in the PM culture medium. This corresponds to a higher proline content for PM as observed in Figure 2(a), which was based on univariate analysis. Furthermore, the score plot shows an overlap of those clusters, which correspond to osteogenic media OM-cAMP (orange), with OM-DC (magenta) and OM-VitD3 (light green) with OM-DV (pink) due to the influence of cAMP in the former and Vit-D3 in the latter. Clusters corresponding to the osteogenic media OM-DB (violet) and OM-Dex (dark blue) overlap with each other and the cluster corresponding to OM-BMP2 (light blue) has the same score along PC4. This signifies the influence of Dex in OM-DB and OM-Dex and of BMP2 in OM-BMP2 and OM-DB. PCA successfully illustrates that the intra-cluster variation was smaller than the inter-cluster variation, which was a result of the influence of the composition of the respective osteogenic and non-osteogeneic media on the iMSCs.

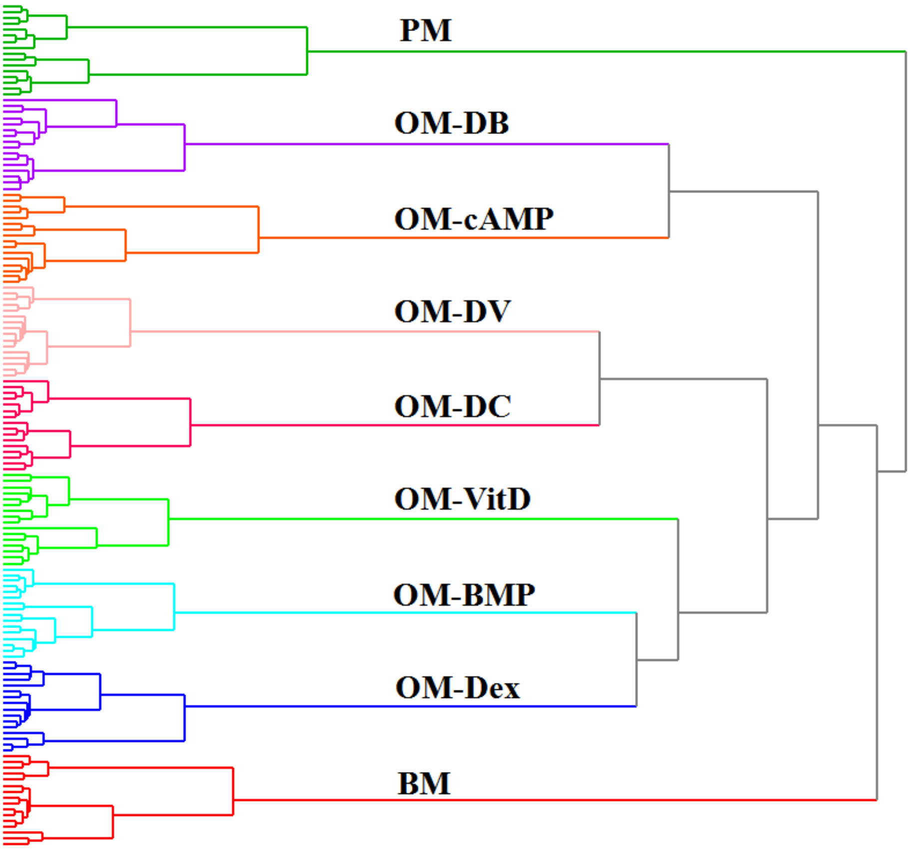

Figure 4. Multivariate data analysis showing hierarchical cluster analysis by Wards clustering method of the spectral information acquired on day 3 of culture from iMSCs cultured in various non-osteogenic and osteogenic culture media conditions. Sixteen randomly acquired spectra from nine different culture media conditions are clustered up to nine levels. The results show clustering of iMSCs cultured in specific media without being influenced by other culture media. Each cluster show grouping of spectral information based on the culture media BM (red), PM (dark green), OM-Dex (dark blue), OM-BMP (light blue), OM-cMAP (orange), OM-VitD (light green), OM-DB (violet), OM-DC (Magneta) and OM-DV (pink).

The HCA can be implanted with various possibilities for parameters. Wards clustering method based on Euclidian inter-point distances[44] was used. The influence of small variations in the baseline can be minimized by preprocessing the data with a first derivative Savitsky-Golay algorithm, which is implemented as a seven point smoothing and a quadratic polynomial fit. The data was further auto-scaled to the mean of the spectra along the frequency axis. The result of the hierarchical cluster analysis can be conveniently represented in a dendrogram (Figure 4), which shows the cluster linking of the 9 times 16 spectra from day 3 of culture. A result from the PCA can also be directly observed in the dendrogram, namely that the variance between the spectra obtained from cells in each medium is much smaller than the variance between spectra of cells in different media. Although Ward's algorithm is an agglomerative approach, it is more convenient to start from the right hand-side of the dendrogram. The first 9 clusters can then each be associated with each of the nine individual culture media. The colors in the dendrogram are related to the PCA components in Figure 3. The first three clusters resulted in grouping of spectra corresponding to PM (dark green), BM (red), and all osteogenic media. The first node separated the spectra corresponding to non-osteogenic medium PM. The second node grouped the spectra from the non-osteogenic medium BM. The PM- and BM- media are both non-osteogenic and cells cultured in these media have a characteristic contribution of proline as seen in Figure 2(a). The third cluster involved all spectra corresponding to osteogenic media. Further clustering showed distinct groups of spectra which correspond to various osteogenic media such as OM-VitD3 (light green), OM-cAMP (orange), OM-DB (Violet), OM-Dex (dark blue), OM-BMP (light blue), OM-DV (pink) and OM-DC (magenta) in the order of clustering. The third and fourth cluster showed grouping of cell spectra acquired from osteogenic media OM-VitD3 and OM-cAMP which again showed significant amounts of proline present in the cells as seen in Figure 2(a). Successive clustering to five, six and seven clusters separated iMSCs cultured in osteogenic media OM-DB, OM-Dex and OM-BMP2 respectively, which can be attributed to the influence of both Dex and BMP2 as seen in Figure 3(c). The eighth and ninth clusters grouped spectra acquired from iMSCs cultured in combinational osteogenic media OM-DV and OM-DC respectively, which showed the smallest levels of proline presence in the cells in accordance with univariate analysis in Figure 2(a). Culture of the cells in different media affects the cell differently, and is reflected in the scatter plot that clusters all cells from an individual medium together. The clustering revealed by HCA rationalizes biological effects that may be expected from the different culture media. The influence of the culture media on the cells is extensive as is indicated and also supported by the dendrogram showing much smaller intra-cluster variation than inter-cluster variation.[45, 46] The exact correlation of the clusters of the Raman spectra of cells with the medium in which they were cultured directly reflects the sensitivity of Raman microspectroscopy to distinguish subtle effects on cell development.

In order to acquire a spectral fingerprint of the differences we prepared a Raman difference spectrum from the results in Figure 2(a). The spectra of the cells cultured in the media BM, PM, OM-BMP2 and OM-VitD3 (group A) were averaged and the spectra from the media OM-Dex, OM-DB, OM-DC and OM-DV were averaged (group B). The spectra from each culture medium were autoscaled to the mean of the spectra for day3 and day 7 of culture, respectively. The resulting Raman difference spectra (group A – group B) on day 3 (black spectrum) and day 7 (red spectrum) of the culture are plotted over the spectral range from 500 - 1800 cm^{-1} and 2700 - 3100 cm^{-1} in Figure 5(a) and 5(b) respectively. The difference spectra show a variation of ~5% of the amplitude in the original spectra of group A and group B. The difference spectra in Figure 5(a) show positive contributions, which is most recognizable by a band at 1045 cm^{-1}, due to proline for both day 3 and day 7 of the culture. Group A has therefore a high proline content as a characteristic feature, while group B has a relatively low proline content. The proline band increases in intensity with culture period, Figure 2(a) and 2(b) respectively. Other bands in Figure 5(a) report an increase in prominent bands for amide-I (1658/1654 cm^{-1}) and amide-III (1315 and 1337 cm^{-1}) on day 7 of culture with respect to day 3 of culture. The high frequency region (Figure 5(b)) reflects an increased protein contribution as well, in agreement with the low frequency spectrum in Figure 5(a). The increase in protein bands in both Figure 5(a) and 5(b) may suggest the formation of collagenous proteins over the cells by day 7 of culture.[17, 18]

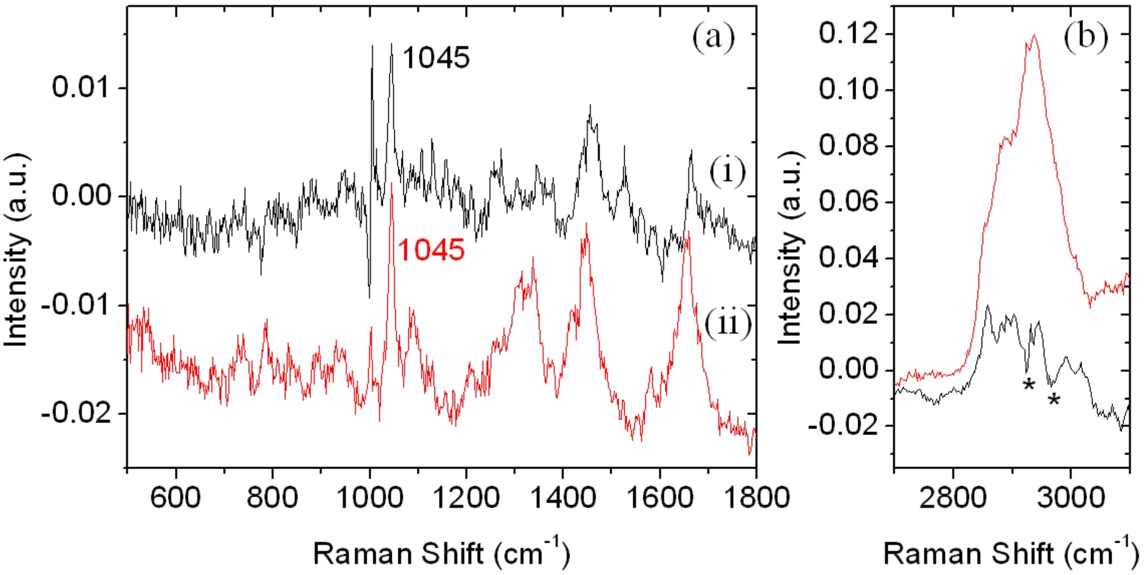

Figure 5. Raman difference spectroscopy for average spectra corresponding to group-A (BM, PM, OM-BMP, and OM-VitD) minus average spectra corresponding to group-B (OM-Dex, OM-DB, OM-DC and OM-DV); showing the influence of proline which is a collagen precursor over the culture period. The spectra are acquired from iMSCs cultured after (i) day 3 (black spectra) and (ii) day 7 (red spectra) of culture period shown in the spectral region (a) 500-1800 cm^{-1} and (b) 2700-3100 cm^{-1} respectively. The stars in Figure 5b indicate features due to residual etaloning of less than 0.5% from the original amplitude.

5.4 Conclusion

This study shows that proline is a biomarker for early differentiation of iMSCs into the osteoblast lineage. Dexamethasone in the osteogenic media OM-Dex, OM-DB, OM-DC and OM-DV induced a reduction in the level of proline with respect to the level in undifferentiated iMSCs. This biomarker was detected as early as on day 3 of culture, well before the cells had fully differentiated to synthesize collagen type-1. Univariate analysis illustrated that the main difference between cells grown in non-osteogenic culture media like BM and PM and cells grown in osteogenic culture media could be assigned to proline. The osteogenic media contained dexamethasone, which suppresses the synthesis of proline by the iMSCs. A progressive decrease of proline was observed on day 7 of culture in these osteogenic media. In the non-osteogenic media BM and PM, on the other hand, the amount of proline was increased on day 7 with respect to day 3.

Unsupervised PCA analysis showed that the Raman spectra of cells from a single medium reflected less variation than the Raman spectra from cells cultured in different media. HCA of the Raman spectra of the iMSCs cultured in various osteogenic and non-osteogenic media also show a clustering of spectra according to culture media. The results reflect the ability of Raman microspectroscopy to investigate the influence of culture media on cell proliferation and differentiation. The results from Raman difference spectroscopy, univariate and multivariate data analysis all reflect the understanding that the reduction in proline can be considered to be a biomarker.

References

1. Pittenger, M. F., Multilineage potential of adult human mesenchymal stem cells. *Science* **1999,** 285, (5428), 665.
2. Caplan, A. I.; Bruder, S. P., Mesenchymal stem cells: building blocks for molecular medicine in the 21st century. *Trends Mol Med* **2001,** 7, (6), 259-64.
3. Caplan, A. I., Adult mesenchymal stem cells for tissue engineering versus regenerative medicine. *J. Cell. Physiol.* **2007,** 213, (2), 341-347.
4. van de Lest, C. H. A.; Vaandrager, A. B., Mechanism of cell-mediated mineralization. *Curr. Opin. Orthop.* **2007,** 18, (5), 434-443.
5. Siddappa, R.; Licht, R.; van Blitterswijk, C.; de Boer, J., Donor variation and loss of multipotency during in vitro expansion of human mesenchymal stem cells for bone tissue engineering. *J. Orthop. Res.* **2007,** 25, (8), 1029-1041.
6. Siddappa, R.; Martens, A.; Doorn, J.; Leusink, A.; Olivo, C.; Licht, R.; van Rijn, L.; Gaspar, C.; Fodde, R.; Janssen, F.; van Blitterswijk, C.; de Boer, J., cAMP/PKA pathway activation in human mesenchymal stem cells in vitro results in robust bone formation in vivo. *Proc. Natl. Acad. Sci. U. S. A.* **2008**, (May 19 2008), 1-6, 6 pp.
7. Notingher, I.; Verrier, S.; Romanska, H.; Bishop, A. E.; Polak, J. M.; Hench, L. L., In situ characterization of living cells by Raman spectroscopy. *Spectroscopy* **2002,** 16, (2), 43-51.
8. Puppels, G. J.; De Mul, F. F. M.; Otto, C.; Greve, J.; Robert-Nicoud, M.; Arndt-Jovin, D. J.; Jovin, T. M., Studying single living cells and chromosomes by confocal Raman microspectroscopy. *Nature* **1990,** 347, (6290), 301-3.
9. Verrier, S.; Notingher, I.; Polak, J. M.; Hench, L. L., In situ monitoring of cell death using Raman microspectroscopy. *Biopolymers* **2004,** 74, (1-2), 157-62.
10. Uzunbajakava, N.; Lenferink, A.; Kraan, Y.; Volokhina, E.; Vrensen, G.; Greve, J.; Otto, C., Nonresonant confocal Raman imaging of DNA and protein distribution in apoptotic cells. *Biophys. J.* **2003,** 84, (6), 3968-3981.
11. Matthaus, C.; Boydston-White, S.; Miljkovic, M.; Romeo, M.; Diem, M., Raman and infrared microspectral imaging of mitotic cells. *Appl. Spectrosc.* **2006,** 60, (1), 1-8.
12. Short, K. W.; Carpenter, S.; Freyer, J. P.; Mourant, J. R., Raman spectroscopy detects biochemical changes due to proliferation in mammalian cell cultures. *Biophys. J.* **2005,** 88, (6), 4274-4288.
13. Notingher, I.; Jell, G.; Lohbauer, U.; Salih, V.; Hench, L. L., In situ non-invasive spectral discrimination between bone cell phenotypes used in tissue engineering. *J. Cell. Biochem.* **2004,** 92, (6), 1180-1192.
14. Matthaus, C.; Chernenko, T.; Newmark, J. A.; Warner, C. M.; Diem, M., Label-free detection of mitochondrial distribution in cells by nonresonant raman microspectroscopy. *Biophys. J.* **2007,** 93, (2), 668-673.
15. van Manen, H.-J.; Kraan, Y. M.; Roos, D.; Otto, C., Single-cell raman and fluorescence microscopy reveal the association of lipid bodies with phagosomes in leukocytes. *Proc. Natl. Acad. Sci. U. S. A.* **2005,** 102, (29), 10159-10164.
16. Boskey, A. L.; Roy, R., Cell Culture Systems for Studies of Bone and Tooth Mineralization. *Chem. Rev.* **2008,** 108, (11), 4716-4733.
17. Carden, A.; Morris, M. D., Application of vibrational spectroscopy to the study of mineralized tissues (review). *J. Biomed. Opt.* **2000,** 5, (3), 259-268.
18. Morris, M. D.; Finney, W. F., Recent developments in Raman and infrared spectroscopy and imaging of bone tissue. *Spectroscopy* **2004,** 18, (2), 155-159.
19. Notingher, I.; Bisson, I.; Bishop, A. E.; Randle, W. L.; Polak, J. M. P.; Hench, L. L., In situ spectral monitoring of mRNA translation in embryonic stem cells during differentiation in vitro. *Anal. Chem.* **2004,** 76, (11), 3185-3193.

20. Kim, B. S.; Lee, C. C. I.; Christensen, J. E.; Huser, T. R.; Chan, J. W.; Tarantal, A. F., Growth, Differentiation, and Biochemical Signatures of Rhesus Monkey Mesenchymal Stem Cells. *Stem Cells Dev.* **2008,** 17, (1), 185-198.
21. Krafft, C.; Salzer, R.; Seitz, S.; Ern, C.; Schieker, M., Differentiation of individual human mesenchymal stem cells probed by FTIR microscopic imaging. *Analyst* **2007,** 132, (7), 647-53.
22. Kale, S.; Biermann, S.; Edwards, C.; Tarnowski, C.; Morris, M.; Long, M. W., Three-dimensional cellular development is essential for ex vivo formation of human bone. *Nat Biotechnol* **2000,** 18, (9), 954-8.
23. Shen, T. F.; Strecker, H. J., Synthesis of proline and hydroxyproline in human lung (WI-38) fibroblasts. *Biochem J* **1975,** 150, (3), 453-61.
24. Advani, S.; Lafrancis, D.; Bogdanovic, E.; Taxel, P.; Raisz, L. G.; Kream, B. E., Dexamethasone suppresses in vivo levels of bone collagen synthesis in neonatal mice. *Bone* **1997,** 20, (1), 41-46.
25. Leitman, D. C.; Benson, S. C.; Johnson, L. K., Glucocorticoids stimulate collagen and noncollagen protein synthesis in cultured vascular smooth muscle cells. *J. Cell Biol.* **1984,** 98, (2), 541-9.
26. Counter, C. M.; Meyerson, M.; Eaton, E. N.; Ellisen, L. W.; Caddle, S. D.; Haber, D. A.; Weinberg, R. A., Telomerase activity is restored in human cells by ectopic expression of hTERT (hEST2), the catalytic subunit of telomerase. *Oncogene* **1998,** 16, (9), 1217-22.
27. Kinsella, T. M.; Nolan, G. P., Episomal vectors rapidly and stably produce high-titer recombinant retrovirus. *Hum. Gene Ther.* **1996,** 7, (12), 1405-1413.
28. Noordhuis, P., *Unpublished results, Manuscript in Preparation*
29. Pully, V. V.; Lenferink, A.; Otto, C., Hybrid Rayleigh, Raman and two-photon excited fluorescence spectral confocal microscopy of living cells. *J. Raman Spectrosc.* **2009,** 10.1002/jrs.2501.
30. Hayashi, H.; Nishimura, Y.; Katahira, M.; Tsuboi, M., The structure of nucleosome core particles as revealed by difference Raman spectroscopy. *Nucleic Acids Res* **1986,** 14, (6), 2583-96.
31. Hightower, K. R., The role of the lens epithelium in development of UV cataract. *Curr Eye Res* **1995,** 14, (1), 71-8.
32. Thomas, G. J., Jr.; Prescott, B.; Olins, D. E., Secondary structure of histones and DNA in chromatin. *Science* **1977,** 197, (4301), 385-8.
33. Tu, A. T., *Raman Spectroscopy in Biology: Principles and Applications*. 1982; p 448.
34. Walton, A. G.; Rippon, W. B.; Koenig, J. L., Raman spectroscopy of proline oligomers and poly-L-proline. *J. Amer. Chem. Soc.* **1970,** 92, (25), 7455-9.
35. Kumar, S.; Rai, A. K.; Singh, V. B.; Rai, S. B., Vibrational spectrum of glycine molecule. *Spectrochim. Acta, Part A* **2005,** 61A, (11-12), 2741-2746.
36. Deveney, M. J.; Walton, A. G.; Koenig, J. L., Raman spectra of imino acids and poly-L-hydroxyproline. *Biopolymers* **1971,** 10, (4), 615-30.
37. Canalis, E.; Centrella, M.; McCarthy, T., Effects of basic fibroblast growth factor on bone formation in vitro. *J Clin Invest* **1988,** 81, (5), 1572-7.
38. Kim, C. H.; Cheng, S. L.; Kim, G. S., Effects of dexamethasone on proliferation, activity, and cytokine secretion of normal human bone marrow stromal cells: possible mechanisms of glucocorticoid-induced bone loss. *J. Endocrinol.* **1999,** 162, (3), 371-379.
39. Oikarinen, A.; Vuorio, E.; Vuorio, T., Comparison of the effects of dexamethasone and 13-cis-retinoic acid on connective tissue biosynthesis in human skin fibroblasts. *Arch. Dermatol. Res.* **1989,** 281, (4), 273-8.
40. Diefenderfer, D. L.; Osyczka, A. M.; Reilly, G. C.; Leboy, P. S., BMP Responsiveness in Human Mesenchymal Stem Cells. *Connect. Tissue Res.* **2003,** 44, (Suppl. 1), 305-311.
41. Baum, B. J.; Moss, J.; Breul, S. D.; Berg, R. A.; Crystal, R. G., Effect of cyclic AMP on the intracellular degradation of newly synthesized collagen. *J. Biol. Chem.* **1980,** 255, (7), 2843-7.
42. Franceschi, R. T.; Romano, P. R.; Park, K. Y., Regulation of type I collagen synthesis by 1,25-dihydroxyvitamin D3 in human osteosarcoma cells. *J. Biol. Chem.* **1988,** 263, (35), 18938-45.

43. Ogston, N.; Harrison, A. J.; Cheung, H. F. J.; Ashton, B. A.; Hampson, G., Dexamethasone and retinoic acid differentially regulate growth and differentiation in an immortalised human clonal bone marrow stromal cell line with osteoblastic characteristics. *Steroids* **2002,** 67, (11), 895-906.
44. Hervada-Sala, C.; Jarauta-Bragulat, E., A program to perform Ward’s clustering method on several regionalized variables. *Comput Geosci.* **2004**, (30), 881-886.
45. Maquelin, K.; Choo-Smith, L.-P. i.; Van Vreeswijk, T.; Endtz, H. P.; Smith, B.; Bennett, R.; Bruining, H. A.; Puppels, G. J., Raman Spectroscopic Method for Identification of Clinically Relevant Microorganisms Growing on Solid Culture Medium. *Anal. Chem.* **2000,** 72, (1), 12-19.
46. Nijssen, A.; Bakker Schut, T. C.; Heule, F.; Caspers, P. J.; Hayes, D. P.; Neumann, M. H. A.; Puppels, G. J., Discriminating basal cell carcinoma from its surrounding tissue by Raman spectroscopy. *J. Invest. Dermatol.* **2002,** 119, (1), 64-69.

Chapter 6

Raman biomarkers for pluripotent stromal cells

Adult human bone marrow derived stromal cells are known for their stemness, and ability to differentiate towards various pluripotent mesenchymal lineages such as bone, cartilage, muscle, neurons, or hepatic tissue. We report the non-invasive and label-free monitoring by Raman microspectroscopy of unique biomarkers that characterize differentiation of in vitro cultured human immortalized bone marrow stromal cells (iMSCs) in a range of cell culture media over a time period of up to 35 days. These media provide specific physical and chemical cues that induce proliferation and differentiation of iMSCs towards adipogenic and osteogenic lineages. Distinct biomarkers for pre-osteoblast, osteoblast, osteocyte and various stages of mineralization were established. Intense lipid signals serve as a Raman biomarker for the adipogenic lineage. The presence of cell-derived glycogen resulted in Raman biomarker bands for the osteogenic lineage. Within this lineage pre-osteoblasts, osteoblasts and osteocytes were typified by respectively low intensity Raman bands of glycogen, high intensity Raman bands of glycogen and low intensity Raman bands of glycogen co-occurring with bands due to mineral depositions. Prominent bands for phosphates and carbonates are functional biomarkers for osteogenic mineralization. The lineage progression of the cells could be determined with confocal Raman microscopy measurements at regular time intervals from early till late stages of differentiation. The Raman biomarkers that define pluripotency of iMSCs could be identified early during culture, and were followed in time by measuring cells on days 3, 7 and 21 of culture. These data were in agreement with the Raman results obtained on day 35 of culture, when respective biomarkers were well expressed. Changes in pH, potentiated by the synthesis *of glycogen, caused variation in mineralization of the iMSCs. A neutral pH gave rise to Raman spectroscopic fingerprints of hydroxyapatite, while an acidic pH resulted in the formation of calcium oxalates. Raman imaging of mineralized nodules reveals a high degree of spatial heterogeneity that suggests that chemical transformations of mineral components occur in nodules.*

Manuscript in preparation

6.1 Introduction

Adult human tissues have pluripotent stem cells that have a remarkable capability for self-renewal after trauma, disease or ageing.[1] Adult human bone marrow contains heterogeneous populations of stem cells such as hematopoietic stem cells and marrow stromal stem cells.[2] These marrow stromal cells, or mesenchymal stem cells, can be differentiated to various mesenchymal tissue lineages such as bone, muscle, cartilage, fat, or tendon in response to specific culture conditions.[3]

These stem cells play an important role as a potential source for bone, cartilage, cardiovascular, and many other tissue replacements.[2, 3] The details of the adult stem cell differentiation towards various lineages has been extensively reviewed.[1-4] Adult human mesenchymal stem cells derived from bone can be differentiated towards multiple lineages, including osteogenic, adipogenic, chondrogenic, or myogenic lineages. The multi-lineage potential of these so-called progenitor stem cells enables their application in tissue engineering, molecular medicine, regenerative medicine and stem cell therapy.[3, 4] Identifying quantifiable biomarkers that characterize the lineage and development of cells during differentiation is an essential element of understanding pluripotency at early stages.

Conventional staining procedures with dyes, fluorescent labels and antibodies have been extensively used to identify the lineages during differentiation of the stem cells.[1] Recently reverse transcriptase-polymerase chain reaction (RT-PCR),[1] flow cytometric analysis,[1] electron microscopy,[5] X-ray diffraction (XRD),[6] nuclear magnetic resonance (NMR) spectroscopy,[7] and Fourier transform infrared spectroscopy (FTIR)[8] techniques have been used to study the process of proliferation and differentiation of stem cells. Here we identify specific spectroscopic signatures that enable sensitive, non-invasive definition of the lineage of differentiated stromal cells using confocal Raman microscopy.

Confocal Raman microspectroscopy is a non-invasive, label-free optical method for analysis of the chemical constituents in sub-femtoliter measurement volumes. Raman microspectroscopy can be performed on living cells and combines a high spatial resolution of ~0.35 μm at an excitation wavelength of 647.1nm with high spectral resolution to observe small frequency shifts and band shapes.

Raman microscopy was first successfully demonstrated[9] in applications to cells and chromosomes, and has since then been widely used.[9-17] The differentiation of embryonic stem cells with respect to variation in mRNA and DNA with culture period was reported by Notingher et. al.[18] Krafft et. al.[19] used FTIR spectroscopy to monitor osteogenic differentiation of human mesenchymal stem cells. Recently Chiang et. al.[20] used Raman microspectroscopy to study the differentiation and mineralization of human mesenchymal stem cells. Raman spectroscopy was also successfully applied to determine the proliferation of mammalian cells,[14] differentiation stage[12] and heterogeneity[21] in the stem cell population. However, Raman spectroscopy has not yet been applied to study stem cell pluripotency towards various lineages.

We cultured iMSCs in non-osteogenic and seven different osteogenic culture media for up to 35 days. The proliferation and differentiation of iMSCs influenced by different culture media were monitored by confocal Raman microspectroscopy after day 0, 3, 7, 21 and 35. By day 35 of culture, iMSCs differentiated towards adipogenic lineage and osteogenic lineage with and without mineralization. Osteogenic lineage was identified by the presence of glycogen and hydroxyapatite (HA), and adipogenic lineage showed an increased distribution of lipid droplets. Multivariate analyses using principal component (PCA) and hierarchical cluster analysis (HCA) of the Raman data illustrate the onset and progress of differentiation of iMSCs. HA mineralization in iMSCs cultured in different osteogenic media for the same time periods showed significant variations in mineral composition. The influence of specific components in some osteogenic media led to the formation of calcium oxalates (CaO) in the cultured iMSCs; medium composition clearly influences the relative amounts of HA or CaO after 35 days in culture.

6.2 Materials and Methods

Cell culture

iMSCs (as described in chapter 5 of this thesis) were seeded on multiple UV grade calcium fluoride substrates (CaF_2) (Crystran Ltd., UK) at cell densities of 1000 cells/cm^2. The seeded iMSCs were cultured in parallel in different osteogenic and non-osteogenic cell culture media in separate Petri dishes. Non-osteogenic cell culture basic medium (BM), which served as the control condition, was prepared from α-MEM (GIBCO, Carlsbad, CA), 10% fetal bovine serum (FBS; Bio Whittaker, Australia), 0.2 mM L-ascorbic acid-2-phosphate (AsAP; Sigma, St. Louis, MO), 100 U/mL Pencillin G (Invitrogen, Carlsbad, CA); 100 µg/mL Streptomycin (Invitrogen) and 2 mM L-Glutamine (L-Glu; Sigma). Different combinations of osteogenic media (OM) were prepared by adding 0.01 M β-Glycerophosphate (βGP; Sigma) and different osteogenic growth factors either individually or in combination to BM. Normal osteogenic media were prepared after separately adding osteogenic growth factors like 10^{-8} M dexamethasone (Dex, Sigma) (OM-Dex), 100 ng/ml Recombinant human bone morphogenetic protein-2 (rhBMP2, Hangzhou Biodoor

Biotechnology co., LTD, China) (OM-BMP2), 1 mM cyclic 3,5adenosine-monophosphate (cAMP, Sigma) (OM-cAMP) and 10^{-8} M 1α, 25-Dihydroxyvitamin D3 (Vit-D3, Sigma) (OM-VitD3). Combined osteogenic media OM-DB, OM-DC and OM-DV were prepared by adding the osteogenic growth factor dexamethasone to osteogenic media OM-BMP2, OM-cAMP and OM-VitD3 respectively.

iMSCs were cultured in BM overnight (day 0) on multiple CaF_2 substrates to enable cells to adhere on these substrates. Cells adhered on CaF_2 substrates were then cultured in parallel in non-osteogenic medium BM and different osteogenic media like OM-Dex, OM-BMP2, OM-cAMP, OM-VitD3, OM-DB, OM-DC and OM-DV up to day 35 of culture. Cell cultures were stopped by day 35 when iMSCs showed significant differentiation towards respective lineage. Throughout the culture, cells on multiple CaF_2 substrates were maintained at 37ºC, 95% humidity and 5% partial pressure of CO_2 to enable cell growth and proliferation. Confocal Raman measurements on living cells were performed after day 0, 3, 7, 21 and 35 of culture. On each measurement day, set of CaF_2 substrates with cell cultures were washed three times with phosphate buffered saline solution (PBS; Gibco) before being transferred to the confocal Raman microspectroscope for measurements.

Confocal Raman microspectroscopy

A custom-built confocal Raman microspectroscope[22] was used to perform measurements on living cells. A Krypton ion laser (Coherent, Innova 90K, Santa Clara, CA) emitting at 647.1 nm was used as an excitation source. The microscope in epi-illumination detection mode used a water immersion objective with 63× magnification and 1.2 NA (Zeiss Plan Neofluar, Carl Zeiss, Thornwood, NY) to focus laser light on the sample of interest and also to collect the Raman scattered photons from the sample. The scattered photons from the sample were then focused on to a confocal pinhole placed in front of custom-designed spectrograph. The spectrograph disperses the Raman scattered photons on an air-cooled EMCCD camera (Newton DU-970N, Andor Technology, Belfast, Northern Ireland) which provided a spectral resolution of 1.85 to 2.85 cm^{-1}/pixel over a wavenumber range -20 to 3670 cm^{-1}.

Raman measurements were acquired in either "*spectral scanning mode*" or "*Raman imaging mode*" from living cells on each measurement day. In *spectral scanning mode*, a single full spectrum is obtained by raster scanning the laser beam over the sample area of 22.5 μm × 22.5 μm with an accumulation time of 10s. Raman spectra were acquired from 16 randomly chosen cells in each culture medium for day 0, 3, 7, 21, and 35 of culture. In

Raman imaging mode, images were obtained by collecting complete spectral information at each step throughout the raster scan caused by the displacement of a scanning mirror (Leica Laser technique, GmbH, Heidelberg, Germany) over the image area. Raman imaging were performed over an area of 22.5 µm × 22.5 µm with a step size resolution of 350 nm and an accumulation time of 100 ms per step. Laser excitation powers of 75 mW were used in all our measurements.

Raman data analysis

For each measurement day, the spectral information acquired from cells grown in non-osteogenic and different osteogenic culture media were preprocessed by 1) removal of cosmic ray events, 2) subtraction of the camera offset, 3) calibration of the wave number axis, and 4) correction of frequency dependent transmission. The well-known band-positions of toluene were used to relate wavenumbers to pixels. The frequency-dependent optical detection efficiency of the setup is corrected using a tungsten halogen light source (Avalight-HAL; Avantes BV, Eerbeek, The Netherlands) with a known emission spectrum. The detector-induced etaloning effect was also compensated for by this procedure.

Raman spectra acquired from 16 randomly chosen iMSCs for each medium were separately averaged. The average Raman spectra were further normalized to their respective means along the frequency axis of the spectra. Raman difference spectroscopy (RDS) was achieved by subtracting the average Raman spectrum of iMSCs grown in non-osteogenic medium from the average spectra of iMSCs grown in the different osteogenic media after day 35 of culture. RDS shows the influence of the osteogenic growth factors in different osteogenic media on the iMSCs.

The data acquired were analyzed by both univariate and multivariate data analysis procedures. Univariate Raman analysis for individual spectra or images of the specific vibrational band of interest as a function of position was constructed by integrating the band intensities after baseline subtraction. In multivariate analysis, both hierarchical cluster analysis (HCA) and principal component analysis (PCA) were performed to visualize regions with high spectral similarities. In PCA, 16 randomly acquired individual cell spectra from non-osteogenic BM after day 0 of culture period and from osteogenic culture media OM-Dex, OM-BMP2 and OM-DC after days 3, 7 and 21 were compared. The scores resulting from PCA were used for making score plots based on the contribution of the particular score.

The spectra were preprocessed by subtracting background spectra from PBS buffer solution acquired on the respective measurement days at the same height in the sample adjacent to the cell. The preprocessing served to remove the influence of background corresponding to CaF_2 and PBS solution, and fluorescence effects, and did not contribute to variance in the dataset. A Savitsky-Golay filtering with seven point smoothing and second order polynomial fitting after first order derivative was performed which was then auto-scaled to mean zero unit variances of the spectra. HCA makes use of the scores obtained from the PCA data.

All data manipulations were performed with routines written in MATLAB 7.4 (The Math Works Inc., Natick, MA). HCA and PCA were performed using PLS toolbox (Eigenvectors Research Inc., Wenatchee, WA) in MATLAB 7.4.

6.3 Results and discussion

iMSCs were successfully cultured for 35 days in non-osteogenic and different osteogenic media. The iMSCs showed normal growth and proliferation during initial stages in different culture media. Further culture of iMSCs in respective osteogenic culture media up to day 35 showed significant differentiation of the iMSCs towards specific lineages based on the growth factors added to the osteogenic culture media. Non-osteogenic medium BM, which acted as a control, showed normal growth and proliferation until day 35 of the culture.

The differentiation of the iMSCs was chemically imaged over time by confocal Raman microspectroscopy on cells grown until day 0, 3, 7, 21 and 35 of culture in non-osteogenic and different osteogenic culture media. Figure 1(a) shows average Raman spectra over the spectral range 400-1800 cm^{-1} obtained from iMSCs cultured separately in different culture media up to day 35 of culture. The spectra corresponding to non-osteogenic media BM (Figure 1(a)(i)) has many bands that are well described in the literature.[23-29] The spectra from osteogenic media OM-cAMP, OM-VitD3, OM-DB and OM-DV in Figure 1(a) (iv), (v), (vi) and (viii) respectively show small spectral band variations compared to non-osteogenic media BM. Spectra corresponding to osteogenic media such as OM-Dex, OM-DB and OM-DC in Figure 1(a)(ii), (iii) and (vii) respectively show significant variations, which are not apparent from the spectra of other osteogenic culture media. These spectral variations from iMSCs are due to the biochemical influence of the specific growth factors added to the osteogenic media. The non-osteogenic BM has no osteogenic differentiation growth factors that could influence the biochemical composition in the cells. The average Raman spectrum acquired from the iMSCs cultured in non-osteogenic media BM (day 35) is thus taken as a control.

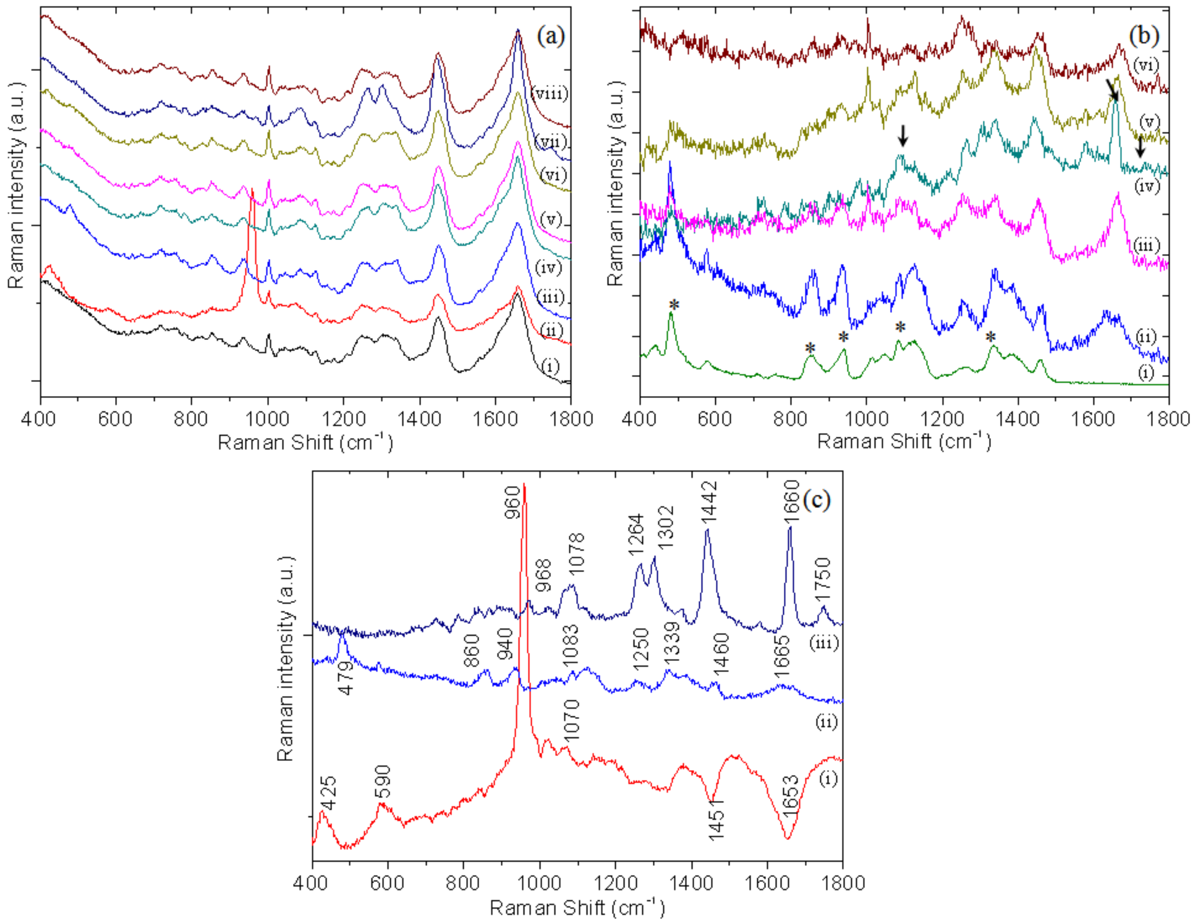

Figure 1: Confocal Raman spectroscopy of iMSCs cultured in different osteogenic and non-osteogenic culture media. (a) Average Raman spectra after normalization for (i) BM, (ii) OM-Dex, (iii) OM-BMP2, (iv) OM-cAMP, (v) OM-VitD3 (vi) OM-DB,(vii) OM-DC and (viii) OM-DV. Spectra are offset for ease of visualization. (b) Raman difference spectroscopy showing influence of osteogenic factors on iMSCs in formation of glycogen after day 35 of culture period. (i) Raman spectra of commercially available Glycogen powder. (ii) RDS spectrum of iMSCs grown in OM-BMP2 indicating extensive glycogen formation. (iii) RDS spectrum of cells grown in OM-VitD3, showing lower glycogen formation compared to (ii). (iv) RDS spectrum of cells grown in OM-cAMP showing limited glycogen formation and significant lipid bands. (v) RDS spectrum of cells grown in OM-DB showing limited glycogen compared to (ii), attributed to influence of Dexamethasone. (vi) RDS spectrum of cells grown in OM-DV showing reduction in glycogen formation compared to (iii), attributed to influence of Dexamethasone. (c) RDS data acquired from average spectra of 16 iMSCs cultured in (i) OM-Dex showing prominent bands for phosphates signifying osteogenic mineralization, (ii) OM-BMP showing bands for glycogen which signifies osteoblast, (iii) OM-DC showing bands for lipids signifying adipogenesis.

RDS was performed as described above to understand the influence of osteogenic growth factors like Dex (glucocorticoids), BMP2 (matrix proteins), cAMP (cyclic nucleotides) and Vit-D3 (secosteroid) on the iMSCs cultured in the respective osteogenic media. RDS spectra in Figure 1(b) and 1(c) show the influence of the growth factors on the iMSCs cultured in different osteogenic media until day 35 of culture. Figure 1(b)(ii) to (vi) show the Raman difference spectra for cells grown in the osteogenic media OM-BMP2, OM-VitD3, OM-cAMP, OM-DB and OM-DV respectively. The Raman difference spectrum in Figure 1(b)(ii) shows prominent bands at 479, 860, 940, 1083, 1250, 1339, 1460 and 1665 cm^{-1} and corresponds well to glycogen[23] as confirmed by the spectrum of pure glycogen powder shown in Figure 1(b)(i). The prominent presence of glycogen in the iMSCs cultured in OM-BMP2 indicates their differentiation towards osteogenic lineage where the cells are in osteoblast/preosteoblast phase.[30] However, the role of BMP2 in the process of mineralization is shown to be negative on human cells.[31] The Raman difference spectrum in Figure 1(b)(iii) shows the influence of Vit-D3 on iMSCs. The Vit-D3 in the osteogenic medium resulted in increase of osteocalcin, a non-collagenous protein present in the osteoblast differentiated cells,[32] and is supported by the prominent bands for proteins at 1003, 1250, 1451 and 1665 cm^{-1} in addition to significant bands for the presence of glycogen. The univariate spectral analysis for the band at 479 cm^{-1} signifying glycogen showed an 85% drop in the iMSCs cultured in OM-VitD3 compared to the iMSCs cultured in OM-BMP2. The Raman difference spectrum in Figure 1(b)(iv) shows the influence of cAMP on iMSCs, and displays prominent bands for lipids (black arrows) at 1267, 1442, 1660 and 1736 cm^{-1} signifying the differentiation towards adiopogenic lineage.[33] The univariate spectral analysis of the glycogen band at 479 cm^{-1} show a drop of 70% in glycogen formation in iMSCs cultured in OM-cAMP compared to OM-BMP2. The addition of Dex in combined osteogenic media such as OM-DB and OM-DV showed lower glycogen formation in iMSCs cultured in these media, as demonstrated by the RDS spectra in Figure 1(b)(v) and (vi) for OM-DB and OM-DV respectively. Univariate spectral analysis of the band at 479 cm^{-1} indicate a drop in glycogen formation by 60% and 85% in the iMSCs cultured in OM-DB and OM-DV respectively when compared with iMSCs cultured in OM-BMP2 and OM-VitD3. This observation confirms that the contribution of glycogen formation in iMSCs cultured in OM-DB and OM-DV is due to BMP2 and VitD3 respectively. The presence of glycogen in the cells is an indication of differentiation of iMSCs towards osteoblasts.[30] Figure 1(b) shows varying amounts of glycogen in the cells cultured up to day 35 in different osteogenic media, indicating that the variation in osteogenic differentiation of the iMSCs is influenced by the growth factors present in respective osteogenic media.

Figure 1(c) highlights osteogenic media that showed particularly significant variations in the RDS spectra. Figure 1(c)(i) shows the RDS spectrum for cells cultured in OM-Dex, and exhibits prominent bands for phosphates at 425, 590, 960 and 1032 cm^{-1} signifying extracellular mineralization of iMSCs that is chemically similar to hydroxyapatite.[28] Negative bands at 1451 and 1653 cm^{-1} indicate that the intracellular protein content is higher in the iMSCs cultured in non-osteogenic BM medium. The RDS spectrum in Figure 1(c)(ii) for cells grown in OM-BMP2 shows prominent bands signifying the formation of glycogen.[23] The RDS spectrum in Figure 1(c) (iii) shows significant bands for lipids[34] at 968, 1078, 1264, 1302, 1442, 1660 and 1750 cm^{-1} pointing to adipogenic differentiation due to the combined influence of Dex and cAMP in osteogenic media OM-DC. OM-DC is known to influence osteogenic mineralization,[35] wherein mineralization is assisted by the lipids in the adipocyte differentiated iMSCs.[36] Finally, we observe that the influence of OM-DC in differentiating the iMSCs towards adipogenic lineage was significantly higher compared to OM-cAMP.

The amount of glycogen formed in the cells determines the level of osteogenic differentiation and is characteristic of the various stages in the osteogenic cycle[30] The iMSCs cultured in OM-BMP2 showed comparatively higher amounts of glycogen than cells cultured in OM-cAMP and OM-VitD3, signifying the osteoblast differentiated stage. Day 35 culture of iMSCs in OM-VitD3 suggest that the cells are in the early pre-osteoblast stage, while for iMSCs cultured in OM-cAMP, the cells appear to be in the early adipogenic stage. Dex in OM-Dex influences extensive osteogenic mineralization, due to which there is hardly any glycogen formation.[30] Combined osteogenic media such as OM-DB and OM-DV show lower glycogen formation due to the presence of Dex in the media. The data suggest that the influence of Dex in OM-Dex results in differentiation of iMSCs towards osteocytes (post-osteoblast stage), which have significantly less glycogen in the iMSCs[30] leading to HA mineralization. The influence of Dex in OM-DV resulted in mineralization of iMSCs. However, the influence of Vit-D3 that impacts bone nodule formation[37] leads to much less mineralization than in OM-Dex. The influence of OM-DC on iMSCs resulted in extensive formation of lipid droplets signifying adipogenesis, and no glycogen formation was detected in cells under the influence of this medium.

Figures 2(a), (b), (c) and (d) show the white light micrographs obtained after day 35 of culture from non-osteogenic medium BM, and the osteogenic media OM-Dex, OM-BMP2 and OM-DC respectively. Of all the culture media, iMSCs cultured in OM-Dex, OM-BMP2 and OM-DC showed significant morphological variations. Non-osteogenic BM resulted in normal growth and proliferation of iMSCs with elongated cell shapes as seen in Figure 2(a). OM-Dex medium resulted in osteogenic mineralization (white stars) in the extracellular matrix formed over osteoblasts differentiated iMSCs as seen in Figure 2(b). iMSCs cultured in OM-BMP resulted in a different morphology (Figure 2(c)), where the cells showed a flat shape compared to those cultured in BM (white circle). In OM-DC, the iMSCs formed large amounts of lipid droplets (Figure 2(d), white arrows), signifying differentiation towards adipogenic lineage.

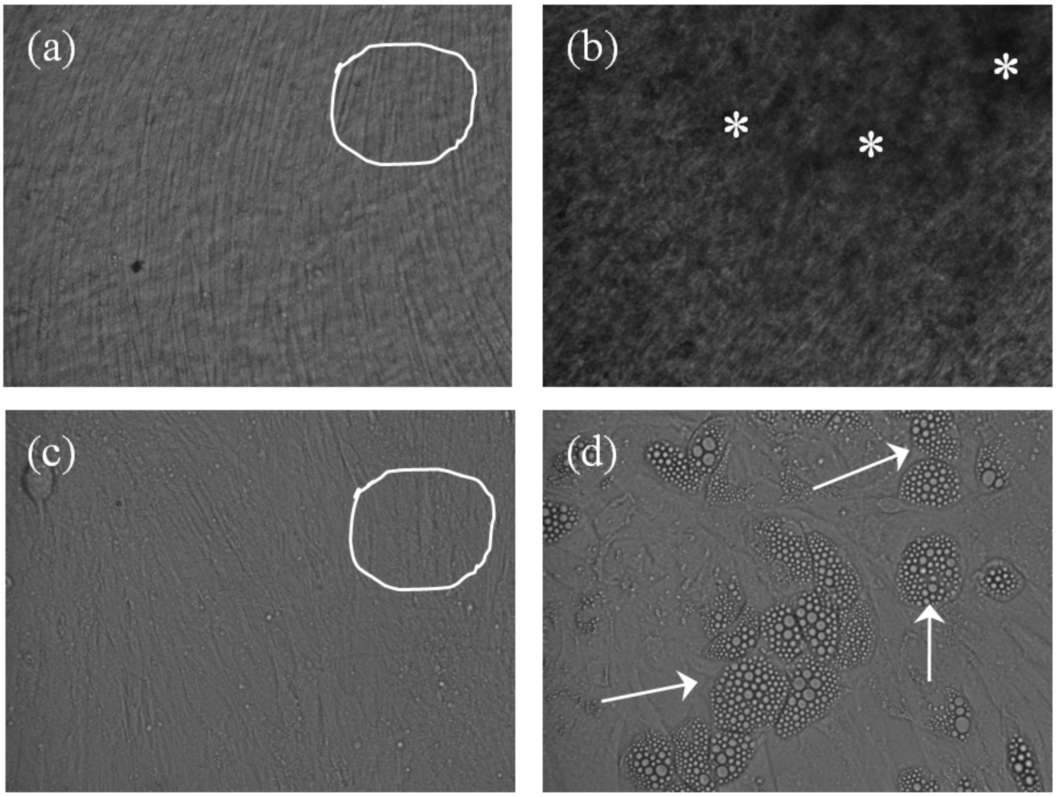

Figure 2: Influence of osteogenic and non-osteogenic media on iMSCs cultured until day 35 of culture period. (a) White light micrograph showing normal growth of iMSCs in BM, (b) White light micrograph of iMSCs showing mineralization (white stars) in iMSCs grown in OM-Dex, (c) White light micrograph of iMSCs cultured in OM-BMP2 showing different cell morphology compared to that seen in (a) (white circle), and (d) White light micrographs showing adipogenesis of iMSCs cultured in OM-DC (white arrows).

The RDS spectra in Figure 1(c) highlight spectral signatures of biomarkers signifying differentiated state of the iMSCs due to influence of osteogenic growth factors by 35 days in culture. PCA, which is a multivariate data analysis technique, shows variations (Figure 3) caused by the osteogenic growth factors in the iMSCs over a period of 21 days, much before the cells are fully differentiated after day 35 of culture. Figure 3 shows a score plot for PC1 against PC3 for the Raman spectral data acquired. Scores of PC1 show variation of the iMSCs with culture period and scores of PC3 show culture media induced variations in the iMSCs, and are plotted against each other. Each set of colored dots in the score plot uniquely correspond to 16 Raman spectra acquired from the respective culture media over the culture period. The score plot shows clear clustering, wherein non-osteogenic BM (day 0, black) and osteogenic cultured media such as OM-Dex (day 3, violet), OM-Dex (day 7, magenta), OM-Dex (day 21, red), OM-BMP2 (day 3, orange), OM-BMP2 (day 7, light green), OM-BMP2 (day 21, green), OM-DC (day 3, cyan), OM-DC (day 7, light blue) and OM-DC (day 21, dark blue) are clustered based on the contributions from PC1 and PC3.

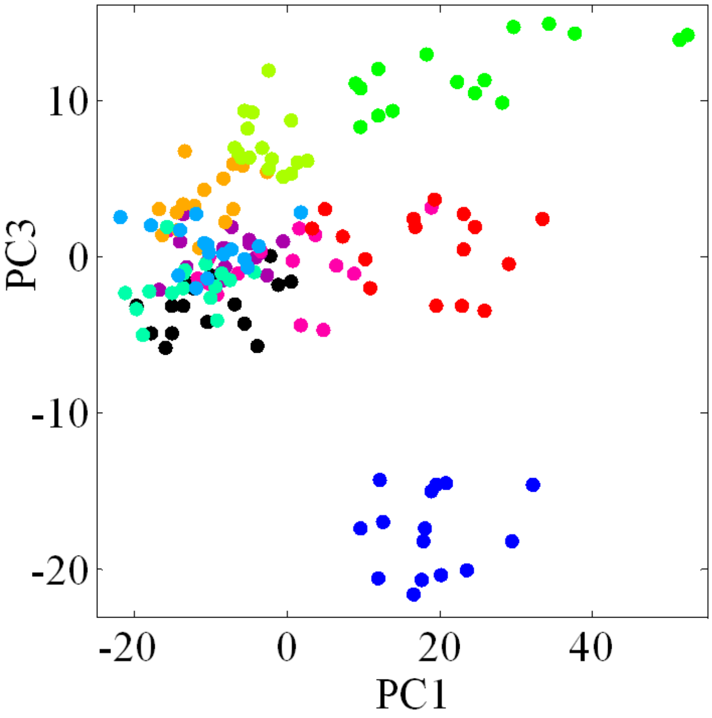

Figure 3: Multivariate data analysis showing PCA score plots of the spectral information acquired from iMSCs cultured in non-osteogenic medium BM until after day 0 (control) and for osteogenic media OM-Dex, OM-BMP2 and OM-DC until after days 3, 7, and 21 of culture. Each score plot shows grouping of spectral information based on osteogenic and non-osteogenic culture media BM (day 0) (black), OM-Dex (day 3, violet), OM-Dex (day 7, magenta), OM-Dex (day 21, red), OM-BMP2 (day 3, orange), OM-BMP2 (day 7, light green), OM-BMP2 (day 21, green), OM-DC (day 3, cyan), OM-DC (day 7, light blue), and OM-DC (day 21, dark blue). Score plot for PC1 against PC3 shows variation along both PC1 and PC3 components with respect to culture period and culture media respectively.

The score plot shows variations along both PC1 and PC3 components. The PC1 component showed progression with culture period that signified the undifferentiated stage (day 0) to the differentiated stage (day 21) of iMSCs. The PC3 component shows influence of culture media on the iMSCs. The score plot shows that cells cultured up to day 3 of culture in OM-Dex (violet), OM-BMP2 (orange) and OM-DC (cyan) are grouped together with BM (black). This low variation along the PC1 and PC3 axes indicates that these media have little influence on the iMSCs after day 3 of culture relative to the BM medium. By day 21, iMSCs cultured in these osteogenic media, OM-Dex (red), OM-BMP2 (green) and OM-DC (dark blue)), showed significant variation along both PC1 and PC3 axes with respect to BM (black). This large variation is indicative of the biochemical changes caused by respective media on the iMSCs. Day 7 culture of iMSCs in OM-Dex (magenta) and OM-BMP2 (light green) show an intermediate variation between days 3 and 21 of growth in the same media. On the other hand day 7 culture of OM-DC (light blue) is grouped along with BM (black) showing no significant variation compared to day 3 in the same medium. iMSCs cultured in OM-Dex and OM-BMP2 show gradual variation along PC1 and PC3 components over day 21 of culture. Although iMSCs cultured in OM-DC show no significant variation until day 7 of culture, by day 21 a huge variation is seen. Score plots for cells cultured in BM up to day 0, 3, 7, 21 and 35 show corresponding clusters grouped together signifying less inter cluster variation. By day 35, iMSCs cultured in OM-Dex and OM-BMP2 show osteogenesis with (HA) and without (glycogen) mineralization. iMSCs cultured in OM-DC resulted in adipogenic lineage with extensive distribution of lipid droplets by day 35 of culture. These results and the PCA analyses indicate that osteogenic differentiation is seen as a gradual process in time compared to adipogenic differentiation. The essential point is that the variations seen in the PC plots for different media illustrate the onset of differentiation well in advance of the fully-differentiated stages observed by day 35 of culture.

The PC3 component showed significant clustering with respect to culture media induced variations of the iMSCs. The clusters for measurements until day 3 for OM-Dex (violet), OM-BMP2 (orange) and OM-DC (cyan) were grouped along with clusters for overnight measurements in BM (black), showing that these osteogenic media induce little or no variations in the iMSCs until day 3 of culture. There is a large inter-cluster variation seen for iMSCs cultured until day 21 in OM-Dex (red), OM-BMP2 (green) and OM-DC (dark blue), which is attributed to the effect of the respective osteogenic factors on the iMSCs. This large inter-cluster variation after day 21 of culture shows the different lineages and differentiation stages to which the iMSCs are directed.

Human bone is a combination of both organic and inorganic phases. Collagen type-I forms approximately 90% of the organic phase and plays an important role in the process of mineralization to the inorganic phase. Collagen type-I has holes and pores composed of phospholipids and non-collagenous proteins. The role of collagen type-I and phospholipids in the mineralization of hydroxyapatite $Ca_{10}(PO_4)_6(OH)_2$ that is a close analogue to *in vivo* bone is well described in the literature.[38, 39]

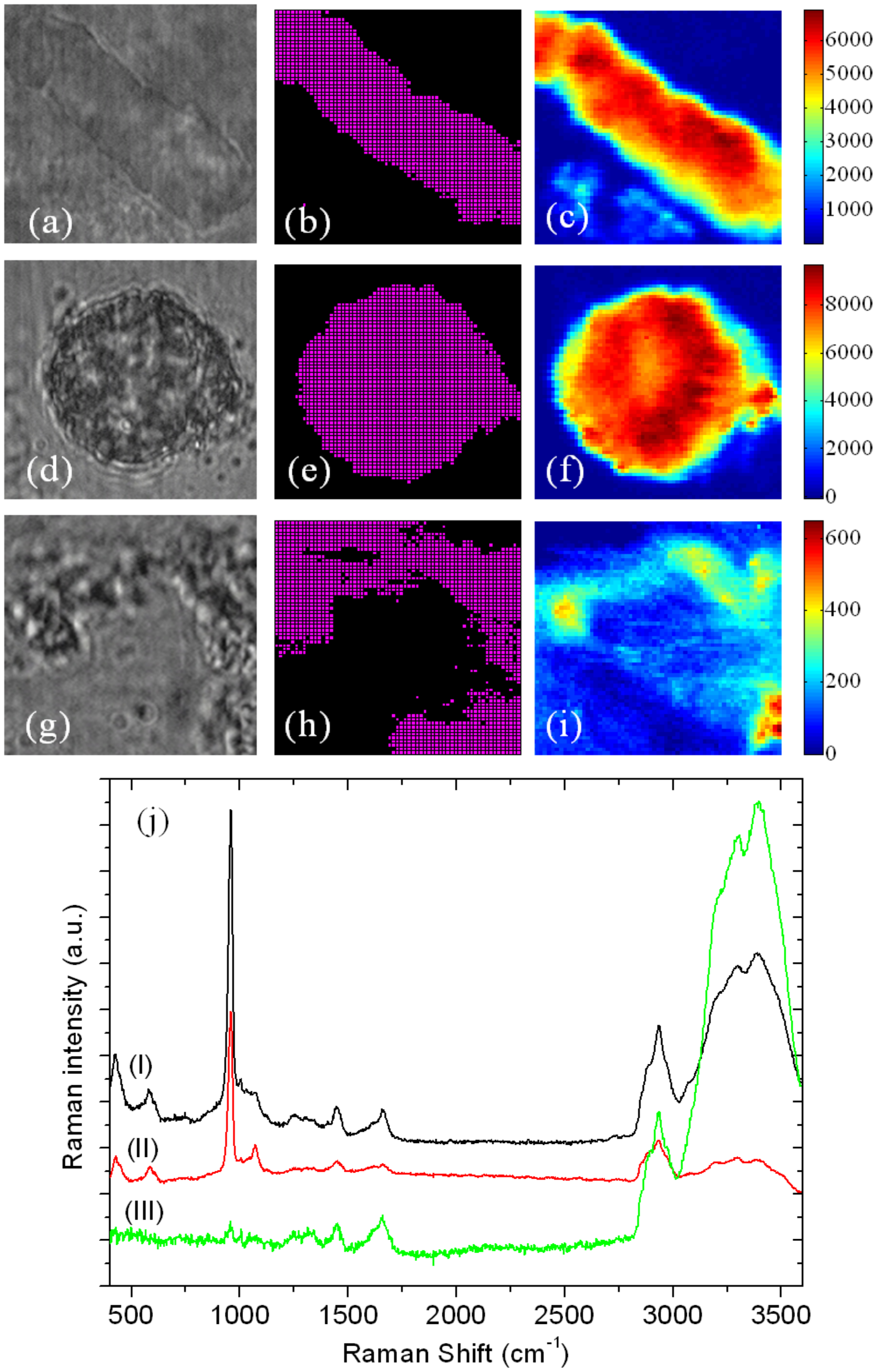

Figure 4: Influence of osteogenic media upon the formation of HA after day 35 of culture. (a) White light micrographs (22.5 µm × 22.5 µm) of HA formed in iMSCs cultured in (a) OM-Dex, (d) OM-DC, (g) OM-DV; Respective two level cluster image of the nodule seen in (b) OM-Dex, (e) OM-DC, (h) OM-DV; Raman band integration image for the band at 958 cm^{-1} (Δ=76 cm^{-1}) showing the distribution of HA formed in (c) OM-Dex, (f) OM-DC, (i) OM-DV; (j) Normalized average Raman spectra of all the pixels corresponding to HA formed in iMSCs (magenta pixels) cultured in (I) OM-Dex, (II) OM-DC and (III) OM-DV.

We show here mineralization of iMSCs cultured over a period of 35 days. Of all the osteogenic media, we observed mineralization of iMSCs cultured in OM-Dex, OM-DC and OM-DV, which appears to be mainly influenced by βGP and Dex. The white light micrographs of iMSCs cultured in OM-Dex, OM-DC and OM-DV for 35 days are shown in Figures 4(a), (d) and (g) respectively. The corresponding two level cluster images are shown in Figure 4(b), (e) and (h), wherein pixels corresponding to the magenta cluster correlate to the nodule that is seen in the respective white light micrographs and the black pixels correspond to buffer and cells. Figures 4(c), (f) and (i) show univariate Raman images for the band around 958 cm^{-1} (Δ = 76 cm^{-1}) signifying v_1 vibrations of phosphates for the nodules formed in OM-Dex, OM-DC and OM-DV respectively. The average spectra derived from all magenta pixels in each image are shown in Figure 4(j)(I), (II) and (III). The average Raman spectrum of the nodule formed under the influence of OM-Dex is shown in Figure 4(j)(I). The spectra show prominent bands at 958, 425, 1032 and 580 cm^{-1} signifying v_1, v_2, v_3 and v_4 vibrations of phosphates.[28] A band at 1070 cm^{-1} for carbonates is seen which signifies B-type carbonation.[28] B-Type carbonation occurs when the carbonate (CO_3^{2-}) ions in the culture media replace the phosphate (PO_4^{3-}) ions in the previously formed hydroxyapatite nodule. Figure 4(j)(II) shows the average spectrum of a nodule formed under the influence of osteogenic OM-DC, exhibiting bands for phosphates at positions similar to that seen in Figure 4(j)(I). The carbonate band at 1070 cm^{-1} is very prominent indicating significant amounts of B-type carbonation in the HA nodule. Higher carbonates results in the crystalline nature of the nodule which is also inferred from the morphology of the nodule in the white light micrograph in Figure 4(d) compared to the nodule in Figure 4(a). The average Raman spectrum of the nodule formed in OM-DV (Figure 4(j)(III)), shows a less intense band around 958 cm^{-1} for v_1 vibrations of phosphates. Due to the influence of Dex and Vit-D3 in OM-DV, the iMSCs were differentiated towards osteoblasts, but have little effect on bone nodule formation.[37] Figure 4(j) shows Raman markers for collagen type-I, which is present in the bone nodules and the ECM, such as amide-I (1660 cm^{-1}), CH_2 bending (1450 cm^{-1}), amide-III (1250 cm^{-1}) and CH stretch (2935 cm^{-1}).[26, 28] In the integrated band intensity ratio of the water band in the region 3125-3565 cm^{-1} to the band at 958 cm^{-1} (Δ = 76 cm^{-1}) (as seen in Figure 5) characteristic for v_1 vibrations of phosphates shows the density of the formed nodule. The highest ratio is shown by the nodule formed in OM-DV (150.45 (± 5.43)), which indicates that the density of the nodule is lower than that in the other media. This may be due to Vit-D3 that has less effect on nodule formation. The ratio is lowest for the nodule formed in OM-DC (1.32 (± 0.58)), and is accompanied by a strong band for carbonates at 1070 cm^{-1}

which is a clear indication of increase in crystallinity in the formed nodule and is proportional to the density of mineral molecules in the nodule. The nodule formed in OM-Dex (3.61 (± 0.49)) has a ratio which is much less than that seen in OM-DV but is slightly higher than OM-DC, which indicates a correspondingly lower density than the nodule formed in OM-DC. These results show the influence of media on variation in composition of the HA mineralization in iMSCs. Due to the presence of cAMP and Vit-D3 in the combined osteogenic media OM-DC and OM-DV, these media present a different stage of mineralization than that showed by OM-Dex over the same culture period.

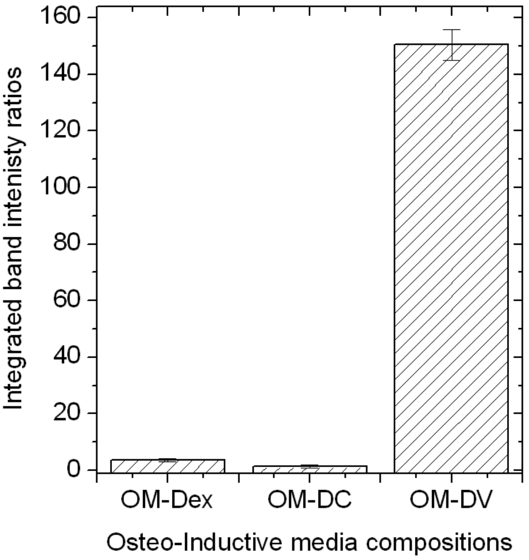

Figure 5: Integrated band intensity ratios showing variation in the density of HA molecules in the formed bone nodules. Band integration ratios of OH band (3125 -3565 cm^{-1}) to v_1 vibration of phosphates (959 cm^{-1}, Δ = 76 cm^{-1}) for three different regions (each region average of ~ 200 spectra) in each bone nodule formed under the influence of respective osteo-inductive media such as OM-Dex, OM-DC and OM-DV. Nodules formed in OM-DC (1.32 (± 0.58)) were very dense, closely followed by OM-Dex (3.61 (± 0.49)); the nodules formed under the influence of OM-DV (150.45 (± 5.43)) were least dense.

iMSCs cultured in OM-DC resulted in formation of lipid droplets in the cell cytoplasm leading to differentiation of these cells towards adipogenic lineage (Figure 2(d)) and supported by significant bands for lipids in the Raman difference spectrum in Figure 1(c)(iii). Lipids are known to play an influential role in the events of mineralization and crystallization of hydroxyapatite.[36, 40, 41] Phosphatidylserine in these lipids droplets has high binding affinity towards Ca^{2+} ions and also reacts with phosphates that results in phospholipid:calcium:phosphate ion complexes which help in early mineralization.[36, 40, 41] Figure 6 shows adipocyte induced osteogenic mineralization of iMSCs cultured in OM-DC. A white light micrograph of bone nodule formation (white star) over lipid droplets (white arrows) is shown in Figure 6(a). The corresponding level two cluster image is shown in Figure 6(b). The univariate Raman band integration images for the band at 958 cm^{-1} (Δ = 76 cm^{-1}) for v_1 vibrations of phosphates and 2857 cm^{-1} (Δ = 105 cm^{-1}) for lipids are shown in Figures 6(c) and (d) respectively. The univariate image in Figure 6(c) for phosphates corresponds well to the magenta pixels in Figure 6(b), showing the distribution of the formed bone nodule, and is similar to the black regions marked by white stars in Figure 6(a). Similarly, the univariate image for lipids in Figure 6(d) corresponds to the lipid regions shown by white arrows in Figure 6(a), confirming the occurrence of osteogenic mineralization in the adipogenic differentiated cells. The nodules formed in OM-DC showed a strong band for carbonates around 1070 cm^{-1} displaying B-type carbonation[28] as seen in Figure 4(j)(II). The average spectra of the cluster for iMSCs cultured in OM-DC until day 21 show a significant band for phosphatidylserine at 733 cm^{-1} (Figure 7) which is absent in the average spectra of iMSCs cultured up to day 21 in OM-Dex or OM-DV. This observation suggests that the mineralization in OM-DC happened much earlier, leading to formation of carbonated hydroxyapatite as seen after day 35 compared to the mineralized nodules seen in OM-Dex over the same period.

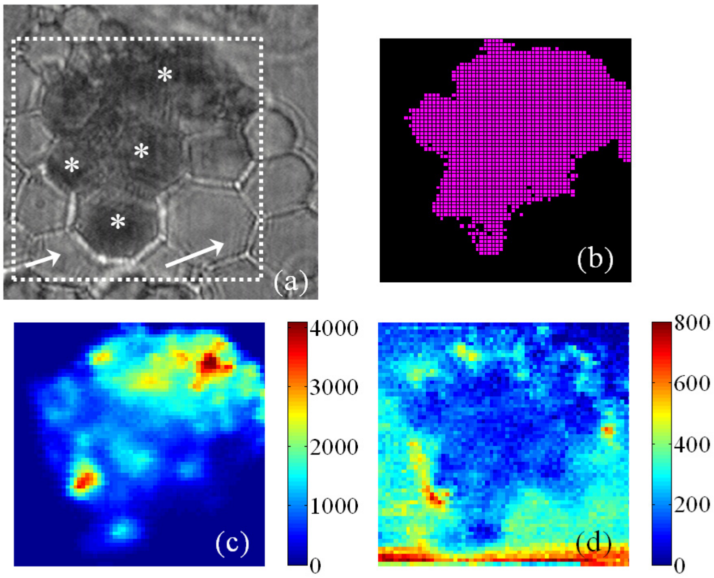

Figure 6: Influence of Dex and cAMP in osteogenic media OM-DC showing adipocyte induced osteogenic mineralization in iMSCs cultured for 35 days. (a) White light micrograph (22.5 µm × 22.5 µm) showing mineralized nodule formation (white stars) over lipid droplets (white arrows) in adipogenic differentiated cell. (b) Two level cluster image performed over the Raman data acquired from the region marked with white dots as seen in (a). (c) Raman band integration image for the band at 958 cm^{-1} (Δ = 76 cm^{-1}) signifying v_1 vibration of phosphates, corresponding to magenta region in Figure (b). (d) Raman band integration image for the band at 2857cm^{-1} (Δ = 105 cm^{-1}) signifying lipids, corresponding to regions of lipid droplets (white arrows) in Figure (a).

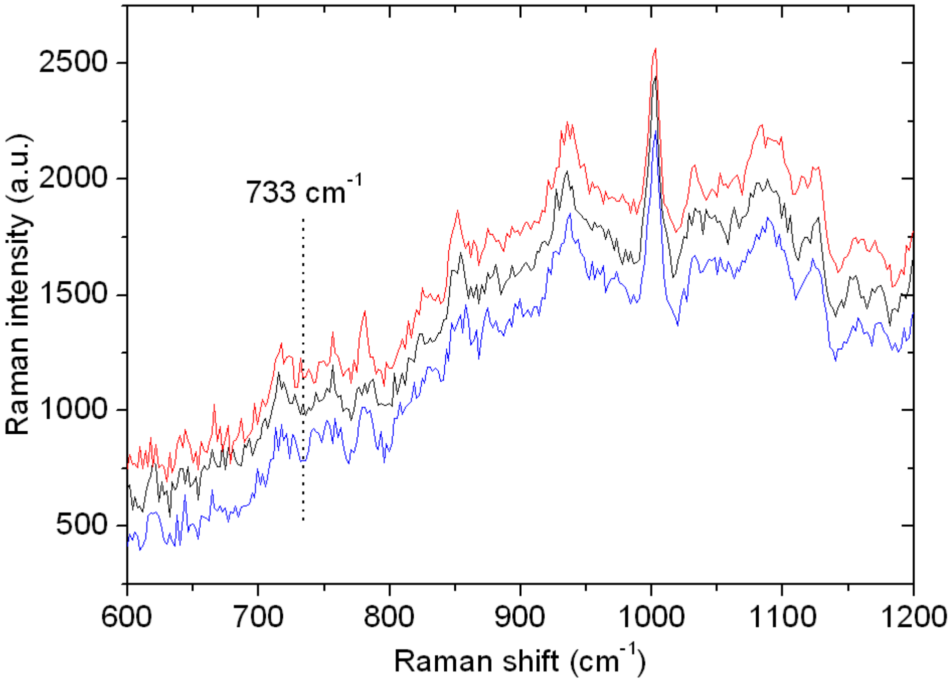

Figure 7: Average spectra of 16 randomly selected iMSCs cultured in osteo-inductive media such as OM- Dex (black spectrum), OM-DC (red spectrum) and OM-DV (blue spectrum). Average spectrum for OM-DC shows a band at 733 cm^{-1} for phosphatidylserine that is not present in OM-Dex or OM-DV.

iMSCs cultured in OM-DV and OM-DB for 35 days resulted in formation of mineralized nodules that chemically resembled the calcium oxalate family.[42, 43] Figure 8(a) shows a white light micrograph of calcium oxalate crystals formed in the iMSCs cultured in OM-DV, which resembled pyramid like structures.[42] The corresponding nine level Raman cluster image is shown in Figure 8(b) whose respective average cluster spectra are shown in Figure 9. Pixels corresponding to cyan, light green, and yellow regions correspond to the structures seen in Figure 8(a). The average Raman spectrum corresponding to all the cyan pixels is shown in Figure 8(g)(I). The spectrum shows prominent bands at 507, 912, 1478 and 1630 cm^{-1} characteristic of calcium oxalate dihydrate.[43] The spectrum shows sharp bands at the specified locations, indicating the crystalline nature of the formed mineral.[43] Pixels corresponding to light green, yellow and light blue also showed bands at 507, 912, 1478 and 1630 cm^{-1}, but were less intense than the peaks from the cyan regions, indicating lower concentration of the mineral. The average spectrum of violet pixels show prominent glycogen bands, which is also seen in the Raman difference spectrum for iMSCs cultured in OM-DV in Figure 1(b)(vi). The presence of glycogen indicates the osteoblast differentiated stage of the iMSCs as mentioned earlier.[30] The respective average spectra corresponding to black, red and magenta pixels show prominent bands signifying presence of proteins as well as lower amounts of glycogen compared to that shown by the average spectrum for violet pixels. The average spectrum of dark blue pixels show bands that correspond to lipids that are accumulated in the iMSCs. Figure 8(c) shows the univariate image of the 1478 cm^{-1} band correspond to the cyan, light green, and yellow pixels in Figure 8(b) in decreasing order of intensity. The initiation of these nodules is influenced by surrounding lipids[44, 45] and the proteins surrounding the nodule might have introduced the crystallinity seen in the formed calcium oxalate dihydrate.[46]

iMSCs cultured in OM-DB also resulted in formation of calcium oxalates whose morphology (Figure 8(d)) was different from those formed in OM-DV. The corresponding nine level Raman cluster image is shown in Figure 8(e), whose respective average cluster spectra show variations in chemical composition compared to those due to OM-DV as seen in Figure 10. The average spectra corresponding to cyan color pixels (Figure 8(g)(II)) also show bands at 507, 912, 1478 and 1630 cm^{-1} that occur at similar band positions as seen in Figure 8(g)(I). The average spectra also show higher intensities of the bands at 507 and 1630 cm^{-1} and a prominent shift at 3500 cm^{-1} for OH stretch of water molecules[47] compared to the spectra in Figure 8(g)(I). The average spectra of the red pixels show similar band position and are less intense than those seen in the average spectra for cyan pixels. The average spectra corresponding to violet pixels as seen in Figure 8(g)(III) also show bands at 507, 912, 1478 1630 and 3500 cm^{-1}. However, the band intensity at 3500 cm^{-1} is much higher and the bands at positions 507, 912 and 1478 cm^{-1} negatively correlate in intensity with respect to those found in Figure 8(g)(II). The average spectra corresponding to magenta pixels have bands that occur at similar positions and are less intense than those seen in the average spectra for violet pixels. The respective average spectra corresponding to light green, yellow, and dark blue color pixels show prominent bands for protein and glycogen in decreasing order of concentration. Black color pixels resulted in average spectra that showed prominent bands for glycogen in combination with lipids. Average spectra of light blue pixels show bands that correspond to lipids that are accumulated in the iMSCs. The univariate Raman band integration image of the 1478 cm^{-1} band in Figure 8(f) corresponds to the nodule seen in white light micrograph of Figure 8(d). The high and low intensity regions in the univariate image correspond to the cyan and violet color pixels respectively in Figure 8(e), which shows the occurrence of two mineral variants in same nodule.

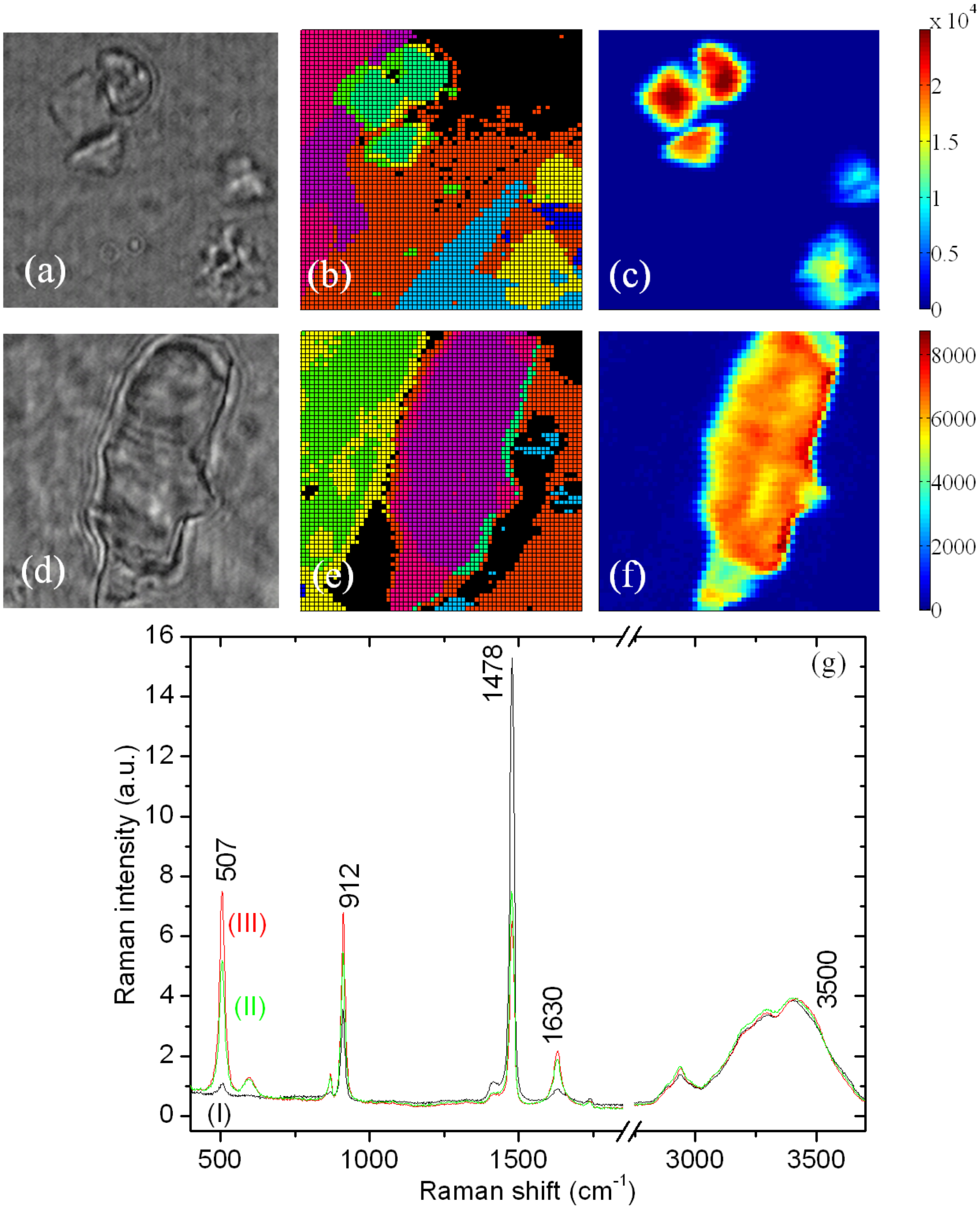

Figure 8: Influence of Vit-D3 and BMP2 in osteo-inductive media OM-DV and OM-DB respectively on formation of calcium oxalate dihydrates (COD) after 35 days in culture. (a) White light image (22.5 µm × 22.5 µm) of CODs formed in iMSCs cultured in OM-DV; (b) Nine level cluster image of the region depicted in (a); (c) Raman band integration image for the band 1478 cm^{-1} (Δ=56 cm^{-1}) showing the distribution of CODs seen in (a) and (b); (d) White light image (22.5 µm × 22.5 µm) of CODs formed in iMSCs cultured in OM-BMP2; (e) Nine level cluster image of the region depicted in (d); (f) Raman band integration image for the band 1478 cm^{-1} (Δ=56 cm^{-1}) showing the distribution of CODs in (d) and (e). (g) Normalized average Raman spectra of clusters from CODs formed in iMSCs corresponding to: (I) Cyan color pixels in (b), (II) Cyan color pixels in (e), and (III) Violet color pixels in (e).

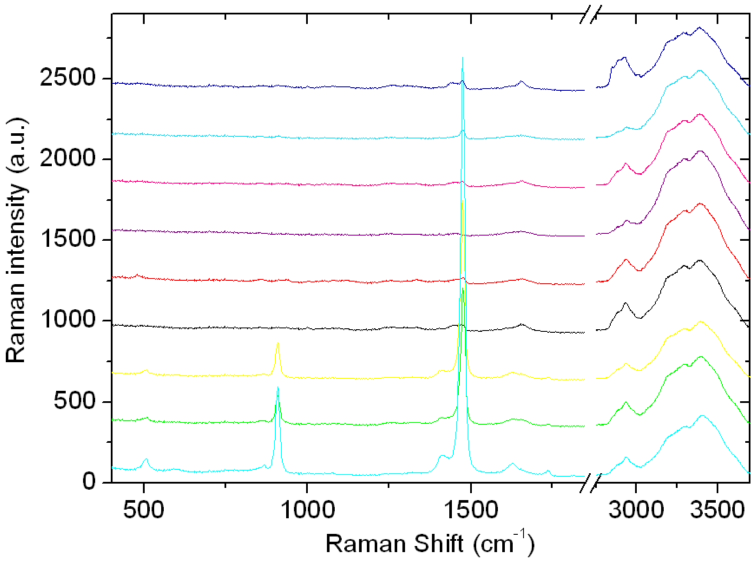

Figure 9**:** Average spectra of pixels corresponding to different clusters in the nine level cluster image seen in Figure 8(a).

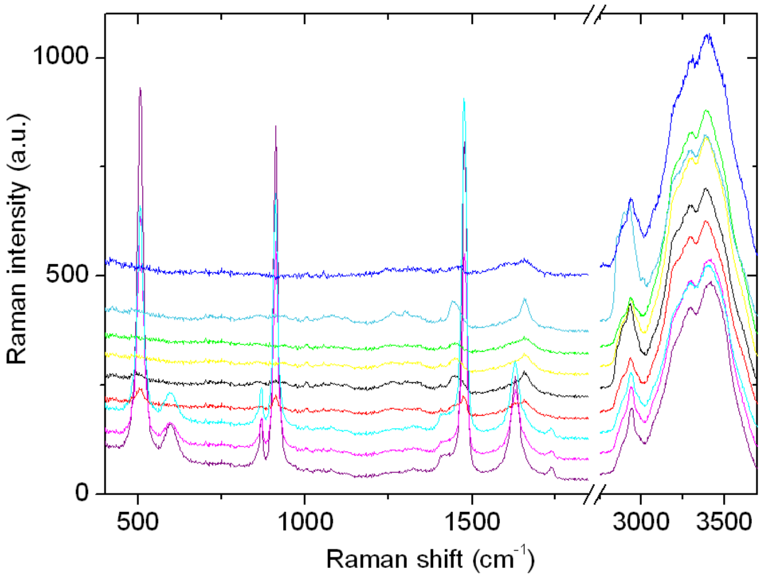

Figure 10**:** Average spectra of pixels corresponding to different clusters in the nine level cluster image seen in Figure 8(e).

The average spectrum for the cyan pixels in Figure 8(b) indicates a crystalline form of calcium oxalate dihydrate. The average spectra for the cyan pixels in Figure 8(e) has bands which are at same position as that of seen in Figure 8(g)(I), however there is a prominent shift at 3500 cm^{-1} and higher band intensity at 507 and 1630 cm^{-1}. The same nodule in Figure 8(e) shows regions for violet pixels, whose average spectrum is seen in Figure 8(g)(III). The spectrum has bands at the same positions as that seen in Figure 8(g)(II). However the bands at 507, 912 and 1478 cm^{-1} negatively correlate in intensity with respect to those found in Figure 8(g)(I) and (II) and has more prominent band for OH stretch at 3500 cm^{-1} for water molecule compared to Figure 8(g)(II) for regions corresponding to cyan pixels. From these results, we hypothesize that the early-formed calcium oxalate dihydrate nodule had spectra similar to Figure 8(g)(III). Upon crystallization, the 3500 cm^{-1} band for OH stretch reduced and negatively correlated bands at 507, 912 and 1478 cm^{-1} are seen similar to that seen in the spectrum in Figure 8(g)(II). Upon further crystallization, the spectrum show bands similar to those seen in Figure 8(g)(I) accompanied by reduction in OH band around 3500 cm^{-1}.

Occurrence of hydroxyapatite or calcium oxalate dihydrate nodules in the cultured iMSCs is initiated by the physiological pH or acidic pH experienced by the cells.[48, 49] In certain cases, hydroxyapatite forms the substrate for heterogeneous nucleation of these oxalates under acidic pH.[48] The iMSCs cultured in OM-DV and OM-DB showed glycogen synthesized in the cells. The synthesis of glycogen occurs in acidic pH.[50] The influence of acidic pH due to glycogen in the cells cultured in OM-DV and OM-DB led to the formation of calcium oxalate dihydrates rather than hydroxyapatite which occurs mostly at neutral pH. Hence iMSCs cultured in OM-DV resulted in differentiation of the cells towards osteoblast lineage and showed very little bone mineralization. The occurrence of the bone nodules or hydroxyapatite formed in the iMSCs cultured in OM-DV is activated under acidic pH that results in the formation of calcium oxalate dihydrate nodules.

6.4 Conclusion

iMSCs were successfully differentiated towards adipogenic lineage and osteogenic lineage with (HA formation) and without (osteoblast) mineralization. Confocal Raman microspectroscopy was used to obtain chemical information from the iMSCs while they were progressing towards these lineages in a non-invasive and label-free manner. Raman difference spectroscopy showed the stemness of iMSCs by revealing specific biomarkers that enabled the identification of the specific lineage of the differentiated iMSCs. Adipogenic lineage of the iMSCs was identified by presence of lipid droplets. Biomarkers for osteogenic lineage with and without mineralization were identified by the distribution of HA and glycogen respectively. The presence of varying concentrations of glycogen in the iMSCs cultured with different osteogenic media suggests varying levels of osteogenic differentiation of the iMSCs (pre-osteoblast, osteoblast, osteocyte and mineralized osteoblast/osteocyte). The identification of onset and progression of differentiation well in advance of the final differentiated stage (day 35) of the cells were illustrated by PC plots.

The HA mineralization of the iMSCs were influenced by the osteogenic culture media, where extensive mineralization was observed for OM-Dex followed by OM-DC and

OM-DV. OM-DC also showed adipogenic lineage where abundant lipid droplets were seen in the cytoplasm of the cell. These lipid droplets played an important role in mineralization much earlier compared to those seen in OM-Dex. This process resulted in carbonated apatites in OM-DC over the same culture period. The iMSCs also showed mineralization of calcium oxalate dihydrates that is feasible in acidic pH. The acidic pH in the cells was influenced by synthesis of glycogen by OM-DV and OM-DB, showing the role of pH in the event of mineralization. The acidic pH resulted in the formation of calcium oxalate dihydrates and neutral pH resulted in the formations of hydroxyapatite. The formed calcium oxalates were initially in hydrated form, which later convert to crystalline form that is evident from the decrease in the OH stretch vibration of water molecule at 3500 cm^{-1}. For both hydroxyapatite and calcium oxalate dihydrates, lipids played an important role during the nucleation stage.

References

1. Pittenger, M. F., Multilineage potential of adult human mesenchymal stem cells. *Science* **1999,** 285, (5428), 665.
2. Fibbe, W. E., Mesenchymal stem cells. A potential source for skeletal repair. *Ann Rheum Dis* **2002,** 61 Suppl 2, ii29-31.
3. Caplan, A. I., Adult mesenchymal stem cells for tissue engineering versus regenerative medicine. *J. Cell. Physiol.* **2007,** 213, (2), 341-347.
4. Caplan, A. I.; Bruder, S. P., Mesenchymal stem cells: building blocks for molecular medicine in the 21st century. *Trends Mol Med* **2001,** 7, (6), 259-64.
5. Gerstenfeld, L. C.; Chipman, S. D.; Glowacki, J.; Lian, J. B., Expression of differentiated function by mineralizing cultures of chicken osteoblasts. *Dev. Biol.* **1987,** 122, (1), 49-60.
6. Stanford, C. M.; Jacobson, P. A.; Eanes, E. D.; Lembke, L. A.; Midura, R. J., Rapidly forming apatitic mineral in an osteoblastic cell line (UMR 106-01 BSP). *J Biol Chem* **1995,** 270, (16), 9420-8.
7. Wu, Y.; Glimcher, M. J.; Rey, C.; Ackerman, J. L., A unique protonated phosphate group in bone mineral not present in synthetic calcium phosphates. Identification by phosphorus-31 solid state NMR spectroscopy. *J Mol Biol* **1994,** 244, (4), 423-35.
8. Boskey, A. L.; Camacho, N. P.; Mendelsohn, R.; Doty, S. B.; Binderman, I., FT-IR microscopic mappings of early mineralization in chick limb bud mesenchymal cell cultures. *Calcif Tissue Int* **1992,** 51, (6), 443-8.
9. Puppels, G. J.; De Mul, F. F. M.; Otto, C.; Greve, J.; Robert-Nicoud, M.; Arndt-Jovin, D. J.; Jovin, T. M., Studying single living cells and chromosomes by confocal Raman microspectroscopy. *Nature* **1990,** 347, (6290), 301-3.
10. Matthaus, C.; Boydston-White, S.; Miljkovic, M.; Romeo, M.; Diem, M., Raman and infrared microspectral imaging of mitotic cells. *Appl. Spectrosc.* **2006,** 60, (1), 1-8.
11. Matthaus, C.; Chernenko, T.; Newmark, J. A.; Warner, C. M.; Diem, M., Label-free detection of mitochondrial distribution in cells by nonresonant raman microspectroscopy. *Biophys. J.* **2007,** 93, (2), 668-673.
12. Notingher, I.; Jell, G.; Lohbauer, U.; Salih, V.; Hench, L. L., In situ non-invasive spectral discrimination between bone cell phenotypes used in tissue engineering. *J. Cell. Biochem.* **2004,** 92, (6), 1180-1192.
13. Notingher, I.; Verrier, S.; Romanska, H.; Bishop, A. E.; Polak, J. M.; Hench, L. L., In situ characterization of living cells by Raman spectroscopy. *Spectroscopy* **2002,** 16, (2), 43-51.
14. Short, K. W.; Carpenter, S.; Freyer, J. P.; Mourant, J. R., Raman spectroscopy detects biochemical changes due to proliferation in mammalian cell cultures. *Biophys. J.* **2005,** 88, (6), 4274-4288.
15. Uzunbajakava, N.; Lenferink, A.; Kraan, Y.; Volokhina, E.; Vrensen, G.; Greve, J.; Otto, C., Nonresonant confocal Raman imaging of DNA and protein distribution in apoptotic cells. *Biophys. J.* **2003,** 84, (6), 3968-3981.
16. van Manen, H.-J.; Kraan, Y. M.; Roos, D.; Otto, C., Single-cell raman and fluorescence microscopy reveal the association of lipid bodies with phagosomes in leukocytes. *Proc. Natl. Acad. Sci. U. S. A.* **2005,** 102, (29), 10159-10164.
17. Verrier, S.; Notingher, I.; Polak, J. M.; Hench, L. L., In situ monitoring of cell death using Raman microspectroscopy. *Biopolymers* **2004,** 74, (1-2), 157-62.
18. Notingher, I.; Bisson, I.; Bishop, A. E.; Randle, W. L.; Polak, J. M. P.; Hench, L. L., In situ spectral monitoring of mRNA translation in embryonic stem cells during differentiation *in vitro*. *Anal. Chem.* **2004,** 76, (11), 3185-3193.
19. Krafft, C.; Salzer, R.; Seitz, S.; Ern, C.; Schieker, M., Differentiation of individual human mesenchymal stem cells probed by FTIR microscopic imaging. *Analyst* **2007,** 132, (7), 647-53.
20. Chiang, H. K.; Peng, F.-Y.; Hung, S.-C.; Feng, Y.-C., In situ Raman spectroscopic monitoring of hydroxyapatite as human mesenchymal stem cells differentiate into osteoblasts. *J. Raman Spectrosc.* **2009,** 40, (5), 546-549.

21. Kim, B. S.; Lee, C. C. I.; Christensen, J. E.; Huser, T. R.; Chan, J. W.; Tarantal, A. F., Growth, Differentiation, and Biochemical Signatures of Rhesus Monkey Mesenchymal Stem Cells. *Stem Cells Dev.* **2008,** 17, (1), 185-198.
22. Pully, V. V.; Lenferink, A.; Otto, C., Hybrid Rayleigh, Raman and two-photon excited fluorescence spectral confocal microscopy of living cells. *J. Raman Spectrosc.* **2009,** 10.1002/jrs.2501.
23. de Jong, B. W. D.; Schut, T. C. B.; Coppens, J.; Wolffenbuttel, K. P.; Kok, D. J.; Puppels, G. J., Raman spectroscopic detection of changes in molecular composition of bladder muscle tissue caused by outlet obstruction. *Vib. Spectrosc.* **2003,** 32, (1), 57-65.
24. Hayashi, H.; Nishimura, Y.; Katahira, M.; Tsuboi, M., The structure of nucleosome core particles as revealed by difference Raman spectroscopy. *Nucleic Acids Res* **1986,** 14, (6), 2583-96.
25. Hightower, K. R., The role of the lens epithelium in development of UV cataract. *Curr Eye Res* **1995,** 14, (1), 71-8.
26. Stewart, S.; Shea, D. A.; Tarnowski, C. P.; Morris, M. D.; Wang, D.; Franceschi, R.; Lin, D. L.; Keller, E., Trends in early mineralization of murine calvarial osteoblastic cultures: A Raman microscopic study. *J. Raman Spectrosc.* **2002,** 33, (7), 536-543.
27. Thomas, G. J., Jr.; Prescott, B.; Olins, D. E., Secondary structure of histones and DNA in chromatin. *Science* **1977,** 197, (4301), 385-8.
28. Timlin, J. A.; Carden, A.; Morris, M. D., Chemical microstructure of cortical bone probed by Raman transects. *Appl. Spectrosc.* **1999,** 53, (11), 1429-1435.
29. Tu, A. T., *Raman Spectroscopy in Biology: Principles and Applications*. 1982; p 448.
30. Schajowicz, F.; Cabrini, R. L., Histochemical studies on glycogen in normal ossification and calcification. *J Bone Joint Surg* **1958,** 40-A, (5), 1081-92.
31. Diefenderfer, D. L.; Osyczka, A. M.; Reilly, G. C.; Leboy, P. S., BMP Responsiveness in Human Mesenchymal Stem Cells. *Connect. Tissue Res.* **2003,** 44, (Suppl. 1), 305-311.
32. Jorgensen, N. R.; Henriksen, Z.; Sorensen, O. H.; Civitelli, R., Dexamethasone, BMP-2, and 1,25-dihydroxyvitamin D enhance a more differentiated osteoblast phenotype: validation of an *in vitro* model for human bone marrow-derived primary osteoblasts. *Steroids* **2004,** 69, (4), 219-226.
33. Petersen, R. K.; Madsen, L.; Pedersen, L. M.; Hallenborg, P.; Hagland, H.; Viste, K.; Doeskeland, S. O.; Kristiansen, K., Cyclic AMP (cAMP)-mediated stimulation of adipocyte differentiation requires the synergistic action of Epac- and cAMP-dependent protein kinase-dependent processes. *Mol. Cell. Biol.* **2008,** 28, (11), 3804-3816.
34. Krafft, C.; Neudert, L.; Simat, T.; Salzer, R., Near infrared Raman spectra of human brain lipids. *Spectrochim. Acta, Part A* **2005,** 61A, (7), 1529-1535.
35. Yang, D.-C.; Tsay, H.-J.; Lin, S.-Y.; Chiou, S.-H.; Li, M.-J.; Chang, T.-J.; Hung, S.-C., cAMP/PKA regulates osteogenesis, adipogenesis and ratio of RANKL/OPG mRNA expression in mesenchymal stem cells by suppressing leptin. *PLoS One* **2008,** 3, (2), No pp given.
36. Xu, S.; Yu, J. J., Beneath the minerals, a layer of round lipid particles was identified to mediate collagen calcification in compact bone formation. *Biophys. J.* **2006,** 91, (11), 4221-4229.
37. Davies, J. E., *Bone Engineering*. 1st ed.; Em Squared Inc: Toronto, 2000.
38. Favus, M. J., *Primer on the Metabolic Bone Diseases And Disorders of Mineral Metabolism*. 6th ed.; ASMBR: Washington D.C., 2006.
39. Simon, S. R., *Orthopaedic Basic Science*. 1st ed.; American Academy of Orthopaedic Surgeons: Illinois, 1994.
40. Boyan, B. D.; Schwartz, Z.; Swain, L. D.; Khare, A., Role of lipids in calcification of cartilage. *Anat. Rec.* **1989,** 224, (2), 211-19.
41. Raggio, C. L.; Boyan, B. D.; Boskey, A. L., *In vivo* hydroxyapatite formation induced by lipids. *J. Bone Miner. Res.* **1986,** 1, (5), 409-15.

42. Baumann, J. M.; Affolter, B.; Caprez, U.; Henze, U., Calcium oxalate aggregation in whole urine, new aspects of calcium stone formation and metaphylaxis. *Eur. Urol.* **2003,** 43, (4), 421-425.
43. Kontoyannis, C. G.; Bouropoulos, N. C.; Koutsoukos, P. G., Use of Raman spectroscopy for the quantitative analysis of calcium oxalate hydrates: application for the analysis of urinary stones. *Appl. Spectrosc.* **1997,** 51, (1), 64-67.
44. Khan, S. R.; Atmani, F.; Glenton, P.; Hou, Z. C.; Talham, D. R.; Khurshid, M., Lipids and membranes in the organic matrix of urinary calcific crystals and stones. *Calcif. Tissue Int.* **1996,** 59, (5), 357-365.
45. Khan, S. R.; Glenton, P. A.; Backov, R.; Talham, D. R., Presence of lipids in urine, crystals and stones: implications for the formation of kidney stones. *Kidney Int.* **2002,** 62, (6), 2062-2072.
46. Weiner, S.; Sagi, I.; Addadi, L., Structural biology: Choosing the crystallization path less traveled. *Science* **2005,** 309, (5737), 1027-1028.
47. Kolo, K.; Claeys, P., *In vitro* formation of Ca-oxalates and the mineral glushinskite by fungal interaction with carbonate substrates and seawater. *Biogeosciences* **2005,** 2, (3), 277-293.
48. Baumann, J. M.; Ackermann, D.; Affolter, B., The influence of hydroxyapatite and pyrophosphate on the formation product of calcium oxalate at different pHs. *Urol. Res.* **1989,** 17, (3), 153-5.
49. Brandao-Burch, A.; Utting, J. C.; Orriss, I. R.; Arnett, T. R., Acidosis Inhibits Bone Formation by Osteoblasts *In Vitro* by Preventing Mineralization. *Calcif. Tissue Int.* **2005,** 77, (3), 167-174.
50. Peak, M.; al-Habori, M.; Agius, L., Regulation of glycogen synthesis and glycolysis by insulin, pH and cell volume. Interactions between swelling and alkalinization in mediating the effects of insulin. *Biochem J* **1992,** 282 (Pt 3), 797-805.

Chapter 7

Events of mineralization in osteogenesis – from *de novo* to crystalline bone

Human immortalized bone marrow derived stromal cells (iMSCs) were differentiated in osteogenic mineralization medium under carefully maintained physiological and biological conditions. The occurrence, development and composition of events of mineralization were followed over a 60 day culture with Raman microspectroscopy and imaging. The earliest events of mineralization occurred around day 30. Mineralization was reflected in the sparse presence of mineralized nodules smaller than 10 micrometer in diameter. Hyperspectral Raman images show that in the early phase the nodules are heterogeneous in composition and contain, sometimes together in a single nodule, amorphous calcium phosphate, mono-calcium phosphate mono-hydrate, di-calcium phosphate di-hydrate and β-tri-calcium phosphate. These de novo formed bone nodules could further be characterized by a lipid-rich organic phase. The transformation of early-phase bone nodules into carbonated hydroxyapatite could be observed over the time period from days 30 to 60. During this period the development of a homogeneous distribution of apatite was observed, which was slowly converted to hydroxyapatite. Hydroxyapatite was subsequently gradually converted into carbonated hydroxyapatite as demonstrated by the detection of Raman markers of increased crystallinity and Raman bands typical for carbonate groups. The organic phase during this process developed from lipid-rich into protein-rich, suggesting a direct role of the composition of the extracellular matrix on the de novo development of bone. Taken together, these Raman markers provide detailed insights into the phases of bone-development. This study highlights *the strength of non-invasive, label-free spontaneous hyperspectral Raman imaging for characterizing long-term development of tissue from iMSCs to bone formation.*

Manuscript in preparation

7.1 Introduction

Bone is a complex tissue, which has an extracellular matrix (ECM) composed of inorganic minerals, organic material, collagen, non-collagenous proteins, lipids and water.[1] Inorganic material in bone is chemically similar to hydroxyapatite (HA) ($Ca_{10}(PO_4)_6(OH)_2$). The *in vivo* or *in vitro* bio-mineralization of bone undergoes a series of intermediate steps beginning with the metastable precursors such as amorphous calcium phosphate (ACP), di-calcium phosphate dihydrate (DCPD), β-tricalcium phosphate (β-TCP) and octacalcium phosphate (OCP).[2, 3] These precursors lead to formation of HA and then result in carbonated hydroxyapatite (CHA) that is comparatively more crystalline and resembles *in vivo* bone.[4] CHA is a thermodynamically more stable mineral than HA, and whose lattice structure contains significant levels of carbonate ions. Carbonates substituted into the OH^- and phosphate sites of HA lead to A- type and B-type carbonation respectively.[5] Although the physical and chemical properties of *in vivo* bone have been extensively investigated, the early stages of mineralization where precursors occur are yet to be fully explored. Identification and analysis of mineral composition during early stages of mineralization is crucial to bone tissue engineering.

Over the years biologists have used von Kossa reagent and alkaline phosphatase to detect the presence of minerals. Bonewald et. al. suggested the need for other techniques in addition to von Kossa staining as it is highly destructive to cells and is not specific to various mineral apatites that are formed.[6] In the last two decades, several techniques like electron microprobe and electron diffraction, X-ray diffraction (XRD), solid state nuclear magnetic resonance (NMR) spectroscopy and vibrational spectroscopy approches like Fourier transform infrared (FTIR) and Raman have been used to characterize the *in vitro* formed bone nodules from precursors to HA stage. The use of XRD was demonstrated by Stanford et. al.[7] to study the initial mineral formation in osteoblast cell cultures. Gerstenfeld et. al.[8] showed the application of the electron microprobe and electron diffraction to detect the presence of mineral apatite and level of crystallinity of the mineralized collagen fibers developed in chicken osteoblasts. The presence of unique protonated phosphate groups in biologically formed apatites was shown by Wu et. al.[9] using solid state NMR spectroscopy; these groups were not seen in synthetically formed apatites. Boskey et. al.[10] were among the first to use FTIR microspectroscopy to detect the mineralization of differentiated chick limb bud mesenchymal cell micromass cultures. The above-mentioned techniques are limited in their applicability to water containing specimens, and require large sample amounts and extensive sample pretreatment that make their application to living tissues impractical. There is thus a pressing need for non-invasive and label free methods for analysis of the formed mineral nodules.

A recent review of applications of vibrational spectroscopy to study mineralized tissue illustrated Raman spectroscopy to be technically more superior to FTIR spectroscopy.[11] Raman spectroscopy enables chemical information that is complementary to FTIR, since many infrared vibrational modes are Raman active. Raman bands have better spatial resolution (~ 0.3 to 1.0 μm) than FTIR. Typical Raman bands are narrow, hence small frequency shifts and band shape changes can be easily observed, and enables distinction of various chemical samples. Raman spectroscopy further has important additional advantages: it requires hardly any sample preparation, is label free and non-destructive, and the sample need not be transparent or dehydrated. With all these advantages, Raman spectroscopy is developing into a valuable tool to analyze a developing tissue over a period of time.[12] The application of Raman spectroscopy to mineralized tissues and cell cultures are well described in the literature.[11-17] Raman spectroscopy has been used to study the process of mineralization from early to late stage showing formation of HA. Sauer et. al.[3] used Raman spectroscopy to study various synthetic and biological calcium phosphates that acted as precursors to HA. de Grauw et. al.[18] determined crystallinity of the synthetically formed apatite by studying the phosphate and carbonate bands using Raman microscopy.

Human mesenchymal stem cells have the potential to differentiate towards any of the mesenchymal lineages such as bone, cartilage, fat, tendon, muscle and marrow stroma.[19] The potential of these stem cells can be used to study the mineralization events over the culture period. Rey et. al.[20-22] showed formation of calcium phosphate crystals in chick osteoblast cells over a 60 day culture. These results indicated early forms of apatite to be poorly crystalline, which by day 30 was similar to early post-natal chick bone. However, by day 60 of culture period, they found higher order arrangements of ion constituents in the mineral apatite. The literature describes model studies leading to formation of HA with intermediate calcium phosphate mineral phases such as ACP, DCPD, β-TCP and OCP.[2, 3] These could be easily distinguished from one another by their specific Raman spectra.[2, 3] Very little work has been done to study the early stages of bone formation in *in vitro* cultured cells. Stewart et. al.[14] cultured mouse calvarial cells and showed β-TCP as a possible precursor for HA formation. Results from Crane et. al.[12] showed the occurrence of ACP and OCP before formation of HA. Recently differentiation and mineralization of human mesenchymal stromal cells/embryonic stem cells were studied by Raman microspectroscopy, showing the growth and increase in crystallinity of mineral apatite with culture period. However, the occurrence of precursors of HA was not reported.[13, 23]

We cultured iMSCs in osteogenic differentiation media for up to 60 days. The events of mineralization in the ECM of the cells were monitored by confocal Raman microspectroscopy after days 30, 40, 50, and 60 of culture. Day 30 culture showed *de novo* mineralization, which was identified by the presence of various metastable precursors like mono calcium phosphate mono hydrate (MCPM), DCPD, ACP, and β-TCP. The *de novo* formed nodule also showed presence of lipids that indicates the heterogeneity of the early formed nodule. Day 40 culture resulted in homogenous distribution of HA in the ECM of the cells. Further culture until day 50 and 60 showed formation of CHA similar to *in vivo* bone. Influence of collagenous proteins was seen on day 50 and 60 of culture. Mineral to matrix band ratios and carbonates to phosphates band ratios shows development of HA with culture period accompanied with increase in crystallinity. These approaches have significant potential to throw light on the early stage of bone formation (*de novo* bone) and its development over time, an issue of great importance in bone tissue engineering.

7.2 Material and methods

Cell culture

iMSCs (as described in chapter 5 of this thesis) were seeded on multiple UV grade calcium fluoride substrates (CaF_2) (Crystran Ltd., UK) at cell densities of 1000 cells/cm^2. The seeded iMSCs were cultured in osteogenic cell culture medium inducing mineralization in separate Petri dishes for a 60 day period. Cell culture basic medium (BM), which served as the control condition, was prepared from α-MEM (GIBCO, Carlsbad, CA), 10% fetal bovine serum (FBS; Bio Whittaker, Australia), 0.2 mM L-ascorbic acid-2-phosphate (AsAP; Sigma, St. Louis, MO), 100 U/mL Pencillin G (Invitrogen, Carlsbad, CA); 100 µg/mL Streptomycin (Invitrogen) and 2 mM L-Glutamine (L-Glu; Sigma). Osteogenic medium was prepared by adding 0.01 M β-Glycerophosphate (βGP; Sigma) and osteogenic growth factor 10^{-8} M dexamethasone (Dex, Sigma) to BM. iMSCs on multiple CaF_2 substrates were cultured in BM overnight (day 0) to enable cells to adhere on these substrates. Cells adhered to CaF_2 substrates were then cultured in osteogenic media until day 60 of culture. Cell cultures were stopped by day 60 when extensive HA mineralization was observed. The culture medium was refreshed every three days until day 60 of culture. Throughout the period, cell cultures were maintained at 37ºC, 95 % humidity and 5% partial pressure of CO_2. iMSCs were cultured until day 30, 40, 50 and 60 of culture to monitor the *in vitro* mineralization events. All measurements were performed on living cells. On respective measurement days, cell cultures on CaF_2 substrates containing mineralized nodules were washed three times with phosphate buffered saline solution (PBS; Gibco) before being transferred to the confocal Raman microspectroscope for measurements.

Confocal Raman microspectroscopy

Raman microspectroscopy and imaging were performed using a custom-built confocal Raman microspectroscope.[24] A Krypton ion laser (Coherent, Innova 90K, Santa Clara, CA) emitting at 647.1 nm was used as an excitation source. The microscope in epi-illumination detection mode used a water immersion objective with 63× magnification and 1.2 NA (Zeiss Plan Neofluar, Carl Zeiss, Thornwood, NY) to focus laser light on the sample of interest and also to collect the Raman scattered photons from the sample. The scattered photons from the sample were then focused on to a confocal pinhole placed in front of a custom-designed spectrograph. The spectrograph disperses the Raman scattered photons onto an air-cooled EMCCD camera (Newton DU-970N, Andor Technology, Belfast, Northern Ireland) which provided a spectral resolution of 1.85 to 2.85 cm^{-1}/pixel over a wavenumber range -20 to 3670 cm^{-1}. Raman images were acquired by recording the full spectra (-20 to 3670 cm^{-1}) from each position of the laser beam effected by the displacement of the scanning mirror in the area of interest on the sample. All Raman measurements were performed in an area of 20 μm × 20 μm with a spectral resolution of 310 nm. An accumulation time of 100 ms/step and an excitation power of 40 mW on the sample were used in all measurements.

Raman data analysis

Each Raman image resulted in a hyperspectral dataset which were pre-processed by 1) removal of cosmic ray events, 2) subtraction of the camera offset, 3) calibration of the wave number axis, and 4) correction of frequency dependent transmission. The well-known band-positions of toluene were used to relate wavenumbers to pixels. The frequency-dependent optical detection efficiency of the setup is corrected using a tungsten halogen light source (Avalight-HAL; Avantes BV, Eerbeek, The Netherlands) with a known emission spectrum. The detector-induced etaloning effect was also compensated by this procedure.

Singular value decomposition (SVD) was applied to the hyperspectral data cubes to reduce the uncorrelated noise resulting in the raw 3D data matrix after converting them to 2D matrix.[25] The SVD treated data was analyzed by both univariate and multivariate data analyses procedures. Univariate Raman images for the specific vibrational band of interest as a function of position were constructed by integrating the band intensities after baseline subtraction.[26] In multivariate analysis, both hierarchical cluster analysis (HCA) and principal component analysis (PCA) were performed. HCA makes use of the scores obtained from the PCA to visualize the regions of high spectral similarities.[27]

Band integration ratios for the data acquired on day 40, 50 and 60 were performed to determine HA growth and variation in composition. The specific bands of interests were baseline corrected before taking ratios. The mineral to matrix band ratios were obtained from the ratios of phosphate band around 957 cm^{-1} (± 1 to 2 cm^{-1}) ($\Delta = \sim 84$ cm^{-1}) corresponding to minerals and phenylalanine at 1001 cm^{-1} ($\Delta = \sim 25$ cm^{-1}) signifying the proteins in the extracellular matrix. The carbonate/phosphate band ratios were calculated from the ratios of carbonate band at 1069 cm^{-1} ($\Delta = \sim 43$ cm^{-1}) and phosphate band at 957 cm^{-1} (± 1 to 2 cm^{-1}).

All data manipulations were performed with routines written in MATLAB 7.4 (The Math Works Inc., Natick, MA). HCA and PCA were performed using PLS toolbox (Eigenvectors Research Inc., Wenatchee, WA) in MATLAB 7.4.

7.3 Results and discussion

iMSCs were successfully cultured on CaF_2 substrates in separate Petri dishes in osteogenic mineralization medium. Cell proliferation, differentiation and mineralization were observed over the period of 60 day culture. Proliferation of iMSCs was observed followed by their differentiation towards osteoblasts. Extracellular matrix marked the osteoblast stage which plays a significant role in HA mineralization. Dex and βGP in osteogenic medium resulted in the differentiation and mineralization of iMSCs. Initial mineralization (*de novo*) was observed around day 30 of culture, which were in the form of small nodules (~10 – 15 µm in size). The nodules were sparsely located in the ECM of the cells cultured on CaF_2 substrate and could be observed by white light transmission microscopy. From day 40 onwards further growth of these nodules and their distribution in the cells cultured on CaF_2 substrate was observed.

In vitro mineralized nodules from day 30 (*de novo*) till day 60 culture were chemically analyzed by high spatial resolution confocal Raman microscopy. Univariate and multivariate data analysis enabled better understanding of mineral composition of these nodules. The chemical composition was observed to vary from *de novo* to late stage of culture due to rapid growth and dynamic variation in the nodules. A strong band for v_1 symmetric stretch vibration for phosphates is the dominant Raman characteristic of these nodules. This band is a biomarker that defines the formation of the apatite and is similar to *in* *vivo* bone. The peak position of this band depends on the type of apatite present in the nodule as observed during the culture.[12] Table 1 illustrates the Raman band position for v_1 vibration modes of phosphates seen for the various apatites over the culture period in comparison with literature.[3, 28] Other bands characteristic of apatite formation in the nodule are v_3 phosphate asymmetric stretch (1030 cm^{-1}), v_2 phosphate symmetric stretch (~ 420 cm^{-1}), v_4 phosphate symmetric stretch (~580 cm^{-1}), A-type carbonation (1106 cm^{-1}) and B-type v_1 carbonate symmetric stretch (1069 cm^{-1}). The occurrence and variation in the B-type and A-type bands determine the bone nodule maturity and degree of crystallinity. The presence of amide-I (1660 cm^{-1}), CH_2 bending (1450 cm^{-1}) and amide-III (1250 cm^{-1}),[14, 16] signify biomarkers for formation of collagen type-I present in the bone nodules and ECM.

Table 1: Raman band position of v_1 symmetric stretch for phosphates for various HA precursors

Mineral	Structure[2]	Wave number of v_1 symmetric stretch for phosphates (cm^{-1})	
		Literature[3, 12, 28-30]	Data from present chapter
Amorphous calcium phosphate (ACP)	$Ca_9(PO_4)_6{\cdot}xH_2O$	945	938
Octacalcium Phosphate (OCP)	$Ca_8H_2(PO_4)_6{\cdot}5H_2O$	957	-
Hydroxyapatite (HAP)	$Ca_{10}(PO_4)_6(OH)_2$	960	956,957,959
Β-Tricalcium phosphate (β-TCP)	$Ca_3(PO_4)_2$	970	968
Monocalcium phosphate monohydrate (MCPM)	$Ca(H_2PO_4)_2{\cdot}H_2O$	988	989
Dicalcium phosphate dihydrate (DCPD)	$CaHPO_4.2H_2O$	998	991

The Raman spectra of *de novo* nodules observed on day 30 of culture are shown in Figure 1. The white light micrographs of nodules are shown in Figures 1A, 1D and 1G. The corresponding HCA images of the nodules are shown in Figures 1B, 1E and 1H. Their respective average spectra after background correction in the spectral region 850 cm^{-1} to 1250 cm^{-1} is shown in Figures 1C, 1F and 1I. Background correction for spectra in each image was performed by subtracting the average spectrum from pixels in the black cluster from the average spectrum from pixels in other clusters. The black cluster corresponds to background which is composed of regions in the ECM of the cells outside the nodules.

Figure 1B shows four cluster HCA image of the nodule shown in Figure 1A. The respective average spectra after background correction are shown in Figure 1C. Green and blue clusters correspond to the nodule and their spectra show bands at 989 cm^{-1} for v_1

symmetric vibration of phosphates, and 1025 cm^{-1} and 1113 cm^{-1} for phosphate symmetric stretch at varying intensity levels. These band positions signify the presence of MCPM.[30] Red spectra correspond to ECM with significant bands for lipids (discussed later in this chapter) along with minor contributions for MCPM. The five cluster HCA image in Figure 1E and respective background corrected average spectra in Figure 1F correspond to the nodule shown in Figure 1D. Magenta, yellow, green and blue clusters correspond to the nodule. The spectra corresponding to the blue, yellow and green clusters show bands at 941 and 968 cm^{-1} for v_1 symmetric vibration, and 1031 cm^{-1} for v_3 symmetric vibration of phosphates, characteristic of the formation of β-TCP[31] in agreement with the literature.[14] The magenta spectrum show bands at 991 cm^{-1} for v_1 symmetric vibration, 1052 cm^{-1} for symmetric stretch and 1147 cm^{-1} for asymmetric stretch of phosphates. These bands signify formation of DCPD.[29] The formation of DCPD is further supported by the absence of bands at 1025 and 1113 cm^{-1} seen for MCPM in Figure 1C. The three cluster HCA image in Figure 1H corresponds to the white light image in Figure 1G. The red and magenta clusters correspond to the nodule. The background corrected average spectra for each cluster are shown in Figure 1I. The red spectrum show bands at 941, 968 and 1031 cm^{-1} depicting formation of β-TCP[31] similar to that seen in Figure 1F. The magenta spectrum show bands at 991 cm^{-1}, 1052 cm^{-1} and 1147 cm^{-1} signifying DCPD which is spectrally similar to the magenta cluster shown in Figure IE.[29] All spectra in Figure 1C, 1F and 1I show a prominent band at around 938 cm^{-1}, which is due to ACP that could be transiently present in the nodule. The formation of ACP was earlier reported by Crane et. al.,[12] and was observed as a spectral shoulder around 945 cm^{-1}.

The ECM formed on the osteoblasts differentiated cells facilitates the initial mineralization by depositing calcium and phosphate ions.[4] This ECM has nucleation sites which consist of non collagenous proteins and acidic phospholipids in addition to calcium and inorganic phosphate that initiate apatite formation.[4] ACP, OCP, β-TCP and DCPD have been observed to act as metastable precursors for synthetically formed HA.[2, 3] Synthesis of DCPD was shown from the reaction of β-TCP and MCPM[32] and by the reaction of MCPM with phosphoric acid.[33] DCPD is also synthesized from the reaction of β-TCP with phosphoric acid. In aqueous medium, DCPD dissolves or hydrolyses resulting in HA in the presence of excess of calcium and HPO_4^{2-} ions.[34, 35] From day 30 culture, the results show the presence of precursors ACP, β-TCP, MCPM and DCPD. Due to the presence of these precursors in the same nodule, the chance of DCPD formation cannot be ruled out.

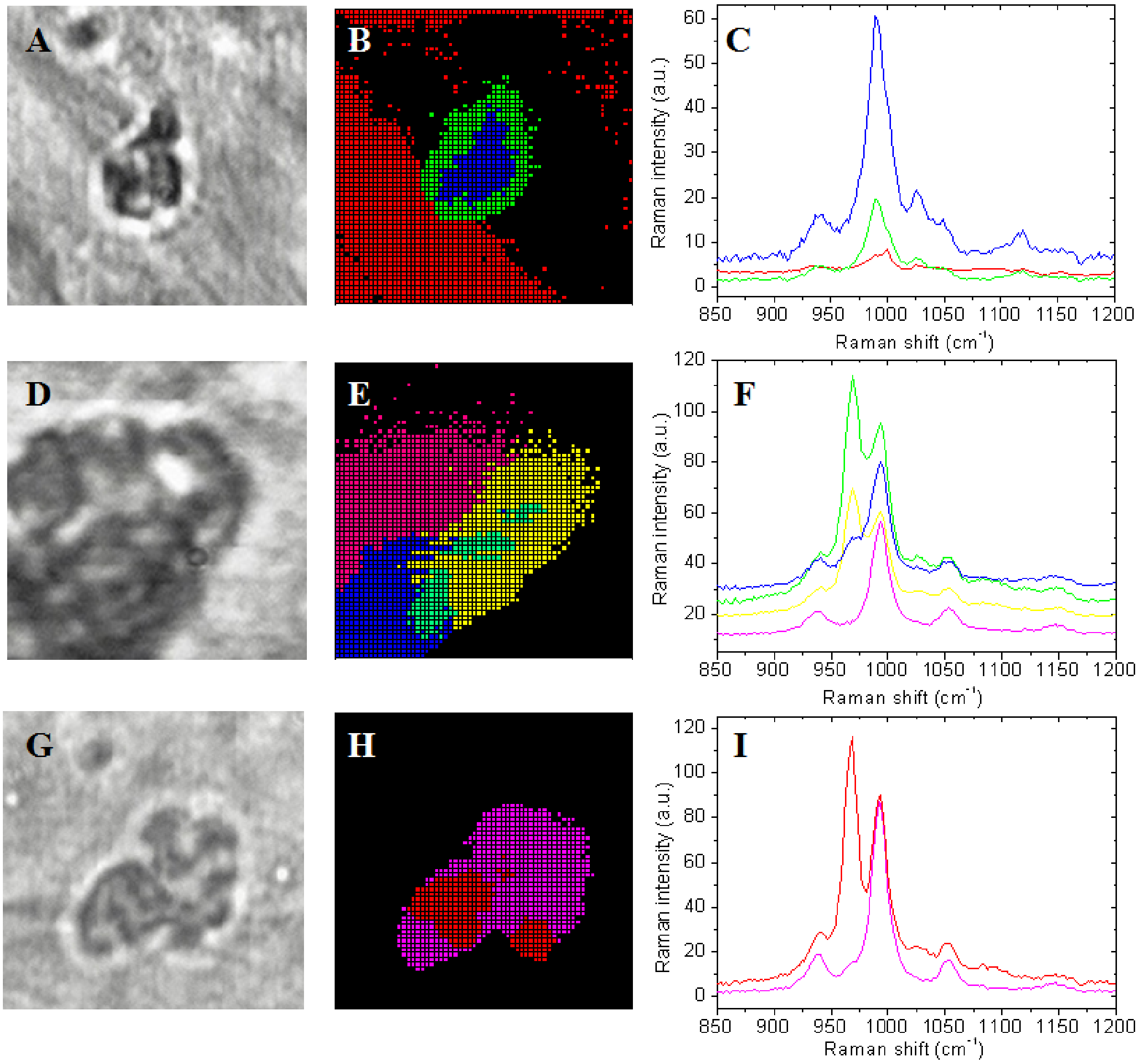

Figure 1: Raman measurements on *de novo* bone nodules measured on day 30 of culture showing heterogeneity in the composition. Measurements performed over an area 20 µm × 20 µm, with spectral resolution of 310 nm and 40 mW laser power. (A), (D) and (G) White light images of *de novo* formed nodules; (B) Four cluster HCA image of the nodule seen in (A); (C) Corresponding average cluster spectra after background correction; (E) Five cluster HCA image of the nodule seen in (D); (F) Corresponding average cluster spectra after background correction. (H) Three cluster HCA image of the nodule seen in (G). (I) Corresponding average cluster spectra after background correction

In Figure 1F, the band at 968 cm^{-1} signifying β-TCP shows significant variation with each cluster compared to 991 cm^{-1} for DCPD. The intensity variations indicate changes in concentration of β-TCP in the respective cluster of the nodule. Green, yellow and blue clusters show presence of both β-TCP and DCPD. The concentration of β-TCP is highest in the green cluster and is seen to decrease in yellow and blue clusters. Magenta spectra do not show the band at 968 cm^{-1}, indicating regions where β-TCP is completely transformed into DCPD. This concentration variation is consistent with the role of β-TCP in the formation of

DCPD as reported in the literature.[34, 35] We observe a similar feature in Figure 1I, wherein the red cluster in Figure 1H show transformation of β-TCP to DCPD and the magenta cluster shows the presence of DCPD with little traces of β-TCP signified by the shoulder band present at 968 cm^{-1}.

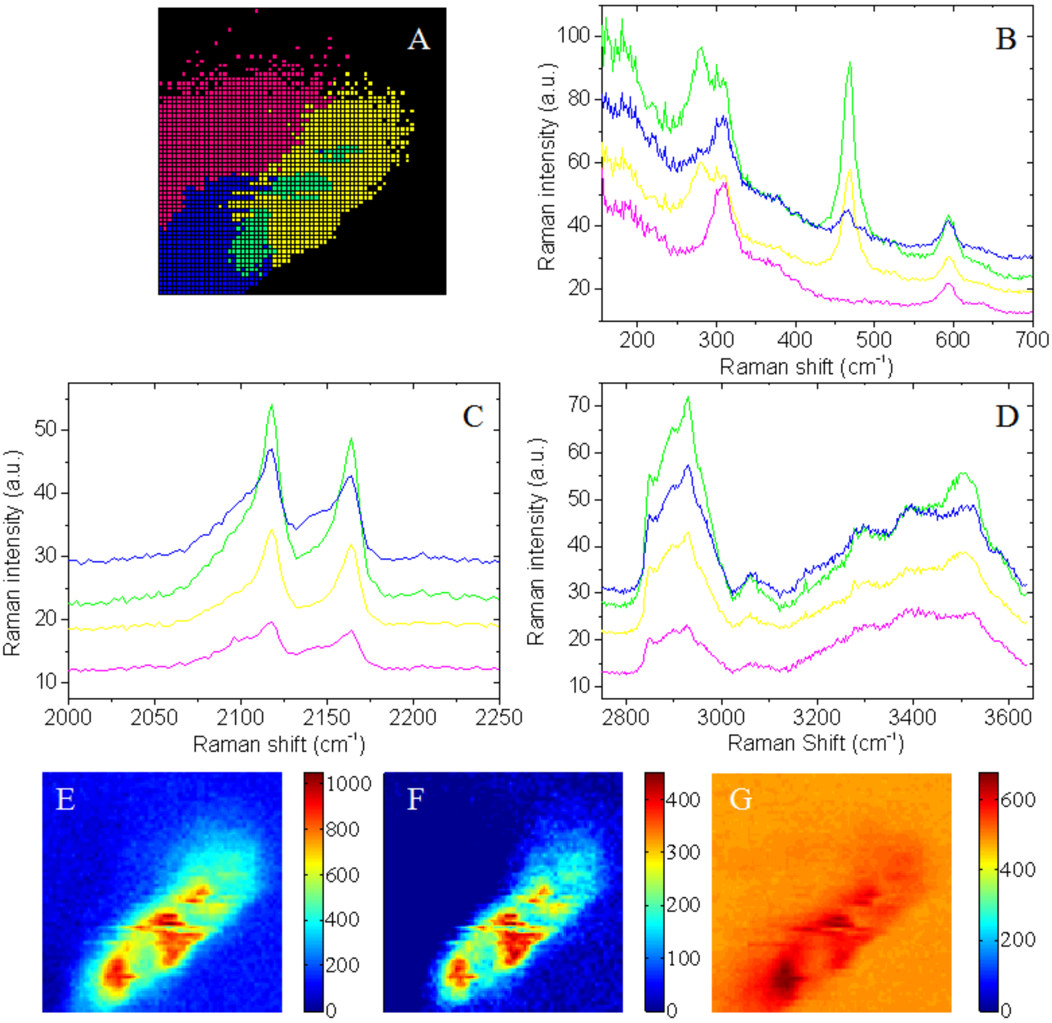

Figure 2: Variations seen in the *de novo* nodule composition showing transformation from β-TCP to DCPD. (A) Five cluster HCA image of the *de novo* bone nodule (see Figure 1E); Corresponding average cluster spectra after background correction in the spectral region (B) 150 - 700 cm^{-1}; (C) 2000 - 2250 cm^{-1}; (D) 2750 - 3650 cm^{-1}; Univariate Raman images for the band (E) 468 cm^{-1} ($\Delta =$ 90 cm^{-1}) for crystal lattice vibration; (F) 968 cm^{-1} ($\Delta =$ 36 cm^{-1}) for v_1 symmetric vibration of phosphates; and (G) 3500 cm^{-1} ($\Delta =$ 100 cm^{-1}) for OH vibrations.

These results provide direct evidence for the formation of HA precursors like ACP, MCPM, DCPD and β-TCP during the early stages of mineralization (day 30) in ECM of cells, in contrast to β-TCP alone as reported earlier.[2, 3, 14] We did not observe the occurrence of the precursor octacalcium phosphate (OCP) during early stages of mineralization, which is in agreement with the literature.[14, 20-22] The presence of different precursors in the same nodule provides evidence of heterogeneity in composition of these nodules formed during early stages of mineralization.

Conversion of mineral from one phase to another results in reorganization of atoms in the crystal lattice structure, and can be studied by confocal Raman microspectroscopy.[29-31] Figure 2A shows a five cluster HCA image of the *de novo* nodule shown in Figure 1E. Background corrected spectra shown in Figure 2B, 2C and 2D correspond to the spectral region 150 cm^{-1} to 700 cm^{-1}, 2000 cm^{-1} to 2250 cm^{-1} and 2750 cm^{-1} to 3650 cm^{-1} respectively. Spectra in Figure 2B show prominent bands at 312 cm^{-1} for v_2 phosphate bending mode, 594 cm^{-1} for v_4 phosphate bending mode, 180 cm^{-1} and 280 cm^{-1} for crystal lattice vibration modes.[31] A band at 468 cm^{-1} is observed to vary in intensity in correspondence with the band at 968 cm^{-1} for β-TCP as shown in Figure 1F. Conversion of β-TCP to DCPD results in reorganization in the crystal lattice structure leading to a band at 468 cm^{-1} which is apparent from the molecular structure (Table 1). The band at 468 cm^{-1} is attributed to the orientation of atoms in the crystal lattice structure, and results from the approximate summation of bands at 180 cm^{-1} and 280 cm^{-1} with respect to both intensity and spectral position.[29, 31] Spectra in Figure 2C show prominent bands at 2117 cm^{-1} and 2163 cm^{-1}. These bands could be due to the presence of magnesium (Mg^{2+}) ions instead of calcium ions (Ca^{2+}) during the early formation of β-TCP. This suggests the presence of magnesium phosphate pentahydrate ($Mg_3(PO_4)_2 \cdot 5H_2O$) which shows bands at 2260 and 2020 cm^{-1} with infrared spectroscopy.[36] Figure 2D show bands at 2849 cm^{-1} for CH_2 symmetric stretch of lipids,[37] 2896 cm^{-1} for CH stretch of proteins[37] and 2931 cm^{-1} CH_2 asymmetric stretch of proteins.[37] The spectra show the dominance of both proteins and lipids in the cluster regions corresponding to the *de novo* nodule. In addition to the different HA precursors, the presence of both lipids and proteins contributes to the heterogeneity in the *de novo* nodule. The proteins and lipids present in the *de novo* nodules are derived from the ECM of the *in vitro* cultured cells.[38] Figure 2D also shows a band at 3500 cm^{-1}, signifying OH vibration in the formed nodule.[39] This band for OH vibration is mainly found in spectra corresponding to β-TCP,[40] which reduces in relation to the conversion of β-TCP to DCPD. Figure 2E, 2F and 2G show the univariate Raman images for the bands at 468 cm^{-1} ($\Delta = 90$ cm^{-1}) for crystal lattice vibration, 968 cm^{-1} ($\Delta = 36$ cm^{-1}) for v_1 symmetric vibration of phosphates for β-TCP and 3500 cm^{-1} ($\Delta = 100$ cm^{-1}) for high frequency OH vibrations respectively. All three univariate images correspond to the cyan and yellow clusters in HCA image (Figure 2A) showing the presence of β-TCP. These images confirm the bands for crystal lattice vibration and OH vibration is due to the presence of β-TCP. Once DCPD is formed from β-TCP, the respective bands disappear.

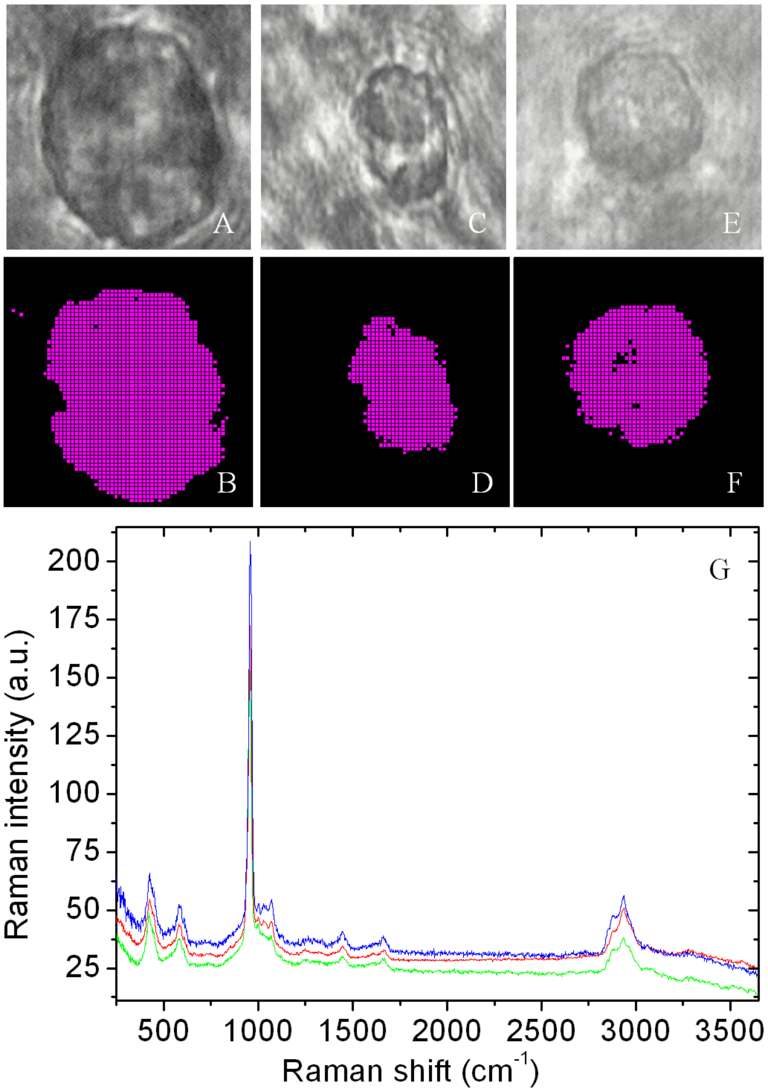

Figure 3: Bone nodules measured on day 40, 50, 60 of culture. Measurements performed over an area 20 µm × 20 µm, with spectral resolution of 310 nm and 40 mW laser power; White light micrographs of nodules measured on (A) day 40 of culture; (C) day 50 of culture; (E) day 60 of culture; (B) two cluster analysis of nodule seen in A; (D) two cluster analysis of nodule seen in C; (F) two cluster analysis of nodule seen in E; (G) Background corrected spectra corresponding to the bone nodules measured on day 40 (green), day 50 (red) and day 60 (blue).

Raman measurements were further performed on samples from day 40, 50, and 60 cultures to understand the growth and development of nodules with time in culture. Figures 3A, 3C and 3E show white light micrographs of the nodules measured on day 40, 50 and 60 of culture, along with their respective two cluster Raman images in Figures 3B, 3D and 3F. The magenta cluster shows the distribution of HA in the nodule and the black cluster showed regions outside the nodule which had information about background/buffer along with minor contributions of HA. The average spectra corresponding to the background is subtracted from average spectra for the nodule to remove the influence of ECM of the cells and buffer in the nodules. Figure 3G shows background corrected spectra of nodules measured on day 40 (green spectrum), day 50 (red spectrum) and day 60 (blue spectrum) of culture in the spectral region from 250 cm^{-1} to 3650 cm^{-1}. The spectra show prominent bands at 423, 582, 957 (±1 to 2 cm^{-1}) and 1030 cm^{-1} for phosphates and a less prominent band at 3550 cm^{-1} for OH vibrations. These bands signify formation of HA[41, 42] from *de novo* nodules seen on day 30 of culture. The occurrence of bands at 1069 cm^{-1} and 1106 cm^{-1} are indicative of the presence of B-type and A-type carbonates respectively, show formation of carbonated hydroxyapatite[5] with culture. The bands at 1660 cm^{-1} for amide-I, 1450 cm^{-1} for CH_2 bending and 1250 cm^{-1} for amide-III signify presence of collagen type-I present in the bone nodules and the ECM.[16]. The presence of bands at 2874 cm^{-1} for CH/CH_2 symmetric stretch[37] and 2935cm^{-1} for CH_2 asymmetric stretch[37] confirms the occurrence of proteins in the formed HA. From day 40 onwards, the formed nodules were homogenous in contrast to the heterogeneous nodules seen early in the culture period. The presence of marker bands for collagen type-I shows the role of proteins in the growth of nodules.

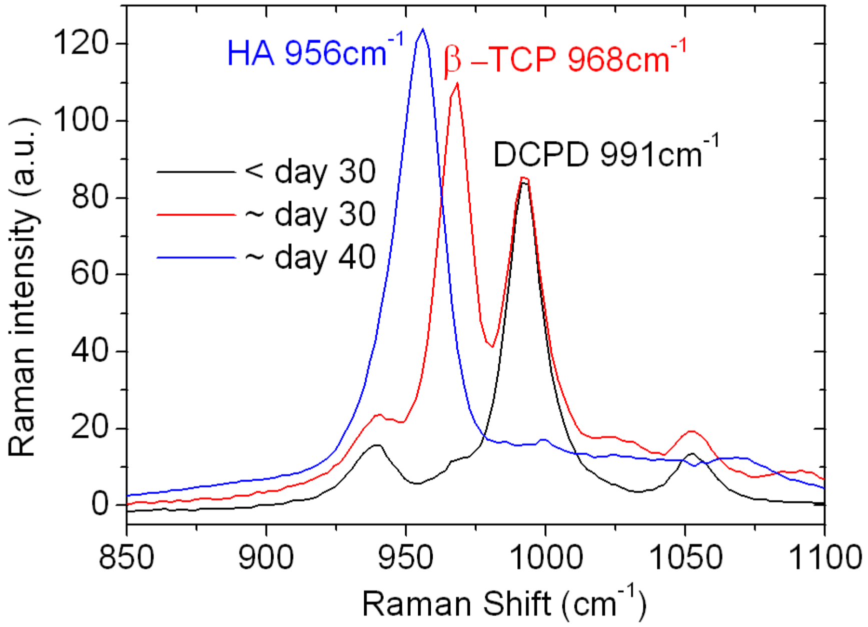

Figure 4: Raman spectra acquired from bone nodules in the spectral range 850 – 1100 cm^{-1} showing shift in peak position along frequency axis for v_1 symmetric vibration of phosphates signifying the transformation of precursors β-TCP (968 cm^{-1}) and DCPD (991 cm^{-1}) on day 30 to HA (956 cm^{-1}) on day 40 of culture.

Figure 4 compares the average spectra of the nodule measured on day 30 and day 40 of culture in the spectral region from 850 cm^{-1} to 1100 cm^{-1}. The plot shows a shift in the v_1 symmetric vibration of phosphates with change in molecular composition of the mineral formed over 30 and 40 days of culture. The red spectrum with bands at 968 cm^{-1} signifies the presence of β-TCP. This β-TCP transforms to DCPD over the same culture time period with a shift in band position to 991 cm^{-1} for phosphates as seen in the black spectra. Further culture until day 40 showed a shift in v_1 vibration of phosphates to 956 cm^{-1} signifying HA formation as seen in the blue spectrum. DCPD, under saturated conditions of calcium and HPO_4^{2-} ions[34, 35] in aqueous media, leads to HA formation in the ECM. This shift in band position signifies the change in chemical composition of the nodule from *de novo* bone nodule to HA.

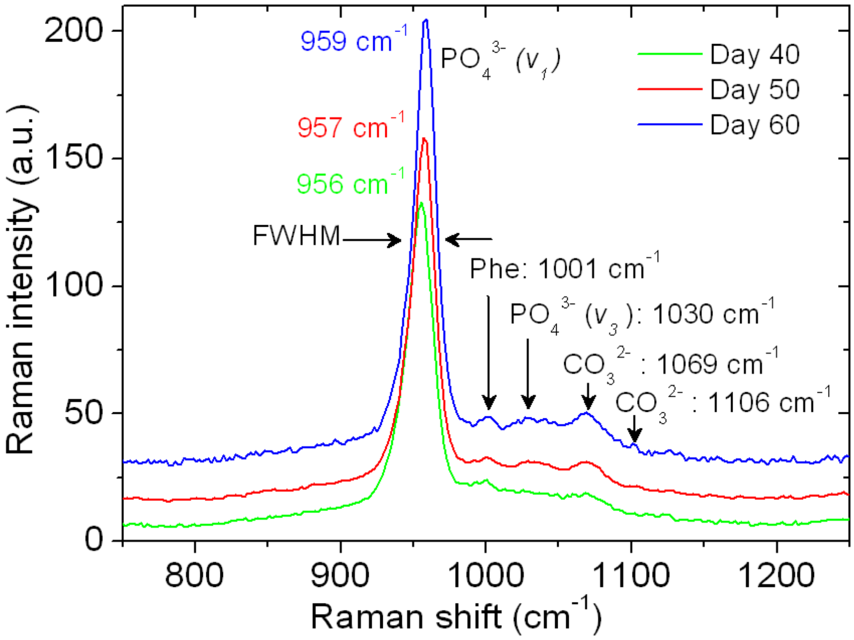

Figure 5: Raman spectra acquired from bone nodules in the spectral range 750 – 1250 cm^{-1} measured on day 40, 50 and 60 of culture illustrating conversion of HA to CHA. The plot shows a shift in band position along the frequency axis and reduction in FWHM for v_1 symmetric vibration of phosphates, and an increase in peak intensity at 1069 and 1106 cm^{-1} for B-type and A-type carbonates.

Figure 5 shows a closer look at the spectral region from 750 cm^{-1} to 1250 cm^{-1} seen in Figure 3G. The spectra depict variation in the formed HA over day 40, 50 and 60 cultures. The band for v_1 symmetric vibration of phosphates shifts from 956 cm^{-1} on day 40 to 957 cm^{-1} on day 50 and finally to 959 cm^{-1} on day 60 of culture. The band at 1069 cm^{-1} corresponding to v_1 carbonate symmetric stretch increases with culture. This signifies onset of B-type carbonation, where the phosphates (PO_4^{3-}) in the HA molecule are substituted by the carbonates (CO_3^{2-}). Similarly, another band for carbonates at 1106 cm^{-1} is seen on day 50 and increases by day 60 of culture, signifying A-type carbonation where CO_3^{2-} replaces OH^- groups in the formed HA.[11] The simultaneous shift in the band position for v_1 symmetric vibration of phosphates and increase in band for B-type v_1 carbonates symmetric stretch signifies change in the apatite molecular structure towards crystalline form.[13, 15, 18] The full width at half maxima (FWHM) value calculated for the band v_1 symmetric vibration of phosphates after baseline correction is shown in Table 2. A gradual decrease in the bandwidth from 23.2 cm^{-1} on day 40 to 21.10 cm^{-1} on day 50 and to 18.8 cm^{-1} on day 60 of culture is observed. The shift in band for v_1 symmetric vibration of phosphates, the increase in bands at 1069 and 1106 cm^{-1} for carbonates, and the reduction in the FWHM of the v_1 symmetric vibration of phosphates confirms the increase in crystallinity of the formed HA with the culture period.[13, 15, 18] The increase in addition of carbonates to the formed HA with time leads to formation of carbonated HA which is reminiscent of *in vivo* bone.[43]

Table 2: Variation in v_1 symmetric stretch for phosphates in relation to peak position and width with culture period

Culture period	Phosphate peak position (v_1)	Phosphate (v_1) FWHM (cm^{-1})
Day 40	956	23.17
Day 50	957	21.05
Day 60	959	18.75

Table 3: Variation in band integration ratios for mineral/ matrix and carbonates/phosphates with culture period

Culture period	Mineral / Matrix ratio	Carbonate /Phosphate ratio
Day 40	84.106 (±43.634)	0.027 (±0.004)
Day 50	148.91 (±28.426)	0.038 (±0.001)
Day 60	235.977 (±50.710)	0.041 (±0.002)

We calculated the ratios of specific integrated Raman bands to determine the growth and crystallinity of the formed HA. The increase in growth of the HA formed in the ECM during the culture was determined by the mineral to matrix ratio,[13] calculated for day 40, 50 and 60 of culture (Figure 6A). The plot shows a gradual increase in ratio with culture, suggesting growth in HA formation from day 40 till 60 of culture (Table 3). However the amount of mineral formed varies for each measured nodule, and is accompanied with a large variation in the standard deviation for each measurement day. The carbonates to phosphates band integration ratios are shown in Figure 6B. The plot shows a gradual increase from day 40 to day 60 of culture (Table 3), which is attributed to the increase in the carbonate content of the formed HA mineral during culture. This resulted in the variation of crystallinity in the molecular structure of HA.[15, 18] The standard deviation for each measurement day shows less variation than the mineral/matrix ratio, and is indicative of the homogeneity in crystallinity of the measured HA nodules. These results indicate that growth of the mineral formed in the ECM over time leads to increase in carbonate deposition of the formed apatite leading to crystalline CHA.

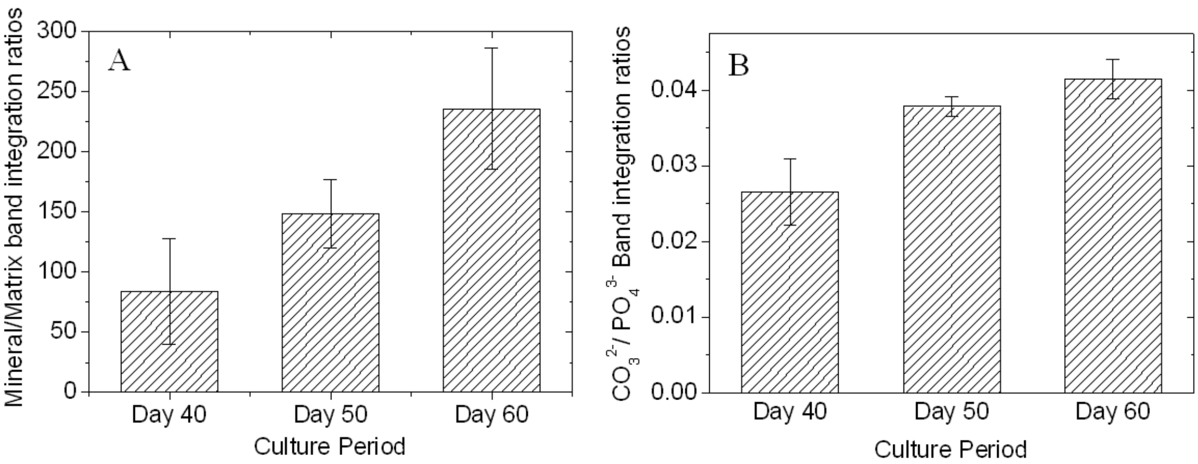

Figure 6: Integrated band intensity ratios for three randomly chosen nodules on day 40, 50 and 60 of culture showing growth in apatite and increase in crystallinity. (A) Mineral to matrix band integration ratio showing increase in mineral content with time, (B) Carbonates to phosphates band integration ratio showing increase in crystallinity with time.

During the 60 day culture period, we observe initiation and growth of apatite accompanied by variation in crystallinity of the formed apatite. The ECM plays a vital role in the said mineralization process. As observed for inorganic minerals/apatites, the organic composition of the bone nodule was observed to vary in time. The differentiated osteoblasts secrete ECM which enables initial mineral deposition. ECM has “nucleation cores”, composed of proteins, acidic phospholipids, calcium and inorganic phosphate which facilitate the process of mineralization.[4] The ECM also provides enzymes like pyrophosphates and proteoglycans which degrade inhibitors of mineralization.[4] Figure 7A shows variation in the composition of the nodules in the spectral range 1175 cm^{-1} to 1750 cm^{-1} from day 30 to day 60 of culture. Day 30 spectra show important bands at 1300 cm^{-1} for CH_2 stretching, 1440 cm^{-1} for CH_2 bending and 1656 cm^{-1} for C=O stretch signifying the prominent presence of lipids. The presence of lipids in the early formed nodules is direct evidence for a proposition by Xu et. al.,[44] who suggested the involvement of lipids during mineralization of collagen type-I. Further culture towards day 40 and day 50 show occurrence of bands at 1250 cm^{-1} for amide-III, 1335 cm^{-1} for CH_2/CH_3 wagging mode of collagen type-I, 1445 cm^{-1} for CH_2/CH_3 bending mode of collagen type-I and 1664 cm^{-1} for amide-I, which are attributed to collagen type-I in the nodules. On day 60 of culture, we see prominent bands at 1250 cm^{-1}, 1445 cm^{-1} and 1664 cm^{-1}, which signify sufficient presence of collagen type-I in the nodule as expected.[16] Day 30 culture shows important bands for lipids at 1440 cm^{-1}, however further culture from day 40 till day 60 shows the bands for proteins 1445 cm^{-1} and 1664 cm^{-1}. The bands at 1583/1603 cm^{-1} which are characteristic of phenylalanine gradually reduces from day 30 till day 60. On day 30 of culture, the bands for phenylalanine are seen at 1583 cm^{-1} (C=C bending) and 1602 cm^{-1}, which shifts to 1607 cm^{-1} on day 40 and day 50 culture. However the intensity of 1607 cm^{-1} on day 50 is less than that of day 40. The dominance of proteins from day 40 till day 60 supports crystallization of the HA as described in Figure 5. Proteins are essential components in the process of crystallization of the formed nodule.[45]

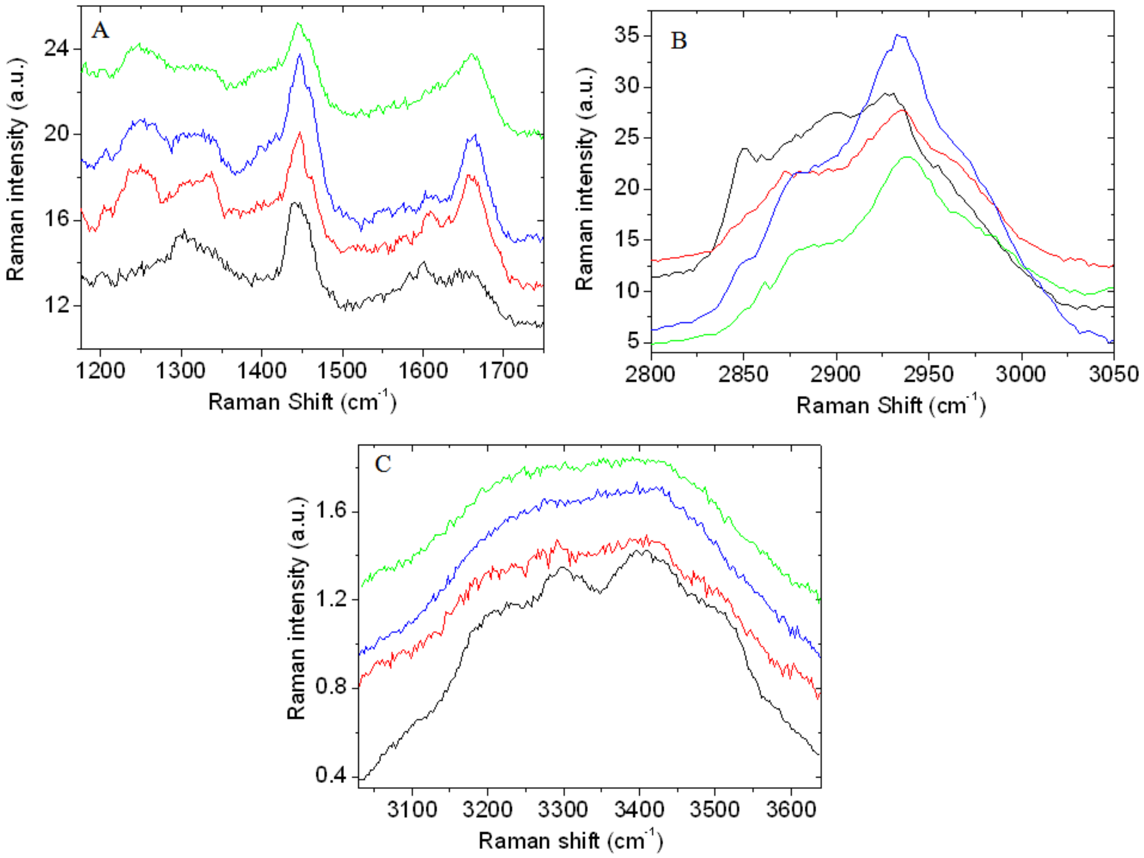

Figure 7: Raman spectra showing change in the organic composition from lipids to proteins in the bone nodule measured on day 30 (black), day 40 (red), day 50 (blue) and day 60 (green) of culture in the spectral region (A) 1175 to 1750 cm^{-1}; (B) 2800 to 3050 cm^{-1}; and (C) 3025 to 3650 cm^{-1}.

The spectral region from 2800 cm^{-1} till 3050 cm^{-1} shown in Figure 7B describes the variation in high frequency vibrational bands for proteins and lipid from day 30 till day 60 of the culture. On day 30 of culture, we see prominent bands at 2849 cm^{-1} for CH_2 symmetric stretch for lipids,[37] 2900 cm^{-1} for CH stretch of lipids[37] and at 2931 cm^{-1} for CH_2 asymmetric stretch. For day 40 till day 60, we see the band at 2849 cm^{-1} for CH_2 symmetric stretch of lipids gradually decreasing, which is accompanied by increase in band at 2938 cm^{-1} for CH vibration of proteins. This variation in bands indicates a decrease in lipids in the nodule after day 30 of culture and increase in presence of proteins from day 40 till day 60 of culture. The results in Figure 7B are in correspondence with that seen in Figure 7A, showing the influence of lipids in early stages of mineral formation which are replaced by proteins during later stage of culture enabling the growth of apatite.

Figure 7C shows variation in the composition of the nodules in the high frequency spectral region ranging from 3025 cm^{-1} to 3650 cm^{-1} from day 30 to day 60 of culture. On day 30 of culture, the spectrum shows prominent bands at 3300 cm^{-1} for OH stretch of lipids[46] and N-H vibration of proteins and 3400 cm^{-1} for OH stretching.[47] We observe bands at 3200 cm^{-1} for O-H and N-H stretching vibrations[48] and 3500 cm^{-1} for O-H vibrations in apatites.[39] On day 40 of culture, the bands occur at similar positions, are less intense compared to day 30 of culture. These bands disappear by day 50 and day 60 of culture. The bands gradually reduce in accordance with the reduction of lipid bands as seen in Figure 7A and 7B. We presume that these are the high frequency vibrational modes for lipids that correspond to N-H and O-H. The band at 3500 cm^{-1} for OH vibrations in apatites reduces from day 30 to day 40 and then disappears on day 50 and day 60 of culture period, which is due to A-type carbonation where CO_3^{2-} replaces the OH^- in the formed HA.

The spectral variations observed from the composition of nodules from day 30 till day 60 of culture shows conversion of mineral composition of the nodule from *de novo* stage till formation of carbonated hydroxyapatite. This variation is guided by the extracellular matrix formed on the differentiated stromal cells. The early stage of the nodule is composed of lipids, which are replaced by proteins during the later stage. This process may leads to change in the pH of the mineralization medium which is necessary for the conversion of apatite from one form to another along with the enzymes present in ECM.[38, 44] These results show the activity of ECM in the events of mineralization which again hints at the role of cells in the process.

7.4 Conclusions

We monitored the progression of mineralization events of *in vitro* differentiated iMSCs by confocal Raman microspectroscopy over a period of 60 days in culture. The non-invasive and label-free approach enabled us to visualize and understand the progression in ECM mineralization from *de novo* stage to carbonate HA. Early *de novo* mineralization was observed around day 30 of culture, which was sparsely distributed in the ECM. *De novo* mineralization was characterized by the formation of metastable precursors such as MCPM, ACP, β-TCP, and DCPD. The presence of these precursors was seen in combination with lipids, signifying the heterogeneity in the early formed bone nodules. Day 40 culture showed the formation of HA, which transformed to carbonate HA by day 50 and 60 of culture that chemically resembles *in vivo* bone. The bone precursor DCPD was formed from MCPM and β-TCP under the influence of acidic phospholipids, proteins, calcium and inorganic phosphates. DCPD resulted in HA formation by day 40 of culture due to dissolution/ hydrolysis by saturated calcium and HPO_4^{2-} ions. Culture periods from day 40 onwards showed homogenous distribution of HA with prominent presence of proteins in the ECM. Incorporation of the carbonates in the HA leading to A- and B-type carbonation at later stages of the culture increased the crystalline nature of the formed HA. The crystalline nature of the HA is supported by the decrease in the FWHM and shift in band position of the v_1 symmetric vibration for phosphates. The mineral to matrix band ratios and carbonates to phosphates band ratios further showed the growth of mineral apatite accompanied by increase in crystallinity with culture period. The presence of lipids in nodules during early stage of mineralization and their replacement with proteins at later stages, show the role of ECM in the events of mineralization.

References

1. Davies, J. E., *Bone Engineering*. 1st ed.; Em Squared Inc: Toronto, 2000.
2. Johnsson, M. S.; Nancollas, G. H., The role of brushite and octacalcium phosphate in apatite formation. *Crit Rev Oral Biol Med* **1992,** 3, (1-2), 61-82.
3. Sauer, G. R.; Zunic, W. B.; Durig, J. R.; Wuthier, R. E., Fourier transform Raman spectroscopy of synthetic and biological calcium phosphates. *Calcif. Tissue Int.* **1994,** 54, (5), 414-20.
4. Favus, M. J., *Primer on the Metabolic Bone Diseases And Disorders of Mineral Metabolism*. 6th ed.; ASMBR: Washington D.C., 2006.
5. Penel, G.; Leroy, G.; Rey, C.; Bres, E., Micro Raman Spectral Study of the PO_4 and CO_3 Vibrational Modes in Synthetic and Biological Apatites. *Calcif. Tissue Int.* **1998,** 63, (6), 475-481.
6. Bonewald, L. F.; Harris, S. E.; Rosser, J.; Dallas, M. R.; Dallas, S. L.; Camacho, N. P.; Boyan, B.; Boskey, A., Von Kossa staining alone is not sufficient to confirm that mineralization *in vitro* represents bone formation. *Calcif. Tissue Int.* **2003,** 72, (5), 537-547.
7. Stanford, C. M.; Jacobson, P. A.; Eanes, E. D.; Lembke, L. A.; Midura, R. J., Rapidly forming apatitic mineral in an osteoblastic cell line (UMR 106-01 BSP). *J Biol Chem* **1995,** 270, (16), 9420-8.
8. Gerstenfeld, L. C.; Chipman, S. D.; Glowacki, J.; Lian, J. B., Expression of differentiated function by mineralizing cultures of chicken osteoblasts. *Dev. Biol.* **1987,** 122, (1), 49-60.
9. Wu, Y.; Glimcher, M. J.; Rey, C.; Ackerman, J. L., A unique protonated phosphate group in bone mineral not present in synthetic calcium phosphates. Identification by phosphorus-31 solid state NMR spectroscopy. *J Mol Biol* **1994,** 244, (4), 423-35.
10. Boskey, A. L.; Camacho, N. P.; Mendelsohn, R.; Doty, S. B.; Binderman, I., FT-IR microscopic mappings of early mineralization in chick limb bud mesenchymal cell cultures. *Calcif Tissue Int* **1992,** 51, (6), 443-8.
11. Carden, A.; Morris, M. D., Application of vibrational spectroscopy to the study of mineralized tissues (review). *J. Biomed. Opt.* **2000,** 5, (3), 259-268.
12. Crane, N. J.; Popescu, V.; Morris, M. D.; Steenhuis, P.; Ignelzi, M. A., Raman spectroscopic evidence for octacalcium phosphate and other transient mineral species deposited during intramembranous mineralization. *Bone* **2006,** 39, (3), 434-442.**2009,**
13. Chiang, H. K.; Peng, F.-Y.; Hung, S.-C.; Feng, Y.-C., In situ Raman spectroscopic monitoring of hydroxyapatite as human mesenchymal stem cells differentiate into osteoblasts. *J. Raman Spectrosc.* 40, (5), 546-549.
14. Stewart, S.; Shea, D. A.; Tarnowski, C. P.; Morris, M. D.; Wang, D.; Franceschi, R.; Lin, D. L.; Keller, E., Trends in early mineralization of murine calvarial osteoblastic cultures: A Raman microscopic study. *J. Raman Spectrosc.* **2002,** 33, (7), 536-543.
15. Tarnowski Catherine, P.; Ignelzi Michael, A., Jr.; Morris Michael, D., Mineralization of developing mouse calvaria as revealed by Raman microspectroscopy. *J Bone Miner Res* **2002,** 17, (6), 1118-26.
16. Timlin, J. A.; Carden, A.; Morris, M. D., Chemical microstructure of cortical bone probed by Raman transects. *Appl. Spectrosc.* **1999,** 53, (11), 1429-1435.
17. Timlin, J. A.; Carden, A.; Morris, M. D.; Rajachar, R. M.; Kohn, D. H., Raman Spectroscopic Imaging Markers for Fatigue-Related Microdamage in Bovine Bone. *Anal. Chem.* **2000,** 72, (10), 2229-2236.
18. De Grauw, C. J.; De Bruijn, J. D.; Otto, C.; Greve, J., Investigation of bone and calcium phosphate coatings and crystallinity determination using Raman microspectroscopy. *Cells Mater.* **1996,** 6, (1-3), 57-62.
19. Pittenger, M. F., Multilineage potential of adult human mesenchymal stem cells. *Science* **1999,** 285, (5428), 665.
20. Kuhn, L. T.; Wu, Y.; Rey, C.; Gerstenfeld, L. C.; Grynpas, M. D.; Ackerman, J. L.; Kim, H.-m.; Glimcher, M. J., Structure, composition, and maturation of newly deposited calcium-phosphate crystals in chicken osteoblast cell cultures. *J. Bone Miner. Res.* **2000,** 15, (7), 1301-1309.

21. Rey, C.; Kim, H. M.; Gerstenfeld, L.; Glimcher, M. J., Structural and chemical characteristics and maturation of the calcium-phosphate crystals formed during the calcification of the organic matrix synthesized by chicken osteoblasts in cell culture. *J. Bone Miner. Res.* **1995,** 10, (10), 1577-88.
22. Rey, C.; Kim, H. M.; Gerstenfeld, L.; Glimcher, M. J., Characterization of the apatite crystals of bone and their maturation in osteoblast cell culture: comparison with native bone crystals. *Connect Tissue Res* **1996,** 35, (1-4), 343-9.
23. Gentleman, E.; Swain, R. J.; Evans, N. D.; Boonrungsiman, S.; Jell, G.; Ball, M. D.; Shean, T. A. V.; Oyen, M. L.; Porter, A.; Stevens, M. M., Comparative materials differences revealed in engineered bone as a function of cell-specific differentiation. *Nat. Mater.* **2009,** 8, (9), 763-770.
24. Pully, V. V.; Lenferink, A.; Otto, C., Hybrid Rayleigh, Raman and two-photon excited fluorescence spectral confocal microscopy of living cells. *J. Raman Spectrosc.* **2009,** 10.1002/jrs.2501.
25. Uzunbajakava, N.; Greve, J.; Otto, C., Raman microscopy of cells: chemical imaging of apoptosis. *Proc. SPIE-Int. Soc. Opt. Eng.* **2003,** 4963, (Multiphoton Microscopy in the Biomedical Sciences III), 223-230.
26. Uzunbajakava, N.; Lenferink, A.; Kraan, Y.; Volokhina, E.; Vrensen, G.; Greve, J.; Otto, C., Nonresonant confocal Raman imaging of DNA and protein distribution in apoptotic cells. *Biophys. J.* **2003,** 84, (6), 3968-3981.
27. van Manen, H.-J.; Kraan, Y. M.; Roos, D.; Otto, C., Single-cell raman and fluorescence microscopy reveal the association of lipid bodies with phagosomes in leukocytes. *Proc. Natl. Acad. Sci. U. S. A.* **2005,** 102, (29), 10159-10164.
28. Penel, G.; Leroy, N.; Van Landuyt, P.; Flautre, B.; Hardouin, P.; Lemaitre, J.; Leroy, G., Raman microspectrometry studies of brushite cement: *in vivo* evolution in a sheep model. *Bone* **1999,** 25, (2 Suppl), 81S-84S.
29. Xu, J.; Butler, I. S.; Gilson, D. F. R., FT-Raman and high-pressure infrared spectroscopic studies of dicalcium phosphate dihydrate (CaHPO4.2H2O) and anhydrous dicalcium phosphate (CaHPO4). *Spectrochim. Acta, Part A* **1999,** 55A, (14), 2801-2809.
30. Xu, J.; Gilson, D. F. R.; Butler, I. S., FT-Raman and high-pressure FT-infrared spectroscopic investigation of monocalcium phosphate monohydrate, Ca(H2PO4)2.H2O. *Spectrochim. Acta, Part A* **1998,** 54A, (12), 1869-1878.
31. de Aza, P. N.; Santos, C.; Pazo, A.; de Aza, S.; Cusco, R.; Artus, L., Vibrational Properties of Calcium Phosphate Compounds. I. Raman Spectrum of beta -Tricalcium Phosphate. *Chem. Mater.* **1997,** 9, (4), 912-915.
32. Lemaitre, J.; Mirtchi, A.; Mortier, A., Calcium phosphate cements for medical use: state of the art and perspectives of development. *Silic. Ind.* **1987,** 52, (9-10), 141-6.
33. Bohner, M.; Lemaitre, J.; Ring, T. A., Effects of sulfate, pyrophosphate, and citrate ions on the physicochemical properties of cements made of beta -tricalcium phosphate-phosphoric acid-water mixtures. *J. Am. Ceram. Soc.* **1996,** 79, (6), 1427-1434.
34. Constantz, B. R.; Barr, B. M.; Ison, I. C.; Fulmer, M. T.; Baker, J.; McKinney, L.; Goodman, S. B.; Gunasekaren, S.; Delaney, D. C.; Ross, J.; Poser, R. D., Histological, chemical, and crystallographic analysis of four calcium phosphate cements in different rabbit osseous sites. *J. Biomed. Mater. Res.* **1998,** 43, (4), 451-461.
35. Frayssinet, P.; Gineste, L.; Conte, P.; Fages, J.; Rouquet, N., Short-term implantation effects of a DCPD-based calcium phosphate cement. *Biomaterials* **1998,** 19, (11-12), 971-7.
36. Carmona, P.; Bellanato, J.; Escolar, E., Infrared and Raman spectroscopy of urinary calculi: a review. *Biospectroscopy* **1997,** 3, (5), 331-346.
37. Koljenovic, S.; Schut, T. B.; Vincent, A.; Kros, J. M.; Puppels, G. J., Detection of Meningioma in Dura Mater by Raman Spectroscopy. *Anal. Chem.* **2005,** 77, (24), 7958-7965.
38. van de Lest, C. H. A.; Vaandrager, A. B., Mechanism of cell-mediated mineralization. *Curr. Opin. Orthop.* **2007,** 18, (5), 434-443.

39. Rey, C.; Miquel, J. L.; Facchini, L.; Legrand, A. P.; Glimcher, M. J., Hydroxyl groups in bone mineral. *Bone* **1995,** 16, (5), 583-6.
40. Cusco, R.; Guitian, F.; De Aza, S.; Artus, L., Differentiation between hydroxyapatite and beta -tricalcium phosphate by means of micro -Raman spectroscopy. *J. Eur. Ceram. Soc.* **1998,** 18, (9), 1301-1305.
41. de Aza, P. N.; Guitian, F.; Santos, C.; de Aza, S.; Cusco, R.; Artus, L., Vibrational Properties of Calcium Phosphate Compounds. 2. Comparison between Hydroxyapatite and beta -Tricalcium Phosphate. *Chem. Mater.* **1997,** 9, (4), 916-922.
42. Morris, M. D.; Finney, W. F., Recent developments in Raman and infrared spectroscopy and imaging of bone tissue. *Spectroscopy* **2004,** 18, (2), 155-159.
43. Rey, C., Calcium phosphate biomaterials and bone mineral. Differences in composition, structures and properties. *Biomaterials* **1990,** 11, (BIOMAT 89), 13-15.
44. Xu, S.; Yu, J. J., Beneath the minerals, a layer of round lipid particles was identified to mediate collagen calcification in compact bone formation. *Biophys. J.* **2006,** 91, (11), 4221-4229.
45. Weiner, S.; Sagi, I.; Addadi, L., Structural biology: Choosing the crystallization path less traveled. *Science* **2005,** 309, (5737), 1027-1028.
46. Krafft, C.; Neudert, L.; Simat, T.; Salzer, R., Near infrared Raman spectra of human brain lipids. *Spectrochim. Acta, Part A* **2005,** 61A, (7), 1529-1535.
47. Caspers, P. J.; Lucassen, G. W.; Carter, E. A.; Bruining, H. A.; Puppels, G. J., *In vivo* confocal Raman microspectroscopy of the skin: noninvasive determination of molecular concentration profiles. *J. Invest. Dermatol.* **2001,** 116, (3), 434-442.
48. Eckel, R.; Huo, H.; Guan, H.-W.; Hu, X.; Che, X.; Huang, W.-D., Characteristic infrared spectroscopic patterns in the protein bands of human breast cancer tissue. *Vib. Spectrosc.* **2001,** 27, (2), 165-173.

Chapter 8

Role of phospholipids and collagen in bone formation

Multipotent adult human bone marrow stromal cells are known to differentiate towards osteogenic lineage followed by mineralization which is similar to in vivo bone. In this chapter, we show non-invasive and label-free monitoring by Raman microspectroscopy, coherent anti-Stokes Raman scattering (CARS) microscopy, and second harmonic generation (SHG) microscopy of in vitro cell-based bone formation. Human immortalized bone marrow derived stromal cells (iMSCs) are cultured in osteogenic culture medium for 60 days, which induces differentiation towards osteogenic lineage followed by mineralization. The detection of Raman biomarkers for collagen fibrils, glycosaminoglycans (GAGs) and cholesterol in cells by day 25 and 30 indicate well differentiated osteogenic lineage. Calcium active phospholipids (phosphatidic acid (PA), phosphatidylserine (PS) and cholesterol) observed from day 25 influenced early mineralization on day 35 of culture. The distribution of phospholipids in the cells increased up to day 45; beyond this point phospholipid content in the cell decreased commensurate with a corresponding increase in mineralization. Cell proliferation showed multiple layers of cells, with each layer identified by distribution of collagen in the extracellular matrix (ECM) of the cells. Collagen fibrils were orthogonally oriented with respect to the adjacent layers of cells. These collagen fibrils guide the initiation and growth of the hydroxyapatite (HA) in the ECM of iMSCs. The initial mineral depositions were similar to HA in composition, followed by accretion with further culture. Gradual conversion of HA to carbonated hydroxyapatite (CHA) was observed from day 45 onwards. The *increase in CHA influenced the increase in crystallinity of formed apatite. Prominent Raman bands for phosphates and carbonates are functional biomarkers for osteogenic mineralization. The ECM during this process developed from a lipid-rich to a protein-rich matrix, suggesting its role in initiation and growth of HA. This long term in vitro study illustrates cell-based bone formation, including differentiation of cells followed by initiation and growth of HA mineralization by a non-invasive and label-free approach.*

Manuscript in preparation

8.1 Introduction

In vivo bone formation occurs as a series of well-controlled biochemical and cellular events. *In vivo* bone formation is characterized by mineralization of HA due to intra-membranous or endochondral ossification which are mediated by osteoblasts and chondrocytes respectively. In intra-membranous ossification, mineralization takes place in the extracellular matrix of osteoblasts that is composed of collagenous (collagen type-I) and non-collagenous proteins.[1, 2] On the other hand, endochondral ossification constitutes a cartilage template formed by chondrocytes enabling mineralization.[2, 3]

Over the last decade, *in vitro* differentiation of multipotent human mesenchymal stromal cells (MSCs) towards osteogenic lineage[4-6] has been explored to understand the biology of bone formation. MSCs differentiate to osteogenic lineage upon the influence of specific growth factors that lead to mineralized bone formation.[6] The mineralization process is hypothesized to occur in one of the following two ways. In the first hypothesis, cells synthesize collagen type-I with holes and pores in the interfibrillar spaces. These holes and pores are composed with non-collagenous proteins such as tissue non-specific alkaline phosphatase, bone sialoprotein, osteocalcin and osteopontin which help in mineralization.[2] The second hypothesis suggests formation of matrix vesicles (0.1-1μm) (MVs) which are cell-derived extracellular membrane-enclosed particles that initialize mineralization.[7] The matrix vesicles are composed of calcium binding phospholipids (Phosphatidic acid (PA), Phosphatidylserine (PS) and Phosphatidylinositol (PL)),[8] phosphates from alkaline phosphate activity, proteins and small amounts of collagen type-II. These MVs enable initial mineralization.[8-10] Recently the role of cholesterol biosynthetic pathway in osteoblast differentiation of MSCs is well demonstrated.[11, 12] This pathway leads to synthesis of cholesterol which are accumulated in the cell membrane and play a vital role in differentiation of MSCs towards osteoblasts. Biomimetic studies of cholesterol in simulated body fluids revealed its active role in HA mineralization.[13, 14]

In recent studies extensive work has been done to understand the mineralization process of bone. Kale et. al. showed that the development of cells into a three dimensional structure is necessary for *ex vivo* bone formation.[15] Bone formation is identified by conventional staining procedures such as von Kossa for phosphates or alizarin red for calcium ions. These staining procedures are highly destructive to cells and not specific to the mineral apatites that are formed.[2, 16] Recently, the formation of nodules in different cell types were studied by Raman spectroscopy, showing that mineralization was influenced by phospholipids in embryonic stem cells and proteins in MSCs and osteoblasts.[17, 18] Electron microscopic studies showed different patterns of mineralization in rat calvarial osteoblasts, when cultured in osteogenic media with and without β-Glycerophosphate.[10] Similar studies of chicken embryo osteoblasts demonstrated three to four layers of cells. Each layer of cells showed ultra structural assembly of the collagen fibrils and their role in the mineralization process.[19] Fourier transform infrared spectroscopy (FTIR) on chicken osteoblasts revealed formation of calcium phosphate and its conversion towards carbonated calcium phosphates with culture.[20, 21] The structure, composition and maturation of these apatites were further classified by X-Ray Diffraction (XRD) and Nuclear Magnetic Resonance (NMR) spectroscopy.[22] Boskey et. al. demonstrated the role of phospholipids in mineralization using chicken osteoblasts.[23, 24] This observation is supported by Xu et. al. who reported the occurrence of lipids underneath the mineralized layer. These lipids played a vital role in calcification of collagen in formation of compact bone.[25]

Analytical techniques such as confocal Raman microspectroscopy and CARS microscopy are powerful methods that enable non-invasive and label-free analysis of chemical and molecular information from samples. Raman spectroscopy has proven to be useful for bone tissue engineering applications.[17, 26, 27] CARS is a chemically selective imaging tool which is capable of three dimensional imaging with sub-micrometer resolution.[28, 29] Due to the coherent nature of the CARS process and high collection efficiency, it is applied for pharmaceutical[30] and biological applications such as studies on lipid distribution,[31] living cells[32] and tissues.[33] Second harmonic generation (SHG), is a non-centrosymmetric sensitive technique, and enables label free imaging similar to Raman and CARS. SHG is successfully applied for visualization of collagen fibrils in biological samples.[34-36] Both SHG and CARS have intrinsic three dimensional resolutions which enable noninvasive imaging at relatively large penetration depths.

In this chapter, we monitor the differentiation and mineralization of iMSCs in osteogenic culture medium for up to 60 days. Cells were periodically monitored by confocal Raman, CARS, and SHG after every fifth day starting from day 25 till day 60 of culture. By day 25 to 30, cells differentiated towards osteoblasts, and were identified by the presence of collagen fibrils, cholesterol and glycosaminoglycans (GAGs). Phospholipids (PA, PS and cholesterol) played an important role in initial HA mineralization which was observed on day 35 of culture. Further culture in the same medium showed increase in bands for carbonates at 1070 cm^{-1} signifying conversion from HA to CHA from day 45 of culture. This conversion influenced the increase in crystallinity of the apatite with culture period, supported by the shift in the band position for v_1 vibration of phosphates from 954 cm^{-1} (day 35) to 959 cm^{-1}

(day 60), and decrease in its full width half maximum (FWHM). Hierarchical cluster analysis (HCA) of the acquired Raman data on day 35 of culture showed that the early HA deposits formed in the phospholipids. The CARS images show decrease in phospholipids and increase in bone deposition with culture period and are in agreement with Raman results. SHG images show the formation of collagen fibrils oriented orthogonally along the adjacent layers of cells. Increase in number of layers of collagen fibrils up to day 45 of culture suggests increase in cell layers due to proliferation. The density of the formed collagen layers increased with culture period, with higher amounts in the lower layer compared to the upper layers. Combined CARS and SHG images show formation of bone along the direction of the collagen fibrils. Day 60 culture shows formation of layers of bone interwoven with collagen fibrils.

8.2 Materials and Methods

Cell culture

iMSCs (as described in chapter 5 of this thesis) were seeded on multiple glass cover slips (thickness ~140 µm) (Menzel Gläser, Braunschweig, Germany) at cell densities of 1000 cells/cm^2. The seeded iMSCs were cultured in parallel with osteogenic cell culture medium in separate Petri dishes over 60 days. Cell culture basic medium (BM), which served as the control condition, was prepared from α-MEM (GIBCO, Carlsbad, CA), 10% fetal bovine serum (FBS; Bio Whittaker, Australia), 0.2 mM L-ascorbic acid-2-phosphate (AsAP; Sigma, St. Louis, MO), 100 U/mL Pencillin G (Invitrogen, Carlsbad, CA); 100 µg/mL Streptomycin (Invitrogen) and 2 mM L-Glutamine (L-Glu; Sigma). Osteogenic medium was prepared by adding 0.01 M β-Glycerophosphate (βGP; Sigma) and osteogenic growth factor 10^{-8} M dexamethasone (Dex, Sigma) to BM. iMSCs on multiple glass cover slips were cultured in BM overnight (day 0) to enable cells to adhere on these substrates. Cells adhered to glass cover slips were then cultured in osteogenic medium until day 60 of culture, when extensive HA mineralization was observed. Cell cultures were maintained at 37ºC, 95 % humidity and 5 % partial pressure of CO_2. Cell measurements were performed every fifth day starting from day 25 till day 60 of culture. On each measurement day, sets of glass cover slips with cell cultures were washed three times with phosphate buffered saline solution (PBS; Gibco) before being transferred to the confocal Raman microspectroscopy setup or CARS/SHG microscopy setup. Confocal Raman measurements were performed on living cells and CARS /SHG measurements were performed after fixing the cells with 1% paraformaldehyde.

Confocal Raman microscopy

A custom-built confocal Raman microspectroscope[37] was used to perform measurements on living cells. A Krypton ion laser (Coherent, Innova 90K, Santa Clara, CA) emitting at 647.1 nm was used as an excitation source. The microscope in epi-illumination detection mode used a water immersion objective with 63× magnification and 1.2 NA (Zeiss Plan Neofluar, Carl Zeiss, Thornwood, NY) to focus laser light on the sample of interest and also to collect the Raman scattered photons from the sample. The scattered photons from the sample were then focused on to a confocal pinhole placed in front of custom-designed spectrograph. The spectrograph disperses the Raman scattered photons on an air-cooled EMCCD camera (Newton DU-970N, Andor Technology, Belfast, Northern Ireland) which provided a spectral resolution of 1.85 to 2.85 cm^{-1}/pixel over a wavenumber range -20 to 3670 cm^{-1}. The confocal Raman images were obtained by collecting complete spectral information at each step throughout the raster scan caused by the displacement of a scanning mirror (Leica Laser technique, GmbH, Heidelberg, Germany) over the image area. Raman imaging were performed over an area of 20 µm × 20 µm with a step size resolution of 310 nm and an accumulation time of 100 ms/step. A laser excitation power of 35 mW was used in all Raman measurements.

CARS and SHG

A custom built CARS setup[38] with SHG imaging capability was used to perform measurements on fixed cells. The setup consisted of a coherent Paladin Nd:YAG laser and an APE Levante Emerald Optical Parametric Oscillator (OPO). In this setup, the fundamental wavelength (1064 nm, 80 MHz, >15 ps) of the laser is used as Stokes, whereas the signal from the OPO (tunable between 700-1000 nm and spectral width of 0.2 nm) is used as the pump and probe. The images are acquired by scanning the beams over the sample by galvano mirrors (Olympus FluoView 300, IX-71) and focused by a 60× magnification and 1.2 NA (Olympus C.A.R.S.) water objective lens on the sample. Both beams have a power of several tens of mW at the sample. The generated CARS signal is obtained in the forward direction and collected by a collimation lens, filtered by several band pass filters, depending on vibrational stretch and detected by a PMT (Hamamatsu R943-02). The second harmonic (SHG) signal created in the forward direction in the sample is detected in the non-descanned backward direction. Due to sample scattering this created signal can be detected in the backward direction. In the measurements SHG is enabled by the second harmonic (450 nm) of the OPO signal beam of 900 nm. SHG signal from the sample is collected by the focusing objective lens, reflected by a dichroic filter and detected by a second PMT (Hamamatsu R3896). CARS and SHG images were acquired over an area of 150 μm × 150 μm with 512 × 512 pixels resulting in a resolution of ~400 nm over the full field of view. Three-dimensional images are obtained by stacking multiple slices along the z-axis. Each slice consists of an average of frames, with each frame acquired in 1.12 s per scan. Images at different vibrational stretches (wavelengths) for various molecules were obtained with temperature tuning of the OPO, where realignment of the optics was not necessary. CARS images of the phospholipid vibrational stretch (Raman band 2845 cm^{-1}) were obtained at a CARS signal of 662.8 nm after tuning the OPO to 816.8 nm, with averaging of 5 frames per slice. Bone images at resonance (Raman 950 cm^{-1}) and off-resonance (Raman 960 cm^{-1}) were obtained from the CARS signal at 885.1 nm and 883.6 nm after tuning the OPO to 966.4 nm and 965.5 nm respectively. Both resonance and off-resonance bone images were obtained by averaging 10 frames per slice. For SHG images showing collagen fibrils, image frames are obtained by averaging 15 frames and 20 frames per slice for 3 dimensional and 2 dimensional images respectively.

Data analysis

The Raman spectra were preprocessed by 1) removal of cosmic ray events, 2) subtraction of the camera offset, 3) calibration of the wave number axis, and 4) correction of frequency dependent transmission. The well-known band-positions of toluene were used to relate wavenumbers to pixels. The frequency-dependent optical detection efficiency of the setup is corrected using a tungsten halogen light source (Avalight-HAL; Avantes BV, Eerbeek, The Netherlands) with a known emission spectrum. The detector-induced etaloning effect was also compensated by this procedure.

The data acquired were analyzed by both univariate and multivariate data analysis procedures. Univariate Raman analysis for individual spectra (or images) of a specific vibrational band of interest, as a function of position, was constructed by integrating the band intensities after baseline subtraction. In multivariate analysis, both hierarchical cluster analysis (HCA) and principal component analysis (PCA) were performed to visualize regions with high spectral similarities. HCA makes use of the scores obtained from the PCA data.

Band integration ratios for the data acquired on days 35 till 60 were performed to determine HA growth and variation in mineral composition based on the spectra acquired from three randomly chosen mineralized nodules. The specific bands of interests were baseline corrected before taking ratios. The mineral to matrix band ratios were obtained from the ratios of v_1 phosphate band around 954-959 cm^{-1} (Δ = ~84 cm^{-1}) corresponding to minerals and phenylalanine at 1001 cm^{-1} (Δ = ~22 cm^{-1}) signifying the proteins in the extracellular matrix. The carbonate/phosphate band ratios were calculated from the ratios of carbonate band at 1069 cm^{-1} (Δ = ~44 cm^{-1}) and v_1 phosphate band. All Raman data manipulations were performed with routines written in MATLAB 7.4 (The Math Works Inc., Natick, MA).

In CARS imaging, the multiple frames per slice acquired are averaged for better signal to noise ratio in the images. Subtraction of the resonance and off-resonance bone images obtained from CARS signal at 885.1 nm and 883.6 nm was performed, which reveals only the resonant vibrational stretch of the bone and removes the non-resonant background of the sample.[39]

8.3 Results and Discussions

iMSCs were successfully cultured over a 60 day culture period in osteogenic medium. Time line Raman and CARS measurements performed every fifth day from day 25 till day 60 of culture illustrate the role of phospholipids and collagen in bone formation. A schematic illustration of cell-based mineralization based on Raman, CARS and SHG results are shown in Figure 1. The iMSCs seeded on glass substrates show cell proliferation and differentiation over the culture period. The proliferation of iMSCs resulted in organization of cells in layers. The cell layers increased until day 45 of culture. The lately divided cells resulted in successive layers on top of the cells adhered to the cover glass. Along with proliferation, the iMSCs differentiated towards osteoblasts by day 25 and 30 of culture. Well differentiated osteoblast stages of the iMSCs are identified by biomarkers for GAGs, collagen fibrils and cholesterol.[2, 11, 12, 17] The Raman signatures for these biomarkers were observed in cells on day 25 and day 30 of culture, confirming differentiation towards osteogenic lineage of the cells in culture (Figure 2a).

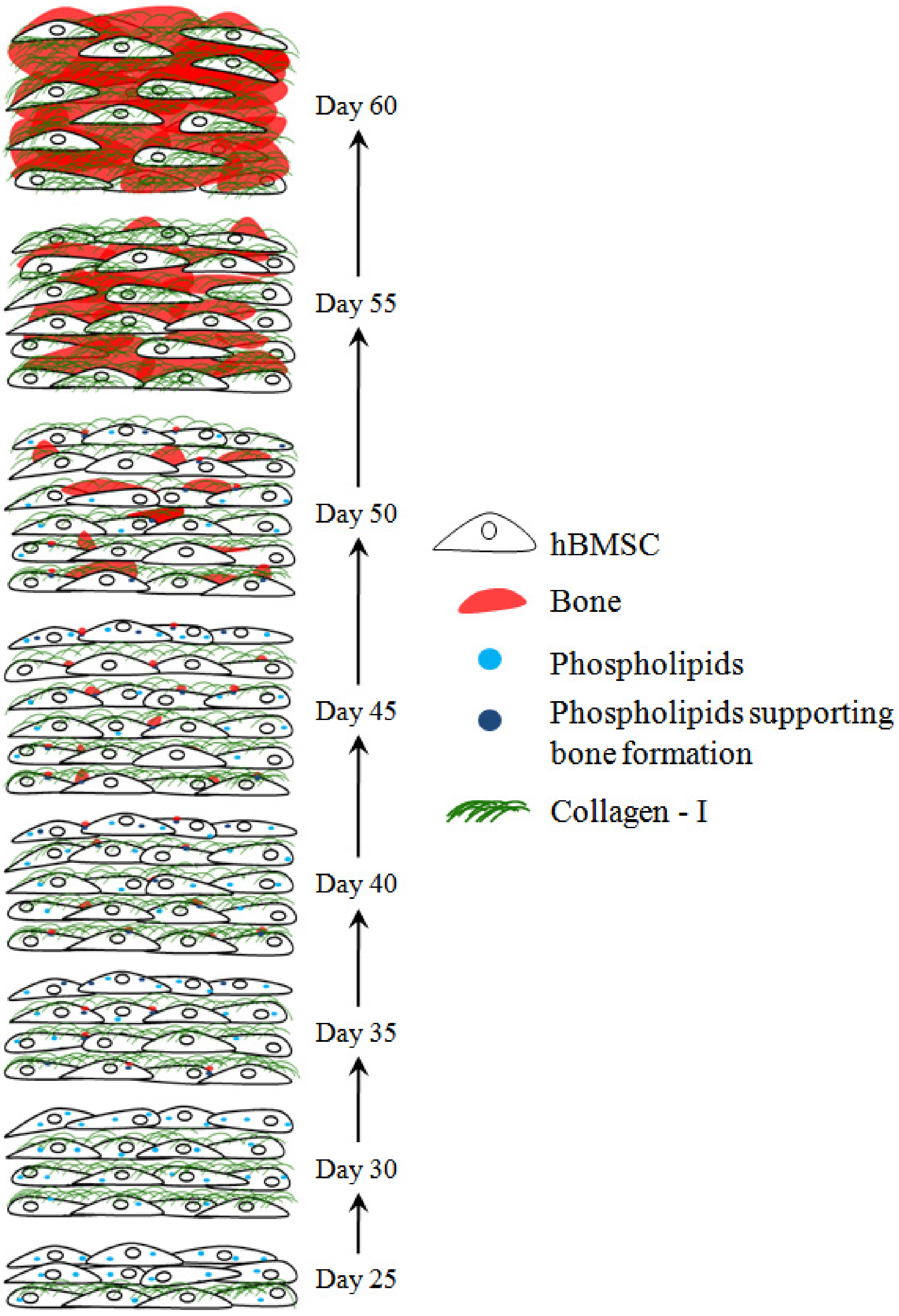

Figure 1: Illustration showing *in vitro* cell mediated bone formation over a period from day 25 till day 60 of culture.

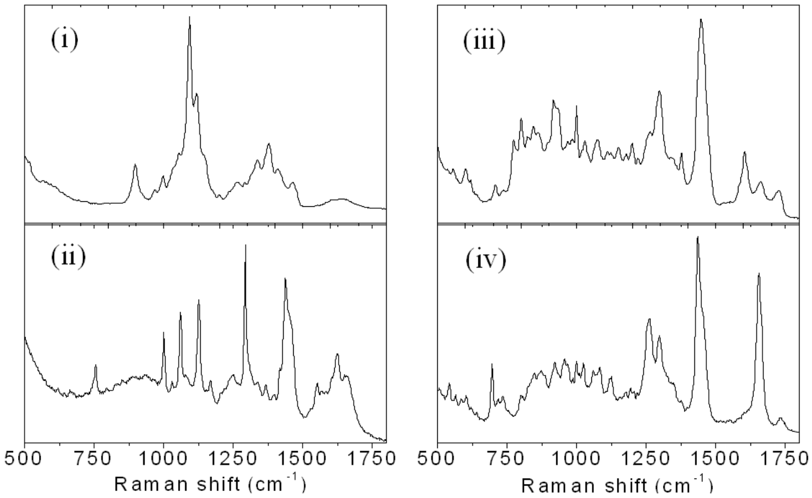

Figure 2a: Raman microspectroscopy showing markers for osteoblast differentiation (i) Glycosaminoglycans, (ii) Phosphatidic acid, (iii) Phosphatidylserine, and (iv) Combination of Cholesterol and Phosphatidylserine.

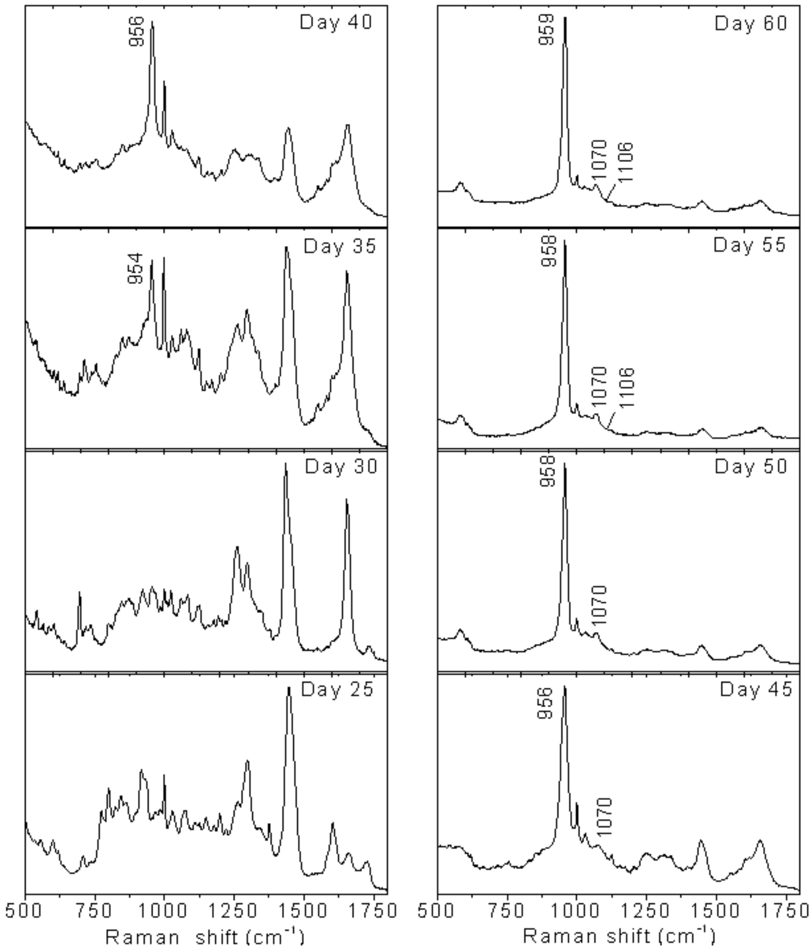

Figure 2b: Raman microspectroscopy showing cell based bone formation observed from day 25 till day 60 of culture. Combination of cholesterol and PS observed on days 25 and 30. Early mineral deposition with band at 954 cm^{-1} for phosphates seen on day 35 of culture. This band gradually shifts to 959 cm^{-1} by day 60. Further culture shows formation of HA and conversion to CHA with bands at 1070 and 1106 cm^{-1} for carbonates.

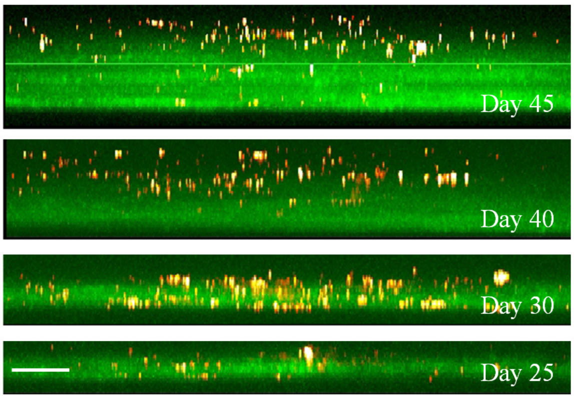

Figure 3a: Lipid distribution (yellow) in Z-stack in collagen (green) layer. Background is removed by thresholding the lipid droplet intensity. Day 25 till 45 of culture shows increase in collagen type-I. Day 25 till 30 show increase in lipids over the full layers, day 40 till day 45 show higher lipid concentration in upper layers where new cells are formed. Day 50 onwards the presence of lipid droplets gradually decreased. Scale bar 15 μm.

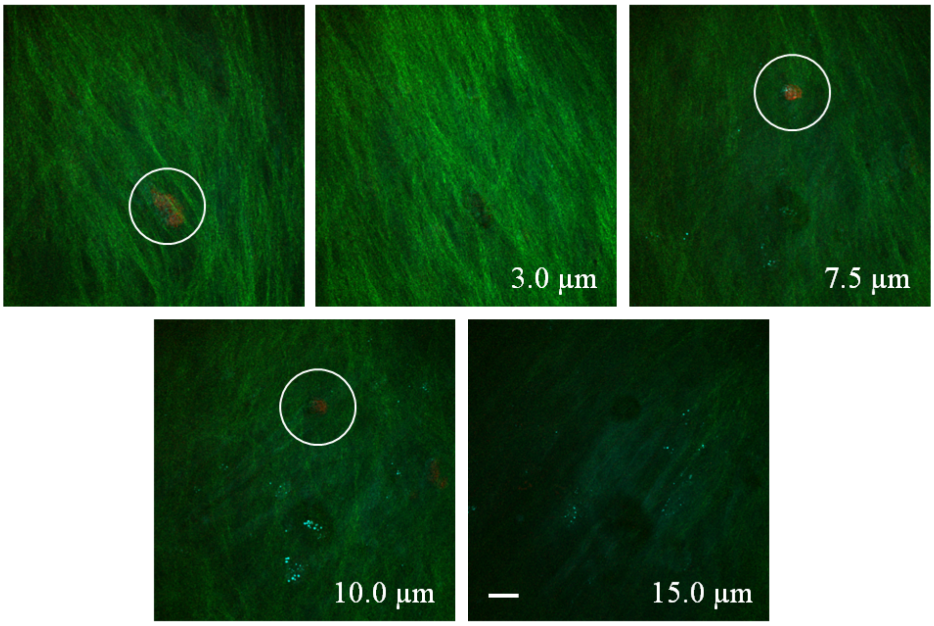

Figure 3b: XY plane image slices at various levels of the Z-stack showing the change in orientation of the collagen fibrils (green) obtained on day 45 of culture.
Formation of bone (red) in different collagen layers.
Phospholipids (blue) are seen in the upper layers of the cell which are more recently formed.
Scale bar 15 μm.

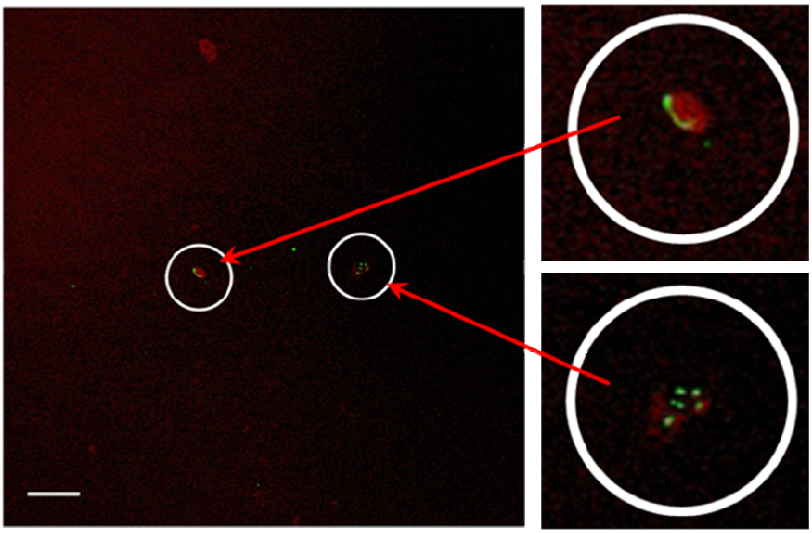

Figure 3c: XY plane image slice showing phospholipids (2845 cm^{-1}, green) and background free bone (~950 cm^{-1}, red). For phospholipid images a threshold for suppressing the non-resonant background is applied. The right panel images show of close association of phospholipids in the mineral deposits. Scale bar 15 μm.

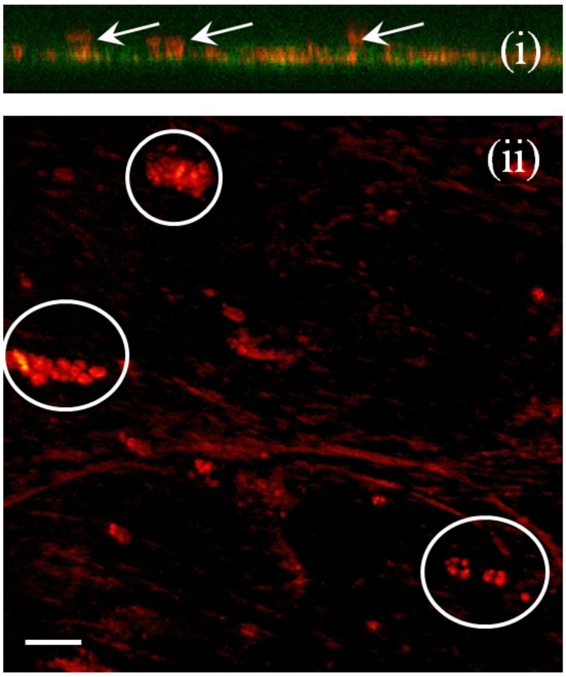

Figure 3d: CARS and SHG images obtained on day 50 of culture. Single slice of (i) Z-stack layer showing HA formation embedded between collagen type-I fibrils. (ii) X-Y plane showing deposition of HA over lipid droplets (white circles). Scale bar 15 µm.

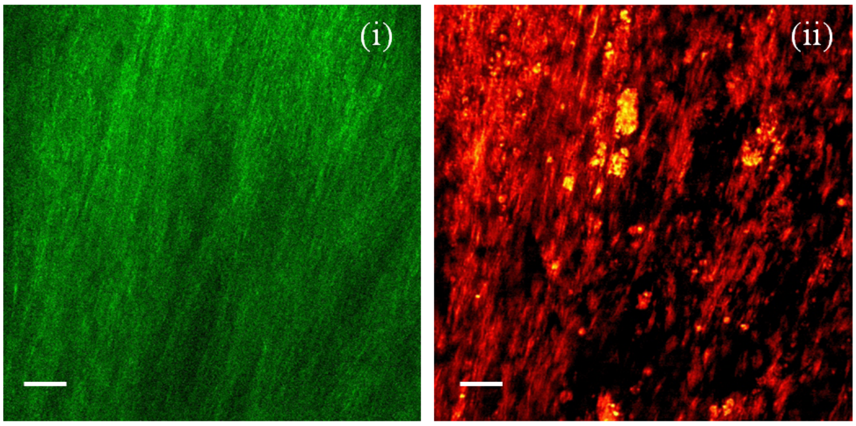

Figure 3e: Formation of HA along the collagen fibrils. (i) Collagen obtained from SHG, (ii) CARS image for bone showing the mineralization over the collagen layers. Scale bar 15 µm.

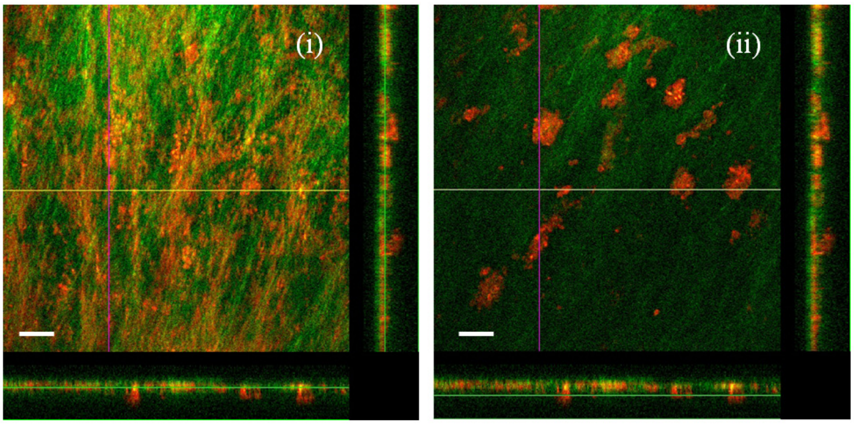

Figure 3f: (i) 10 µm and (ii) 13 µm depth slice obtained from day 50 of culture. HA (Red) orients along the collagen (green) fibrils at various layers. Scale bar 15 µm.

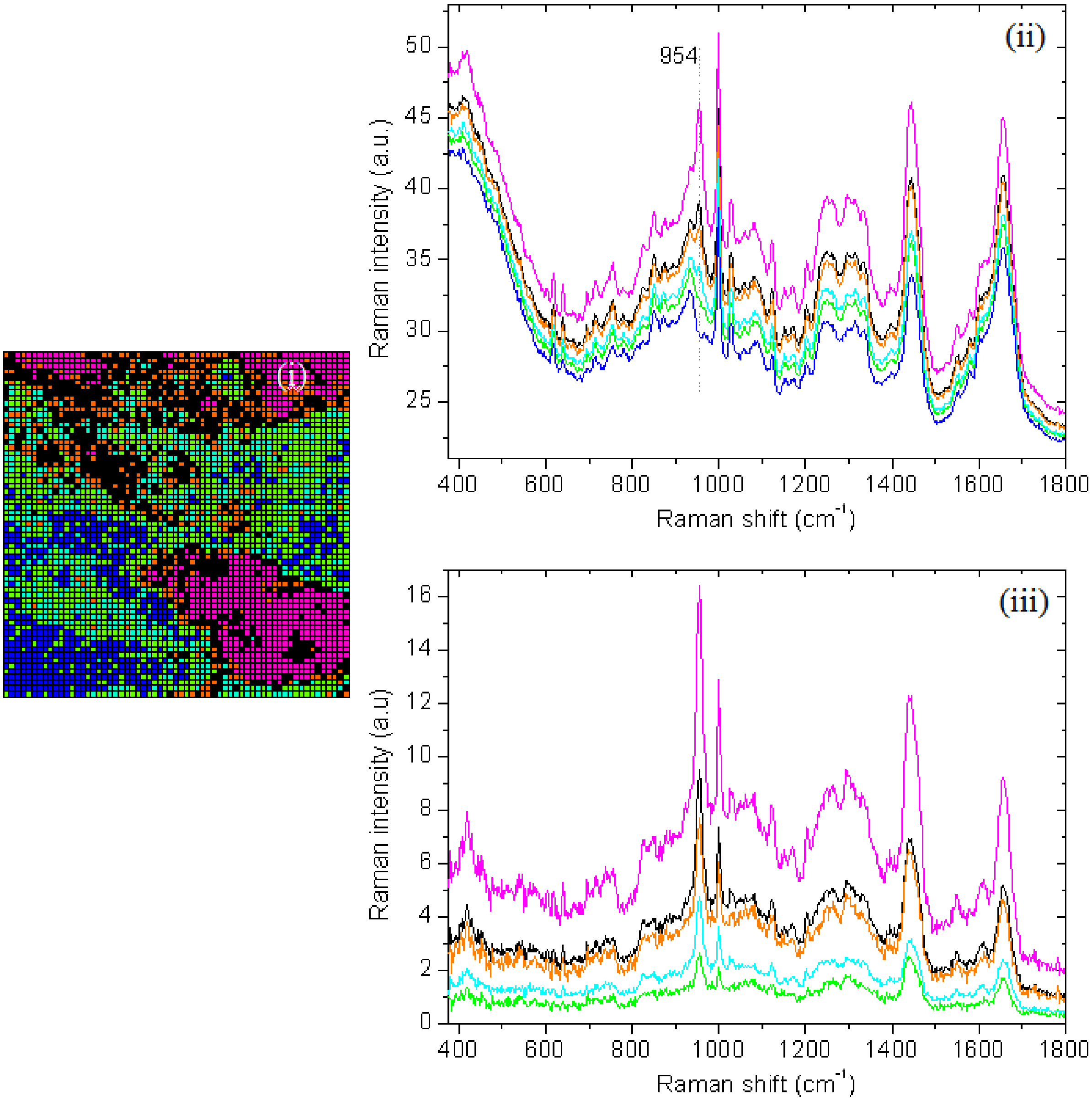

Figure 4a: Illustration of HA deposition over the cells over a region of 20 µm × 20 µm on day 35 of culture period. (i) Six cluster HCA image of the measured area, (ii) Average spectra corresponding to the clusters in image (i) Showing variations in intensity of the band at 954 cm^{-1} signifying concentration variation in the HA deposition. (iii) Raman difference spectroscopy of average spectrum of blue cluster (no band at 954 cm^{-1}) minus other clusters showing concentration variation in the HA deposition. Image acquired with a spatial resolution of 310 nm and 35 mW laser power.

CARS and SHG images acquired on day 25 show distribution of phospholipids droplets and collagen in the cells (Figure 3(a)). By day 25 of culture, three layers of cells are observed. Lower layers of cells show both presence of collagen fibrils and distribution of phospholipids, while the upper layers show the presence of collagen alone. This observation suggests that the lower cell layers are well differentiated towards osteogenic precursors compared to cells in upper layers that are more recently formed. In due course, the cells in the upper layers also differentiate towards osteogenic precursors. However, the possibility of proliferation by well-differentiated osteoblasts cannot be ruled out due to the presence of PA in the cells.[40] Further culture showed proliferation of iMSCs resulting in new layers of cells above the earlier formed layers (Figure 1). By day 45 of culture, up to six cell layers could be observed with well-developed collagen fibrils on each layer. The collagen found in the lower layers is much denser than that formed over the upper layers (Figure 3(a)). The distribution of phospholipids droplets in the cells increases from day 25 till day 45 of culture. Over time, these phospholipids are found mostly in the most recently formed cells present in the upper layer (Figure 3(a) and 3(b)). The collagen fibrils formed on the cells are orthogonally arranged with respect to the next layer of cells. Each newly formed layer of cells has different orientation for collagen, which is apparent from the SHG images in Figure 3(b).

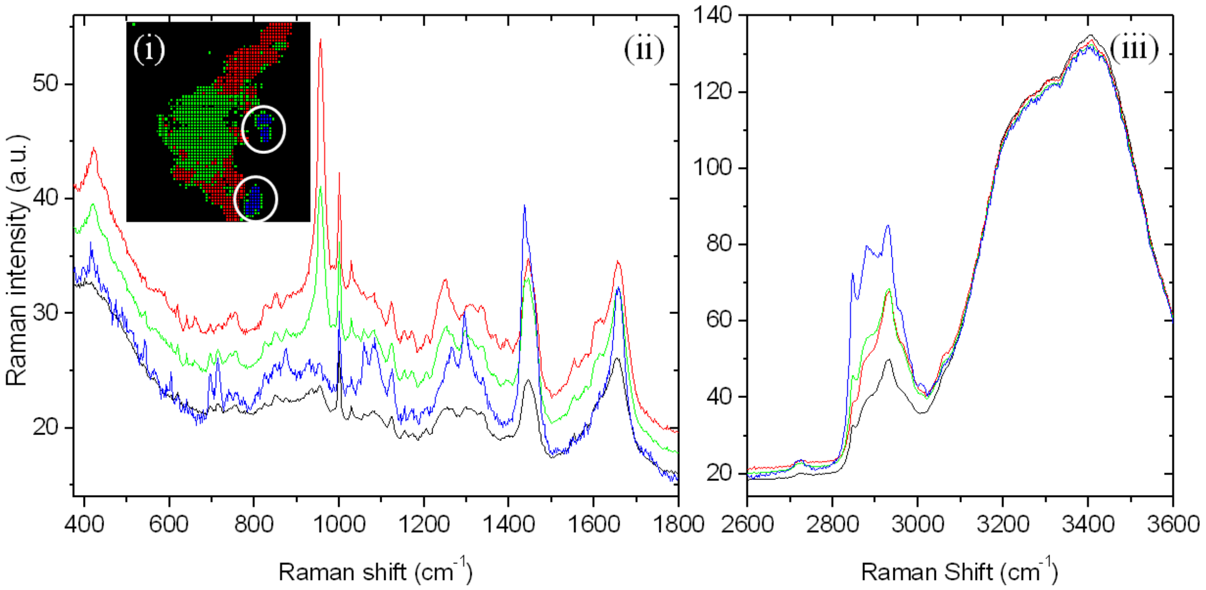

Figure 4b: Illustration of HA deposition over the cells over a region of 20 µm × 20 µm on day 40 of culture period. (i) Four cluster HCA image of the measured area, (ii) Average spectra corresponding to the clusters in fingerprint region, and (iii) Average spectra corresponding to the clusters in high frequency region. White circles in image (i) Indicated HA deposition over phospholipids. Image acquired with a spatial resolution of 310 nm and 35 mW laser power.

The organization of collagen fibrils over the cells result in holes and pores which are composed of phospholipids.[2] Apart from these structures phospholipids droplets are distributed in the cell membranes. These phospholipids droplets are composed of PA, PC and PS[8, 9, 41] and play a vital role in mineralization, which has been well-demonstrated. The Raman spectra of phospholipids found in the cells are shown in Figure 2(a)(ii), (iii) and (iv). These phospholipids act as storage sites for calcium ions (Ca^{2+}) which helps in initial mineralization. The cholesterol and PS synthesized during the osteoblast phase supports initial mineralization,[13, 14, 42] due to the good crystallographic fit between the crystal structures of HA and cholesterol. Hence an eventual epitaxial growth of HA on cholesterol and vice versa is feasible. This hypothesis is supported by spectra obtained from cells on day 25 and 30 of culture (Figure 2(a)(iv)) showing the presence of a combination of PS and cholesterol. Cholesterols in the cell membrane are closely associated with the phospholipids. This is due to the interaction of hydroxyl group of cholesterol with the polar head groups of the membrane phospholipids. On day 35 of culture (Figure 2(b)(iii)), a band at 954 cm^{-1} for v_1 vibrations of phosphates appears along with the spectra of phospholipids showing initial HA mineral depositions. A six cluster Raman image obtained from iMSCs cultured up to day 35 of culture is shown in (Figure 4(a)(i)). The respective average cluster spectra (Figure 4(a)(ii)) show prominent intensity variations of the band at 954 cm^{-1}, indicating regions with varying concentrations showing absence of HA formation (dark blue cluster) to significant bone formation. The average spectra show bands at 851, 872, 920, 934, 1250, 1450 and 1659 cm^{-1} indicating the formation of collagen fibrils over the osteoblasts.[17] Raman difference spectra (Figure 4(a)(iii)) for regions showing no mineralization (blue cluster) with other regions showing mineralization display significant bands for phospholipids (PS and cholesterol). The difference spectra show higher bone deposition for regions with larger concentration of phospholipids, which is due to accumulation of significantly higher amounts of Ca^{2+} ions in these phospholipids.

On day 40 of culture, an increase in intensity of the band shows an increase in deposition of phosphate ions with a significant shift in the band to 956 cm^{-1} compared to day 35 of culture (Figure 2(b)). The mineral/matrix ratio (Figure 5(a)) confirms the growth of HA. The role of phospholipids in HA mineralization is further illustrated by the four cluster Raman image obtained from iMSCs cultured till day 40 of culture (Figure 4(b)(i)). The respective average cluster spectra in Figure 4(b)(ii) show blue and green pixels with spectral bands corresponding to phospholipids and HA respectively. Phospholipid droplets surrounded by HA (white circles) confirm the role of phospholipids in early mineralization. CARS images (white circles in Figure 3(c)) obtained from the finger print region for HA (red regions) and high frequency region for phospholipids (green regions) show close association of phospholipids with HA, confirming the role of phospholipids in mineralization.

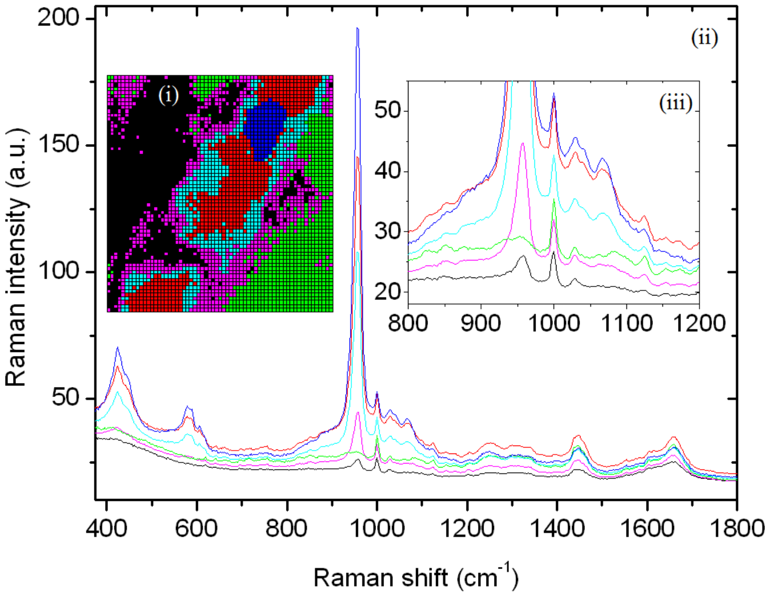

Figure 4c: Illustration of HA and CHA deposition over the cells over a region of 20 µm × 20 µm on day 50 of culture period. (i) Six cluster HCA image of the measured bone nodule, (ii) Average spectra in the region 375-1800 cm^{-1} corresponding to the respective clusters in image (i) Showing variations in intensity of the band at 958 and 1070 cm^{-1} signifying phosphates and carbonates respectively. (iii) Zoom in over the spectral region 800-1200 cm^{-1} showing the presence of CO_3^{2-} band (1070 cm^{-1}) corresponding to dark blue, light blue and red clusters. Image acquired with a spatial resolution of 310 nm and 35 mW laser power.

Further growth from day 40 till day 60 shows accretion of HA over initial deposits seen on day 35. Further culture shows increase in the mineral to matrix ratio (Figure 5(a)), confirming increase in phosphate deposition leading to the growth of HA. Increase in HA with culture period is accompanied by a appearance of band at 1070 cm^{-1} for v_1 carbonate symmetric stretch on day 45 of culture. This band is observed to increase with time signifying B-type carbonation where the phosphates (PO_4^{3-}) in the HA molecule are substituted by the carbonates (CO_3^{2-}) from the culture medium. The carbonate to phosphate ratio (Figure 5(b)) increases with culture period indicating the formation of CHA. A six cluster Raman image of HA deposition formed in iMSCs cultured up to day 50 of culture is shown in Figure 4(c)(i). The respective average cluster spectra in Figure 4(c)(ii) show prominent intensity variations of the band at 958 cm^{-1} for phosphates and 1070 cm^{-1} for carbonates. Figure 4(c)(iii) shows a zoom-in over the spectral region 800-1200 cm^{-1}. Clusters whose average spectra show a band at 1070 cm^{-1} indicate the topographic regions corresponding to formation of CHA while the remaining clusters correspond to HA. Day 55 and 60 of culture show a band for carbonates at 1106 cm^{-1} signifying A-type carbonation where CO_3^{2-} replaces OH^- in HA.[26] This formation of CHA results in increase of crystalline nature of the formed apatite, and is supported by the shift in v_1 phosphate vibration from 954 cm^{-1} (Day 35) to 959 cm^{-1} (Day 60), and decrease in full width at half maximum (FWHM) of the band corresponding to v_1 phosphate vibration from 21.2 cm^{-1} (Day 40) to 17.4 cm^{-1} (Day60).[43, 44] FWHM of v_1 phosphate vibration seen on day 60 of culture is close to that seen in *in vivo* bone.[17]

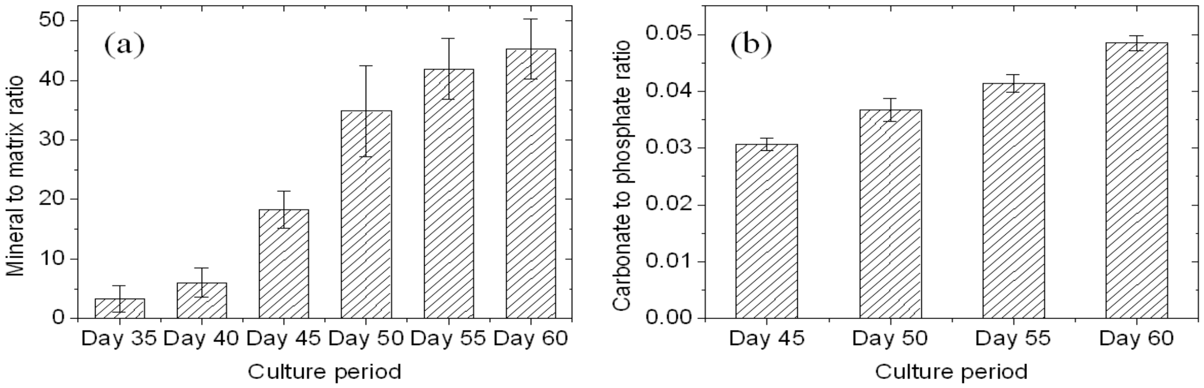

Figures 5: Raman band integration ratios obtained from three randomly chosen nodules on each measurement day. Each nodule is represented by an average of 500 spectra; (a) Mineral (Phosphates) to matrix (Phenylalanine) ratio showing formation of HA from day 35 till day 60 of culture. (b) Mineral (carbonates) to mineral (phosphates) ratio showing bone crystallization from day 45 till day 60 of culture.

From day 35 till day 60, we observe an increase in *in vitro* HA mineralization of osteoblasts. From day 35 onwards, we see spectra being influenced by bands from collagen and simultaneous disappearance of bands for phospholipids (700, 718 cm^{-1}) by day 50 of culture (Figure 2(b)). This suggests the role of phospholipids in early deposition[8, 9, 41] and the influence of proteins in growth of HA.[45] This observation is evident from the cross-section of combined images from HA and collagen acquired by CARS and SHG imaging respectively on day 50 of culture (Figure 3(d)(i)). The image illustrates a layer of HA embedded between collagen fibrils. The white arrow points to a possible early formed HA nodule that has grown in size over the culture period. The dimensions of these nodules are larger than few layers of cells. These nodules are formed due to the early deposition of HA over the phospholipid droplets (white circles in Figure 3(d)(ii)) that later on grow in size with culture period. The regions other than such nodules correspond to HA mineralization formed by the influence of phospholipids and non collagenous proteins present in the holes and pores of collagen fibrils. Collagen fibrils provide mechanical support for HA deposition,[19, 46] which occurs along the orientation of the collagen fibrils as seen in Figure 3(e)(i) and 3(e)(ii) for SHG and CARS of collagen fibrils and HA respectively. By day 50 multiple layers of collagen are formed which support bone formation. Figure 3(f)(i) shows a combined image from HA and collagen acquired by CARS and SHG imaging respectively. The image shows HA deposition and its orientation along the collagen fibrils. Approximately three micrometers above this layer (Figure 3(f)(ii)), the orientation of collagen fibrils changes, which is due to presence of a different layer of cells. The HA nodules seen in Figure 3(f)(ii) align along the direction of collagen fibrils from this layer. The early mineralized nodules are independently formed in ECM of different layers of cells (Figure 3(b)). With time, the growth and accretion of these nodules in different layers by deposited HA leads to a three-dimensional structure (illustrated in Figure 1). By day 60 of culture, we observe three-dimensional HA formation embedded with cells and collagen. The mineral composition on day 60 of culture was similar to that of native bone.[17]

8.4 Conclusion

iMSCs were cultured towards osteogenic lineage followed by HA mineralization in osteogenic media over a 60 day period. Time-line studies by non-invasive and label-free techniques such as confocal Raman microscopy, CARS and SHG imaging were successfully applied to understand the progress in cell mediated bone formation. The Raman biomarker bands for GAGs, PS, PA and cholesterol, and SHG images for the distribution of collagen by day 25 and day 30 of culture confirmed differentiation of iMSCs towards osteogenic lineage. Collagen fibrils were formed in the ECM of iMSCs, which increased with culture period. By day 45, five to six layers of cells were formed due to cell proliferation. Each layer has a different orientation of collagen fibrils that is orthogonal to the collagen fibrils formed in adjacent layers of cells. Calcium active phospholipids such as PA, PS and cholesterol in the differentiated cells enabled initial mineralization on day 35, which was seen to occur in multiple layers of cells. Further culture resulted in growth and development of these initial mineral depositions towards a three dimensional structure by day 60. The distribution of phospholipids increased with culture up to day 45, and decreased with growth of HA with further culture. The role of phospholipids in initial mineralization was shown in Raman imaging and confirmed by CARS images from HA and phospholipids. Cultures after day 45 show a gradual increase in the band at 1070 cm^{-1} for carbonates resulting from the formation of CHA from HA. The formation of CHA eventually resulted in the increase in crystallinity of the formed apatite, supported by the shift in v_1 vibration of phosphate from 954 cm^{-1} (day 35) to 959 cm^{-1} (day 60) and decrease in FWHM of that band. Collagen in the ECM of the cells guided the deposition of HA along the orientation of fibrils. Day 60 of culture showed three dimensional mineral formations completely embedded with collagen fibrils and composition similar to *in vivo* bone.

References

1. Boskey, A. L.; Gadaleta, S.; Gundberg, C.; Doty, S. B.; Ducy, P.; Karsenty, G., Fourier transform infrared microspectroscopic analysis of bones of osteocalcin-deficient mice provides insight into the function of osteocalcin. *Bone* **1998,** 23, (3), 187-196.
2. Favus, M. J., *Primer on the Metabolic Bone Diseases And Disorders of Mineral Metabolism, 6th Edition.* 2006.
3. Olsen, B. R.; Reginato, A. M.; Wang, W., Bone development. *Annu Rev Cell Dev Biol* **2000,** 16, 191-220.
4. Caplan, A. I., Adult mesenchymal stem cells for tissue engineering versus regenerative medicine. *J. Cell. Physiol.* **2007,** 213, (2), 341-347.
5. Long, M. W., Osteogenesis and bone-marrow-derived cells. *Blood Cells Mol Dis* **2001,** 27, (3), 677-90.
6. Pittenger, M. F., Multilineage potential of adult human mesenchymal stem cells. *Science* **1999,** 285, (5428), 665.
7. Anderson, H. C., Molecular biology of matrix vesicles. *Clin Orthop Relat Res* **1995**, (314), 266-80.
8. Boyan, B. D.; Schwartz, Z.; Swain, L. D.; Khare, A., Role of lipids in calcification of cartilage. *Anat. Rec.* **1989,** 224, (2), 211-19.
9. Felix, R.; Fleisch, H., The role of matrix vesicles in calcification. *Calcif. Tissue Res.* **1976,** 21, Suppl., 344-8.
10. Zimmermann, B.; Wachtel, H. C.; Noppe, C., Patterns of mineralization *in vitro*. *Cell Tissue Res* **1991,** 263, (3), 483-93.
11. Parhami, F.; Mody, N.; Gharavi, N.; Ballard, A. J.; Tintut, Y.; Demer, L. L., Role of the cholesterol biosynthetic pathway in osteoblastic differentiation of marrow stromal cells. *J. Bone Miner. Res.* **2002,** 17, (11), 1997-2003.
12. Viccica, G.; Vignali, E.; Marcocci, C., Role of the cholesterol biosynthetic pathway in osteoblastic differentiation. *J Endocrinol Invest* **2007,** 30, (6 Suppl), 8-12.
13. Craven, B. M., Crystal structure of cholesterol monohydrate. *Nature* **1976,** 260, (5553), 727-9.
14. Laird, D. F.; Mucalo, M. R.; Yokogawa, Y., Growth of calcium hydroxyapatite (Ca-HAp) on cholesterol and cholestanol crystals from a simulated body fluid: a possible insight into the pathological calcifications associated with atherosclerosis. *J. Colloid Interface Sci.* **2006,** 295, (2), 348-363.
15. Kale, S.; Biermann, S.; Edwards, C.; Tarnowski, C.; Morris, M.; Long, M. W., Three-dimensional cellular development is essential for ex vivo formation of human bone. *Nat Biotechnol* **2000,** 18, (9), 954-8.
16. Bonewald, L. F.; Harris, S. E.; Rosser, J.; Dallas, M. R.; Dallas, S. L.; Camacho, N. P.; Boyan, B.; Boskey, A., Von Kossa staining alone is not sufficient to confirm that mineralization *in vitro* represents bone formation. *Calcif. Tissue Int.* **2003,** 72, (5), 537-547.
17. Gentleman, E.; Swain, R. J.; Evans, N. D.; Boonrungsiman, S.; Jell, G.; Ball, M. D.; Shean, T. A. V.; Oyen, M. L.; Porter, A.; Stevens, M. M., Comparative materials differences revealed in engineered bone as a function of cell-specific differentiation. *Nat. Mater.* **2009,** 8, (9), 763-770.
18. Stewart, S.; Shea, D. A.; Tarnowski, C. P.; Morris, M. D.; Wang, D.; Franceschi, R.; Lin, D. L.; Keller, E., Trends in early mineralization of murine calvarial osteoblastic cultures: A Raman microscopic study. *J. Raman Spectrosc.* **2002,** 33, (7), 536-543.
19. Gerstenfeld, L. C.; Chipman, S. D.; Kelly, C. M.; Hodgens, K. J.; Lee, D. D.; Landis, W. J., Collagen expression, ultrastructural assembly, and mineralization in cultures of chicken embryo osteoblasts. *J. Cell Biol.* **1988,** 106, (3), 979-89.
20. Rey, C.; Kim, H. M.; Gerstenfeld, L.; Glimcher, M. J., Structural and chemical characteristics and maturation of the calcium-phosphate crystals formed during the calcification of the organic matrix synthesized by chicken osteoblasts in cell culture. *J. Bone Miner. Res.* **1995,** 10, (10), 1577-88.
21. Rey, C.; Kim, H. M.; Gerstenfeld, L.; Glimcher, M. J., Characterization of the apatite crystals of bone and their maturation in osteoblast cell culture: comparison with native bone crystals. *Connect Tissue Res* **1996,** 35, (1-4), 343-9.

22. Kuhn, L. T.; Wu, Y.; Rey, C.; Gerstenfeld, L. C.; Grynpas, M. D.; Ackerman, J. L.; Kim, H.-m.; Glimcher, M. J., Structure, composition, and maturation of newly deposited calcium-phosphate crystals in chicken osteoblast cell cultures. *J. Bone Miner. Res.* **2000,** 15, (7), 1301-1309.
23. Boskey, A. L.; Camacho, N. P.; Mendelsohn, R.; Doty, S. B.; Binderman, I., FT-IR microscopic mappings of early mineralization in chick limb bud mesenchymal cell cultures. *Calcif Tissue Int* **1992,** 51, (6), 443-8.
24. Boskey, A. L.; Mendelsohn, R., Infrared spectroscopic characterization of mineralized tissues. *Vib. Spectrosc.* **2005,** 38, (1-2), 107-114.
25. Xu, S.; Yu, J. J., Beneath the minerals, a layer of round lipid particles was identified to mediate collagen calcification in compact bone formation. *Biophys. J.* **2006,** 91, (11), 4221-4229.
26. Carden, A.; Morris, M. D., Application of vibrational spectroscopy to the study of mineralized tissues (review). *J. Biomed. Opt.* **2000,** 5, (3), 259-268.
27. Chiang, H. K.; Peng, F.-Y.; Hung, S.-C.; Feng, Y.-C., In situ Raman spectroscopic monitoring of hydroxyapatite as human mesenchymal stem cells differentiate into osteoblasts. *J. Raman Spectrosc.* **2009,** 40, (5), 546-549.
28. Cheng, J.-X.; Volkmer, A.; Xie, X. S., Theoretical and experimental characterization of coherent anti-Stokes Raman scattering microscopy. *J. Opt. Soc. Am. B* **2002,** 19, (6), 1363-1375.
29. Jurna, M.; Korterik, J. P.; Offerhaus, H. L.; Otto, C., Noncritical phase-matched lithium triborate optical parametric oscillator for high resolution coherent anti-Stokes Raman scattering spectroscopy and microscopy. *Appl. Phys. Lett.* **2006,** 89, (25), 251116/1-251116/3.
30. Windbergs, M.; Jurna, M.; Offerhaus, H. L.; Herek, J. L.; Kleinebudde, P.; Strachan, C. J., Chemical imaging of oral solid dosage forms and changes upon dissolution using coherent anti-Stokes Raman scattering microscopy. *Anal. Chem.* **2009,** 81, (6), 2085-2091.
31. Hellerer, T.; Axaeng, C.; Brackmann, C.; Hillertz, P.; Pilon, M.; Enejder, A., Monitoring of lipid storage in Caenorhabditis elegans using coherent anti-Stokes Raman scattering (CARS) microscopy. *Proc. Natl. Acad. Sci. U. S. A.* **2007,** 104, (37), 14658-14663.
32. Nan, X.; Cheng, J.-x.; Xie, X. S., Vibrational imaging of lipid droplets in live fibroblast cells with coherent anti-stokes Raman scattering microscopy. *J. Lipid Res.* **2003,** 44, (11), 2202-2208.
33. Evans, C. L.; Potma, E. O.; Puoris'haag, M.; Cote, D.; Lin, C. P.; Xie, X. S., Chemical imaging of tissue *in vivo* with video-rate coherent anti-Stokes Raman scattering microscopy. *Proc. Natl. Acad. Sci. U. S. A.* **2005,** 102, (46), 16807-16812.
34. Chen, H.; Wang, H.; Slipchenko, M. N.; Jung, Y.; Shi, Y.; Zhu, J.; Buhman, K. K.; Cheng, J.-X., A multimodal platform for nonlinear optical microscopy and microspectroscopy. *Opt. Express* **2009,** 17, (3), 1282-1290.
35. Freund, I.; Deutsch, M.; Sprecher, A., Connective tissue polarity. Optical second-harmonic microscopy, crossed-beam summation, and small-angle scattering in rat-tail tendon. *Biophys. J.* **1986,** 50, (4), 693-712.
36. Wang, H.-W.; Le, T. T.; Cheng, J.-X., Label-free imaging of arterial cells and extracellular matrix using a multimodal CARS microscope. *Opt. Commun.* **2008,** 281, (7), 1813-1822.
37. Pully, V. V.; Lenferink, A.; Otto, C., Hybrid Rayleigh, Raman and two-photon excited fluorescence spectral confocal microscopy of living cells. *J. Raman Spectrosc.* **2009,** 10.1002/jrs.2501.
38. Jurna, M.; Korterik, J. P.; Otto, C.; Herek, J. L.; Offerhaus, H. L., Vibrational Phase Contrast Microscopy by Use of Coherent Anti-Stokes Raman Scattering. *Phys. Rev. Lett.* **2009,** 103, (4), 043905/1-043905/4.
39. Ganikhanov, F.; Evans, C. L.; Saar, B. G.; Xie, X. S., High-sensitivity vibrational imaging with frequency modulation coherent anti-stokes raman scattering (FM CARS) microscopy. *Opt. Lett.* **2006,** 31, (12), 1872-1874.
40. Carpio, L. C.; Dziak, R., Phosphatidic acid effects on cytosolic calcium and proliferation in osteoblastic cells. *Prostaglandins, Leukotrienes Essent. Fatty Acids* **1998,** 59, (2), 101-109.
41. Boskey, A. L.; Posner, A. S., *In vitro* nucleation of hydroxyapatite by a bone calcium-phospholipid-phosphate complex. *Calcif. Tissue Res.* **1977,** 22, Suppl., 197-201.

42. Boskey, A. L.; Dick, B. L., The effect of phosphatidylserine on *in vitro* hydroxyapatite growth and proliferation. *Calcif. Tissue Int.* **1991,** 49, (3), 193-6.
43. Timlin, J. A.; Carden, A.; Morris, M. D., Chemical microstructure of cortical bone probed by Raman transects. *Appl. Spectrosc.* **1999,** 53, (11), 1429-1435.
44. Timlin, J. A.; Carden, A.; Morris, M. D.; Rajachar, R. M.; Kohn, D. H., Raman Spectroscopic Imaging Markers for Fatigue-Related Microdamage in Bovine Bone. *Anal. Chem.* **2000,** 72, (10), 2229-2236.
45. Weiner, S.; Sagi, I.; Addadi, L., Structural biology: Choosing the crystallization path less traveled. *Science* **2005,** 309, (5737), 1027-1028.
46. Lees, S., Mineralization of type I collagen. *Biophys. J.* **2003,** 85, (1), 204-207.

Chapter 9

Future perspectives and outlook

This thesis describes the realization and application of a novel hybrid microscopy system that enables simultaneous two photon excited fluorescence and Raman measurements. The system offers measurements with high spatial resolution, which is a prerequisite for studies of single cells. The brief overview of examples described in this chapter illustrates the capabilities of the instrumentation to provide biophysical insights into cellular processes. A major part of the thesis deals with non-invasive and label free Raman microspectroscopy approaches to study the differentiation of bone marrow derived stromal cells towards osteogenic lineage leading to bone formation. Similar studies at tissue level demand different measurement approaches like line scan Raman imaging that offers higher field of view and faster imaging speed.

Section 9.1 of this chapter has been published in Vibrational Spectroscopy, DOI:10.1016/j.vibspec.2009.11.004.
Section 9.2 of this chapter has been published in the Journal of Raman Spectroscopy, 2009, 40(5): 473-475.

9.1 Hybrid microscopy to distinguish DNA and RNA in cell nucleus

Hybrid confocal microspectroscopy described in chapter 2 identifies the distribution of DNA in the nucleus of the cells. We have extended the application to select cells based on different stages of nuclear development and studied the molecular composition of the nucleus. Two-photon excited (TPE) fluorescence microscopy enables fast detection of the cell based on morphology of the nucleus after staining with nucleotide sensitive dyes (DAPI or Hoechst-33342). Areas of interest showing bright and dark fluorescence regions are selected from the TPE image and subsequently analyzed with chemically selective Raman microspectroscopy.

9.1.1 TPE fluorescence microscopy of cells

Figure 1 shows the cwTPE fluorescence images of Hoechst-33342-stained nuclei in various stages of the cell cycle measured over an area 22.5 μm × 22.5 μm. A typical cwTPE image of a nucleus of such a human bone marrow stromal cells (hBMSCs) after overnight culture is shown in Figure 1(a). In an overnight culture, after seeding the cells, the nuclei are typically round and somewhat smaller as the cells are not well adhered. Typical interphase morphology of well-adhered hBMSC cells after proliferation for 14 days in cell culture is shown in Figure 1(b). The interphase of the cell cycle characterizes the growth and development of the cell and the nucleus before mitosis. A few percent of the cells are in mitosis. In Figure 1(c) a cell nucleus is shown after the end of the telophase with the cell undergoing cytokinesis. A distinct separation between the nuclei of the two daughter cells can be observed (indicated by white arrows), while the chromatin in each cell is becoming decondensed. Figure 1(d) shows the (early) apoptotic stage of the hBMSCs cultured in a medium without refreshment until day 14 of culture period. Due to the lack of nutrients over the culture period, symptoms like cell shrinkage, nuclear fragmentation and chromatin condensation (indicted by white arrows) were observed which are signs of apoptosis in the cell. The nuclei are surrounded by dark areas, which reflect that no dye could be detected in the cytoplasm of the cells. All the images of the nuclei in the respective phases show brighter and darker regions reflecting the variation in the density of DNA. The bright regions relate to high concentrations of Hoechst-33342 and therefore a high DNA concentration. The dark regions have approximately 5 to 30 times lower Hoechst-33342 concentration suggesting a correspondingly lower DNA concentration.

The interphase of the cell is also accompanied by the growth of the nucleolus. The dark region in Figure 1(b) indicated by a white arrow corresponds to the nucleolus inside the nucleus.[1] The nucleolus grows throughout the interphase and reaches a maximal size during G1 and half way through the S phase of the cell cycle.[2] The nucleolus hoist ribosomal RNA (rRNA), transfer RNA (tRNA), precursors to messenger RNA (pre-mRNA), and enzymes and genes responsible for the synthesis of these RNAs. When the cells need proteins during their cell cycle and metabolism, messenger RNA (mRNA) is transcribed from DNA. Due to the high concentration of RNA in the nucleolus, these regions are not stained with Hoechst-33342 and are hence low in TPE fluorescence.

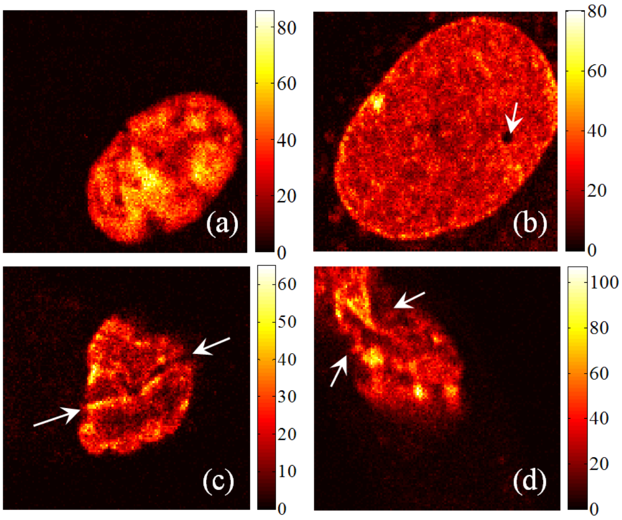

Figure 1: cwTPE images showing various stages of the cell cycle acquired from the APD over an area of 22.5 µm × 22.5 µm in 128 ×128 steps with an overall imaging time of 16.4 s. (a) Nucleus of overnight cultured hBMSC, (b) Well developed nucleus of a hBMSC which is in interphase stage on day 14 of culture period, (c) Mitosis stage of the hBMSC seen after day 14 of culture period (white arrows show division of the nucleus), and (d) Apoptotic hBMSC showing cell shrinkage (white arrows) cultured in a medium without refreshment until day 14 of culture period.

9.1.2 Raman microspectroscopic imaging to detect RNA in nucleus of the cell

The cwTPE fluorescence image of Hoechst-33342 in Figure 2(a) shows the nucleus of a living hBMSC cell in interphase in correspondence with Figure 1(b). The molecular compositions of an area containing bright and dark regions were analyzed by hyperspectral Raman imaging. A region of interest, region 'A', was selected with a size of 4.9 µm × 4.9 µm as indicated by a white square (dotted line) in Figure 2(a). The hyperspectral data from the Raman image is subjected to multivariate HCA over the spectral region from 600 to 1800 cm^{-1}. The first four clusters from cluster analysis are presented in the HCA image in Figure 2(b) and the spectral information corresponding to each cluster is illustrated in Figure 2(c). The "red" and "green" clusters correspond to a dark region in the nucleus in correspondence with Figure 2(a), while the “blue” and “black” cluster correspond to an area which is more representative of the average cellular DNA content. The spectra show intense bands at 725 cm^{-1} for Adenine and 782 cm^{-1} for nucleotides (T, U and C), 1095 cm^{-1} for phosphate backbone vibration of DNA and 1573 cm^{-1} for ring breathing modes of DNA bases, 1002 cm^{-1} for phenylalanine, 1125 cm^{-1} for C-N stretch vibration, 1447 cm^{-1} for C-H deformation of proteins and 1655 cm^{-1} for Amide-I of proteins. In addition to these bands, the average red and green spectra in Figure 2(c), associated with the red and green cluster regions in Figure 2(b), show prominent bands at 666 cm^{-1} for guanine in RNA, 813 cm^{-1} for A-type helices in RNA and 1244 cm^{-1} for a ring mode of uracil in RNA. These bands for RNA and DNA are in close agreement with the literature.[3-5]

The Raman difference spectrum [green-red] is shown in Figure 2(d)(i). The difference spectrum shows positive bands at positions 666, 725, 782, 813, 1095, 1244, 1317, 1337, 1478 and 1574 cm^{-1} signifying the presence of RNA.[3] The spectra do not show intense negative bands. The observation of Raman marker-bands for RNA and the absence of Raman bands at 980, 1560 and 1610 cm^{-1} corresponding to Hoechst-33342 implies that dark areas in TPE imaging correlate with a high RNA concentration. The Raman difference spectrum [blue-black] (Figure 2(d)(ii)) of the respective areas in the cluster image reflects very weak RNA marker-bands at 782, 813, 1244 and 1574 cm^{-1} in the area of the blue cluster. The spectrum also shows negative bands at positions 1560 and 1610 cm^{-1} which corresponds to an increase of Hoechst-33342, and hence DNA, in the black cluster with respect to the blue cluster. The low fluorescent areas (dark areas) in the TPE image are dominated by RNA contributions, and the RNA concentration decreases from the green via red and blue to the black area. The black area contains more DNA, which corresponds with the presence of a relatively bright TPE signal in the respective image (Figure. 2(a)).

These regions with high presence of RNA can be attributed to the nucleolus. These results correspond well with the literature which shows the presence of RNA in nucleolus[1] and are in agreement with Raman and FTIR spectroscopic results, which detected increased RNA in whole cells during the transition of G_1 to S of the interphase.[6, 7] The spectra for RNA corresponding to the dark regions in region ‘A’ with high TPE fluorescence regions in region ‘B’ are shown in Figure 2(a). The Raman data provide the chemical information of the variation in the distribution of the nucleotides in the nucleus of the cell. Figure 2(e)(i) corresponds to the average spectra of pixels corresponding to RNA as seen in Figure 2(d)(i). The spectra show significant bands confirming the presence of RNA.[3] Average spectra in Figure 2(d)(ii) correspond to brighter regions in the nucleus of the cell indicated by region

'B' in Figure 2(a). The spectra show prominent bands for nucleotides corresponding to DNA along with bands for Hoechst-33342 bound to AT base pairs of DNA in the nucleus of the cell.[8]

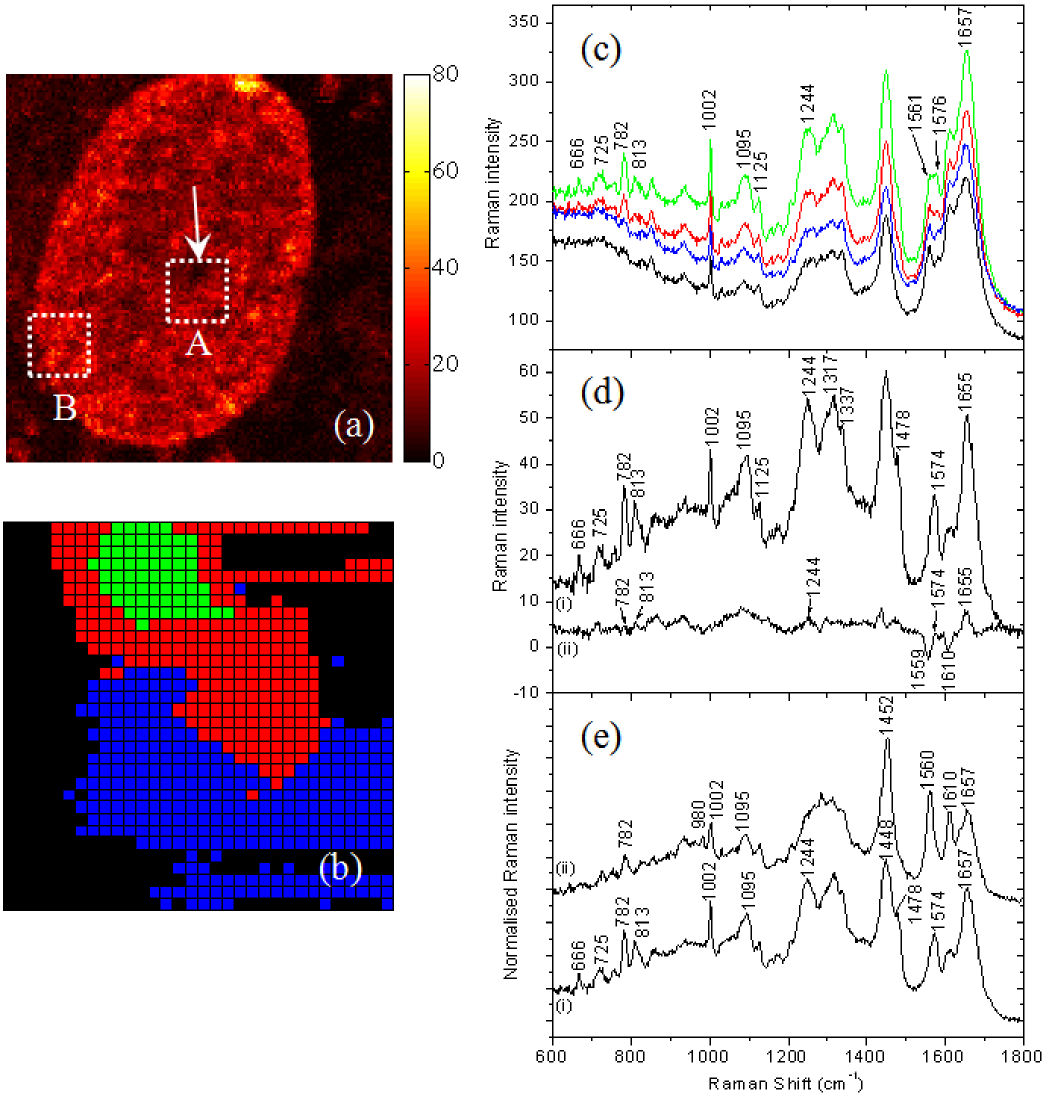

Figure 2: (a) cwTPE fluorescence image of Hoechst-33342 stained hBMSC showing well developed nucleus in interphase stage on day 14 of culture, which was acquired over an measurement area of 22.5 µm × 22.5 µm at 100mW laser power and overall accumulation time of 16.4s, region 'A' and region 'B' shown by white square box with dotted lines correspond to the areas of low and high TPE fluorescence for Raman measurements; (b) Four level HCA image over the range 600 to 1800 cm^{-1} of hyperspectral Raman data acquired over the region 'A' in (a); (c) Corresponding average Raman spectrum of pixels in each cluster seen in (b) over the spectral region 600-1800 cm^{-1}; (d) Raman difference spectroscopy for, (i) average Raman spectrum of green cluster minus red cluster and (ii) average Raman spectrum of blue cluster minus black cluster; (e) Average Raman spectrum acquired from the nucleus of hBMSC showing the variation in the distribution of nucleotides, (i) Average Raman spectrum acquired from region 'A' corresponding to low TPE fluorescence indicating presence of RNA, (ii) Average Raman spectrum acquired from region 'B' corresponding to high TPE fluorescence showing prominent bands for Hoechst-33342 bound to AT base pairs of DNA.

9.2 Ca^{2+} activity on mitochondria of the mammalian cells.

The Raman band at 1602 cm^{-1} in the spectra of human cells, which previously had only been observed in mitochondria of yeast cells,[9] was also found in spectra of other mammalian cell types. The band is an indicator of the activity of mitochondria in cells upon variations in the calcium ion concentration in the surrounding medium.

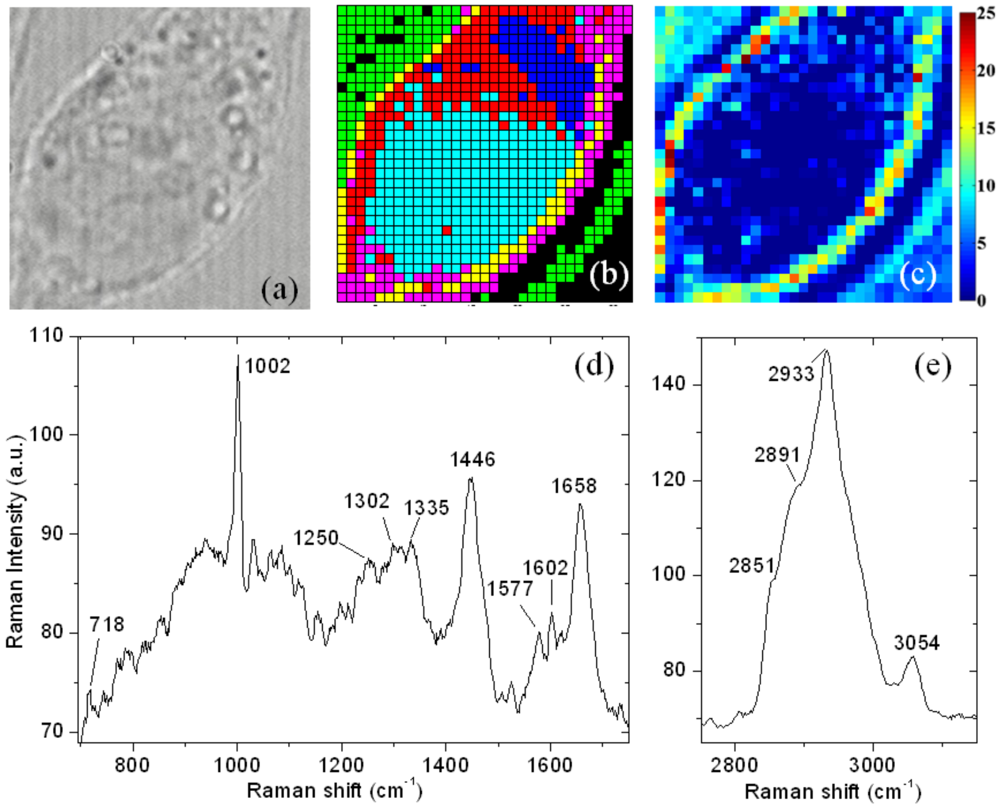

Figure 3: Raman microspectroscopy of HeLa cell. (a) White light micrograph of measured cell. The size of the area is 20 × 20 μm^2. The pixel size is 625nm; (b) An image from hierarchical cluster analysis (7 clusters) of the HeLa cells shown in (a); (c) Univariate Raman image over the band 1602 cm^{-1} (Δ=22 cm^{-1}); Raman difference spectrum of the average spectrum of the yellow pixels minus the average spectrum of the black pixels (which correspond to the buffer) in (d) Fingerprint region and (e) High frequency region.

Figure 3(a) shows the white light micrograph of the nucleus and the peri-nuclear region of a HeLa cell, whose corresponding hierarchical cluster image (7 levels), is shown in Figure 3(b). In Figure 3(c) the univariate Raman image is shown of the band area between 1591 cm^{-1} and 1613 cm^{-1} encompassing the 1602 cm^{-1} band. A high correspondence between the univariate image in Figure 3(c) and the yellow cluster in Figure 3(b) was observed. The Raman difference spectrum of the yellow cluster spectrum minus the cluster spectrum corresponding to buffer (black pixels) is shown in Figure 3(d). The spectrum reveals a clear band at 1602 cm^{-1}. The corresponding high wavenumber spectrum is presented in Figure 3(e).

A band at 2851 cm^{-1} due to lipids can be observed as a weak shoulder on the strong bands at higher wavenumber, which are dominated by the, partially branched, aliphatic amino acid residues normal to proteins. The band at 1602 cm^{-1} correlates with both lipid bands and protein bands at 1002 cm^{-1} (Phenylalanine), 1250 cm^{-1} (Amide III), 1302 cm^{-1} (CH_3, CH_2 bending and twisting of lipids and proteins), 1446 cm^{-1} (protein and lipid CH_2 bending mode), 1658 cm^{-1} (Amide I). The 1602 cm^{-1} band also correlates with a band at 718 cm^{-1}. This band can be assigned to the C-N stretching vibration in phosphatidylcholine lipid head groups, which are abundant in the mitochondrial membrane.

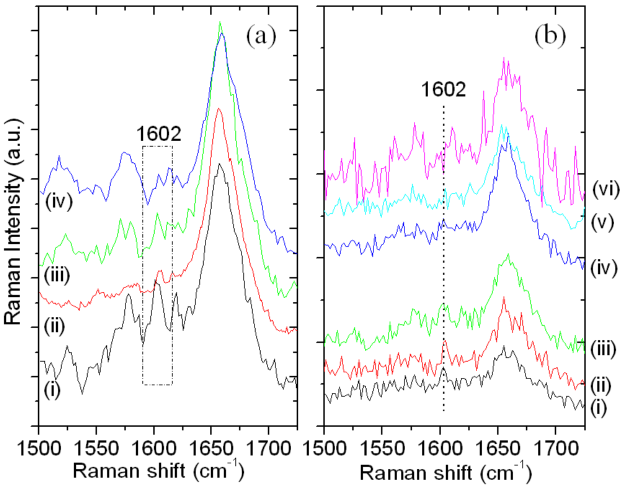

Figure 4: Raman difference spectra (cytoplasm minus buffer). (a) Raman spectroscopy showing the presence of 1602 cm^{-1} band in different eukaryotic cells (i) HeLa cell, (ii) bovine chondrocyte, (iii) hMSC and (iv) PBL cell; and (b) Influence of PBS (- Ca^{2+}) and HBSS (+ Ca^{2+}) buffer media on the intensity of the 1602 cm^{-1} band in HeLa-cells. (i) With serum and with PBS wash, (ii) Without serum and with PBS wash, (iii) With serum starvation and with PBS wash, (iv) With serum and with HBSS wash, (v) Without serum and with HBSS wash and (vi) With serum starvation and with HBSS wash.

The band at 1602 cm^{-1} can also be observed in the cytoplasm of other eukaryotic cells like bovine chondrocytes, peripheral blood lymphocytes and human bone marrow stromal cells as shown in Figure 4(a). The intensity of the band varied with cell type. The understanding behind this observation awaits an interpretation of the band. However, it may simply be due to variations in the concentration of mitochondria or differences in the mitochondrial Ca^{2+}-ion concentration. The Raman difference spectra of cells washed with phosphate buffer saline solution (PBS buffer) and with Hank's balanced salt solutions (HBSS buffer) are shown in Figure 4(b). The spectra in Figure 4(b)(i), 4(b)(ii) and 4(b)(iii) showed a significant band for 1602 cm^{-1} for the cell culture conditions that were washed with PBS solution. However, the band was much weaker or not observed in Figure 4(b)(iv), 4(b)(v) and

4(b)(vi) when the cells were washed with Ca^{2+}-ion-containing HBSS solution. The influence of Ca^{2+}-ions on the intensity of the band at 1602 cm^{-1} corresponds well with results shown by Tang et al.[10] The results in Figure 4(b) show that the occurrence/absence of the 1602 cm^{-1} band is not dependent on the culture methodology, i.e. with serum, without serum or with serum starvation, but depends on the Ca^{2+} ion concentration. The assignment of 1602 cm^{-1} band to a particular molecular species is not clear. So far the band has revealed correlations with lipid-type modes and also with a mixture of phospholipid and protein bands.

9.3 Carotenoid variations in Gall body of CD4+ PBL cells

In chapter 3 of this thesis, we show study of peripheral blood lymphocyte (PBL) cells which revealed distribution of carotenoids in the cytoplasm of the cell. The concentration of carotenoids in these PBL cells is in the order of ~10^{-6} M. Other phenotypes of PBL cells show varying amounts of carotenoids. One such example is CD4+ PBL cell which shows a high concentration of carotenoids (~10^{-3} M) in the Gall body in the cell. A Gall body is typical to CD4+ PBL cells and not present in other phenotypes.[11, 12]

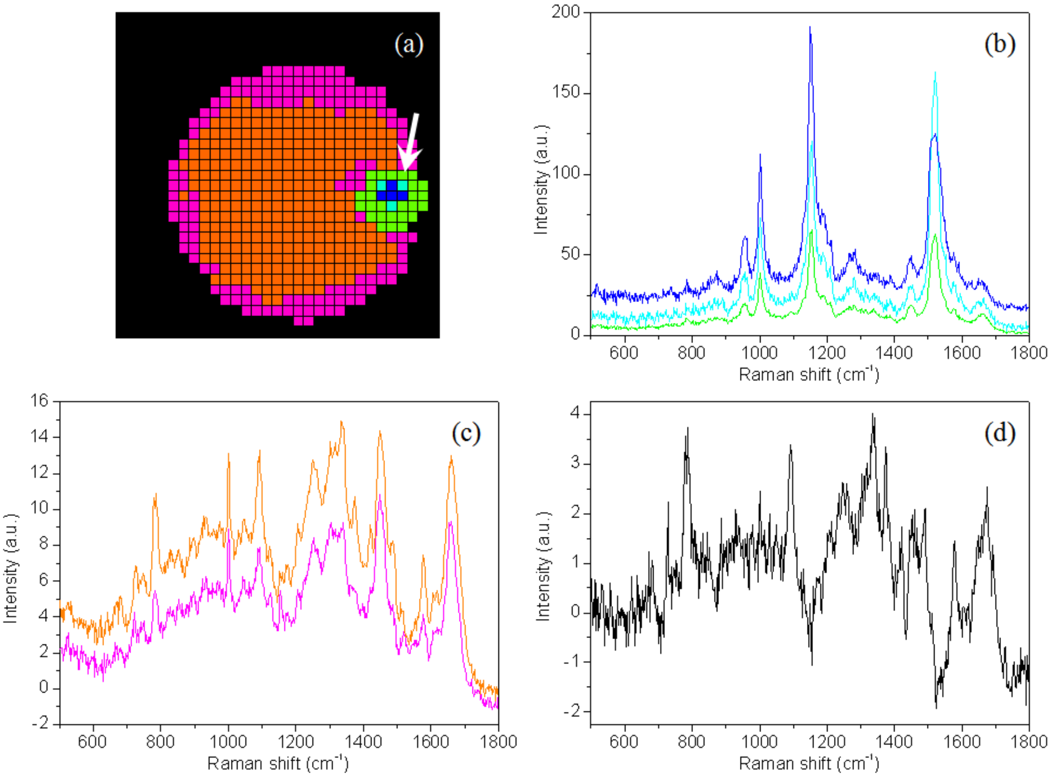

Figure 5: (a) HCA image showing up to six clusters of a CD4+ PBL cell with a Gall body indicated with a white arrow (green, light blue and dark blue clusters), (b) Background free Raman spectra corresponding to Gall body, (c) Background free Raman spectra corresponding to nucleus (orange spectrum) and cytoplasm (magenta spectrum), and (d) Raman difference spectrum corresponding to nucleus minus cytoplasm.

Raman microspectroscopy of a CD4+ PBL cell was performed by scanning in 32 × 32 steps respectively in an area of 9 µm × 9 µm with an accumulation time of 100 ms per pixel and 35 mW laser power. The resultant six cluster image after hierarchical cluster analysis (HCA) of the acquired hyperspectral data is shown in Figure 5(a). Five of the six clusters correspond to the PBL cell and the remaining cluster to the background (black cluster). Raman difference spectroscopy is performed to remove the influence of background from each of the clusters corresponding to the PBL cell. Figure 5(b) shows background free spectra of green, light blue and dark blue clusters corresponding to the Gall body (indicated by the white arrow in Figure 5(a)). All three spectra show three distinct Raman bands around 1520 (ν_1), 1154 (ν_2) and 1002 (ν_3) cm^{-1} corresponding to the –C=C– stretch, =C–C= stretch and CH_3 in plane rocking vibrations of carotenoids.[13] The green spectrum shows equal intensities for bands at 1520 and 1154 cm^{-1}. The light blue spectrum shows the intensity of the band at 1520 cm^{-1} to be higher than that of the band at 1154 cm^{-1}, while this relation is inverted in the dark blue spectrum. The band at 1520 cm^{-1} for the dark blue spectrum is broader than that seen for the light blue spectrum and shows shoulders 1509 and 1540 cm^{-1}. These spectral features in the three clusters indicate that the Gall body is composed of different types of carotenoids. The close association of dark blue and light blue clusters that are again surrounded by the green cluster shows a variation in carotenoid type in the core of the Gall body.

The background free spectra of the orange and magenta clusters are shown in Figure 5(c). A significant part of the PBL cells is occupied by a well defined nucleus indicated by the orange cluster in Figure 5(a). Corresponding spectra in Figure 5(c) show prominent bands at 785, 1092, 1335, 1374, 1421, 1487, 1576, 1663 cm^{-1}, which are typical for nucleotides and proteins. The magenta spectrum shows significant vibrations at 718, 1087 and 1654 cm^{-1} for lipids that are present in cytoplasm. The magenta spectrum also has prominent bands at 1154 and 1520 cm^{-1}. The bands correspond to vibrations of carotenoids. The Raman difference spectrum of nucleus minus cytoplasm (i.e. orange minus magenta spectrum) is shown in Figure 5(d). The positive Raman bands at 785, 1092, 1250, 1335, 1374, 1490, 1576 and 1674 cm^{-1} indicate the presence of proteins and nucleotides in the nucleus and negative Raman bands at 702, 1154, 1434, and 1524 cm^{-1} indicates presence of lipids and carotenoids in cytoplasm which are possibly bound to the Golgi complex. The concentration of carotenoid molecules varies with various organelles. The band intensity of the carotenoids bound to Golgi body seen in Figure 5(d) are approximately 150 – 200 times less than those seen in

Figure 5(b) for Gall body. These results show the capability of classifying the PBL cell based on the phenotype by Raman microspectroscopy.

9.4 Role of carotenoids in the mineralisation of bone marrow derived stromal cells.

Retinol, a common form of vitamin-A, is an essential biochemical compound necessary for normal cell proliferation and differentiation in addition to specialized functions such as vision, embryogenesis, reproduction, and maintenance of epithelial tissues. The other forms of vitamin-A include retinal (aldehyde form), retinoic acid (acid form) and retinyl ester (ester form). Retinol plays an active role in bone growth and skeletal development, however overdosage can result in bone resorption, fractures and osteoporotic lesions.[14] The dietary source for retinol is either from active sources like animal products or in the form of precursors like carotenoids (mainly β-carotene) from plant products (fruits and vegetables). The precursors are converted to active forms by specific enzymes in the body. The source of carotenoids for *in vitro* cultured cells is obtained from the retinols or carotenoids present in the serum, supplemented in the cell culture media.[15, 16]

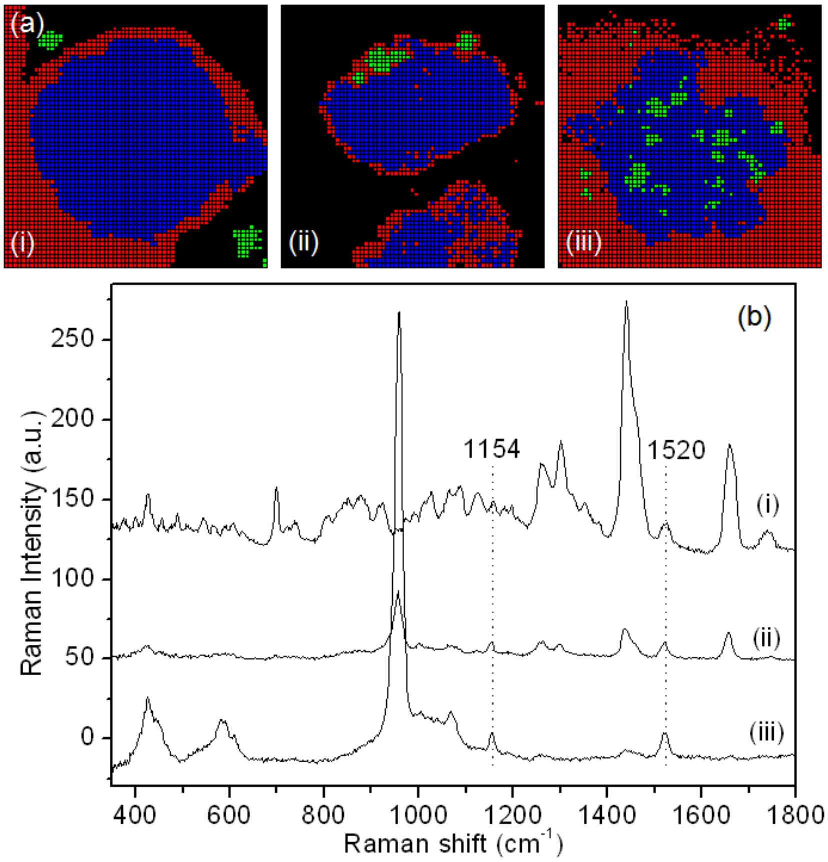

Figure 6: (a) HCA images showing up to four clusters of bone nodules formed over the culture period corresponding to (i) Day 30, (ii) Day 40, and (iii) Day60, (b) Average Raman spectra of the green cluster corresponding to (i) Day 30, (ii) Day 40, and (iii) Day60.

Figure 6 illustrates the association of carotenoids with *in vitro* mineralized bone nodules formed in the human immortalized bone marrow stromal cells iMSCs. The iMSCs were cultured in osteogenic mineralization medium as indicated in chapter 5. The four level HCA images of the Raman data of bone nodules measured on day 30, day 40, and day 60 of culture period are shown in Figure 6(a)(i), 6(a)(ii) and 6(a)(iii) respectively. In Figure 6(a)(i), 6(a)(ii) and 6(a)(iii), the blue and red clusters correspond to areas of bone nodule with varying concentration of hydroxyapatite mineral formation. The black clusters show unmineralized iMSCs on day 30 to less mineralized iMSCs on day 60 of culture period. The green clusters in all the three images have respective spectra as shown in Figure 6(b). The spectra show prominent bands at 1154 and 1520 cm^{-1}, which correspond to vibrations of carotenoids. Figure 6(b)(i) shows typical spectra of cholesterol with bands at 697, 1439, 1660 and 1737 cm^{-1}. Cholesterol plays an active role mineralization was reported in chapter 8 of this thesis. The spectra in Figure 6(b)(ii) for day 40 of culture period show bands for cholesterol at 697, 1439, 1660 and 1737 cm^{-1} and also a band at 956 cm^{-1} for phosphates suggesting a role of cholesterol in mineralization. By day 60 of culture period, there is an increase in the band for phosphates showing the increase in apatites. The phosphate band shifts to 959 cm^{-1} and also a band for carbonates appears at 1170 cm^{-1} indicating the crystalline nature of the formed bone nodule as seen in Figure 6(b)(iii). Due to the lipophilic nature of the carotenoids, they are found in association with cholesterol on day 30 and day 40 of the culture period. On day 60, due to the growth of bone, we could hardly detect the presence of cholesterol/lipids. The distribution of carotenoids is observed both inside and outside the bone nodule. The bands at 1154 and 1520 cm^{-1} do not show much variation in intensity and also the band at 1520 cm^{-1} does not show a significant shift for different phenotypes or photoproducts of carotenoids. However, the functional use of carotenoids to form retinol for the *in vitro* formation of bone over the iMSCs could be underlying the observations.

9.5 Line scan Raman microscopy

Over the last two decades, Raman microscopy is gaining more popularity in biological research areas to study molecular distribution in cells and tissues. For the effective use of Raman microscopy on living cells or tissues, certain requirements need to be met. These are shorter measurement times and larger field of view respectively. Decreasing measuring time eventually enables measurement over a larger part of the sample. Shorter measurement times are necessary since the biological samples cannot stay alive for very long durations of time at room temperatures. The most widely demonstrated illumination and detection techniques for Raman microscopy are wide-field Raman microscopy, confocal spot scanning Raman microscopy and semi-confocal line scanning Raman microscopy.[17] Wide field Raman imaging is the simplest and fastest when a certain wavelength has to be detected for a sample. In a confocal spot scanning setup the sample is illuminated by a diffraction-limited laser spot, the Raman scattered photons are detected from that spot by using a pinhole in front of the detector, and the sample is scanned through the confocal spot in two directions. This technique has high lateral and axial resolution due to the rejection of out-of focus light by the pinhole. Confocal spot Raman imaging provides a whole spectrum from one point in a sample, but takes time if a whole sample needs to be imaged. In semi-confocal line scanning Raman microscopy a laser line, diffraction limited in one direction, illuminates the sample and Raman photons are detected from the line by using a slit in front of the detector.[18] While in a spot scanning microscope only one direction of the detector is used to detect spectral information, in line scanning microscopy the second direction is used to detect lateral information along the line. By scanning the line through the sample, information along the second lateral direction is gathered. The consequence of the slit is that the setup is still confocal across the slit. Along the slit the confocality is reduced. Due to this the resolution decreases along the line. The advantage however is that a Raman image can be made faster than the confocal spot Raman imaging, because the line has to be scanned only in one direction through the sample to cover the scanning range.

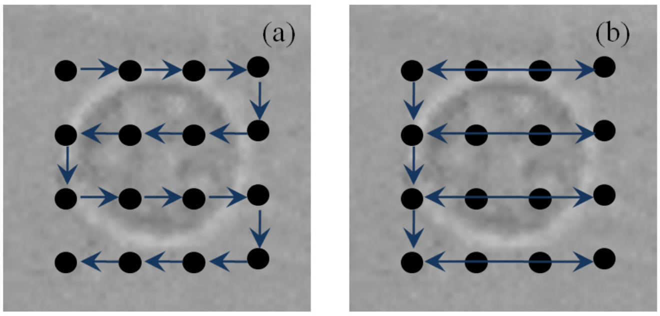

Figure 7: Raman imaging by (a) Confocal spot scanning Raman microscopy and (b) Semi-confocal line scanning Raman microscopy

Figure 7(a) shows an image of a PBL cell which needs to be measured by 4 × 4 pixels by confocal spot Raman microscopy. The image is made by acquiring the spectra from 16 positions by moving the spot 15 times by the scanning mirror. On the other hand, semi-confocal line scan Raman microscopy enables image over the same area by acquiring spectra from each line and moving the line 3 times as seen in Figure 7(b) by the scanning mirror. For the same 4 pixels measured by confocal spot Raman microscopy, semi-confocal line scan Raman microscopy measures it in a single line. Similar laser power used for both methods show the power dissipated by the confocal spot is much larger than confocal line which is due the power that is spread out along the line for the latter. The factor with which the power will decrease is given by the length of the scanned line divided by the size of a point, which is given by the size of the diffraction limited spot, under the conditions that the distribution of the light can be considered as homogeneous in time and space. To detect the same intensity of Raman photons the acquisition time should be increased by the same factor so that the total energy for a certain volume is equal to point scanning.

References

1. Uzunbajakava, N.; Lenferink, A.; Kraan, Y.; Volokhina, E.; Vrensen, G.; Greve, J.; Otto, C., Nonresonant confocal Raman imaging of DNA and protein distribution in apoptotic cells. *Biophys. J.* **2003,** 84, (6), 3968-3981.
2. Sacristaan-Gaarate, A.; Navarrette, M. H.; de la Torre, C., Nucleolar development in the interphase of the cell cycle. *J Cell Sci* **1974,** 16, (2), 333-47.
3. Benevides, J. M.; Tsuboi, M.; Bamford, J. K.; Thomas, G. J., Jr., Polarized Raman spectroscopy of double-stranded RNA from bacteriophage phi6: local Raman tensors of base and backbone vibrations. *Biophys J* **1997,** 72, (6), 2748-62.
4. Thomas, G. J., Jr.; Prescott, B.; Olins, D. E., Secondary structure of histones and DNA in chromatin. *Science* **1977,** 197, (4301), 385-8.
5. Tu, A. T., *Raman Spectroscopy in Biology: Principles and Applications*. 1982; p 448.
6. Holman, H.-Y. N.; Martin, M. C.; Blakely, E. A.; Bjornstad, K.; McKinney, W. R., IR spectroscopic characteristics of cell cycle and cell death probed by synchrotron radiation based fourier transform IR spectromicroscopy. *Biopolymers* **2000,** 57, (6), 329-335.
7. Singh, G. P.; Volpe, G.; Creely, C. M.; Grotsch, H.; Geli, I. M.; Petrov, D., The lag phase and G1 phase of a single yeast cell monitored by Raman microspectroscopy. *J. Raman Spectrosc.* 2006, 37, (8), 858-864.
8. Pully, V. V.; Lenferink, A.; Otto, C., Hybrid Rayleigh, Raman and two-photon excited fluorescence spectral confocal microscopy of living cells. J. Raman Spectrosc. 2009, 10.1002/jrs.2501.
9. Huang, Y.-S.; Karashima, T.; Yamamoto, M.; Hamaguchi, H.-o., Molecular-level pursuit of yeast mitosis by time- and space-resolved Raman spectroscopy. J. Raman Spectrosc. 2003, 34, (1), 1-3.
10. Tang, H.; Yao, H.; Wang, G.; Wang, Y.; Li, Y.-Q.; Feng, M., NIR Raman spectroscopic investigation of single mitochondria trapped by optical tweezers. Opt Express 2007, 15, (20), 12708-16.
11. Puppels, G. J.; Garritsen, H. S.; Kummer, J. A.; Greve, J., Carotenoids located in human lymphocyte subpopulations and natural killer cells by Raman microspectroscopy. Cytometry 1993, 14, (3), 251-6.
12. Ramanauskaite, R. B.; Segers-Nolten, I. G. M. J.; de Grauw, K. J.; Sijtsema, N. M.; van der Maas, L.; Greve, J.; Otto, C.; Figdor, C. G., Carotenoid levels in human lymphocytes, measured by Raman microspectroscopy. Pure Appl. Chem. 1997, 69, (10), 2131-2134.
13. Van Wijk, A. A. C.; Spaans, A.; Uzunbajakava, N.; Otto, C.; De Groot, H. J. M.; Lugtenburg, J.; Buda, F., Spectroscopy and Quantum Chemical Modeling Reveal a Predominant Contribution of Excitonic Interactions to the Bathochromic Shift in alpha -Crustacyanin, the Blue Carotenoprotein in the Carapace of the Lobster Homarus gammarus. J. Am. Chem. Soc. 2005, 127, (5), 1438-1445.
14. Dickson, I.; Walls, J., Vitamin A and bone formation. Effect of an excess of retinol on bone collagen synthesis *in vitro*. Biochem J 1985, 226, (3), 789-95.
15. McDevitt, T. M.; Tchao, R.; Harrison, E. H.; Morel, D. W., Carotenoids normally present in serum inhibit proliferation and induce differentiation of a human monocyte/macrophage cell line (U937). J. Nutr. 2005, 135, (2), 160-164.
16. Michaelsson, K.; Lithell, H.; Vessby, B.; Melhus, H., Serum retinol levels and the risk of fracture. N. Engl. J. Med. 2003, 348, (4), 287-294.
17. Arikan, S.; Sands, H. S.; Rodway, R. G.; Batchelder, D. N., Raman spectroscopy and imaging of beta -carotene in live corpus luteum cells. Anim. Reprod. Sci. 2002, 71, (3,4), 249-266.
18. Hamada, K.; Fujita, K.; Smith, N. I.; Kobayashi, M.; Inouye, Y.; Kawata, S., Raman microscopy for dynamic molecular imaging of living cells. J. Biomed. Opt. 2008, 13, (4), 044027/1-044027/4.

Summary

This thesis presents a body of interdisciplinary research aimed at visualizing bone tissue engineering using microbioreactors and non-invasive and label-free vibrational Raman microspectroscopy. Confocal Raman microspectroscopy is an optical microspectroscopic technique enabling spatially resolved chemical imaging and analysis. In this thesis this approach was used to monitor the temporal development of *in vitro* bone formation, that is, from proliferation of human bone marrow derived stromal cells, their differentiation towards osteogenic precursors, till early and late stages of mineralized tissue formation. The results yield deeper insights into, and understanding of, *in vitro* formation of mineralized tissue from stromal cells derived from human bone marrow that are consistent with the characteristics of *in vivo* bone formation.

A general introduction into the concepts of bone tissue engineering, microbioreactors and Raman microspectroscopy is presented in ***Chapter 1***. An overview of Raman microscopy for cell and tissue based applications is described. The overview also briefly illustrates the feasibility and advantages of Raman microspectroscopy in bone tissue engineering compared to other techniques. ***Chapter 2*** describes a custom-built versatile hybrid microscopy system based on a single laser wavelength for cell and tissue based applications. The system combines low wavenumber resolution Raman imaging, Rayleigh scatter imaging and two photon fluorescence (TPE) spectral imaging, fast “amplitude-only” TPE-fluorescence imaging and high spectral resolution Raman imaging. The optical contrast from the TPE-fluorescence imaging is used to select a region of interest from Hoechst-33345 stained cells which is subsequently followed by high and low resolution Raman chemical imaging and Rayleigh scatter imaging.

In ***Chapter 3***, we introduce the concept of Time Lapse Raman Imaging to spectrally monitor the molecular changes in single living peripheral blood lymphocyte (PBL) cells. We show high spectral resolution Raman images acquired in ~102.4 seconds; typically 10-15

Raman images were obtained before cell damage was observed in the form of cell blebs. Repeated imaging on single lymphocytes reveals photo-induced biochemical changes in specific molecules like carotenoids.

Chapter 4 describes the development of microbioreactors that could be optically coupled to the confocal Raman microspectroscope. The microbioreactors were successfully used for long-term cell-based bone tissue engineering applications under continuous perfusion of cell culture media. The microbioreactors ensured optimal culture conditions for the cells throughout culture periods, at least for as long as 21 days. Cellular activities such as growth, proliferation, differentiation and mineralization inside the microbioreactor were effectively monitored by chemically sensitive confocal Raman microspectroscopy.

A comparison of the influence of various osteogenic and non-osteogenic cell culture media on the development of human immortalized bone marrow stromal cells (iMSCs) is presented in ***Chapter 5***. Reduction in the intracellular concentrations of proline was observed by day 3 of culture in osteogenic media containing dexamethasone. The reduction in proline was identified as a Raman biomarker for early stage of differentiation of iMSCs towards osteogenic lineage well before the formation of collagen molecules. Univariate and multivariate data analysis along with Raman difference spectroscopy of the data acquired on days 3 and 7 of culture confirm the variation in proline with different osteogenic and non-osteogenic culture media.

In ***Chapter 6***, Raman biomarkers reflecting the pluripotency of iMSCs towards osteogenic and adipogenic lineages are described. Different osteogenic cell culture media affected the expression of pluripotency. Variation in intracellular glycogen concentration defines different stages of osteogenic lineages such as pre-osteoblast, osteoblast and osteocyte. A pronounced presence of lipid globules confirmed differentiation towards adipogenic lineage. Changes in pH influencing the glycogen synthesis in cells resulted in variations in the chemical composition of mineralization in the extracellular matrix towards either hydroxyapatite or calcium oxalates. The hydroxyapatite mineralization is further influenced by the presence of osteogenic growth factors in the cell culture media, which resulted in normal or carbonated hydroxyapatite. Mineralization was also observed in cells differentiated towards adipogenic lineage, and is attributed to the presence of phosphatidylserine that transports sufficient calcium ions to induce hydroxyapatite formation.

Chapter 7 illustrates the events of mineralization in the extracellular matrix of iMSCs differentiated towards osteogenic lineage. Early mineralized nodules of highly heterogeneous composition were observed around day 30 of culture. The Raman spectral information from these nodules revealed the presence of amorphous calcium phosphate, mono-calcium phosphate mono-hydrate, di-calcium phosphate di-hydrate and β-tri-calcium phosphate, sometimes even together in a single nodule. In prolonged cultures, these nodules transformed to a more homogeneous nodule showing the presence of hydroxyapatite by day 40 and resulting in carbonated hydroxyapatite by day 60 of culture. The conversion of hydroxyapatite to carbonated hydroxyapatite resulted in increased crystallinity of the apatite, and was spectroscopically verified by the presence of Raman bands for carbonates, and upward shift in frequency and reduction in bandwidth at full width half maximum of the band characteristic of v_1 vibration of phosphates. The lipid-rich organic phase observed during the formation of heterogeneous bone nodules developed to a protein-rich inorganic phase by days 40 and 60 of culture.

In ***Chapter 8***, we perform studies over extended time-periods using confocal Raman microscopy, coherent anti-Stokes Raman spectroscopy (CARS) and second harmonic generation (SHG) imaging to understand cell-based bone formation. CARS and SHG enabled a 3-dimensional understanding from early to late stages of cell-based bone formation. The presence of collagen, glycosaminoglycans (GAGs), cholesterol, phosphatidic acid (PA), and phosphatidylserine (PS) in cells by days 25 and 30 indicate well-differentiated osteogenic lineage of iMSCs. The amount of collagen showed an increase with culture period. Cholesterol, PA, and PS influenced initial hydroxyapatite (HA) mineralization by day 35. Initial HA mineralization was observed to occur simultaneously in different layers of cells which got interconnected during the culture period. HA deposition increased with time, and was well-guided by the orientation of the collagen fibrils in the extracellular matrix. With time, gradual conversion of carbonated hydroxyapatite from HA was clearly observed.

Chapter 9 illustrates the potential of Raman microspectroscopy for various cell- and tissue-based applications. We used hybrid microscopy to identify the physical status of the cells based on the morphology of the nucleus, which further enabled us to localise the distribution of RNA and DNA in the cell nucleus. Raman microscopy was used to identify the distribution of mitochondria in the cells and the influence of variations in concentration of ambient Ca^{2+} ions on mitochondrial activity. Raman microspectroscopic imaging revealed the presence of the Gall body in CD4+ PBL cells composed of different types of carotenoids. These were identified by the variation in the band intensities and bandwidths for the bands around 1154 and 1520 cm^{-1} characteristic of carotenoids. Furthermore, evidence was acquired from Raman imaging of the role of carotenoids in the events of mineralization of iMSCs.

Finally we briefly discuss the development of a line scan Raman microscopy system for faster imaging in tissue based applications.

Samenvatting

In dit proefschrift staat een interdisciplinair onderzoek op het gebied van botweefseltechnologie centraal, waarbij gebruik wordt gemaakt microbioreactoren en niet-invasieve, ongelabelde Raman microspectroscopie. Confocale Raman microspectroscopie is een optische microspectroscopische techniek die afbeelding en analyse mogelijk maakt van de chemische samenstelling met een hoge resolutie. Deze techniek is hier gebruikt om in de tijd de vorming van bot *in vitro* te volgen: van de proliferatie van menselijke stromale cellen uit het beenmerg, hun differentiatie tot osteogene (botvormende) precursor cellen tot aan vroege en late stadia in de vorming van mineralen die overeenkomen met de mineralen in *in vivo* botvorming.

Hoofdstuk 1 vormt een algemene introductie in de concepten van de weefseltechnologie, microbioreactoren en Raman microspectroscopie. Er wordt een overzicht gegeven van Raman microscopische toepassingen op cel- en weefselgebied. Daarnaast geeft het een beknopte illustratie van de mogelijkheden en voordelen van Raman microspectroscopie in de botweefseltechnologie in vergelijking met andere technieken. In ***Hoofdstuk 2*** wordt een door ons ontwikkeld veelzijdig hybride microscopiesysteem beschreven, dat gebaseerd is op een enkele lasergolflengte voor cel- en weefselgebaseerde toepassingen. Het systeem combineert Raman beeldvorming en Rayleigh verstrooiing met twee-foton-fluorescentie (TPE) microscopie. Het optische contrast van de TPE fluorescentie beeldvorming wordt gebruikt om een interessegebied te selecteren in met Hoechst-33345 gemerkte cellen, vervolgens wordt microspectroscopie gebruikt om een chemische afbeelding te maken.

In ***Hoofdstuk 3*** worden meerdere Raman afbeeldingen van een levende cel in de tijd gemaakt. Hiermee kunnen de moleculaire veranderingen in levende periferale lymfocyten spectraal gezien gevolgd worden. We laten Raman beelden zien die opgenomen zijn in minder dan twee minuten: over het algemeen kunnen 10-15 Raman afbeeldingen verkregen worden voordat beschadigingen aan de cel in de vorm van membraanuitsulpingen zichtbaar werden. Herhaaldelijke beeldvorming van lymfocyten laat biochemische veranderingen in specifieke moleculen zoals carotenoïden zien, welke door het laserlicht geïnduceerd zijn.

Hoofdstuk 4 beschrijft de ontwikkeling van microbioreactoren die optisch aan de confocale Ramanmicroscoop gekoppeld kunnen worden. De microbioreactoren zijn, onder continue doorstroming met celkweekmedia, met succes gebruikt voor lange termijn toepassingen op botweefseltechnologie die op cellen gebaseerd is. De microbioreactoren maakten optimale kweekomstandigheden mogelijk voor de cellen gedurende kweekperioden tot 21 dagen. Celactiviteiten als groei, voortplanting, differentiatie en mineralisatie in de microbioreactor werden op efficiente wijze en met een chemische gevoeligheid gevolgd door confocale Raman microspectroscopie.

Een vergelijking van de invloeden van verschillende osteogene en niet-osteogene celkweekmedia op de ontwikkeling van iMSCs wordt in ***Hoofdstuk 5*** gepresenteerd. Op dag drie van celkweek in osteogene media voorzien van dexamethason, werd een reductie in de concentratie proline in de cellen geobserveerd. Deze reductie in prolineconcentratie werd geïdentificeerd als Raman biologische markering (biomarker) voor differentiatie van onsterfelijke menselijke stromale cellen uit het beenmerg (iMSCs) naar osteogene cellijnen in een vroeg stadium. Samen met Raman verschilspectroscopie, bevestigen univariate en multivariate analyses van de spectrale data, verkregen op dag 3 en dag 7 van de celkweek, de variatie in proline niveaus als gevolg van de verschillende osteogene en niet-osteogene kweekmedia.

In ***Hoofdstuk 6*** worden de Raman biomarkers beschreven die de pluripotentie van iMSCs naar osteogene en adipogene cellijnen weerspiegelen. Verschillende osteogene celkweekmedia beïnvloeden de expressie van pluripotentie. Variatie in de glycogeenconcentratie in de cellen definieert de verschillende stadia van osteogene cellijnen, zoals pre-osteoblasten, osteoblasten en osteocyten. Een uitgesproken aanwezigheid van lipide globuli (bolwolkjes) bevestigde differentiatie naar de adipogene cellijn. Veranderingen in pH, die de glycogeensynthese in cellen beïnvloeden, resulteerden in veranderingen n de chemische samenstelling van mineralisatie van de extracellulaire matrix richting hydroxyapatiet of calciumoxalaat. De mineralisatie van hydroxyapatiet wordt verder beïnvloed door de aanwezigheid van osteogene groeifactoren in de celkweekmedia, hetgeen resulteerde in normaal of gecarboniseerd hydroxyapatiet. Mineralisatie is ook geobserveerd in cellen die differentieerden naar adipogene cellijnen en wordt toegeschreven aan de aanwezigheid van fosfatidylserine dat voldoende calciumionen transporteert om tot hydroxyapatietvorming aan te zetten.

Hoofdstuk *7* illustreert de mineralisatie in de extracellulaire matrix van iMSCs, gedifferentieerd naar osteogene cellijnen. Vanaf kweekdag 30 werden vroeg gemineraliseerde noduli (knoopjes) met sterk heterogene compositie geobserveerd. De informatie uit de Ramanspectra van deze noduli legde de aanwezigheid van amorf calciumfosfaat, mono-calciumfosfaat-mono-hydraat, di-calciumfosfaatdi-hydraat en b-tri-calciumfosfaat bloot, in sommige gevallen in dezelfde nodulus. In langdurige celkweek transformeerden deze noduli naar een meer homogene nodulus, waarin op dag 40 hydroxyapatiet aanwezig was, resulterend in gecarboniseerd hydroxyapatiet op dag 60. De omzetting van hydroxyapatiet naar gecarboniseerd hydroxyapatiet resulteerde in toenemende kristalliniteit van het apatiet, hetgeen spectroscopisch geverifieerd werd door de aanwezige Raman banden van carbonaten, vergezeld van een toename in frequentie en afname in bandbreedte van de band karakteristiek voor de fosfaat ν_1 vibratie. Tussen kweekdag 40 en 60 ontwikkelde de lipiderijke organische fase, die waargenomen werd gedurende de vorming van heterogene botnoduli, zich tot een anorganische fase rijk aan proteinen.

In ***Hoofdstuk 8*** beschrijven we langetermijnstudies ter begrip van op cel gebaseerde botvorming, waarbij we gebruik maken van confocale Ramanmicroscopie, coherentie anti-Stokes Raman spectroscopie (CARS) en tweede harmonische generatie (SHG) beeldvorming. CARS en SHG maakten een driedimensionaal begrip mogelijk van vroege tot late stadia van op cel gebaseerde botvorming. De aanwezigheid van collageen, glycosaminoglycanen (GAGs), cholesterol, fosfatidinezuur (FZ) en fosfatidylserine (FS) in de cellen rond dag 25 en 30 wijzen op goed gedifferentieerde osteogene cellijnen van iMSCs. De hoeveelheid collageen nam toe met de kweektijd. Cholesterol, FZ en FS beïnvloedden de aanvankelijke hydroxyapatiet (HA) mineralisatie rond dag 35. Aanvankelijke HA mineralisatie werd in verschillende cellagen waargenomen. HA-depositie nam toe met de kweektijd en werd geleid door de oriëntatie van de collageenfibrillen in de extracellulaire matrix. In de loop van de tijd werd geleidelijke omzetting van HA naar gecarboniseerd hydroxyapatiet duidelijk geobserveerd.

Hoofdstuk 9 illustreert de potentie van Raman microspectroscopie voor een verscheidenheid aan cel- en weefselgebaseerde toepassingen. We hebben hybride microscopietechnieken gebruikt om de fysieke status van de cellen te identificeren, gebaseerd op de morfologie van de celkern, hetgeen het bovendien mogelijk maakte de distributie van RNA en DNA in de celkern te localiseren. Raman microspectroscopie werd gebruikt om de distributie van mitochondria in de cellen, alsmede de invloed van variaties in de concentratie ambiente Ca^{2+} ionen op mitochondriale activiteit te identificeren.

Beeldvorming door middel van Raman microspectroscopie onthulde de aanwezigheid van het Gall lichaam in CD4+ PBL cellen, dat bestaat uit verschillende typen carotenoïden. Deze carotenoiden werden geïdentificeerd door de variatie in bandintensiteit en -breedte van de banden rond 1154 en 1520 cm^{-1}, die karakteristiek zijn voor carotenoïden. Bovendien werd de rol van carotenoïden in mineralisatievoorvallen van iMSCs bewezen vanuit de Raman beeldvorming. Tot slot bediscussiëren we kort de ontwikkeling van een lijn-scan Raman microscoopsysteem, voor snellere beeldvorming voor toepassingen op het gebied van weefseltechnologie.

Acknowledgements

The research described in this thesis started four years ago. Those four years turned out to be an unforgettable and wonderful learning experience. I take this opportunity to express my sincere gratitude to all the people who have significantly contributed to making my professional and social life in The Netherlands a worthwhile experience. With great pleasure, I write these pages which I am sure will be the ones most widely read....

Vinod, thank you very much for the opportunity to pursue my Ph.D. at the Biophysical Engineering group. I owe my deepest gratitude to you for all the encouragements and invaluable suggestions in shaping up the beginning of my professional career. I am extremely grateful to you for the unparalleled support and motivation with my project and writing my thesis.

Cees, thank you very much for the wonderful guidance, untiring discussions, infinite enthusiasm and total flexibility you granted me with my research. I am very much grateful to you for giving me an opportunity to work in this interesting line of research. Your support and confidence from the very beginning enabled me to successfully perform research which eventually instilled a scientific attitude in me.

Clemens, I still remember the day when I first met you at Bilthoven (Jan 24th, 2006) where I was being invited for an interview from India. Thank you very much for the timely suggestion and direction to the Biophysical Engineering group. I am very much grateful that I could work within the framework of the “Continuous real-time 3D Raman monitoring of cell behaviour in bioreactors” project and could use all the facilities at the Tissue Regeneration group.

I express my gratitude to the Dutch Program for Tissue Engineering (DPTE, TGT.6737) for the generous financial support which enabled the smooth running of the project and my attendances to numerous conferences and seminars.

I would like to thank my external graduation committee members Prof. Dr. G. van der Steenhoven, Prof. Dr. C. A. van Blitterswijk and Prof. Dr. J. L. Herek, Prof. Dr. M. Morris and Dr. A. B. Vaandrager for their time and effort reviewing this thesis and for their valuable comments and suggestions.

I am very much grateful to the past and present amicable Biophysical Engineering group colleagues who played a vital role in my scientific, technical and/or social Ph.D. life. Aufried, heart and soul of the Raman setup, thank you for the wonderful support and technical help with it. Henk Jan, thanks for initiating me to the Raman set-up and data processing, without you I would have had to re-invent the wheel. Sylvia, you kept the group going, thanks for all the great administrative support with orders, conferences and group outings. Yvonne, Kirsten and Wilma, you managed to keep the cell culture and biochemical lab running, thank you very much for helping me

with timely orders and the initial chemistry and biology at the lab. Wiendelt, I am thankful to you for helping me with downloading all those journal articles. FRINS-groupies, Maryana (for all the suggestions and advices), Chien-Ching, Liesbeth, Chandra, Dianwen, Niek (for the help with revamping the codes), Gerrit, and Jasper, thank you for all the good time and interesting discussions during the work meetings. Dodo, special thanks to you for all the wonderful help, support and advice. Remco, you were a good prankster, thanks to you for all the unforgettable help and providing a nice time at the office. Liesbeth and Remco, thank you for the kind help with the 'Samenvatting' of my thesis. Bart, thanks for all the pre-defense and pre-thesis printing suggestions. Christian Breukers thanks for keeping my computer up and running which at times was not an easy task (four hard drives!). Special thanks to my office mates for providing a cordial work atmosphere in Zuidhorst: Dodo, Joost, Frank, Henk Jan, Martijn and Jan Halamek, and at Hogekamp: Kiran, Babu, Vinay, Alex and Matthijs. All the people from BPE, thanks for providing a memorable time. Ine, Alma-Aurel, Roy, Martin Bennink, Mireille, Srirang, Kees, Marloes, Robert, Erwin, Johan, Frans, Christian Blum, Yanina, Tom, Arjen, Cynthia, Cicerone, Raja Gopal, Arun, Jithen, Shashank, Constantin-Felicia, Dirk, Marieke, Kim, Guus, Sjoerd, Peter, Martijn Stopel and Tycho.

Jennifer and Herman thank you for the wonderful collaboration with the Optical Science group. Martin thanks to you for all the CARS measurements on my samples. It was great fun working with you.

I would like to thank Edwin and Mingliang from BIOS – The lab on a chip group, and Bas and Nicole from Utrecht University for the kind collaborations which exposed me to new scientific areas.

From Tissue Regeneration group, Marcel, thank you very much for providing us with the cells, I could not have done without them. Many thanks to Jan, Aart, Anouk, Joyce, Jun, Ram Siddappa, André, Hugo, Ana, Gustavo, Nicolas and Hemant for discussions and advices regarding cell culture experiments. Audrey, special thanks to you for all the timely administrative help and popularising my name as "Mr. Pully".

Thanks to the clean room staff at the MESA$^+$ for all the introductions, discussions and advice regarding the microfabrication part in Chapter 4 of my thesis.

I extend my heartfelt gratitude to my friends who made the past four years memorable ones. Sheshan-Jayanthi, Raghav, Anand Chakinala, Ganesh-Karthika (little-Nirupa), Anand-Shubashini, Kiran-Kavitha, Anand-Renuka, Vijay-Ranjani, Shodhan-Chaitanya, Vishy-Aliz, Srikumar-Sowjanya, Hrudya, Jitendra, Ashok, Srivatsa, Sandeep, Srikanth Shastry, Suresh, Ashwin and many other Indian friends. Dodo-Pascal, Remco-Ilze and Dirk thanks for wonderful company and delicious dinners, and being a victim of my Indian cuisines.

I am fortunate to have met with Prof. Shankaranarayanan uncle and Kokila aunty. Thank you very much for the great company and for making me feel at home.

I am extremely thankful to Prof. Ramareddy V. Guntaka, Prof. G. Durairaj and Prof. Lazar Mathew, without their timely advice and assistance I wouldn't have come this far.

I would not have been what I am today if it was not for the love, care and encouragement from my parents. I am extremely fortunate and grateful to have such excellent parents and a wonderful sister, Sruthi. Thank you very much for all the support and faith in me.

P. Vishnu Vardhan

Enschede, March 2010

About the author

Vishnu Vardhan Pully was born on September 9th, 1981 in Bellary, India. After graduating from high school in Chennai in 1998 he went to study Bachelor of Engineering in Electronics and Communications at the University of Madras, India. He joined the Master of Technology in Biomedical Engineering at the Vellore Institute of Technology, India in July 2003. He completed his Masters degree with first class and distinction in June 2005. Later, he worked as a software program analyst at Cognizant Technology Solutions-Chennai for a brief period of time.

In May 2006 he joined the Biophysical Engineering Group at the University of Twente, The Netherlands as a PhD candidate under the supervision of Dr. Cees Otto and Prof. Dr. Vinod Subramaniam on the topic "From Cells to Bone: Raman Microspectroscopy of the Mineralization of Stromal Cells". The results of this multidisciplinary research involving vibrational spectroscopy, bone tissue engineering and microbioreactors, are described in this thesis.

List of publications

Journal Articles

- *V.V. Pully* and C. Otto, “The intensity of the 1602 cm^{-1} band in human cells is related to mitochondrial activity,” Journal of Raman Spectroscopy, 2009, 40(5): 473-475.
- *V.V. Pully*, A. Lenferink and C. Otto, “Hybrid Rayleigh, Raman and TPE fluorescence spectral confocal microscopy of living cells”. Journal of Raman Spectroscopy, DOI: 10.1002/jrs.2501.
- *V.V. Pully*, A. Lenferink, C. Otto, "Raman-fluorescence hybrid microspectroscopy of cell nuclei". Vibrational Spectroscopy, DOI:10.1016/j.vibspec.2009.11.004.
- *V.V. Pully*, A. Lenferink, H.J van Manen, V. Subramaniam, C.A. van Blitterswijk and C. Otto, “Microbioreactors for Raman microscopy of stromal cell differentiation”. Analytical Chemistry, DOI: 10.1021/ac902515c.
- *V.V. Pully*, A. Lenferink, and C. Otto, “Time lapse Raman imaging of single live lymphocytes”. Journal of Raman Spectroscopy, (accepted).
- *V.V. Pully*, A. Lenferink, V. Subramaniam, C.A. van Blitterswijk and C. Otto, “Proline as an early Raman biomarker for differentiation of human bone marrow stromal cells”. Analytical Chemistry, (in review).

Journal Articles (in preparation)

- *V.V. Pully*, A. Lenferink, V. Subramaniam, C.A. van Blitterswijk and C. Otto, “Raman markers for stem cell pluripotency”.
- *V.V. Pully*, A. Lenferink, V. Subramaniam, C.A. van Blitterswijk and C. Otto, “Events of mineralization in osteogenesis – from de novo to crystalline bone”.
- *V.V. Pully*, M. Jurna, L.N. Azar, A. Lenferink, J.P. Korterik, V. Subramaniam, C.A. van Blitterswijk, J. Herek, H.L. Offerhaus and C. Otto, “How cells make bone”.
- *V.V. Pully*, A. Lenferink, V. Subramaniam, C.A. van Blitterswijk and C. Otto, “Role of retinol in bone formation”.
- *V.V. Pully*, A. Lenferink and C. Otto, “Variation in composition of carotenoids in Gall Bodies of CD4+ PBL cell”.
- M. Escalante, *V.V. Pully*, I. Segers-Nolten, C. Otto and V. Subramaniam, “Template Assisted growth of superfibrils”.

Book Chapter (in preparation)

- *V.V. Pully* and C. Otto, “Raman microspectroscopy to monitor tissue development in microbioreactors”, in Biomedical Applications of Raman and Infrared Spectroscopies, IOP press.

Conference Contribution (Oral Presentation)

- *V.V. Pully*, A. Lenferink, V. Subramaniam, C.A. Van Blitterswijk, C. Otto. “Stemness of stem cells as determined by confocal Raman microspectroscopy”. European Conference on the Spectroscopy of Biological Molecules-2009, Palermo, Italy.
- M. Jurna, J.P. Korterik, *V.V. Pully*, C. Otto, H.L. Offerhaus. "Vibrational phase contrast microscopy". 8th European Conference on Nonlinear Optical Spectroscopy- 2009, Rome, Italy.
- *V.V. Pully*, A. Lenferink*, V. Subr*amaniam, C.A. Van Blitterswijk, C. Otto. “Non invasive and label free analysis of osteogenic events during mineralization of human bone marrow derived stem cells”. Focus on Microscopy-2009, Krakow, Poland.
- N. Testerink, M. Ajat, M. Houweling, J. Brouwers, *V.V. Pully*, H.J. van Manen, C. Otto, J.B. Helms, A.B. Vaandrager. "Raman imaging and lipidomic analysis of lipid droplets in (activated) hepatic stellate cells". Frontier Lipidology: Lipidomics in Health and Disease-2009, Gothenburg, Germany.
- A.B. Vaandrager , N. Testerink, M. Ajat, M. Houweling, J. Brouwers, *V.V. Pully*, H.J. van Manen, C. Otto, J.B. Helms. "Raman imaging and lipidomic analysis of lipid droplets in (activated) hepatic stellate cells". 50th International Conference on the Bioscience of Lipids-2009, Regensburg, Germany.
- *V.V. Pully*, A. Lenferink, V. Subramaniam, C.A. Van Blitterswijk, C. Otto. “The changing cell as observed by hybrid microscopy”. Annual Dutch meeting on Molecular and Cellular Biophysics-2008, Veldhoven, The Netherlands.
- *V.V. Pully*, A. Lenferink, A.A. Van Apeldoorn, V. Subramaniam, C.A. Van Blitterswijk, C. Otto. “Hybrid Raman and two photon fluorescence imaging of osteogenesis of human bone marrow derived cells in a micro–bioreactor”. 21st International Conference on Raman Spectroscopy-2008, Middlesex, United Kingdom.
- *V.V. Pully*, A. Lenferink, A.A. Van Apeldoorn, V. Subramaniam, C.A. Van Blitterswijk, C. Otto. “Osteogenesis of human bone marrow derived cells in a PDMS microbioreactor”. 8th World Biomaterial Conference-2008, Amsterdam, The Netherlands.
- *V.V. Pully*, A. Lenferink, C. Otto. “Time lapse Raman imaging of living cells”. Focus on Microscopy-2008, Osaka, Japan.

Conference Contribution (Poster Presentation)

- *V.V. Pully*, A. Lenferink, V. Subramaniam, C. van Blitterswijk, C. Otto. “Dynamics of bone production by cells, as observed by Raman microscopy”. Annual Dutch meeting on Molecular and Cellular Biophysics 2009, Veldhoven, The Netherlands.
- M. Jin, D. Wijnperlé, *V.V. Pully*, C. Otto, A. van den Berg, E.T. Carlen. "Nano-pyramid arrays for surface enhanced Raman spectroscopy". Materials Research Society-2009, San Francisco, USA.
- *V.V. Pully*, A. Lenferink, V. Subramaniam, C.A. Van Blitterswijk, C. Otto. “Raman microscopy for determining the osteogenesis of human bone marrow derived cells in a PDMS microbioreactor”. Highlight in Biomedical Technology 2008, Enschede, The Netherlands.
- *V.V. Pully*, A. Lenferink, V. Subramaniam, C.A. Van Blitterswijk, C. Otto. “Raman microscopy for determining the osteogenesis of human bone marrow derived cells in a PDMS microbioreactor”. DPTE-Symposium on Tissue Engineering 2008: Noordwijkerhout, The Netherlands.
- *V.V. Pully*, A. Lenferink, A.A. Van Apeldoorn, V. Subramaniam, C.A. Van Blitterswijk, C. Otto. “A 3-dimensional PDMS microbioreactor for label free Raman analysis of the osteogenesis of human mesenchymal stem cells”. First international workshop on label free bio-sensing 2008, Enschede, The Netherlands.
- *V.V. Pully*, A. Lenferink, A.A. Van Apeldoorn, V. Subramaniam, C.A. Van Blitterswijk, C. Otto. “Confocal Raman microspectroscopic imaging of tissues in a PDMS microbioreactor”. Annual Dutch meeting on Molecular and Cellular Biophysics 2007: Veldhoven, The Netherlands.
- *V.V. Pully*, A. Lenferink, H.J. van Manen and C. Otto. "Time lapse Raman imaging of living cells". Annual Dutch meeting on Molecular and Cellular Biophysics 2007, Veldhoven, The Netherlands.

- *V.V. Pully*, A.A. Van Apeldoorn, V. Subramaniam, C.A. Van Blitterswijk, C. Otto. “A 3-Dimensional PDMS microbioreactor for fluorescence and raman analysis of human mesenchymal stem cells”. 12th ECSBM 2007: Paris, France.
- *V.V. Pully*, A. Lenferink, S. Schlautmann, A.A. Van Apeldoorn, V. Subramaniam, C.A. Van Blitterswijk, C. Otto. “Confocal Raman microspectroscopic imaging of tissues in a PDMS microbioreactor”. DPTE-Symposium on Tissue Engineering 2007: Noordwijkerhout, The Netherlands.
- *V.V. Pully*, A. Lenferink, A.A. van Apeldoorn, V. Subramaniam, C.A. van Blitterswijk, C. Otto. “Confocal Raman microspectroscopic imaging of tissues in a PDMS microbioreactor”. Focus on Microscopy 2007: Valencia, Spain.
- *V.V. Pully*, A. Lenferink, A.A. van Apeldoorn, V. Subramaniam, C. Olivo, C.A. van Blitterswijk, C. Otto. “Confocal Raman microspectroscopic imaging of tissues in a bioreactor”. Annual Dutch meeting on cellular and molecular biophysics 2006: Lunteren, The Netherlands.